Measurement of the proton scalar polarizabilities at MAMI

Dissertation by

Edoardo Mornacchi
born in Milan

Submitted to attain
the academic degree of
Doctor of Natural Sciences

to the

Faculty of Physics, Mathematics and
Computer Science (FB 08)
of the Johannes Gutenberg-Universität Mainz

Mainz, March 2021

Measurement of the proton scalar polarizabilities at MAMI

1. Reviewer:
2. Reviewer:

Date of the defense: June, 8th 2021

Edoardo Mornacchi
A2 Collaboration
Institut für Kernphysik
Johannes Gutenberg-Universität
Johann-Joachim-Becher-Weg 45
D-55128 Mainz
emornacc@uni-mainz.de

Abstract

The scalar polarizabilities, α_{E1} and β_{M1}, are fundamental static properties of the nucleon, like the mass or the charge. Together with the four spin polarizabilities, they describe the response of the nucleon's internal structure to an external electromagnetic field. An experimental determination of these parameters is possible via nuclear Compton scattering on protons and neutrons.

Within this dissertation, Compton scattering on protons was studied in an experiment performed at the tagged photon facility of the Mainz Microtron (MAMI). A linearly polarized photon beam impinged on a liquid hydrogen target and the scattered photons were detected using the Crystal Ball/TAPS calorimeter, which provides large acceptance together with an excellent energy and angular resolution for photon detection. The unpolarized differential cross-section and photon beam asymmetry were measured with unprecedented precision for photon beam energies from 85 to 140 MeV, in a scattered photon polar angle range from 30° to 150°.

Using only these data, new values of the two proton scalar polarizabilities

$$\begin{aligned} \alpha_{E1} &= (11.43 \pm 0.17 \pm 0.59 \pm 0.33) \times 10^{-4}\text{fm}^3, \\ \beta_{M1} &= (3.08 \pm 0.24 \pm 0.20 \pm 0.28) \times 10^{-4}\text{fm}^3 \end{aligned}$$

were extracted. The quoted uncertainties are related to the statistical and systematic errors of the experiment and to a model dependence in the extraction of the polarizabilities, respectively. These new results have a precision which is comparable to several current global extractions using different theoretical frameworks and combining all previous data. They will be crucial to resolve ambiguities in these existing extractions.

The new data provide an important contribution to the experimental Compton scattering program at MAMI. They will be used in combination with already published results on single and double spin observables allowing for a combined extraction of all the six proton polarizabilities from experimental data measured at the MAMI tagged photon facility.

Contents

List of Figures

List of Tables

Acronyms

χEFT Chiral Effective Field Theory

ADC Analog-to-Digital Converter

BχPT Baryon Chiral Perturbation Theory

BNL Brookhaven National Laboratory

CATCH Compass, Accumulation, Transfer and Control Hardware

CB Crystal Ball

CERN Conseil Européen pour la Recherche Nucléaire (European Organization for Nuclear Research)

CFD Constant Fraction Discriminator

CGS Centimeter–Gram–Second

COMPASS COmmon Muon and Proton Apparatus for Structure and Spectroscopy

CW Continuous Wave

DAQ Data AcQuisition

DESY Deutsches Elektronen-SYnchrotron

DR Dispersion Relation

EFT Effective Field Theory

EWT ElectroWeak Theory

GoAT Generation of Analysis Trees

GUI Graphical User Interface

HBχPT Heavy Baryon Chiral Perturbation Theory

HDSM Harmonic Double Sided Microtron

LEC Low-Energy Constant

LEX Low-Energy eXpansion

LG Long Gate

LHCb Large Hadron Collider beauty

LQCD Lattice Quantum ChromoDynamics

MAMI Mainz Microtron

MESA Mainz Energy-recovering Superconducting Accelerator

MWPC Multi Wire Proportional Chamber

PDG Particle Data Group

PID Particle Identification Detector

PMT PhotoMultiplier Tube

PSA Pulse Shape Analysis

QCD Quantum ChromoDynamics

QED Quantum ElectroDynamics

RTM RaceTrack Microtron

SADC Sampling ADC

SAL Saskatchewan Accelerator Laboratory

SG Short Gate

SiPM Silicon PhotoMultiplier

SLAC Stanford Linear Accelerator Center

TAPS Two-Arm Photon Spectrometer

TCS Trigger Control System

TDC Time-to-Digital Converter

ToF Time-of-Flight

Chapter 1

Introduction

A memorable series of experiments performed between 1908 and 1913 by Hans Geiger and Ernest Mardsen, under the supervision of Ernest Rutherford, posed the basis for the discovery of the proton. The unexpected results showed that in every atom all the positive charge and almost all the mass is concentrated in a tiny core, called the atomic nucleus. As is widely known, they inferred these results by studying the angle at which an alpha particle is scattered when it impinges on a thin gold foil [1]. They also went one step further and hypothesized that the nucleus of an atom consists of a fixed number of the nucleus of the smallest possible atom, hydrogen, and this is the simplest brick of matter, later called "proton". This new particle was considered point-like for many years, but around the middle of the last century it became clear that, despite its name, the proton is not a basic constituent of matter — in fact it has its own internal structure. Since then, there have been both huge theoretical and huge experimental efforts to describe and study the internal structure and dynamics of the proton. But despite this, we are still far from having a complete understanding of it, as clearly illustrated by the recent proton radius puzzle [2].

Currently the structure of the proton is partially described by the so-called Standard Model of particle physics. It is a theoretically self-consistent model that describes three — electromagnetic, weak and strong — out of the four (the gravitational force is not included, yet) fundamental forces in the universe, together with all the known elementary particles. It was constructed during the second half of the last century, collecting together all the experimental and theoretical efforts and results. Its current theoretical formulation was finalized with the experimental discovery of the quarks — theoretically predicted by Murray Gell-Mann [3] and George Zweig [4, 5] in 1964 — at the Stanford Linear Accelerator Center (SLAC) in 1968 [6]. In the following years, many other experimental

confirmations, from the top quark to the very famous Higgs boson, brought more reliability to the Standard Model. Nevertheless, it still leaves various phenomena unexplained, such as neutrino oscillations, the emergent structure of the hadrons, or the incorporation of the last fundamental interaction: gravitation. This indicates that still a lot of effort is needed to completely understand the four forces and the theory that describes them.

The weak interaction is necessary to describe the radioactive beta decay between the subatomic particles and it is mediated by the massive vector bosons $W^{\pm}$ and Z^0. It is usually unified with the electromagnetic interaction in the so-called ElectroWeak Theory (EWT). The latter is well described by Quantum ElectroDynamics (QED), governing the interactions between charged point-like particles mediated by photons. However, when the interaction occurs among non-point-like particles, such as protons, a model of the internal structure is also required in order to describe the charge and magnetic distributions probed by the photon. This last part is done by Quantum ChromoDynamics (QCD), the quantum field theory describing the strong force, or the interaction between quarks and gluons. In fact, at the scale of the proton radius (~ 0.8 fm), the strong interaction is responsible for linking the quarks together and confining them into hadronic particles. At larger scales, around 1 to 3 fm, this strong force is still present, effectively described by the exchange of mesons, and is responsible for binding protons and neutrons together to form the nucleus of an atom. This particular behavior comes from the two main properties of QCD: confinement and asymptotic freedom. The former is a consequence of the force acting between quarks, which increases with the distance. In fact, in order to pull apart two quarks within a hadron, a constantly increasing amount of energy is required. At some point, this energy becomes large enough to spontaneously produce a quark-antiquark pair, and to split the hadron into two hadrons. This property has been confirmed by different experiments and makes it impossible to have one single isolated quark. The second property, asymptotic freedom, causes the interaction between gluons and quarks to become weaker and weaker as the energy scale increases (and so the distance between them decreases). This particular behavior that earned Gross, Wilczek and Politzer the Nobel prize in 2004, allows for perturbative QCD calculations in the high energy range. In fact, this approach provides a very powerful, even if limited, tool to produce valid predictions in the region where QCD is dominated by asymptotic freedom. In this region, the strong force coupling constant α_s is small and hence in a perturbative expansion, the higher order terms can be neglected. On the other hand, as the distance increases and the energy decreases,

the coupling constant becomes larger and already at the distance scale of the size of a proton, perturbative QCD cannot provide acceptable solutions. This means that it cannot be used to directly calculate global properties of the hadron, such as mass, size, shape, or stiffness (polarizability). In this regime, the most promising non-perturbative approach is lattice QCD [7,8], a theory that discretizes the space-time into a lattice of points, where the points represent the quark fields and the links between the points are the gluons. As the lattice spacing a goes to zero and the lattice size goes to infinity, the description of space-time becomes more complete. On the other hand, the calculations are unfortunately incredibly computationally expensive and they require huge clusters of computers and a lot of machine-time. For this reason, results from lattice QCD at $a = 0$ are normally extrapolated from the results obtained at bigger values of a. A different approach is given by the effective field theories, which are models with same symmetries as QCD that include an appropriate number of degrees of freedom to describe the physical processes at a given energy (or distance) scale, ignoring the substructures and the degrees of freedom at higher energy, or shorter distances. In the past years, different QCD-inspired effective models have been developed, and nowadays there is still a big common effort in trying to connect and to match these models with the experimental results.

This thesis finds part of its motivation in this context. It aims to provide a new high precision extraction of the scalar polarizabilities, which are structure observables of the proton accessible via nuclear Compton scattering. Discovered by Arthur Holly Compton in 1923 [9] (he was awarded the Nobel prize for this four years later), it is a two-body inelastic scattering of a photon by a charged particle that could be an electron, as in the original Compton experiment, or a proton, as in our case:

$$\gamma + p \to \gamma' + p'. \tag{1.1}$$

At very low energy (few MeV), the proton can be considered a point-like particle, and so the scattering cross-section depends only on its charge and mass. When increasing the energy up to the pion photoproduction threshold ($\simeq$ 140 MeV), the scattering cross-section starts to be sensitive to the internal structure of the proton, and in particular to the electric and magnetic dipole scalar (spin independent) polarizabilities, α_{E1} and β_{M1}, respectively. They describe the response of the proton structure to an electric or magnetic field. Above the pion photoproduction threshold, the higher terms in the cross-section must be included, and these include the spin polarizabilities — γ_{E1E1}, γ_{M1M1}, γ_{E2M1} and γ_{M1E2} — that describe the response of the proton spin to the electromagnetic interac-

tion. In the last decade there has been significant interest in extracting both the scalar and the spin polarizabilities using both subtracted dispersion relations and chiral effective field theory [10–13]. In fact, in addition to being fundamental properties of the nucleon, they play a profound role in the evaluation of the nuclear corrections to atomic energy levels. For example, the uncertainties of the recent muonic-hydrogen experiments at the Paul Scherrer Institut (PSI) [2, 14] are dominated by the proton polarizability contributions. More specifically, the scalar polarizabilities affect the Lamb shift and hence the proton radius extraction, whereas the spin polarizabilities affect the hyperfine structure and hence the extraction of the Zemach radius, which is defined as a convolution of the charge distribution with the magnetic moment distribution. Analogous effects arise in muonic deuterium [15]. They also play a big role in the determination of the electromagnetic contribution to the proton-neutron mass difference [16]. Moreover, the various moments of the spin structure functions of the nucleon are related to the spin polarizabilities and one of them, δ_{LT}, is difficult to understand within chiral effective field theory [17]. More generally, a precise extraction of the polarizabilities from the data can provide strong guidance by favoring, or disfavoring, models of hadron structure and of non-perturbative QCD.

Due to this keen interest, a series of both polarized and unpolarized Compton scattering experiments was proposed and conducted at the Mainz Microtron (MAMI) tagged photon facility in Mainz, Germany. The measurements used both linearly and circularly polarized photon beams together with an unpolarized LH_2 or a polarized butanol target. Different combinations of these beam and target configurations allowed for the measurement of single and double polarization asymmetries (Σ_3, Σ_{2x} and Σ_{2z}), as well as for the measurement of the unpolarized differential cross-section. This very exciting (but complex) experimental program has already led to the publication of the first two experimental extractions of the spin polarizabilities from data [18, 19] as well as to the first measurement of the beam asymmetry Σ_3 below the pion photoproduction threshold [20]. The work of this thesis is the missing part of the program on the proton, and provides a measurement of the Compton scattering unpolarized differential cross-section and the beam asymmetry Σ_3 from $85 - 140$ MeV, with unprecedented precision. These results, together with those published already, will allow for a precise extraction of all the six (two scalar + four spin) proton polarizabilities from experimental data coming from the MAMI facility.

First, a theoretical overview of Compton scattering and the proton polarizabilities is given in Chapter 2, together with a discussion on the two measured

observables (the unpolarized cross-section and the beam asymmetry) and their sensitivity to the scalar polarizabilities. Chapter 3 is devoted to the existing experimental measurements and the different theoretical extractions of the proton scalar polarizabilities from those data. After this, the focus will move to the experiment, which is the main subject of all this work. Chapter 4 is dedicated to a short description of the experimental setting used for the measurements, and Chapter 5 to the calibration and the reconstruction of those data. Chapter 6 is focused on the analysis of the photon beam for the extraction of the degree of linear polarization and the photon flux. In Chapter 7, the analysis that has been done to select the final sample and to extract the observables is explained in detail. In Chapters 8 and 9 the results of the unpolarized cross-section and beam asymmetry Σ_3 are presented, together with a discussion on the many systematic checks done in order to assure a complete understanding of the data used. Finally, in Chapter 10 the impact of these data will be discussed, together with an extraction of the proton scalar polarizabilities α_{E1} and β_{M1}.

1.1 Units and conventions

In this dissertation, the natural units $\hbar = c = 1$ are used. Other used conventions are:

- the laboratory frame of reference is used for all the angles and energies, if not differently specified,
- γ and γ' refer to the incoming and the scattered photon, respectively,
- ω_γ and $\omega_{\gamma'}$ are used to indicate the incoming and the scattered photon energies, respectively,
- the values of the scalar polarizabilities are always reported in units of 10^{-4} fm^3, and
- the values of the spin polarizabilities are always reported in units of 10^{-4} fm^4.

Chapter 2

Theoretical review

The behavior of light in matter can be described by three main processes that are prominent at different energies:

- Photoelectric effect,
- Compton scattering, including Rayleigh (scattering on a whole atom) and Thomson (scattering on a free electron in the classic limit) scattering, and
- Pair production.

The photoelectric effect, which for hydrogen is the dominant process up to $\sim$ 3 MeV, involves the absorption of a photon by an atomic electron that is subsequently ejected from the atom. Above this energy, atomic (incoherent) Compton scattering becomes more relevant. In this process, the photon scatters on an atomic electron, transferring part of its energy to it and allowing it to escape from the atom. At even higher energies, the photon can interact electromagnetically with the nucleus and produce a electron-positron pair, via pair production. Even though the threshold for this process starts at 1.022 MeV (the rest mass of the e^+/e^- pair), it does not become the main process for hydrogen until the incoming photon energy reaches above 80 MeV. This is not the only pair that can be created; if the energy is high enough also a pion or muon pair can be created via a similar process. Additionally there are several other interesting processes that can happen when a photon interacts with matter, and among them nuclear Compton scattering is the one of interest for this thesis.

2.1 Nuclear Compton Scattering

In nuclear Compton scattering (from now on Compton scattering and nuclear Compton scattering will be used interchangeably) the photon scatters on the

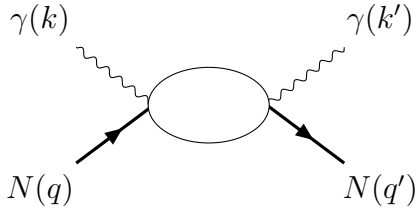

Figure 2.1: Nuclear Compton scattering.

nucleus. As stated in the previous Chapter, this reaction can be used to probe the electromagnetic properties of the nucleus and to access the internal structure of its constituents, the nucleons. The case of hydrogen is of particular interest, since it means scattering on (and therefore accessing) a single proton:

$$\gamma(k) + p(q) \rightarrow \gamma(k') + p(q') \tag{2.1}$$

where, k and k' are the four-momenta of the photon in the initial and final states, respectively, and q and q' are the four-momenta of the proton in the initial and final states, respectively.

2.1.1 Effective Hamiltonian

The scattering amplitude for this process can be conveniently expanded in terms of the incident photon energy ω. In the next paragraph this expansion will be given using the derivation formulated by Levchuk and L'vov [21] up to the fourth order, and the interesting terms will be discussed.

2.1.1.1 Born contribution

The zeroth order expansion describes the scattering of a photon on a point-like charged particle, and it depends only on the charge and mass of the particle. The effective Hamiltonian for scattering on a proton can be written as:

$$H_{\text{eff}}^{(0)} = e\varphi + \frac{\vec{\pi}^2}{2m}, \tag{2.2}$$

where m and e are the nucleon mass and charge, respectively, φ is the scalar potential, and $\vec{\pi}$ is the covariant momentum defined as

$$\vec{\pi} = \vec{q} - e\vec{A}, \tag{2.3}$$

where $\vec{q}$ is the momentum and $\vec{A}$ is the vector potential. At the first order, the effective Hamiltonian is also dependent on the anomalous magnetic moment κ:

$$H_{\text{eff}}^{(1)} = -\frac{e(1+\kappa)}{2m}\vec{\sigma}\cdot\vec{H} - \frac{e(1+2\kappa)}{8m^2}\vec{\sigma}\cdot[\vec{E}\times\vec{\pi} - \vec{\pi}\times\vec{E}], \tag{2.4}$$

where $\vec{E}$ and $\vec{H}$ are the electric and magnetic fields, respectively, $\vec{\sigma}$ are the proton's Pauli spin matrices, and $(1+\kappa)(e/2m)$ represents the contribution from the magnetic moment. These first two terms are usually referred to as the "Born contribution".

2.1.1.2 Proton scalar polarizabilities

As the incident photon energy increases, the Born contribution is not a valid approximation anymore, and the internal proton structure starts to play a role in the Hamiltonian:

$$H_{\text{eff}}^{(2)} = -4\pi\Big[\frac{1}{2}\alpha_{E1}\vec{E}^2 + \frac{1}{2}\beta_{M1}\vec{H}^2\Big], \tag{2.5}$$

where α_{E1} and β_{M1} are the static electric and magnetic scalar polarizabilities, respectively. They describe the response of the electric and magnetic density of the nucleon to an applied external static electromagnetic field [10].

Generally speaking, the polarizability is an intrinsic property of matter, describing the ability to form dipoles. The electric polarizability α, in particular, is "well" known for atoms and molecules. It is the tendency of the electron cloud of these constituents of matter to be distorted by an external electric field and it can be defined as the ratio between the generated dipole moment $\vec{p}$ and the electric field $\vec{E}$. In the Centimeter–Gram–Second (CGS) units system it has the dimension of a volume and for the atoms it usually is of the order of an atomic volume. At a macroscopic level, the atomic polarizability is connected to the average electric susceptibility via the Clausius-Mossotti relation [22].

The polarization mechanism inside a nucleon is far less obvious, but one could think of a proton as a system composed of three quarks (uud) surrounded by a cloud of charged virtual pions, quark-antiquark ($q\bar{q}$) pairs whose constituents are known as sea quarks. Similarly to what happens in an atom, an external electric field generates a dipole moment due to the stretching of the pion cloud within the electric field. The generated electric dipole moment $\vec{p}$ is proportional to the electric field ($\vec{E}$), with α_{E1} being the coefficient of proportionality:

$$\vec{p} = 4\pi\alpha_{E1}\vec{E}. \tag{2.6}$$

In a similar way, an external magnetic field ($\vec{H}$) generates a magnetic dipole moment ($\vec{m}$) in the proton that is proportional to the strength of the field itself, with β_{M1} being the coefficient of proportionality:

$$\vec{m} = 4\pi\beta_{M1}\vec{H}. \tag{2.7}$$

The subscript in the two polarizabilities classifies the multipole radiation: E_ℓ (M_ℓ) indicates a electric (magnetic) dipole ($\ell = 1$) — or quadrupole ($\ell = 2$) — radiation with total angular momentum ℓ.

Since nearly all the mass of a nucleon comes from the binding force, it is a much tighter system than an atom. This causes the proton polarizabilities α_{E1} and β_{M1} to be about three orders of magnitude smaller than the nucleon's volume, and it is therefore conventional to express them in units of 10^{-4} fm^3.

2.1.1.3 Proton spin polarizabilities

The dependence on the spin of the proton enters at the third order in energy of the effective Hamiltonian:

$$\begin{aligned} H_{\text{eff}}^{(3)} = -4\pi\Big[&\frac{1}{2}\gamma_{E1E1}\vec{\sigma}\cdot(\vec{E}\times\dot{\vec{E}}) + \frac{1}{2}\gamma_{M1M1}\vec{\sigma}\cdot(\vec{H}\times\dot{\vec{H}}) \\ &- \gamma_{M1E2}E_{ij}\sigma_i H_j + \gamma_{E1M2}H_{ij}\sigma_i E_j\Big], \end{aligned} \tag{2.8}$$

where $\dot{\vec{E}}$ and E_{ij} are partial derivatives with respect to time and space defined as $\dot{\vec{E}} = \partial_t\vec{E}$ and $E_{ij} = \frac{1}{2}(\nabla_i E_j + \nabla_j E_i)$, respectively. Finally, the four γ factors in Eq. (2.8) — γ_{E1E1}, γ_{M1M1}, γ_{E2M1} and γ_{M1E2} — are the so-called spin polarizabilities. Even though they do not have a simple visualization like the scalar polarizabilities, they can be thought of as an induced precession of the nucleon spin, with the frequency being proportional to the magnitude of the spin polarizabilities and the direction connected to the sign of them [23]. Two linear combinations of the four γs can be defined, and they are known as the forward spin polarizability [24, 25]:

$$\gamma_0 = -\gamma_{E1E1} - \gamma_{E1M2} - \gamma_{M1E2} - \gamma_{M1M1} = (1.0 \pm 0.08) \times 10^{-4}\ \text{fm}^4, \tag{2.9}$$

and the backward spin polarizability [26]

$$\gamma_\pi = -\gamma_{E1E1} - \gamma_{E1M2} + \gamma_{M1E2} + \gamma_{M1M1} = (8.0 \pm 1.8) \times 10^{-4}\ \text{fm}^4. \tag{2.10}$$

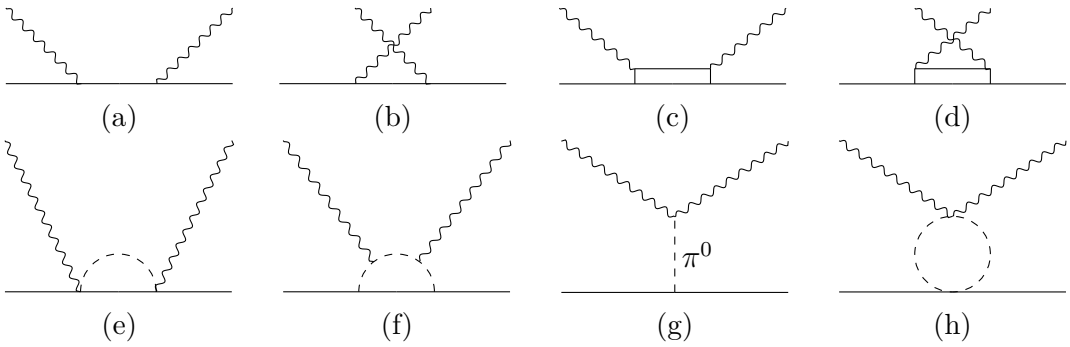

Figure 2.2: Some typical intermediate states contributing to nuclear Compton scattering. (a) and (b) represent the Born diagrams in the s- and u-channel, respectively. (c) shows a typical resonance excitation and (d) its crossed version. (e) and (f) show typical Nπ contributions. (g) is the pion pole diagram. (h) shows a correlated two-pion exchange such as the σ meson.

Their names are due to the fact that they directly appear in the Compton scattering cross-section at $\theta_{\gamma'} = 0°$ and 180°, respectively [27].

2.1.1.4 Quadrupole proton scalar polarizabilities

The Compton scattering amplitude can be extended further in the incoming photon energy ω, even if this is beyond the purpose of this thesis. The fourth order term of the effective Hamiltonian for Compton scattering can be then written as [27]:

$$H_{\text{eff}}^{(3)} = -4\pi\Big[\frac{1}{2}\alpha_{E_\nu}\dot{\vec{E}}^2 + \frac{1}{2}\beta_{M_\nu}\dot{\vec{H}}^2\Big] - 4\pi\Big[\frac{1}{12}\alpha_{E2}E_{ij}^2 + \frac{1}{12}\beta_{M2}H_{ij}^2\Big], \tag{2.11}$$

where α_{E2} and β_{M2} are the quadrupole terms of the electric and magnetic polarizabilities, while α_{E_ν} and β_{H_ν} are the so-called dispersion polarizabilities. They represent dispersive corrections to the static polarizabilities α_{E1} and β_{M1} and they describe the response of the proton to time-dependent electric and magnetic fields [28].

2.1.2 Differential cross-section

The Low-Energy eXpansion (LEX) of the Compton scattering cross-section has been developed by Petrun'kin [29, 30] up to the order ω^2. It is usually divided into two parts:

$$\left(\frac{d\sigma}{d\Omega}\right)_{Pet} = \left(\frac{d\sigma}{d\Omega}\right)_{\text{point}} + \left(\frac{d\sigma}{d\Omega}\right)_{\text{pol}}, \tag{2.12}$$

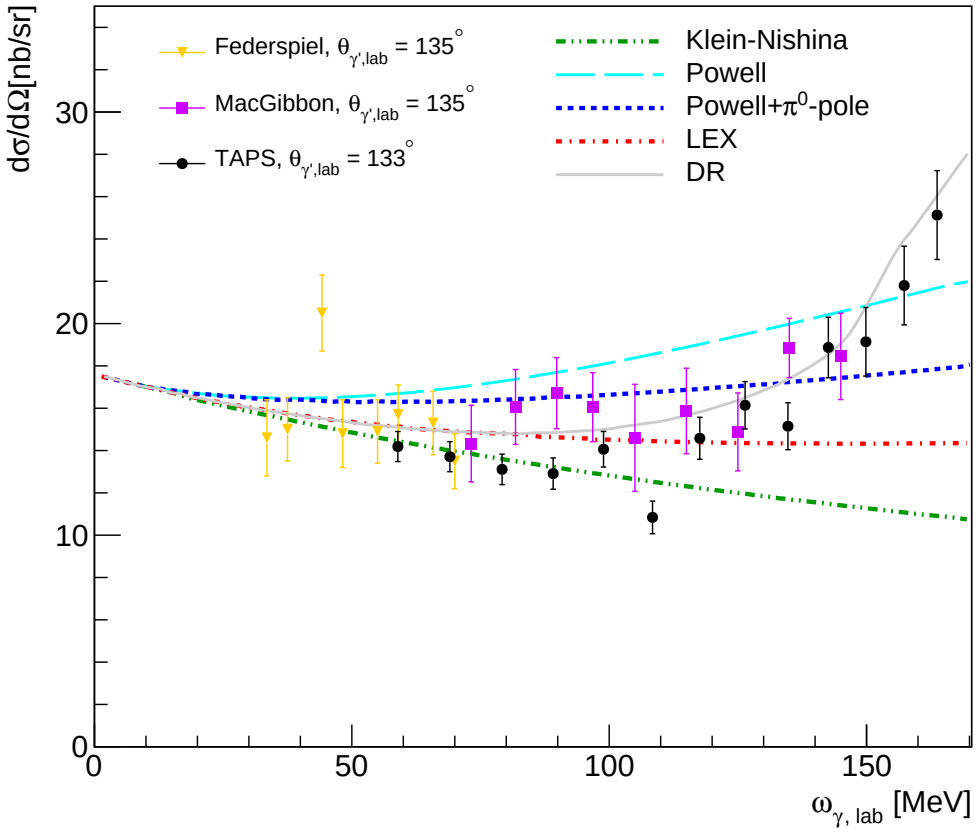

Figure 2.3: Differential cross-section for nuclear Compton scattering on the proton, plotted as a function of the incoming photon energy ω_γ, for fixed scattering angle $\theta_{\gamma'} = 135°$. The curves represent the Klein-Nishina cross-section (green, dashed-dotted-dotted), the Powell cross-section (cyan, long dashed), the Powell cross-section with the contribution from the π^0 pole (blue, short dashed), the Low-Energy eXpansion (LEX) that also includes the leading order contribution from the two scalar polarizabilities (red, dashed-dotted), and the full cross-section calculation from fixed-t subtracted dispersion relations (gray, solid). The points represent some of the available experimental results from different experiments presented in Section 3.1. The higher order terms become more and more important with increasing photon energy, in particular after the pion threshold seen at about 150 MeV.

where the first term on the right side describes Compton scattering on a point-like particle, while the second term accounts for the contribution from the polarizabilities.

2.1.2.1 Point-like contribution

The Compton scattering cross-section of a point-like proton is the so-called Born term described in Section 2.1.1.1, represented in the diagrams in Figs. 2.2a and 2.2b. For incoming photon energy approaching zero, i.e. $\omega \to 0$, the cross-section depends only on the mass and the charge of the proton corresponding to the well-known Thomson scattering formula:

$$\left(\frac{d\sigma}{d\Omega}\right)_{\text{Th}} = \frac{1}{2}\left(\frac{e^2}{m}\right)^2[1+z^2], \tag{2.13}$$

where $z = \cos\theta_{\gamma'}$. $\left(\frac{d\sigma}{d\Omega}\right)_{\text{point}}$ has another term that depends on the anomalous component of the magnetic moment k, and these two terms together give the final expression for the Born contribution [31]:

$$\left(\frac{d\sigma}{d\Omega}\right)_{\text{point}} = \frac{1}{2}\left(\frac{e^2}{m}\right)^2\left(\frac{\omega'}{\omega}\right)^2 \times \left\{1+z^2+\frac{\omega\omega'}{m^2}([1-z]^2+a_o+a_1 z+a_2 z^2)\right\}, \tag{2.14}$$

where the coefficients are:

$$a_0 = 2\kappa + \frac{9}{2}\kappa^2 + 3\kappa^3 + \frac{3}{4}\kappa^4, \tag{2.15}$$

$$a_1 = -4\kappa - 5\kappa^2 - 2\kappa^3, \tag{2.16}$$

$$a_2 = 2\kappa + \frac{1}{2}\kappa^2 - \kappa^3 - \frac{1}{4}\kappa^4. \tag{2.17}$$

Moreover, the energy of the scattered photon ω' in Eq. (2.14) can be calculated with the standard Compton scattering formula:

$$\omega' = \frac{\omega}{1+(\omega/m)(1-z)}. \tag{2.18}$$

In the literature, the cross-section for a point-like particle with an anomalous magnetic moment κ is usually shown in the form evaluated by Powell [32], that

looks slightly different from the one in Eq. (2.14), even though they are equivalent:

$$\begin{aligned}\left(\frac{d\sigma}{d\Omega}\right)_{\text{Pow}} = \frac{1}{2}\left(\frac{e^2}{m}\right)^2\left(\frac{\omega'}{\omega}\right)^2\Big\{&\frac{\omega}{\omega'}+\frac{\omega'}{\omega}-(1-z^2)\\ &+\kappa\frac{\omega\omega'}{m^2}2(1-z)^2\\ &+\kappa^2\frac{\omega\omega'}{m^2}\Big[4(1-z)+\frac{1}{2}(1-z)^2\Big]\\ &+\kappa^3\frac{\omega\omega'}{m^2}[2(1-z)+(1-z)^2]\\ &+\kappa^4\frac{\omega\omega'}{m^2}\Big[1+\frac{1}{2}(1-z)^2\Big]\Big\}.\end{aligned} \tag{2.19}$$

It is interesting (and straightforward) to note that for $\kappa = 0$, one obtains the well-known Klein-Nishina cross-section [33], the first line in Eq. (2.19), that corresponds to scattering on a point-like charged particle with spin-1/2. The effect of the anomalous magnetic moment on the unpolarized cross-section can be seen in Fig. 2.3, as the difference between the Klein-Nishina and the Powell curves.

2.1.2.2 Polarization contribution

The second term on the right in Eq. (2.12) includes information on the internal structure of the proton and it is expressed in terms of the two scalar polarizabilities α_{E1} and β_{M1}:

$$\left(\frac{d\sigma}{d\Omega}\right)_{\text{pol}} = -\omega\omega'\left(\frac{\omega'}{\omega}\right)^2\frac{e^2}{m}\Big[\frac{\alpha_{E1}+\beta_{M1}}{2}(1+z)^2+\frac{\alpha_{E1}-\beta_{M1}}{2}(1-z)^2\Big]. \tag{2.20}$$

The contribution of the scalar polarizabilities to the cross-section can be seen in Fig. 2.3, as the difference between the Powell calculation and the LEX. The equation developed by Petrun'kin does not include any terms higher than ω^2, so the spin polarizabilities do not enter in Eq. (2.20). These terms were further developed by Guiaşu [34, 35], but the equation will be omitted since it is quite lengthy and beyond the scope of the thesis.

2.1.2.3 π^0-pole contribution

The LEX of the differential cross-section in Eq. (2.20), discussed in the last paragraph, is valid at forward angles. At larger angles and energies $\gtrsim 50$ MeV, the contribution from the so-called π^0 pole term becomes relevant and cannot be neglected anymore [34, 35], as can be seen in Fig. 2.3 from the comparison between the cyan and the blue curves. This term comes from a π^0 created in the inter-

mediate state that couples to the incoming and outgoing photons, from one side, and to the nucleon on the other, as sketched in the diagram in Fig. 2.2g. Due to the small width of the π^0 resonance, this contribution is described by a pole in the t-channel at $t = m_\pi^2$ (with t being the Mandelstam variable in Eq. (2.24)) [36]. This additional contribution was calculated by Guiaşu and colleagues [34,35], and it should be added to the cross-section in Eq. (2.12):

$$\left(\frac{d\sigma}{d\Omega}\right)_{Gui} = \left(\frac{d\sigma}{d\Omega}\right)_{\text{Pet}} + \frac{2}{m_\pi^2}\frac{\omega\omega'}{m^2}\left(\frac{\omega'}{\omega}\right)^2(1-z)B_\pi(B_\pi + E), \tag{2.21}$$

where the two coefficients are:

$$B_\pi = \frac{m_\pi}{16\pi} g_{\pi NN} F_{\pi^0\gamma\gamma} \frac{t}{m_\pi^2 - t} \tag{2.22}$$

$$E = \frac{e^2}{m}\frac{m_\pi}{2}[1 - z + k^2 + k(3 - z)]. \tag{2.23}$$

In Eq. (2.22), $t = (k - k')^2 = -2\omega\omega'(1 - z)$ is the four-momentum transfer squared, and $F_{\pi^0\gamma\gamma}$ and $g_{\pi NN}$ are the $\pi^0\gamma\gamma$ and the πNN coupling constants.

2.1.3 Dispersion relation at fixed-t

The low-energy expansion calculation described in the last sections is a very useful tool to calculate the Compton cross-section at very low incoming photon energy ω. On the other hand, Fig. 2.3 shows that this approximation is in agreement with the data only for $\omega \lesssim 100$ MeV. Above this energy, the use of a more fundamental theory is needed. Unfortunately, while perturbative QCD works very well at high energies, at low energies — as a result of the confinement — quarks and gluons cannot be used anymore as relevant degrees of freedom. In this energy range therefore a different approach is needed. The effort of the theorists in the last decades was mainly focused on the development of two different frameworks: chiral perturbation theory, an effective field theory derived by Weinberg [37], and dispersion relations. The former is briefly illustrated in Section 2.1.4, while the current section is devoted to the description of the latter.

Dispersion Relations (DRs) have been successfully used in the last thirty years to study Compton scattering for energies up to the Δ-resonance region, and it can describe the existing experimental data very well (Fig. 2.3). Using the notation of Eq. (2.1), we can define the well-known Mandelstam variables as:

$$s = (k + q)^2, \quad t = (k - k')^2 \quad u = (k - q')^2, \tag{2.24}$$

which are constrained by

$$s + t + u = 2m^2 \tag{2.25}$$

with m being the mass of the nucleon. The crossing-symmetry variable (ν) can also be defined as

$$\nu = \frac{s-u}{4m}. \tag{2.26}$$

The T-matrix from Compton scattering can be written using six independent structure functions $A_i(\nu, t)$, with $i = 1, ..., 6$, first proposed in this form by L'vov, Petrun'kin and Schumacher in 1996 [38]. These scattering amplitudes are functions of the two Lorentz invariant variables ν and t, which can be written in terms of the incident (ω) and scattered (ω') photon energies and angle $\theta_{\gamma'}$ in the lab frame as [38]

$$\nu = \omega + \frac{t}{4m} = \frac{\omega + \omega'}{2}, \tag{2.27}$$

$$t = -4\omega\omega' \sin(\theta_{\gamma'}/2)^2 = -2m(\omega - \omega'). \tag{2.28}$$

The main advantages of these structure functions $A_i(\nu, t)$ are the absence of kinematic singularities and kinematic constraints and the fact that they obey crossing symmetry $A_i(\nu, t) = A_i(-\nu, t)$. The T-matrix for the Compton scattering can then be written as [27]:

$$\begin{aligned}
T_{fi} = \Big\{ & \Big[\Big(1 - \frac{t}{4m^2}\Big)(-A_1 - A_3) - \frac{\nu^2}{m^2}A_5 - A_6\Big] 2m\omega\omega' \vec{\epsilon'^*} \cdot \vec{\epsilon} \\
& + \Big[\Big(1 - \frac{t}{4m^2}\Big)(A_1 - A_3) + \frac{\nu^2}{m^2}A_5 - A_6\Big] 2m\omega\omega' \vec{s'^*} \cdot \vec{s} \\
& - \Big[A_2 + \Big(1 + \frac{\omega}{m}\Big)A_4 - \frac{\nu}{m}A_5 + A_6\Big] i\omega\omega'^2 \vec{\sigma} \cdot \vec{\hat{k}'} \vec{\epsilon'^*} \cdot \vec{s} \\
& + \Big[A_2 + \Big(1 - \frac{\omega'}{m}\Big)A_4 + \frac{\nu}{m}A_5 + A_6\Big] i\omega^2\omega' \vec{\sigma} \cdot \vec{\hat{k}} \vec{s'^*} \cdot \vec{\epsilon} \\
& - \Big[-A_2 + \Big(1 - \frac{\omega'}{m}\Big)A_4 - \frac{\nu}{m}A_5 + A_6\Big] i\omega^2\omega' \vec{\sigma} \cdot \vec{\hat{k}} \vec{\epsilon'^*} \cdot \vec{s} \\
& + \Big[-A_2 + \Big(1 + \frac{\omega}{m}\Big)A_4 + \frac{\nu}{m}A_5 + A_6\Big] i\omega\omega'^2 \vec{\sigma} \cdot \vec{\hat{k}'} \vec{s'^*} \cdot \vec{\epsilon} \\
& - \Big[A_5 + A_6\Big] 2i\nu\omega\omega' \vec{\sigma} \cdot \vec{\epsilon'^*} \times \vec{\epsilon} \\
& + \Big[A_5 - A_6\Big] 2i\nu\omega\omega' \vec{\sigma} \cdot \vec{s'^*} \times \vec{s} \Big\} \frac{1}{N(t)},
\end{aligned} \tag{2.29}$$

where $\vec{\epsilon}$ and $\vec{\epsilon'}$ are the polarization vectors of the incoming and the scattered

photons, respectively, and the two magnetic vectors $\vec{s}$ and $\vec{s'}$ are defined as:

$$\vec{s} = \vec{\hat{k}} \times \vec{\epsilon}, \quad \vec{s'} = \vec{\hat{k}'} \times \vec{\epsilon'}, \tag{2.30}$$

and

$$N(t) = \sqrt{1 - \frac{t}{4m^2}}. \tag{2.31}$$

The T-matrix of Eq. (2.29) can be used to calculate the differential cross-section as:

$$\begin{aligned} \frac{d\sigma}{d\Omega} &= \frac{1}{64\pi^2 m^2}\left(\frac{\omega'}{\omega}\right)^2 |T_{fi}|^2, \quad \text{in the lab frame, or} \\ \frac{d\sigma}{d\Omega} &= \frac{1}{64\pi^2 s}|T_{fi}|^2, \quad \text{in the c.m. frame.} \end{aligned} \tag{2.32}$$

The properties of the amplitudes $A_i(\nu, t)$ have been described in detail by Pasquini, Drechsel and Vanderhaeghen [10, 39, 40] using dispersion relations. First, it is convenient to decompose these invariant amplitudes into Born and non-Born contributions [27], similarly to what has been done for the LEX:

$$A_i(\nu, t) = A_i^B(\nu, t) + A_i(\nu, t)^{NB} \quad (i = 1, ..., 6). \tag{2.33}$$

The amplitudes now fulfill unsubtracted DRs at fixed-t, and so we can express the real part of each amplitude — $\mathrm{Re}(A_i(\nu, t))$ — in relation to the imaginary part as:

$$\mathrm{Re}(A_i(\nu, t)) = A_i^B(\nu, t) + \frac{2}{\pi}\mathrm{P}\int_{\nu_{thr}}^{+\infty} \frac{d\nu'\nu'}{\nu'^2 - \nu^2}\,\mathrm{Im_s}(A_i(\nu', t)), \tag{2.34}$$

where P is the notation for the Cauchy principal value and $\mathrm{Im_s}(A_i(\nu, t))$ are the discontinuities in the s-channel cut of the Compton scattering. Each amplitude A_i can be then reconstructed from the Born part, including also the π^0-pole contribution, and its imaginary part $\mathrm{Im_s}(A_i)$. The latter are calculated from the unitarity relation, taking into account the pion-nucleon intermediate states (e.g. Fig. 2.2e) and so the integral starts from the pion production threshold ν_{thr}:

$$\nu_{thr} = m_\pi + \frac{2m_\pi^2 + t}{4m}. \tag{2.35}$$

This can be observed also in Fig. 2.3, where the DR calculation shows a kink after crossing the pion threshold.

For $\nu \to +\infty$, the integral part of the unsubtracted DRs in Eq. (2.34) does

not converge for the amplitudes A_1 and A_2 [41]. To avoid this behavior and to make sure that all terms converge, the fixed-t dispersion relations are calculated at $\nu = 0$ and subtracted from the one in Eq. (2.34), resulting in:

$$\mathrm{Re}(A_i(\nu,t)) = A_i^B(\nu,t) + \left[A_i(0,t) - A_i^B(0,t)\right] + \frac{2}{\pi}\nu^2 \mathrm{P}\int_{\nu_{thr}}^{+\infty} \frac{d\nu' \,\mathrm{Im_s}(A_i(\nu',t))}{\nu'(\nu'^2-\nu^2)}. \tag{2.36}$$

The two additional powers of ν' in the denominator ensure that these once-subtracted DRs now converge for all of the scattering amplitudes $A_i(\nu,t)$. Moreover, due the energy denominator $1/(\nu'(\nu'^2-\nu^2))$, the most important contribution to the dispersion integral can be evaluated using the existing empirical data on single and double pion photoproduction up to $\omega_\gamma \sim 1.5$ GeV, while the mechanisms involving more pions or heavier mesons in the intermediate states are largely suppressed. Usually, these contributions are calculated using the multipole amplitudes from different models, e.g. SAID [42,43] and MAID [44] among the others.

The six subtraction functions $A_i(\nu,t)$ of Eq. (2.36) can be expressed using once-subtracted DRs in the variable t [40]:

$$\begin{aligned} A_i(0,t) - A_i^B(0,t) = &\left[A_i(0,0) - A_i^B(0,0)\right] + \left[A_i^{t-pole}(0,t) - A_i^{t-pole}(0,0)\right] \\ &+ \frac{t}{\pi}\int_{-\infty}^{-2m_\pi^2-4mm_\pi} \frac{dt' \,\mathrm{Im_t}(A_i(0,t'))}{t'(t'-t)} \\ &+ \frac{t}{\pi}\int_{4m_\pi^2}^{+\infty} \frac{dt' \,\mathrm{Im_t}(A_i(0,t'))}{t'(t'-t)}, \end{aligned} \tag{2.37}$$

where $A_i(0,t)^{t-pole}$ is the contribution of the poles in the t-channel (e.g. the π^0 pole for $i = 2$, see [41]). The subtraction constants

$$a_i = A_i(0,0) - A_i^B(0,0) \tag{2.38}$$

are of particular interest for us since they are related to the polarizabilities. The two scalar static polarizabilities, α_{E1} and β_{M1}, introduced in Section 2.1.1.2, can be written as:

$$\alpha_{E1} = -\frac{1}{4\pi}(a_1 + a_3 + a_6), \quad \beta_{M1} = \frac{1}{4\pi}(a_1 - a_3 - a_6), \tag{2.39}$$

and the four spin polarizabilities — γ_{E1E1}, γ_{M1M1}, γ_{E2M1} and γ_{M1E2} — introduced

in Section 2.1.1.3 can be written as:

$$\gamma_{E1E1} = \frac{1}{8\pi m}(a_2 - a_4 + 2a_5 + a_6), \quad \gamma_{E1M2} = \frac{1}{8\pi m}(a_2 - a_4 - a_6), \tag{2.40}$$

$$\gamma_{M1M1} = \frac{-1}{8\pi m}(a_2 + a_4 + 2a_5 - a_6), \quad \gamma_{E1M2} = \frac{-1}{8\pi m}(a_2 + a_4 + a_6). \tag{2.41}$$

Furthermore, the two linear combinations, γ_0 and γ_π, defined in Eqs. (2.9) and (2.10), can be expressed in terms of these subtraction constants:

$$\gamma_0 = \frac{1}{2\pi m}a_4, \quad \gamma_\pi = \frac{-1}{2\pi m}(a_2 + a_5). \tag{2.42}$$

In a similar way, both the sum and the difference of the two scalar polarizabilities α_{E1} and β_{M1} can be expressed as:

$$\alpha_{E1} + \beta_{M1} = \frac{-1}{2\pi}(a_3 + a_6), \tag{2.43}$$

and

$$\alpha_{E1} - \beta_{M1} = \frac{-1}{2\pi}(a_1). \tag{2.44}$$

2.1.4 Effective chiral perturbation theory

A different approach to describe Compton scattering is by using an Effective Field Theory (EFT). The basic idea here is to effectively characterize a certain process by using a non-elementary description instead of attempting to use an underlying fundamental theory. Since the details of nucleon internal structure are not probed by low-energy electromagnetic radiation, a low-energy EFT which includes pions, photons and nucleons as a whole, could be a useful tool to extract information about the nucleon polarizabilities. To develop an EFT, there should be a clear separation between the scales of the energies involved in the relevant process and the ones needed to excite the processes that are not treated [45]. When constructing an EFT Lagrangian, all terms compatible with the symmetries of the underlying theory must be included, each weighted with unknown parameters, the so-called Low-Energy Constants (LECs), which are not explained within the theory under construction. These parameters can be related to some of the properties of the particles involved — such as mass, charge, decay constant, etc. — or they can be calculated from the underlying fundamental theory or, in particular in the last years, they could come from lattice simulations. This gives an infinite succession of terms that are organized subsequently to the power of p_{typ}/Λ, providing the contribution of each operator to the amplitude, where p_{typ} is the

typical momentum of the process described and Λ, so-called breakdown scale, is the mass of the lightest degree of freedom omitted by the theory. For example, in the EFT used to describe Compton scattering in the energy region relevant for this thesis, the amplitudes are expanded in powers of

$$P/\Lambda_\chi \equiv (p_{typ}, m_\pi)/m_p \ll 1, \tag{2.45}$$

where the light EFT scale P is the pion mass and momenta and the breakdown scale $\Lambda_\chi \simeq m_p$ is defined with hadrons that are not included in the theory. This particular EFT is known as Chiral Effective Field Theory (χEFT), or zero-quark-mass limit EFT. There are currently two main approaches: the first one does not include the $\Delta(1232)$ as an explicit degree of freedom while the second does, but it is not anymore manifestly Lorenz invariant. The former is called BχPT (see [17, 46, 47]), while the latter is known as Heavy Baryon Chiral Perturbation Theory (HBχPT) (see [45, 48–52]).

2.2 Baldin sum rule

The sum of the static scalar electric (α_{E1}) and magnetic (β_{M1}) polarizabilities defined in Eq. (2.43) can be constrained using the experimental total cross-section for meson photoproduction ($\sigma_{tot}(\omega)$) by the well-known Baldin-Lapidus sum rule [53, 54]:

$$\alpha_{E1} + \beta_{M1} = \frac{1}{2\pi^2}\int_{\omega_0}^{\infty} \frac{d\omega}{\omega^2}\sigma_{tot}(\omega) = -\frac{1}{2\pi}A^{NB}_{3+6}(0,0), \tag{2.46}$$

where the lower limit of the integral ω_0 is the threshold energy for meson photoproduction ($\gamma N \to \pi N$), namely the minimum energy required to produce a pion, given by approximately $\omega_0 \approx 140$ MeV. The last term in Eq. (2.46) follows from Eqs. (2.38) and (2.43) using the notation $A^{NB}_{3+6}(0,0) = \left[A^{NB}_3(0,0) + A^{NB}_6(0,0)\right]$. It is normally divided into two terms:

$$\alpha_{E1} + \beta_{M1} = \frac{-1}{2\pi}\left[A^{\text{int}}_{3+6}(0,0) + A^{\text{as}}_{3+6}(0,0)\right], \tag{2.47}$$

with

$$A^{\text{int}}_{3+6}(0,0) = \frac{2}{\pi}\int_{\nu_{thr}}^{\nu_{max}} \frac{d\nu'}{\nu'}\,\text{Im}\,A_{3+6}(\nu',0), \tag{2.48}$$

$$A^{\text{as}}_{3+6}(0,0) = \frac{2}{\pi}\int_{\nu_{max}}^{\infty} \frac{d\nu'}{\nu'}\,\text{Im}\,A_{3+6}(\nu',0), \tag{2.49}$$

where the asymptotic part contributes only $\sim 6\%$, fixing $\nu_{max} = 1.5$ GeV [38].

As a consequence of the ω^2-weighting, and since single pion photoproduction is the largest contribution to the total photoproduction cross-section, the physics related to the Δ-resonance region dominates the integral in Eq. (2.46).

2.3 Polarized Compton scattering

Polarized nuclear Compton scattering can be a powerful tool to study the internal structure of the proton, or the nucleon in general. There are different possible combinations that give access to different single and double polarization observables, depending on the polarized component of the reaction: it can be the photon, in the initial or in the final state, or the proton, in the initial or in the final state, or any of the possible combinations. The apparatus of the A2 Collaboration used for the experiment described in this thesis will be discussed in Chapter 4, and allows for a polarized photon beam, linearly or circularly, and a polarized proton target, longitudinally or transversely. For this reason, only the cases of the singly and doubly polarized Compton scattering

$$\vec{\gamma}\vec{p} \to \gamma p \tag{2.50}$$

are considered here, without taking into consideration the recoil proton polarization. The most general case was extensively discussed by Babusci and colleagues in the seminal paper given in Ref. [27].

2.3.1 Stokes parameters

The photon polarization can be conveniently described using the Stokes parameters ξ_i with $i = 1, 2, 3$. They are constrained by the fact that the total degree of the photon polarization cannot be greater than 1 [27]:

$$\sqrt{\xi_1^2 + \xi_2^2 + \xi_3^2} \leq 1, \tag{2.51}$$

and when using them, the photon polarization matrix density can be defined as:

$$\langle \epsilon_\alpha \epsilon_\beta^* \rangle = \frac{1}{2}(\mathbb{1} + \vec{\sigma} \cdot \vec{\xi})_{\alpha\beta} = \frac{1}{2} \begin{pmatrix} 1 + \xi_3 & \xi_1 - i\xi_2 \\ \xi_1 + i\xi_2 & 1 - \xi_3 \end{pmatrix}_{\alpha\beta}. \tag{2.52}$$

The photon polarization vector ϵ_ν is defined in the radiation gauge $\vec{\epsilon} \cdot \hat{k} = 0$, and $\alpha, \beta = 1, 2$ indicates one of the two orthogonal directions x_γ, y_γ with respect

to the photon momentum direction $z_\gamma = \hat{k}$. The ξ_i parameters transform under parity, time inversion and crossing as:

$$\xi_1 \xrightarrow{P} -\xi_1, \quad \xi_2 \xrightarrow{P} -\xi_2, \quad \xi_3 \xrightarrow{P} \xi_3 \tag{2.53}$$

$$\xi_1 \xrightarrow{T} -\xi_1, \quad \xi_2 \xrightarrow{T} \xi_2, \quad \xi_3 \xrightarrow{T} \xi_3 \tag{2.54}$$

$$\xi_1 \xrightarrow{\mathrm{C}} \xi_1', \quad \xi_2 \xrightarrow{\mathrm{C}} -\xi_2', \quad \xi_3 \xrightarrow{\mathrm{C}} \xi_3'. \tag{2.55}$$

Even though this definition of the Stokes parameters is frame dependent, the quantities ξ_l defined as:

$$\xi_l = \sqrt{\xi_1^2 + \xi_3^2} \tag{2.56}$$

and ξ_2 are Lorentz invariant. In this context, ξ_2 gives the degree of circular polarization of a photon, and it can be either 1 or -1, corresponding to right and left helicity, respectively. ξ_l instead indicates the degree of linear polarization. The angle ϕ between the electric field and the $x_\gamma z_\gamma$-plane of scattering is defined as:

$$\cos(2\phi) = \frac{\xi_3}{\xi_l}, \quad \sin(2\phi) = \frac{\xi_1}{\xi_l}. \tag{2.57}$$

2.3.2 Scattering amplitudes

The differential cross-section for Compton scattering has been introduced in Eq. (2.32) as a function of the T-matrix. In the same Section 2.1.3, the T-matrix has been expressed in Eq. (2.29) as function of six independent amplitudes $A_i(\nu, t)$. This same matrix can also be expressed using a set of invariant functions W_{ij}, that are particularly convenient in the case of polarized Compton scattering. In fact, they directly intervene in the definition of the independent polarized observables which can be measured experimentally. Referring to the specific case with an incoming polarized photon beam and polarized target, the T-matrix can be written as:

$$\begin{aligned} |T_{fi}(\vec{\gamma}\vec{p} \to \gamma p)|^2 = {} & W_{00} + W_{03}\xi_3 \\ & + N \cdot S(W_{30} + W_{33}^+\xi_3) \\ & + K \cdot S(W_{11}^+\xi_1 + W_{12}^+\xi_2) \\ & + Q \cdot S(W_{21}^+\xi_1 + W_{22}^+\xi_2), \end{aligned} \tag{2.58}$$

where N, K and Q are orthogonal four-vectors defined as:

$$N_\nu = \epsilon_{\nu\alpha\beta\gamma} P'^\alpha Q^\beta K^\gamma \quad \text{with} \quad P'_\nu = P_\nu - K_\nu \frac{P \cdot K}{K^2},$$

$$P = \frac{(q+q')}{2}, \quad K = \frac{(k+k')}{2}, \quad Q = \frac{(q-q')}{2} = \frac{(k'-k)}{2}, \tag{2.59}$$

where the asymmetric tensor fulfills the condition $\epsilon_{0123} = 1$. Furthermore, the four-vector S in Eq. (2.58) represents the nucleon polarization, which is orthogonal to the proton four-momentum q.

It is very interesting to note that for the case of unpolarized target and unpolarized beam only the first term in Eq. (2.58) survives, and from Eq. (2.32) a simple equation for the unpolarized cross-section is obtained:

$$\frac{d\sigma}{d\Omega}_{unpol} = \frac{1}{64\pi^2 m^2}\left(\frac{\omega'}{\omega}\right)^2 W_{00}, \tag{2.60}$$

where W_{00} can be written as function of the six independent amplitudes $A_i(\nu, t)$ as:

$$\begin{aligned} W_{00} = &\frac{1}{4}(4m^2 - t)(t^2|A_1|^2 + \eta^2|A_3|^2) - \frac{1}{4}(t^3|A_2|^2 + \eta^3|A_4|^2) \\ &- \nu^2 t(t + 8\nu^2)|A_5|^2 + \frac{1}{2}\eta(t^2 + 2m^2\eta)|A_6|^2 \\ &+ \mathrm{Re}\Big\{2\nu^2 t^2(A_1 + A_2)A_5^* + \frac{1}{2}\eta^2(4m^2 A_3 + tA_4)A_6^*\Big\}, \end{aligned} \tag{2.61}$$

where t and ν where already defined in Eqs. (2.24) and (2.26), respectively, while η is given as:

$$\eta = \frac{(m^4 - su)}{m^2} = 4\nu^2 + t - \frac{t^2}{4m^2}. \tag{2.62}$$

In the case of interest for this thesis, namely linearly polarized photon beam with an unpolarized target, only the first entire line in Eq. (2.58) survives, where ξ_3 is the third Stokes parameter and W_{03} can be written as:

$$W_{03} = \frac{\eta t}{2}\,\mathrm{Re}\{[(4m^2 - t)A_1 + 4\nu^2 A_5]A_3^* + 4m^2 A_1 A_6^*\}. \tag{2.63}$$

For the sake of completeness, the remaining W_{ij} terms in Eq. (2.58) are explicitly reported here:

$$\begin{aligned} W_{11}^{\pm} = \mathrm{Im}\Big\{&\frac{t}{2m}[(4m^2 - t)A_1 + 4\nu^2 A_5](\eta A_4^* + tA_6^*) \\ &\pm 2\nu t(tA_2 - 4\nu^2 A_5)A_6^*\Big\}, \end{aligned} \tag{2.64}$$

$$\begin{aligned} W_{12}^{\pm} = \mathrm{Re}\Big\{&-\frac{\eta}{2m}[(4m^2 - t)A_3 + 4m^2 A_6](\eta A_4^* + tA_6^*) \\ &\pm 2\nu t(tA_2 - 4\nu^2 A_5)A_5^*\Big\}, \end{aligned} \tag{2.65}$$

$$W_{21}^{\pm} = 2\,\mathrm{Im}\Big\{-m(tA_2 - 4\nu^2 A_5)[\eta A_3^* + (t+4\nu^2)A_6^*] \pm \nu[tA_1 - (t+4\nu^2)A_5](\eta A_4^* + tA_6^*)\Big\}, \tag{2.66}$$

$$W_{22}^{\pm} = 2\,\mathrm{Re}\Big\{-mt(tA_2 - 4\nu^2 A_5)A_1^* \mp \nu\eta A_3(\eta A_4^* + tA_6^*)\Big\}, \tag{2.67}$$

$$W_{30}^{\pm} = -8\nu\,\mathrm{Im}(tA_1 A_5^* + \eta A_3 A_6^*), \tag{2.68}$$

$$W_{33}^{\pm} = \mathrm{Im}\Big\{-8\nu\{[tA_1 - (t+4\nu^2)A_5]A_6^* + \eta A_3 A_5^*\} \pm \frac{2}{m}(tA_2 - 4\nu^2 A_5)(\eta A_4^* + tA_6^*]\Big\}. \tag{2.69}$$

It is worth noting here that below the pion photoproduction threshold, the six amplitudes A_i are real. In this energy range only the invariant functions W_{00}, W_{03}, $W_{12}^{\pm}$, $W_{22}^{\pm}$ survive.

2.3.3 Asymmetries

In polarized Compton scattering, using different polarization for the beam and/or for the target, a set of experimentally accessible observables called asymmetries can be defined. They quantify the effects of the different polarizabilities to the Compton scattering cross-section. They can be single- or double-polarization observables, depending on the number of polarization degrees of freedom involved in the scattering. They can be defined using a very convenient notation introduced by Babusci *et. al* [27]: Σ_i and Σ_j for the single polarization asymmetries and Σ_{ij} for the double polarized ones. For the polarized photons, the index $i = (1, 2, 3)$ refers to the Stokes parameters ϵ_i. While, for the polarized protons, $j = (x, y, z)$ refers to the proton's polarization axis. For the double polarization asymmetries, the i and the j indices similarly refer to the polarization of the photons and protons, respectively. This notation can be extended to the photon and the proton in the final state, in which case the primed indices i' and j' are used.

Limiting to the case of Eq. (2.50), seven different linear independent asymmetries can be defined: two single and five double polarization asymmetries. In the definition of these asymmetries $d\sigma$ indicates the differential cross-section $\frac{d\sigma}{d\Omega}$, where the superscripts indicate the photon polarization — $\parallel$ and $\perp$ for the polarization parallel ($\xi_3 = 1$) and perpendicular ($\xi_3 = -1$) to the scattering plane, respectively — subscripts refer to the nucleon polarization. The asymmetries are:

- one beam asymmetry for a linearly polarized photon beam with an unpo-

larized target:

$$\Sigma_3 = \frac{d\sigma^{\parallel} - d\sigma^{\perp}}{d\sigma^{\parallel} + d\sigma^{\perp}} = \frac{W_{03}}{W_{00}}. \tag{2.70}$$

- one target asymmetry for proton polarized along the $\pm y$ direction and unpolarized photon beam:

$$\Sigma_y = \frac{d\sigma_y - d\sigma_{-y}}{d\sigma_y + d\sigma_{-y}} = C_y^N \frac{W_{30}}{W_{00}}, \tag{2.71}$$

with $C_y^N = \frac{m}{2}\omega\omega' \sin\theta_{\gamma'}$.

- two double polarization asymmetries for circularly polarized photon beam with right (R) and left (L) helicity with a target polarized along the $\pm x$ and $\pm z$ axis, respectively:

$$\Sigma_{2x} = \frac{d\sigma_x^R - d\sigma_x^L}{d\sigma_x^R + d\sigma_x^L} = \frac{C_x^K W_{12}^+ + C_x^Q W_{22}^+}{W_{00}}, \tag{2.72}$$

with $C_x^K = C_x^Q = -\frac{1}{2}\omega' \sin\theta_{\gamma'}$ and

$$\Sigma_{2z} = \frac{d\sigma_z^R - d\sigma_z^L}{d\sigma_z^R + d\sigma_z^L} = \frac{C_z^K W_{12}^+ + C_z^Q W_{22}^+}{W_{00}}, \tag{2.73}$$

with $C_z^K = -\frac{1}{2}(\omega + \omega'\cos\theta_{\gamma'})$ and $C_z^Q = \frac{1}{2}(\omega - \omega'\cos\theta_{\gamma'})$.

- three double asymmetries for a linearly polarized photon beam and a polarized target:

$$\Sigma_{1x} = \frac{d\sigma_x^{\pi/4} - d\sigma_x^{-\pi/4}}{d\sigma_x^{\pi/4} + d\sigma_x^{-\pi/4}} = \frac{C_x^K W_{11}^+ + C_x^Q W_{21}^+}{W_{00}}, \tag{2.74}$$

$$\Sigma_{1z} = \frac{d\sigma_z^{\pi/4} - d\sigma_z^{-\pi/4}}{d\sigma_z^{\pi/4} + d\sigma_z^{-\pi/4}} = \frac{C_z^K W_{11}^+ + C_z^Q W_{21}^+}{W_{00}}, \tag{2.75}$$

$$\Sigma_{3y} = \frac{(d\sigma_y^{\parallel} - d\sigma_y^{\perp}) - (d\sigma_{-y}^{\parallel} - d\sigma_{-y}^{\perp})}{(d\sigma_y^{\parallel} + d\sigma_y^{\perp}) + (d\sigma_{-y}^{\parallel} + d\sigma_{-y}^{\perp})} = C_y^N \frac{W_{33}^+}{W_{00}}, \tag{2.76}$$

with $C_y^N = \frac{m}{2}\omega\omega' \sin\theta_{\gamma'}$.

By time-reversal invariance, the eight recoil asymmetries are related, but not identical, to those defined above. As noted at the end of the previous subsection, only some of the invariant functions W_{ij} are different from zero below the pion photoproduction threshold, since at these energies the amplitudes A_i are purely real. This leaves us with the fact that only three of the seven asymmetries defined

are non-zero below this threshold: Σ_3, Σ_{2x} and Σ_{2z}.

2.3.4 Polarized cross-section

Introducing the polarization three-vector $\vec{\zeta}$ of the nucleon, it can be related to the polarization four-vector S through the boost transformation [27]

$$\vec{S} = \vec{\zeta} + \frac{S_0}{q_0 + m}\vec{q}, \quad S_0 = \frac{\vec{q}\cdot\vec{S}}{q_0} = \frac{\vec{q}\cdot\vec{\zeta}}{m}. \tag{2.77}$$

Using the definition of the Stokes parameters given in Section 2.3.1 and $\vec{\zeta}$, the polarized cross-section can be parameterized as:

$$\begin{aligned}\frac{d\sigma}{d\Omega}\Big|_{\text{pol}} = \frac{d\sigma}{d\Omega}\Big|_{\text{unpol}} \Big\{ & 1 + \xi_3\Sigma_3 + \zeta_y\Sigma_y + \xi_1(\zeta_x\Sigma_{1x} + \zeta_z\Sigma_{1z}) \\ & + \xi_2(\zeta_x\Sigma_{2x} + \zeta_z\Sigma_{2z}) + \xi_3\zeta_y\Sigma_{3y}\Big\}.\end{aligned} \tag{2.78}$$

In the case of unpolarized target, $\vec{\zeta} = 0$, as in the experiment subject of this thesis, only the first two terms of Eq. (2.78) survives:

$$\frac{d\sigma}{d\Omega}\Big|_{\text{pol}} = \frac{d\sigma}{d\Omega}\Big|_{\text{unpol}} \Big\{1 + \xi_3\Sigma_3\Big\}, \tag{2.79}$$

and using the first relation in Eq. (2.57), the polarized contribution can be written as function of the degree of photon linear polarization ξ_l as:

$$\frac{d\sigma}{d\Omega}\Big|_{\text{pol}} = \frac{d\sigma}{d\Omega}\Big|_{\text{unpol}} \Big\{1 + \xi_l\Sigma_3\cos(2\phi)\Big\}. \tag{2.80}$$

As it will be explain later in this thesis, using this equation with Σ_3 as free parameter to fit the ϕ-distribution of the experimental polarized cross-section, allows for the extraction of the beam asymmetry from the data.

2.4 Sensitivity studies

A simple but effective way to explore the sensitivity of the proton static polarizabilities on nuclear Compton scattering is to produce different sets of theoretical predictions using different polarizability values. To produce these curves, a fixed-t dispersion relation code from B. Pasquini was used [10, 39, 40]. The predictions were produced for two different observables, the unpolarized differential cross-section $d\sigma/d\Omega$ and the beam asymmetry Σ_3, mainly because they are the two

quantities measured in this thesis, but also because these are the most sensitive observables below the pion photoproduction threshold. This was done at six different beam energies for the unpolarized cross-section — $85 - 135$ MeV in 10-MeV steps — and three different beam energies for the beam asymmetry Σ_3 — 90 MeV, 110 MeV, and 130 MeV. For all the theoretical predictions, the values of the spin polarizabilities were fixed at the most recent experimental values available, published in 2019 by the A2 Collaboration [19]:

$$\gamma_{E1E1} = -2.87 \times 10^{-4}\ \text{fm}^4, \quad \gamma_{M1M1} = 2.70 \times 10^{-4}\ \text{fm}^4$$
$$\gamma_{E1M2} = -0.85 \times 10^{-4}\ \text{fm}^4, \quad \gamma_{M1E2} = 2.04 \times 10^{-4}\ \text{fm}^4$$

and these values are considered without errors. In this way, it is possible to isolate the changes in the predictions due to the use of different scalar polarizabilities values, without the possible influence of other parameters. Nevertheless, a precise knowledge of the spin polarizabilities is of crucial importance in the extraction of α_{E1} and β_{M1}.

Four different parameters were considered in this study: α_{E1}, β_{M1}, $\alpha_{E1}+\beta_{M1}$, and $\alpha_{E1}-\beta_{M1}$, and four different sets of calculation were done. In each of them a single parameter was varied by ± 1 and $\pm 2 \times 10^{-4}$ fm^3 from the value quoted by the PDG [55]:

a) varying α_{E1}, and fixing $\beta_{M1} = 2.5 \times 10^{-4}$ fm^3 [55]. No constraints were given for $\alpha_{E1} + \beta_{M1}$, and $\alpha_{E1} - \beta_{M1}$. The effect of α_{E1} on the unpolarized cross-section and on the beam asymmetry can be seen in Fig. 2.4.

b) varying β_{M1}, and fixing $\alpha_{E1} = 11.2 \times 10^{-4}$ fm^3 [55]. No constraints were given for $\alpha_{E1} + \beta_{M1}$, and $\alpha_{E1} - \beta_{M1}$. The effect of β_{M1} on the unpolarized cross-section and on the beam asymmetry can be seen in Fig. 2.5.

c) varying $\alpha_{E1}+\beta_{M1}$, and fixing $\alpha_{E1}-\beta_{M1} = 8.7\times10^{-4}$ fm^3 [55]. No constraints were given for α_{E1} and β_{M1}. The effect of $\alpha_{E1} + \beta_{M1}$ on the unpolarized cross-section and on the beam asymmetry can be seen in Fig. 2.6.

d) varying $\alpha_{E1} - \beta_{M1}$, and fixing $\alpha_{E1} + \beta_{M1} = 13.7 \times 10^{-4}$ fm^3 [55]. No constraints were given for α_{E1} and β_{M1}. The effect of $\alpha_{E1} - \beta_{M1}$ on the unpolarized cross-section and on the beam asymmetry can be seen in Fig. 2.7.

In all the figures, the solid line indicates the prediction obtained using the PDG quoted values for all the four parameters. To help visualize the variation in the predictions due to the different values of the scalar polarizabilities used, a relative

variation is also plotted as a black curve in the gray canvas. This relative variation is calculated as the difference between the predictions obtained using the bigger and the smaller value of the parameter, divided by the prediction obtained using the central value of the parameter. In other words, it is the difference between the magenta and the red curves, divided by the blue one.

From these simple studies, it can be noted that the unpolarized cross-section has generally higher sensitivity to the two scalar polarizabilities compared to the beam asymmetry Σ_3. The unpolarized cross-section at $\theta_{\gamma'} = 90°$ seems to be independent of β_{M1} and at this angle the dependency of the former to the latter changes behavior. Furthermore, it is interesting to note how the sensitivity to $\alpha_{E1} + \beta_{M1}$ is only in the forward region, while, conversely, the sensitivity to $\alpha_{E1} - \beta_{M1}$ becomes significant only in the backward region. This behavior can be easily understood by looking at the polarization contribution to the differential cross-section calculated by Petrun'kin, introduced in Section 2.3.4 (see Eq. (2.20)). The beam asymmetry Σ_3 instead shows a higher overall sensitivity to the magnetic scalar polarizability β_{M1}, in particular for the higher incoming photon energy ($\omega_\gamma = 130$ MeV) and in the forward scattering angle region. The sensitivity to the electric scalar polarizability α_{E1} is lower and more concentrated in the central scattering angle region, around $\theta_{\gamma'} = 90°$.

These studies are purely qualitative and they can be useful to get a general understanding of how a variation of the scalar polarizabilities influences the experimental observables measured in this dissertation. Deeper and more general quantitative studies were published in the recent years; for example see Refs. [13, 56], and all of them seems to indicate that a precise measurement of the unpolarized Compton scattering cross-section below the pion photoproduction threshold in a wide range of angles is the best way to precisely extract the proton scalar polarizabilities.

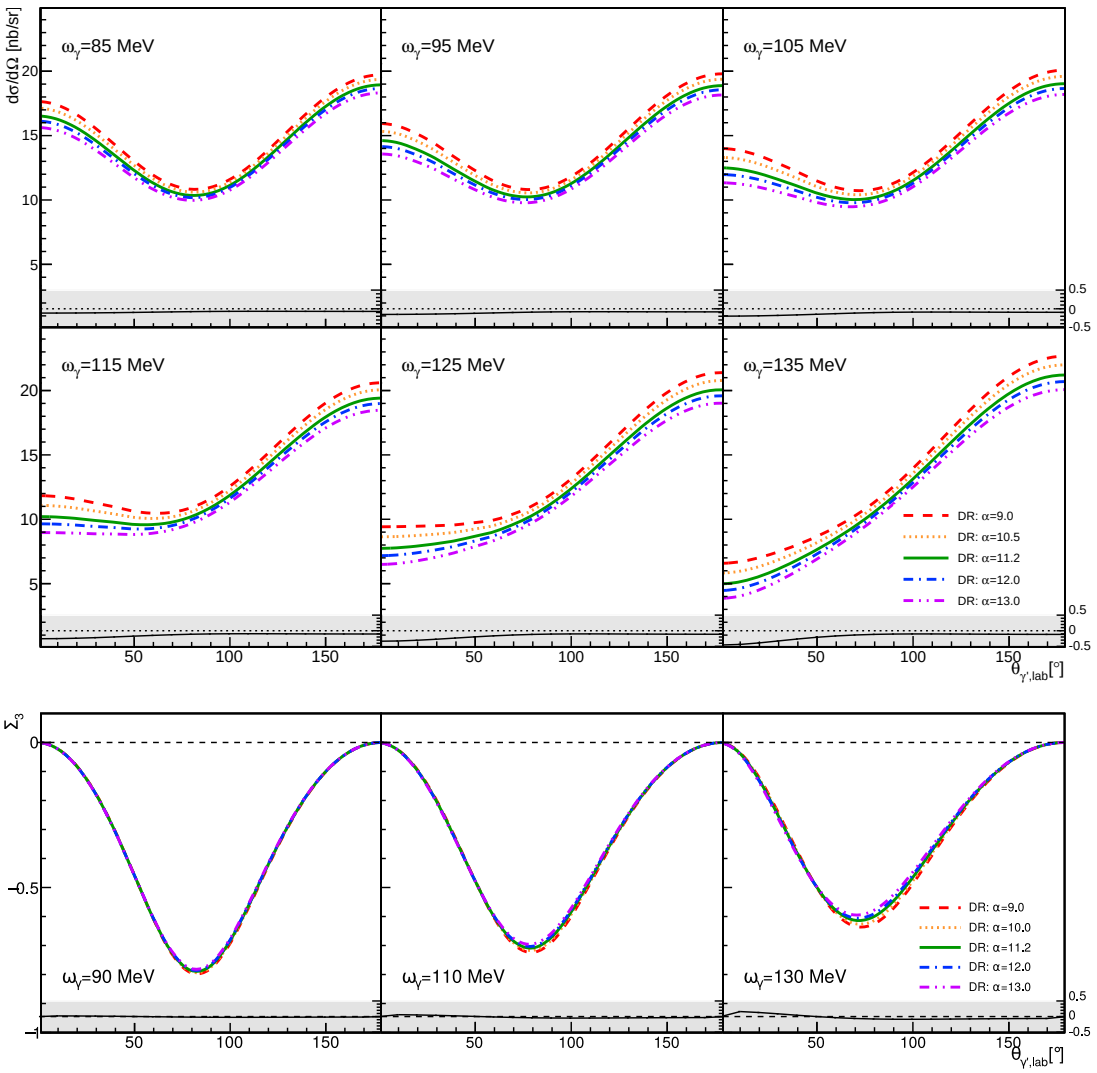

Figure 2.4: Theoretical calculations for the unpolarized Compton scattering cross-section (above) and for the beam asymmetry Σ_3 (below), obtained with different values of α_{E1} and with $\beta_{M1} = 2.5 \times 10^{-4}$ fm^3. The black curve in the gray canvas indicates the relative variation in the experimental observable, calculated as the difference between the predictions obtained using the biggest and the smallest values of α_{E1} divided by the one obtained using the central value. The y-axis on the right gives the scale of the variation.

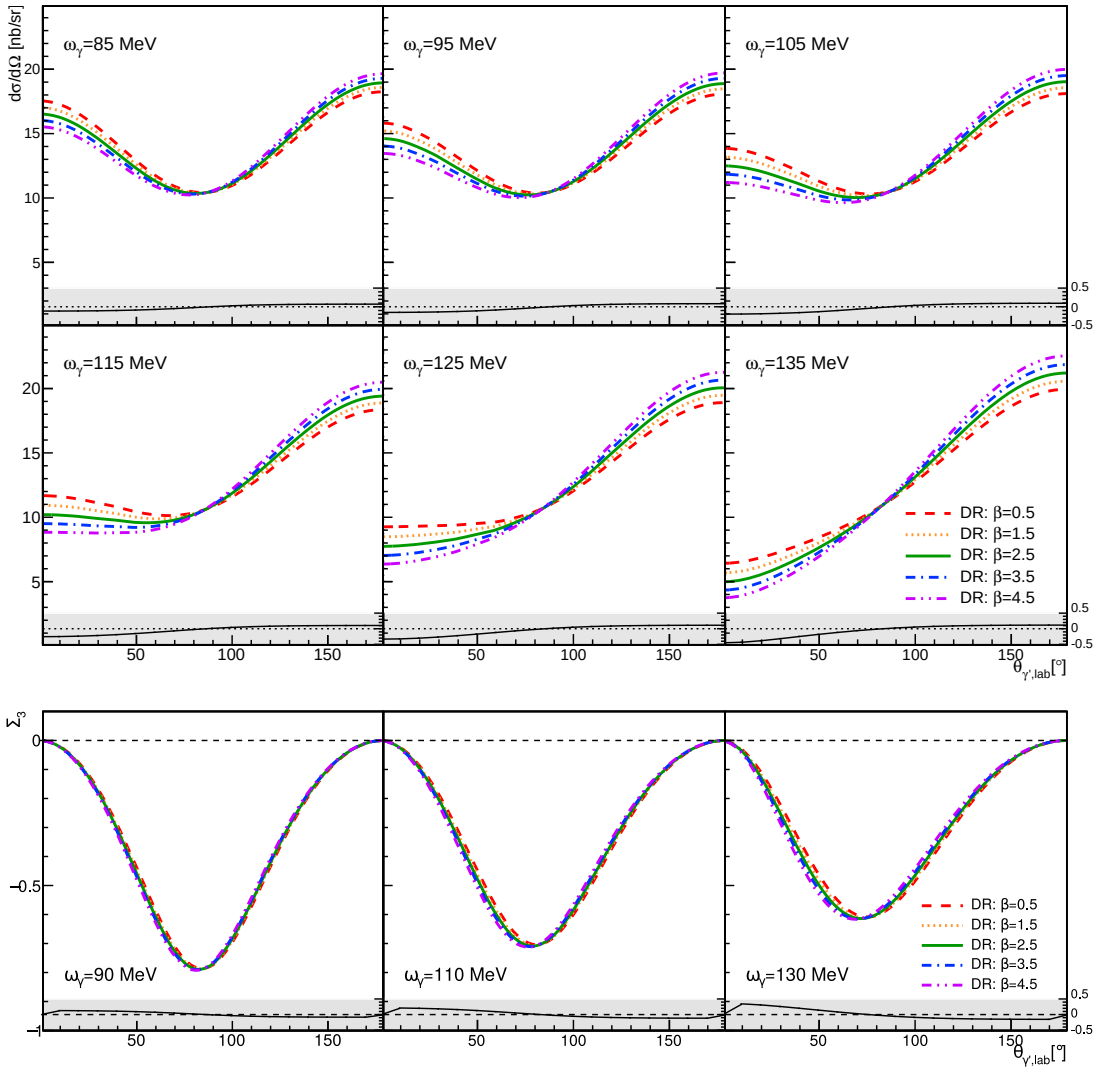

Figure 2.5: Theoretical calculations for the unpolarized Compton scattering cross-section (above) and for the beam asymmetry Σ_3 (below), obtained with different values of β_{M1} and with $\alpha_{E1} = 11.2 \times 10^{-4}$ fm^3. The black curve in the gray canvas indicates the relative variation in the experimental observable, calculated as the difference between the predictions obtained using the biggest and the smallest values of β_{M1} divided by the one obtained using the central value. The y-axis on the right gives the scale of the variation.

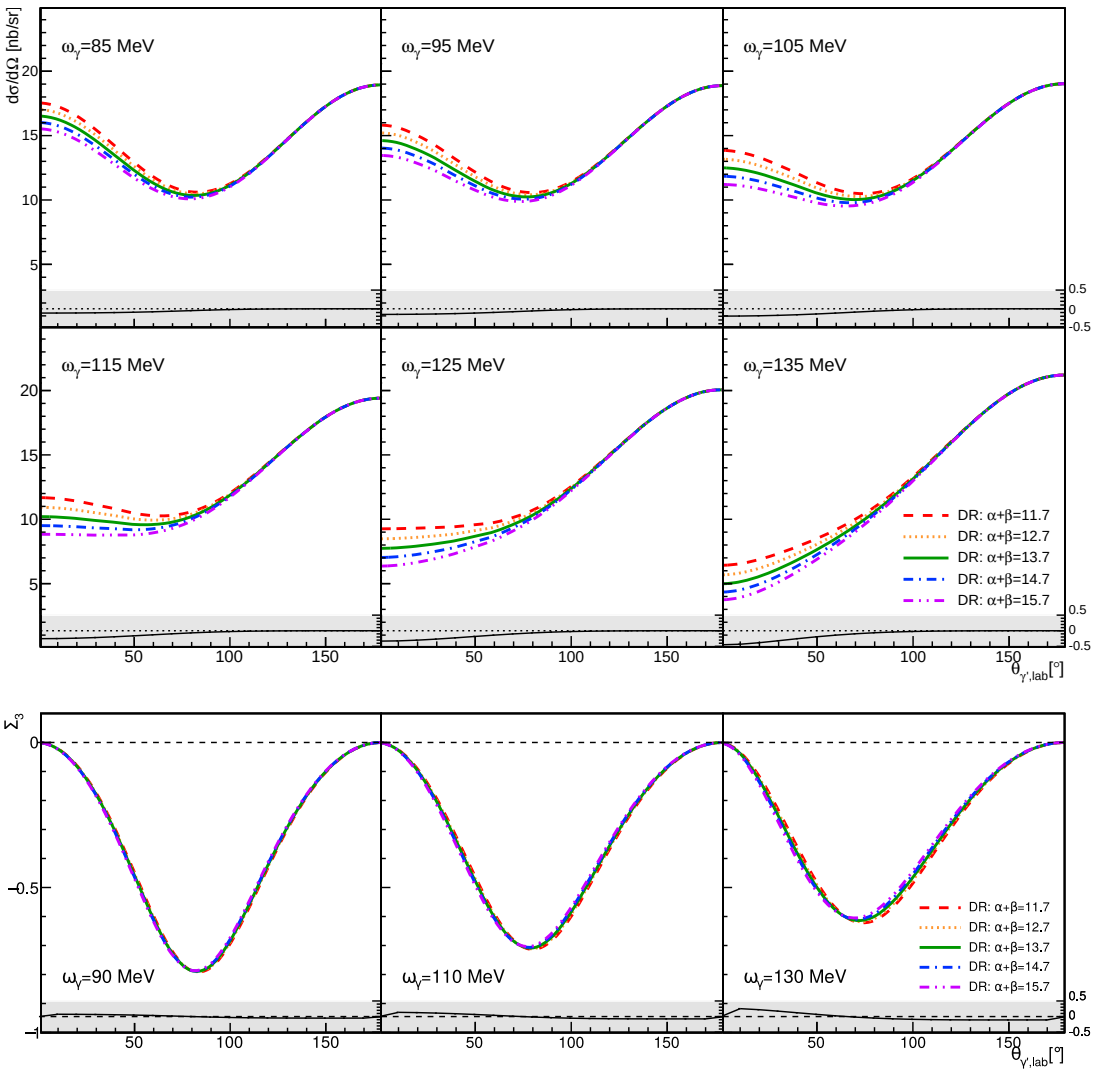

Figure 2.6: Theoretical calculations for the unpolarized Compton scattering cross-section (above) and for the beam asymmetry Σ_3 (below), obtained with different values of $\alpha_{E1} + \beta_{M1}$ and with $\alpha_{E1} - \beta_{M1} = 8.7 \times 10^{-4}$ fm^3. The black curve in the gray canvas indicates the relative variation in the experimental observable, calculated as the difference between the predictions obtained using the biggest and the smallest values of $\alpha_{E1}+\beta_{M1}$ divided by the one obtained using the central value. The y-axis on the right gives the scale of the variation

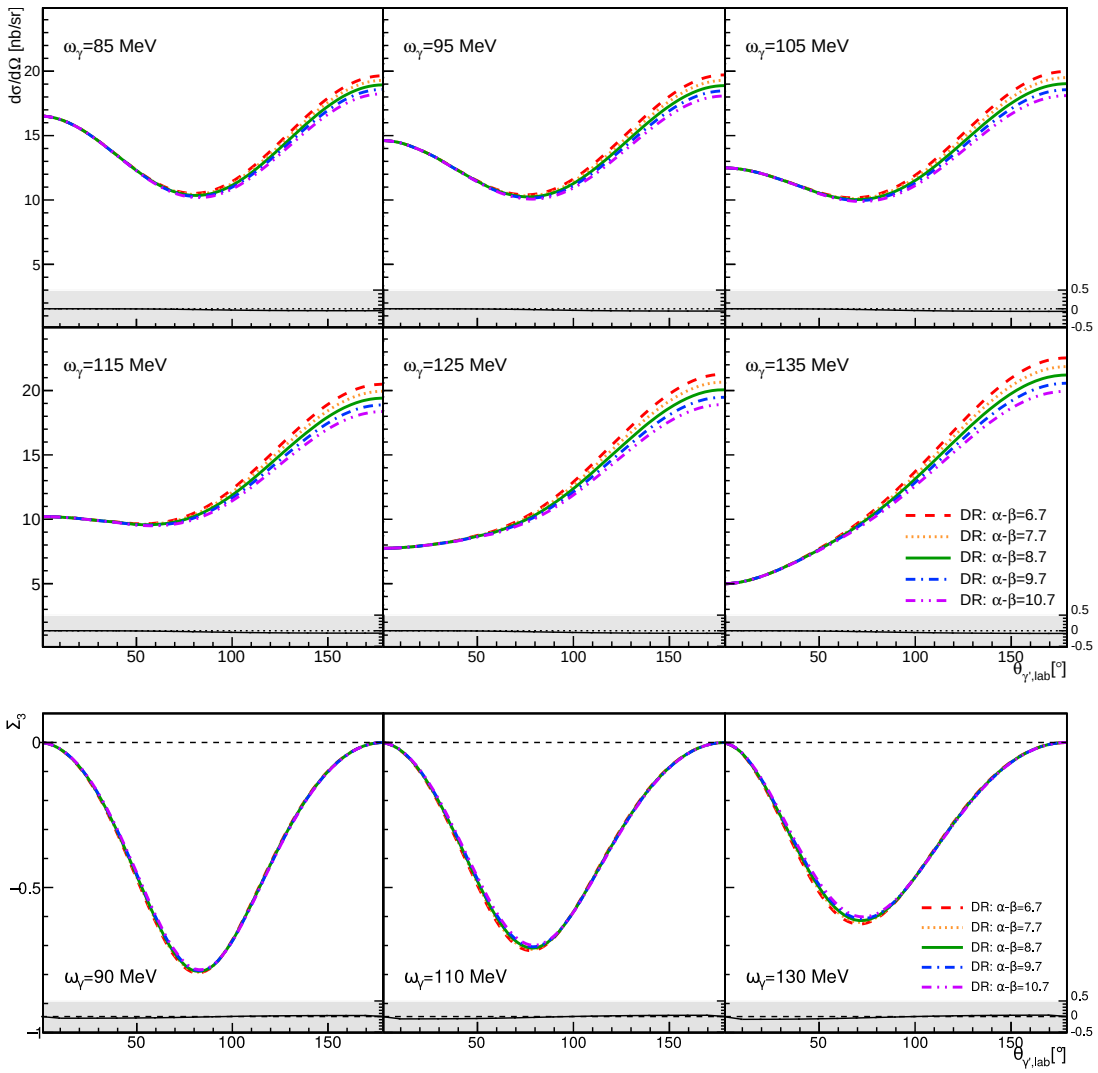

Figure 2.7: Theoretical calculations for the unpolarized Compton scattering cross-section (above) and for the beam asymmetry Σ_3 (below), obtained with different values of $\alpha_{E1} - \beta_{M1}$ and with $\alpha_{E1} + \beta_{M1} = 13.7 \times 10^{-4}$ fm^3. The black curve in the gray canvas indicates the relative variation in the experimental observable, calculated as the difference between the predictions obtained using the biggest and the smallest values of $\alpha_{E1} - \beta_{M1}$ divided by the one obtained using the central value. The y-axis on the right gives the scale of the variation

Chapter 3

Experimental and theoretical studies

Starting from the middle of the last century, there have been both a theoretical and an experimental effort to study the nucleon structure and in particular to access the nucleon polarizabilities. The first experiments date from the 1950s, even if the precise measurements that contribute to a deeper understanding of these quantities did not arrive until the 1990s. The complementary theoretical interest led to the development of different models (see Sections 2.1.3 and 2.1.4) as well as different strategies for fitting the data to extract the polarizability values that better describe the data. Among them, one of the most promising is a Monte Carlo-based fitting method developed by Pedroni, Sconfietti and Pasquini that uses fixed-t subtracted DRs [11, 57].

3.1 Low-energy Compton scattering experiments

The first nuclear Compton scattering experiments on the proton were reported in the 1950s and 60s by Pugh *et al.* [58], Oxley [59], Hyman *et al.* [60], Bernardini *et al.* [61], and Goldansky *et al.* [62]. All of these were low-energy experiments ($\omega_\gamma \lesssim 100$ MeV) mostly aimed of testing the dispersion theories that were developing at that time. The technical difficulties in performing photon experiments caused these measurements to have considerable statistical and systematic errors and nowadays they are normally not considered in any global fits to extract the polarizabilities. Nevertheless, these experiments managed to obtain results that are in reasonable agreement with the current values. Notable examples are the work from Goldansky *et al.* that led to an extraction of the scalar polarizabilities $\alpha_{E1} = (9 \pm 2) \times 10^{-4}$ fm^3 and $\beta_{M1} = (2 \mp 2) \times 10^{-4}$ fm^3, and the paper by

Oxley that quotes an unpolarized cross-section between 10.6 and 14.7 nb/sr in the scattering angle region $\theta_{\gamma'} = 70° - 150°$, despite the extremely poor incoming photon energy resolution $\omega_\gamma = 60 \pm 27.5$ MeV.

To have the first precise Compton scattering experiment, twenty years after these first measurements, two major upgrades in the experimental physics techniques had to happen. First of all, was the introduction of the photon tagging technique, which was used to collect the data presented in this thesis. This has been, and still is, a key factor for photo-nuclear experiments, since it allows for a precise determination of the incoming photon energy, as well as for a precise measurement of the photon beam luminosity, essential to accurately extract the cross-section. The other improvement that opened up new possibilities for Compton scattering experiments was the availability of high-volume calorimeters with a high resolution. These two improvements paved the way for a new era of precision Compton scattering experiments and, as it will be shown in the next chapter, they are still two important factors in the work of this dissertation.

Limiting the scope to the low-energy data, namely mostly below the pion photoproduction threshold, the main experiments of this new era are: Federspiel *et al.* [63], Zieger *et al.* [64], Hallin *et al.* [65], MacGibbon *et al.* [66], and Olmos de Léon *et al.* [67]. These experiments were all concentrated in 10 years, from 1991 to 2001, and besides Hallin and Zieger they are all very similar. In the next sections, a brief description of all of them will be given, and more words will be spent on the work by Olmos de Léon and colleagues, since it is the most comprehensive and recent one.

3.1.1 Federspiel experiment

The first of these tagged-photon Compton scattering experiments was performed at The Nuclear Physics Laboratory of the University of Illinois, Champaign, USA, by Federspiel and colleagues [63]. The incoming tagged photons were divided into 8 bins, 4 MeV each, from $\omega_\gamma = 32$ to 72 MeV. After being collimated, the photon beam impinged on a liquid hydrogen target, and the particles in the final state were detected by two large NaI detectors placed at scattering angles $\theta_{\gamma'} = 60°$ and $\theta_{\gamma'} = 135°$, respectively. They obtained 16 points of unpolarized differential cross-section, with a statistical error of about $\pm 10\%$ and a total systematic error of about $\pm 2.2\%$. They performed a fit to the data using L'vov DR model [68], assuming the Baldin sum rule constraint $\alpha_{E1} + \beta_{M1} = (14.2 \pm 0.5) \times 10^{-4}$ fm^3. The final results quoted a value for $\alpha_{E1} = (10.9 \pm 2.2 \pm 1.3) \times 10^{-4}$ fm^3 and for $\beta_{M1} = (3.3 \mp 2.2 \mp 1.3) \times 10^{-4}$ fm^3, where the first error is statistical and the

second is systematic. The opposite sign indicates that the errors on α_{E1} and β_{M1} are completely anticorrelated. This is always true whenever the Baldin sum rule constraint is imposed in the fit.

3.1.2 MacGibbon experiment

The MacGibbon experiment [66] was performed at the Saskatchewan Accelerator Laboratory (SAL) in Saskatoon, Canada, as a follow-up of the one published by Federspiel, 4 years earlier. They used the same two large NaI detectors, placed at scattering angles $\theta_{\gamma'} = 90°$ and $\theta_{\gamma'} = 135°$, and they simultaneously measured a large incoming photon energy range from $\omega_\gamma = 70$ to 148 MeV, extracting 9 points of unpolarized differential cross-section, per scattering angle. Of these 9 bins in ω_γ, the first 4 were tagged ($\omega_\gamma = 72.2$ to 96.8 MeV), while the other 5 were untagged. The normalization of the untagged bins was done based on the well-known normalization of the data in the tagged region, extrapolated to the higher energy region using the bremsstrahlung distribution shape. The statistical errors in the unpolarized differential cross-section were in the range from $\pm 10\%$ to $\pm 20\%$, and the total systematic errors about $\pm 2.9\%$ for the untagged and from 3 to 4% for the tagged bins. The fit to the data was done using the L'vov DR model [68], both with and without the Baldin sum rule constraint as an additional point at $\alpha_{E1} + \beta_{M1} = (14.2 \pm 0.5) \times 10^{-4}$ fm^3. The final results for the two proton scalar polarizabilities, independent of the inclusion of the Baldin sum rule, are $\alpha_{E1} = (12.5 \pm 0.6 \pm 0.7 \pm 0.5) \times 10^{-4}$ fm^3 and $\beta_{M1} = (1.7 \mp 0.6 \mp 0.7 \mp 0.5) \times 10^{-4}$ fm^3, where the first error is statistical, the second systematic and the last one is due to the model.

3.1.3 Hallin experiment

Among the five experiments considered here, the Hallin experiment covered the highest incoming photon energy range ($\omega_\gamma = 136 - 289$ MeV) [65], and it was performed at the SAL (Saskatoon, Canada) using the large NaI calorimeter BUNI, developed at Boston University. This particular detector covers only a small fraction of the solid angle, and so the measurements at different scattering angles were done sequentially, one after the other. Moreover, four different bremsstrahlung end point energies were used (170, 200, 244 and 298 MeV) for each measurement at different scattering angles, and only the incoming photons with an energy close to the end point of the bremsstrahlung distribution were used. Every measurement required about one day to collect enough statistics and a dedicated

detector calibration for every different end point energy value. This huge work produced a consistent number of points for both differential unpolarized cross-section and excitation function. The statistical errors are lower in the differential cross-section compared to the ones in the excitation function, since the bins in energy are wider in the former compared to the latter, and they range from about $\pm 3.5\% - 5\%$ in the backward to $\pm 10\% - 18\%$ in the forward region. The systematic errors, instead, are composed of two parts, one correlated and one point-to-point uncorrelated, and in total they are about $\pm 3.7\% - 4.2\%$. The fit to the data using L'vov DR model [68], and assuming the Baldin sum rule constraint $\alpha_{E1} + \beta_{M1} = (14.2 \pm 0.5) \times 10^{-4}$ fm^3, gave the lowest χ^2 value for $\alpha_{E1} = (9.8 \pm 0.4 \pm 1.1) \times 10^{-4}$ fm^3 and $\beta_{M1} = (4.4 \mp 0.4 \mp 1.1) \times 10^{-4}$ fm^3, where the two errors are respectively statistical and systematic.

3.1.4 Zieger experiment

This experiment led to the first, and up to now only, measurement of the unpolarized Compton scattering cross-section at scattering angle $\theta_{\gamma'} = 180°$ [64]. This is a very interesting measurement since the cross-section at this scattering angle is only sensitive to the difference $\alpha_{E1} - \beta_{M1}$, as seen in Chapter 2. To perform this innovative measurement, the forward proton (recoiling at $\theta_{p'} = 0°$) was detected in a spectrometer. The cross-section was determined by comparing the Compton proton and Compton electron yields, allowing for absolute normalization without a precise knowledge of the shape and the intensity of the incoming photon beam. Two different points at $\omega_\gamma = 98$ and 132 MeV were measured, both 16 MeV wide. The statistical errors for the two points are $\pm 18.4\%$ and $\pm 5.4\%$, respectively, while the systematic errors are $\pm 6.4\%$ and 4.3%. A fit to the data was done using the L'vov DR model [68], with the difference of the electric and the magnetic scalar polarizabilities as the only free parameter. The best fit was obtained for $\alpha_{E1} - \beta_{M1} = \left(7.03^{+2.49+2.14}_{-2.37-2.05}\right) \times 10^{-4}$ fm^3, where the two errors are statistical and systematic, respectively. Assuming $\alpha_{E1} + \beta_{M1} = 14.2 \times 10^{-4}$ fm^3, individual values for the two proton scalar polarizabilities were determined to be $\alpha_{E1} = \left(10.62^{+1.25+1.07}_{-1.19-1.03}\right) \times 10^{-4}$ fm^3 and $\beta_{M1} = \left(3.58^{-1.19-1.03}_{+1.25+1.07}\right) \times 10^{-4}$ fm^3.

3.1.5 Olmos de Léon experiment

The highest statistics experiment published up to now was performed by the TAPS Collaboration at the MAMI facility, in Mainz (Germany) [67]. The unpolarized Compton scattering cross-section was measured in both a wide energy

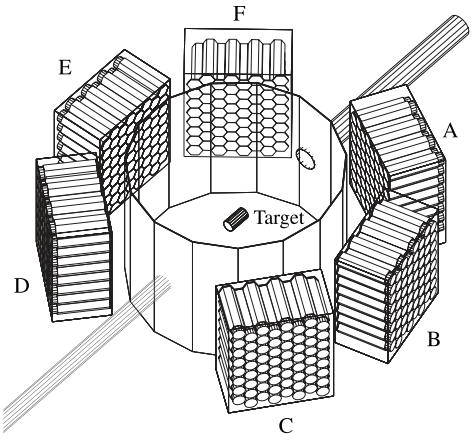

Figure 3.1: TAPS apparatus used for the Olmos de Léon *et al.* measurement. The photon beam enters from the top-right corner, between blacks F and A. The figure is reproduced from Ref. [67].

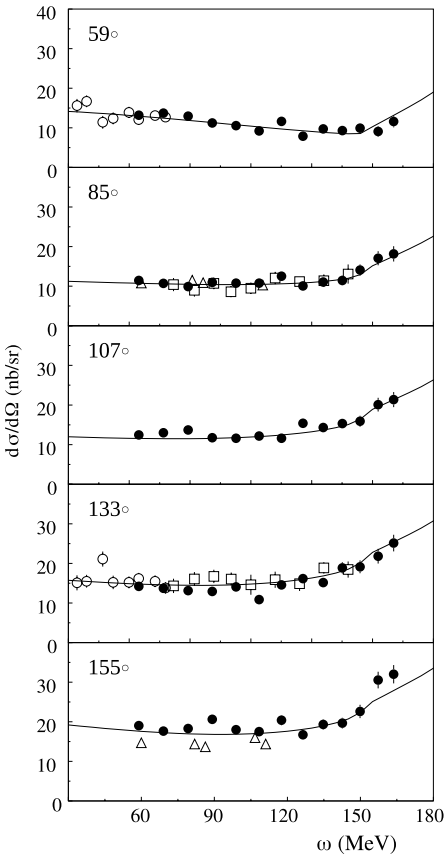

Figure 3.2: Differential Compton scattering cross-section in the lab system for different values of the scattering angle $\theta_{\gamma'}$. Solid circles (●) are the results from Olmos de Léon *et al.*, open circles (◯) are results from Federspiel *et al.*, open squares (□) are MacGibbon *et al.*, and open triangles (△) are taken from here [69]. The figure is reproduced from Ref. [67].

($\omega_\gamma = 55 - 165$ MeV) and scattering angle ($\theta_{\gamma'} = 59 - 155°$) range. It was done by using the large Two-Arm Photon Spectrometer (TAPS) array, a modular detector arranged in six different blocks of BaF_2 crystals. The TAPS apparatus is still used in a different configuration to cover the forward region in the setup used for this thesis. The apparatus used in the measurement is represented in Fig. 3.1 (taken from the original paper, Ref. [67]). They collected almost 200 hours of unpolarized data, for a total selected sample of $\sim 2 \times 10^5$ Compton events. The final results consist of a significant number of data-points: 5 scattering angles per 13 different incoming photon energies, with a statistical error from ±5%, for the lower energy bins, up to ±10%, for the highest energy bins, and a correlated total systematic error of about 3%. In addition, a point-to-point systematic error of about 5% has to be added, due to uncertainties in the apparatus geometry and in the simulation. The published results are reported in Fig. 3.2 (taken from Ref. [67]), together with some of the results from the experiments described in the previous sections. A fit including only the data from this experiment was done within the DRs framework [38] using the π photoproduction multipoles of Arndt *et al.* [42], solution SAID-SM99K. The best-fit values for the two polarizabilities are $\alpha_{E1} = (11.9 \pm 0.5 \mp 1.3) \times 10^{-4}$ fm^3 and $\beta_{M1} = (1.2 \pm 0.7 \pm 0.3) \times 10^{-4}$ fm^3, without the Baldin sum rule constraint, where the errors are statistical and systematic, respectively.

3.1.6 Sokhoyan experiment

This work can be thought as a pilot experiment used as a proof of concept to show the feasibility of the precise measurements described in this dissertation. It consists of about 200 hours of linearly polarized data collected in June 2013 using the experimental setup of the A2 Collaboration. The analysis performed on this data is very similar to the one described in next chapters. This work resulted in the first extraction of the beam asymmetry Σ_3 below the pion photoproduction threshold. The results were published in 2017 [20] together with an extraction of the magnetic polarizability β_{M1}. The fit to the asymmetry data was performed by fixing the value of $\alpha_{E1} + \beta_{M1} = 14.0 \times 10^{-4}$ fm^3, and using both BχPT and HBχPT frameworks, resulting respectively in $\beta_{M1} = \left(2.8^{+2.3}_{-2.1}\right) \times 10^{-4}$ fm^3 and $\beta_{M1} = \left(3.7^{+2.5}_{-2.3}\right) \times 10^{-4}$ fm^3 [20]. The results, reported in Fig. 3.3 for BχPT, are in good agreement with the other measurements described in the previous sections, despite the errors are not really competitive. Nevertheless, this experiment showed that Σ_3 provides a new and different input for the determination of the scalar polarizabilities, and the experience gained in that work was crucial for the

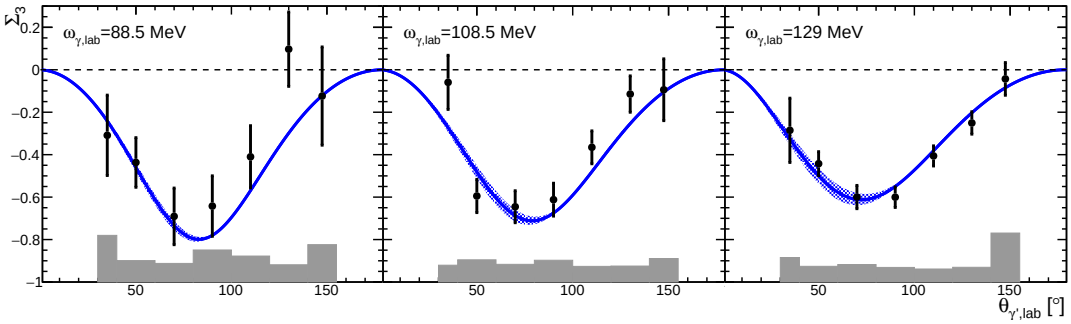

Figure 3.3: Beam asymmetry Σ_3 for three photon beam energy ranges: $\omega_\gamma = 79 - 98$ MeV (left), $\omega_\gamma = 98 - 119$ MeV (middle), $\omega_\gamma = 119 - 139$ MeV (right). The error bars represent the statistical errors, the gray bars the systematic errors. The fit results within BχPT are shown as a blue curve. Shaded blue bands are determined by the fit errors on β_{M1}. These results were published as a proof of principle for the experiment discussed in this dissertation [20].

success of the high precision experiment described in this thesis.

3.2 Baldin sum rule evaluation

A first experimental evaluation of the Baldin sum rule from photo-absorption data was published by Damashek and Gilman, using results published by SLAC and Deutsches Elektronen-SYnchrotron (DESY) in the 1960s. They determined the sum of the two scalar polarizabilities to be:

$$\alpha_{E1} + \beta_{M1} = (14.2 \pm 0.3) \times 10^{-4} \text{ fm}^3. \tag{3.1}$$

With the publication of new data, more recent evaluations of this sum rule have been published. In particular, precise data were published by MacCormick *et al.* [70] from an experiment performed at the MAMI facility, using the electron beam in conjunction with the DAPHNE detector [71]. These high-accuracy data points cover a wide incoming photon energy range $\omega_\gamma = 200 - 800$ MeV and they were used, together with a complementary dataset from the Daresbury Nuclear Physics Lab [72], for a re-evaluation of the Baldin sum rule published by Babusci and colleagues [73]. In this analysis, the total photo-absorption cross-section has been calculated using the SAID analysis [42] (solution SP97K) and the data were fitted to get the best function that describes them. The authors obtained a new value for the Baldin sum rule:

$$\alpha_{E1} + \beta_{M1} = (13.69 \pm 0.14) \times 10^{-4} \text{ fm}^3. \tag{3.2}$$

Another re-evaluation was published a few years later by the TAPS collaboration [67]. They determined the total photo-absorption cross-section using the partial wave analysis method. Close to the pion photoproduction threshold they used multipole solutions of Arndt *et al.* [42], while for the energy above they used SAID partial wave analysis (solution SM99K). They determined a value for the Baldin sum rule of:

$$\alpha_{E1} + \beta_{M1} = (13.8 \pm 0.4) \times 10^{-4} \text{ fm}^3. \tag{3.3}$$

3.3 Scalar polarizabilities extraction

The experiments described above represent the vast majority of the current world database on Compton scattering on the proton. It is interesting to note that all these experiments, with the exception of Sokhoyan *et al.* [20], measured the unpolarized cross-section only, and the first results on the beam asymmetry Σ_3 at low beam energy were published only four years ago. In the previous sections, the values of the two scalar polarizabilities extracted using only the single dataset from each experiment were given, together with a short description of the experiments and the relative size of the errors. A first global extraction was published together with the results from the TAPS Collaboration, obtained by fitting all the available points at low energy (four out of the six experiments described above, with the exception of Hallin *et al.* and Sokhoyan *et al.*) using a DR code from L'vov [38]. The quoted values are [67]

$$\begin{aligned} \alpha_{E1} &= (12.1 \pm 0.3 \mp 0.4) \times 10^{-4} \text{ fm}^3, \\ \beta_{M1} &= (1.6 \pm 0.4 \pm 0.4) \times 10^{-4} \text{ fm}^3, \end{aligned} \tag{3.4}$$

fixing the value of $\alpha_{E1} + \beta_{M1} = (13.8 \pm 0.4) \times 10^{-4}$ fm^3; and

$$\begin{aligned} \alpha_{E1} &= (11.9 \pm 0.5 \mp 0.5) \times 10^{-4} \text{ fm}^3, \\ \beta_{M1} &= (1.5 \pm 0.6 \pm 0.2) \times 10^{-4} \text{ fm}^3, \end{aligned} \tag{3.5}$$

without the Baldin sum rule constraint.

From the experimental extractions of these two parameters, it turns out that β_{M1} is about one order of magnitude smaller than α_{E1}. This can be explained by the presence of two different and competitive processes that contribute to the magnetic scalar polarizabilities. The quark core shows a paramagnetic contribution, while the virtual pion cloud exhibits both diamagnetic and paramagnetic

contributions. Since the paramagnetic contribution is stronger, as usual, the overall effect is an alignment of the generated dipole moment with the magnetic field ($\vec{H}$), and so a positive value of the magnetic scalar polarizability β_{M1}.

After this first extraction, other estimates for the two proton scalar polarizabilities have been published, both predicted from the theory and extracted from the data. In the next sections a small review of these analyses is given, together with the quoted values. Lastly, in Section 3.3.5, a summary of the current world situation is reported, together with a critical discussion on it.

3.3.1 χPT predictions for the proton scalar polarizabilities

A study of low-energy Compton scattering on the proton within the framework of BχPT was published in 2010 by Lensky and Pascalutsa [47]. It includes all the effects up to the next-to-next-to-leading order, namely the effects of orders p^2, p^3 and p^4/Δ (with $\Delta \approx 300$ MeV being the Δ-resonance excitation energy). In the calculation, there are no unknown LECs up to this order, and the first enters one order higher (p^4). As explained in Section 2.1.4, the big advantage of effective field theories is the possibility to estimate the theoretical uncertainties using truncated calculations, and in this case the authors showed that these uncertainties are of the same size as the experimental uncertainties of the existing low-energy Compton scattering data. The differential unpolarized cross-section predicted by this calculation showed a good agreement with the existing data, as can be seen in Fig. 7 of Ref. [47]. Despite this, the values predicted for the two proton scalar polarizabilities turned out to be in significant disagreement with the one extracted from the global fit of the data, showed in Eq. (3.5). In fact, the values of the scalar polarizabilities predicted by the BχPT are:

$$\begin{aligned} \alpha_{E1} &= (10.8 \pm 0.7) \times 10^{-4}\ \text{fm}^3, \\ \beta_{M1} &= (4.0 \pm 0.7) \times 10^{-4}\ \text{fm}^3. \end{aligned} \tag{3.6}$$

This significant discrepancy reflects the unfortunately modest sensitivity of the unpolarized Compton scattering cross-section to the scalar polarizabilities, meaning that significant differences in the two parameters are not strongly visible in the experimental observables. Conversely, small variations in the observables yield to significant differences in the scalar polarizability values. This is a further indication of the importance of performing a precise experiment, covering an angular region as wide as possible, and performing an exhaustive study of the systematic uncertainties.

3.3.2 HBχPT fit to extract the proton scalar polarizabilities

An extensive fitting study of both the low- and high-energy existing data on Compton scattering on the proton was performed using HBχPT by McGovern, Phillips and Grießhammer [52]. In this work, the authors divided the energy range in two different parts: a low-energy region ($\omega_\gamma \lesssim m_\pi$), where they used an amplitude completed up to the N^{4}LO ($\mathcal{O}(e^2\delta^4)$); and a high-energy region (ω_γ similar to the Δ-resonance excitation energy), where the Compton amplitude is truncated at the NLO ($\mathcal{O}(e^2\delta^0)$).

An extensive explanation of the fit procedure can be found in the original paper [52], together with the numerical values used for the non-free parameters. The free parameters in the final fit were the two scalar polarizabilities α_{E1} and β_{M1}, the spin polarizability γ_{M1M1} and the Lagrangian parameter b_1, that describes the $\gamma N\Delta$ M1 transition strength. This last parameter has been determined by fitting the high-energy part of the database, i.e. in the Δ-resonance region. The fits to this high-energy part and to the low-energy database were iterated until they converged. Furthermore, since the data in the forward region are scarce, and this is the region where the sensitivity to the value of $\alpha_{E1}+\beta_{M1}$ is higher, the Baldin sum rule constraint was used in the fit: $\alpha_{E1}+\beta_{M1} = (13.8 \pm 0.4) \times 10^{-4}$ fm^3. The values of the two scalar polarizabilities that minimized the χ^2 function turned out to be:

$$\begin{aligned} \alpha_{E1} &= (10.65 \pm 0.35 \pm 0.2 \pm 0.3) \times 10^{-4} \text{ fm}^3, \\ \beta_{M1} &= (3.15 \mp 0.35 \pm 0.2 \mp 0.3) \times 10^{-4} \text{ fm}^3, \end{aligned} \tag{3.7}$$

where the errors come from statistics, Baldin sum rule and theory model, respectively. The best values obtained for the other two parameters are:

$$\begin{aligned} \gamma_{M1M1} &= (2.2 \pm 0.5) \times 10^{-4} \text{ fm}^4, \\ b_1 &= (3.61 \pm 0.02), \end{aligned}$$

where the quoted errors are statistical only.

A peculiarity of this study is the definition of a "selected" database to be used for the fit. In a previous paper from the same group [45], all the existing datasets have been compared in the phase-space regions where they overlap, searching for possible disagreements and outliers. According to the authors, this study showed the presence of some outliers in the so-called modern low-energy data — the

experiments described at the beginning of this chapter: two single points, namely Federspiel [63] ($\omega_\gamma = 45$ MeV, $\theta_{\gamma'} = 135°$), Olmos de Léon [67] ($\omega_\gamma = 108$ MeV, $\theta_{\gamma'} = 133°$), plus all the points from Hallin [65] with energy $\omega_\gamma > 150$ MeV. Furthermore, two of the old low-energy experiments were completely excluded from the fit, namely [59] and [61], as well as the points from Baranov [69] at $\theta_{\gamma'} = 150°$. The definition of this "selected" database was performed by the authors using a qualitative approach, by simply studying the agreement among different datasets and predictions in the same phase-space region. This led to the exclusion of single points, at given energies and angles, from entire datasets, without any experimental reason (i.e. detector inefficiencies, higher level of background, etc.) and without constructive discussions with the authors of the measurements. The main arguments in favor of this "selected" database is a general improvement of the final χ^2 of the fit. In a recent work by Pasquini, Pedroni and Sconfietti [11], the authors spent a big effort in systematically checking the consistency of the full database, using different statistical strategies in order to achieve a quantitative and objective result. They concluded that their consistency tests did not show any strong statistical motivations for the exclusion of any data points from the global database below the pion photoproduction threshold, even though they observed significant deviations of a few points at the backward scattering angles. Furthermore, they showed how the use of this "selected" database in the fit for the extraction of the scalar polarizabilities can affect the central value of β_{M1}, leading to a $40-50\%$ increase [11]. This effect seems to partially explain the disagreement between the different extraction of the scalar polarizabilities reported in this chapter. This is further discussed in Section 3.3.5.

3.3.3 BχPT fit to extract the proton scalar polarizabilities

A fit similar to what was described in the previous section was also performed in the framework of covariant BχPT [74]. As explained in Section 3.3.1, this theory is fully predictive to the NNLO and the values of α_{E1} and β_{M1} turned out to be in disagreement with the ones extracted from the TAPS collaboration dataset (see Eq. (3.5)), using DR based code, and in good agreement with the results of the fit within the HBχPT framework. To further explore this apparent discrepancy, the authors added to the covariant theory the terms with the bigger contribution at the N^{4}LO, including the counter terms $\delta\alpha_{E1}$ and $\delta\beta_{M1}$ that have to be fitted to the low-energy data. The same "selected" low-energy database of Ref. [52] was used for this fit, up to a photon energy $\omega_\gamma = 170$ MeV. No data were fitted at higher energies, just a check by eye of the agreement between the fit and

the data was required. The fit was done both with and without the Baldin sum rule constraint. The best values obtained for the two scalar polarizabilities in the latter case are:

$$\begin{aligned} \alpha_{E1} &= (10.9 \pm 0.45 \pm 0.4) \times 10^{-4} \text{ fm}^3, \\ \beta_{M1} &= (3.6 \pm 0.55 \pm 0.4) \times 10^{-4} \text{ fm}^3, \end{aligned} \tag{3.8}$$

where the errors are statistical and theoretical, respectively. Instead, the results quoted by the authors for the Baldin sum rule ($\alpha_{E1}+\beta_{M1} = (13.8\pm0.4)\times10^{-4}$ fm^3) constrained fit are:

$$\begin{aligned} \alpha_{E1} &= (10.6 \pm 0.25 \pm 0.2 \pm 0.4) \times 10^{-4} \text{ fm}^3, \\ \beta_{M1} &= (3.2 \mp 0.25 \mp 0.2 \pm 0.4) \times 10^{-4} \text{ fm}^3, \end{aligned} \tag{3.9}$$

where the errors come from statistics, Baldin sum rule and theory model, respectively.

These results are in very good agreement with the ones obtained within the HBχPT framework, and they are also consistent with the one predicted by the model at the NLO. On the other hand, it is interesting to note how these values are in substantial disagreement with those in Eq. (3.5), despite no new experimental results were published in the meantime.

3.3.4 Bootstrap-based fit to extract the proton scalar polarizabilities

All the extractions of the scalar polarizabilities from the data discussed in the previous sections are obtained using the standard fitting technique, the so-called least squares method. It is based on the χ^2 function:

$$\chi^2(\varphi) = \sum_{i=1}^{N} \Big(\frac{O_i - T_i(\varphi)}{\sigma_i} \Big)^2, \tag{3.10}$$

where O_i is the i-th of the N experimental observations, σ_i is its statistical uncertainty in root mean square (rms) units and $T_i(\varphi)$ is the prediction from the theoretical model, depending on the values used for the set of unknown parameters φ. The optimal set of parameters $\hat{\varphi}$ is the one that minimize the value of $\chi^2(\hat{\varphi}) = \chi^2_{min}$. Despite this being a standard technique when fitting a large variety of scientific data, it presents some difficulties in the inclusion of the sys-

tematic uncertainties associated with the experimental data, especially if they do not follow a Gaussian distribution. In fact, in such cases, the resulting χ^2_{min} parameter does not follow the standard χ^2 distribution, since it is no longer a sum of squared, independent, standard Gaussian random variables [57]. This is a situation that can commonly happen when fitting results from a wide range of different experiments, and it is also the case of the low-energy Compton scattering database, where each experiment has many sources of systematic errors that should be properly treated. As an example, the results from the TAPS collaboration [67], which is the largest subset of the existing database, has both correlated and point-to-point uncorrelated systematic errors.

A new Monte Carlo-based fitting method was very recently developed by Pedroni and Sconfietti [57]. It is based on the parametric bootstrap technique [75] and it has also been used to fit the low-energy Compton scattering dataset to extract the proton scalar polarizabilities [11]. Generally speaking, it basically consists of randomly generating N Monte Carlo replicas of the experimental database, and to fit each of these simulated databases. From each of these fits, a set of best-values $\hat{\varphi}_j$ can be extracted, where j is the j-th bootstrap iteration. From this sample, all the properties of the unknown probability distribution of the parameter set φ can be evaluated. This method is very general and was applied to the Compton data fit under the following assumptions:

- every experimental point is Gaussian distributed around the measured value, with standard deviation given by the statistical error;
- if not explicitly stated by the experimental group in the paper, every systematic error is uniformly distributed. If there are more sources, they are considered as independent;
- the systematic errors affect the data as a constant scaling factor for the whole dataset;
- all the n_{set} datasets are independent.

Under these conditions, a generic bootstrapped point P_{ij} can be written as:

$$P_{ij} = (1 + \delta_{sj})(E_i + \gamma_{ij}\sigma_i) \quad \forall s = 1, \ldots, n_{set}, \tag{3.11}$$

where the index i runs over the number of experimental points in each dataset (n_s), the index j runs over the Monte Carlo iterations (N) and the index s runs over the number of independent dataset (n_{set}). E_i is a given experimental point

with error σ_i. The Gaussian normal variable $\gamma_{ij} \in \mathcal{G}[0,1]$ is used to sample the bootstrapped point inside the statistical error of the experimental one, and $\delta_{sj} \in \mathcal{U}[-\Delta_s, \Delta_s]$ is a box distributed variable, common for all the n_s points within a given dataset s, that accounts for the published systematic error $\pm\Delta_s$ and is extracted independently at every iteration for each dataset. In case of multiple independent sources of systematic errors, δ_{sj} is the product of the δ_{sjk} box distributed variables, where $k = 1, ..., n_{source}$.

The minimization function in Eq. (3.10) can then be modified as

$$\chi^2_{boot,j}(\varphi) = \sum_{i=1}^{n_{data}} \left(\frac{P_{ij} - T_i(\varphi)}{\sigma_{ij}} \right)^2, \tag{3.12}$$

where the σ_{ij} has been modified to account for the scaling due to the systematic error:

$$\sigma_{ij} = (1 + \delta_{sj})\sigma_i, \tag{3.13}$$

for the s-th dataset. The minimum of the function in Eq. (3.12), $\hat{\chi}^2_{boot,j} \equiv \chi^2_{boot,j}(\hat{\varphi})$, gives a set of parameters $\hat{\varphi}_j$ for every bootstrap cycle. After N iterations, the observed distribution $\mathcal{P}(\hat{\varphi}_j)$ of the set of random parameters $\hat{\varphi}_j$ gives an estimate of the true probability distribution $\mathcal{P}(\varphi)$. Now, the best value and the standard deviation of the set of unknown parameters φ can be determined as:

$$\hat{\varphi} \equiv \frac{1}{N} \sum_{j=1}^{N} \hat{\varphi}_j, \quad \text{and} \quad \sigma_{\hat{\varphi}} \equiv \sqrt{\frac{1}{N-1} \sum_{j=1}^{N} (\hat{\varphi}_j - \hat{\varphi})^2}. \tag{3.14}$$

The quality of the fit can be estimated by using the minimum value $\hat{\chi}^2_{boot,j}$ of the χ^2 distribution defined in Eq. (3.10). A demonstration of the link between Eq. (3.12) and Eq. (3.10), as well as a more detailed and comprehensive discussion of this new fit procedure, is given in Ref. [57].

The fit procedure briefly discussed above has many advantages, such as the possibility to easily include or exclude from the fit any kind of systematic errors, the possibility to evaluate the expected theoretical probability distribution of the set of unknown parameters even in the presence of systematic errors, and the possibility to include uncertainties on additional model parameters (such as the spin polarizabilities for the case of low-energy Compton scattering) that are not directly fitted to the data. This technique was successfully applied for the first time to extract the scalar proton polarizability from low-energy Compton data, using fixed-t subtracted DRs for the model predictions [11]. The authors performed the fit procedure under various conditions: with and without the Baldin

sum rule constraint $\alpha_{E1} + \beta_{M1} = (13.8 \pm 0.4) \times 10^{-4}$ fm^3, with γ_π as free or fixed parameter, with and without the systematic errors, and including just the TAPS dataset [67] or using the full low-energy database (including both "old-" and "new-"era experiments as explained in Section 3.1). To include the uncertainties of the model parameters not treated as free in the fit, such as the spin polarizabilities, the value of each of these parameters p was sampled at each iteration from a Gaussian distribution defined as $\mathcal{G}[p, \sigma_p^2]$. Furthermore, only for the TAPS dataset, a 5% point-to-point systematic error was added in quadrature to the statistical error, in order to be able to use the procedure described above to include the other sources of systematic errors.

The authors observed that the obtained values of the two proton scalar polarizabilities depend on the choice of the dataset and on the inclusion or not of the Baldin sum rule constraint, but the variations are well inside the uncertainties. Furthermore, as expected, the inclusion of the systematic errors does not change the central values of the two fitted parameters, but increases their uncertainties. Interestingly, this inclusion does not change the minimum $\hat{\chi}^2_{boot}$ of the χ^2 distribution, but shifts its cumulative distribution function to the right, meaning that higher values of $\hat{\chi}^2_{boot,j}$ are more likely to occur. Last of all, they found a very good agreement between the value of γ_π extracted from the fit and the one existing in literature. In conclusion, including the entire database in the fit, with the systematic errors, and using the Baldin sum rule constraint, they obtained these values for the two proton scalar polarizabilities:

$$\begin{aligned} \alpha_{E1} &= 12.03^{+0.48}_{-0.53} \times 10^{-4} \text{ fm}^3, \\ \beta_{M1} &= 1.77^{+0.52}_{-0.54} \times 10^{-4} \text{ fm}^3, \end{aligned} \tag{3.15}$$

that are in good agreement with the ones obtained by the TAPS collaboration (Eq. (3.5)), but disagree with the results obtained within EFT frameworks using the "selected" database (Eqs. (3.7) and (3.9)).

3.3.5 PDG global average values for the proton scalar polarizabilities

The Particle Data Group (PDG) includes in its annual review a global average value for the two proton scalar polarizabilities α_{E1} and β_{M1}. The current quoted values are [55]

$$\alpha_{E1} = (11.2 \pm 0.4) \times 10^{-4} \text{ fm}^3,$$

Table 3.1: Summary of the main experimental extractions of the scalar polarizabilities. All the values of α_{E1} and β_{M1} reported in this table were obtained from a DR-based fit of the unpolarized Compton scattering cross-section data measured in each single experiment. All the fits were done using the Baldin sum rule constraint $\alpha+\beta = 14.2\times10^{-4}$ fm^3 (in Ref [67] authors used $\alpha+\beta = 13.8\times10^{-4}$ fm^3). The quoted errors, when given, are statistical, systematic and theoretical, respectively.

First author	**Ref.**	ω_γ **[MeV]**	$\theta_{\gamma'}$ **[°]**	α_{E1} **[10^{-4}fm^3]**	β_{M1} **[10^{-4}fm^3]**
Federspiel	[63]	$32-72$	$60, 135$	$10.9 \pm 2.2 \pm 1.3$	$3.3 \mp 2.2 \mp 1.3$
MacGibbon	[66]	$70-148$	$90, 135$	$12.5 \pm 0.6 \pm 0.7 \pm 0.5$	$1.7 \mp 0.6 \mp 0.7 \mp 0.5$
Hallin	[65]	$136-289$	$25-135$	$9.8 \pm 0.4 \pm 1.1$	$4.4 \mp 0.4 \mp 1.1$
Zieger	[64]	$98, 132$	180	$10.62^{+1.25+1.07}_{-1.19-1.03}$	$3.58^{-1.19-1.03}_{+1.25+1.07}$
Olmos de Léon	[67]	$55-165$	$59-155$	$12.1 \pm 0.4 \mp 1.0$	$1.6 \pm 0.4 \pm 0.8$

$$\beta_{M1} = (2.5 \pm 0.4) \times 10^{-4} \text{ fm}^3. \tag{3.16}$$

These averaged values are obtained using the results from [49, 52, 66, 67, 76]. It is interesting to note how the averaged values quoted by the current review are significantly different from the ones quoted in the 2012 review [77]:

$$\begin{aligned} \alpha_{E1} &= (12.0 \pm 0.6) \times 10^{-4} \text{ fm}^3, \\ \beta_{M1} &= (1.9 \pm 0.5) \times 10^{-4} \text{ fm}^3. \end{aligned} \tag{3.17}$$

This shift is due to the introduction in the average of the fit results obtained using HBχPT from McGovern *et al.* [52]. This causes also a contraction in the uncertainties of the two scalar polarizabilities, despite this additional analysis not being based on new data but the same dataset already used before.

The results mentioned in this chapter are summarized in Tables 3.1 and 3.2. Figure 3.4 shows the experimental results discussed in Sections 3.1.1, 3.1.2, 3.1.4 and 3.1.5 together with the BχPT prediction (Section 3.3.1) and the fit results obtained using HBχPT (Section 3.3.2) and DR (Section 3.3.4) frameworks. The black circle represents the global average quoted by the PDG. From the bubble plot in Fig. 3.4, it is easy to see how the value of β_{M1} extracted using DR-based models — black full and dashed circles as well as the red circles — is systematically lower than the ones obtained using χEFT — green and blue circles. This observation seems to indicate that the source of the differences between the various extractions of the scalar polarizabilities could arise from the differences in the theories. Nevertheless, as it was already discussed at the end of Section 3.3.2, the choice of the "selected" database with the exclusion of some of the points from

Table 3.2: Summary of the main theoretical average of the scalar polarizabilities. The first row is a pure theoretical prediction without the fit of any experimental data. The last row is a global average of some of the averages present in this table. All the other values of α_{E1} and β_{M1} were obtained from a fit of the unpolarized Compton scattering cross-section data published in the given references. All the fits were done using the Baldin sum rule constraint $\alpha+\beta = 13.8\times10^{-4}$ fm^3. The quoted errors, when given, come from statistics, theory models and Baldin sum rules, respectively.

First author	**Ref.**	**Datasets**	**Theory**	$\boldsymbol{\alpha_{E1}}$ **[10^{-4}fm^3]**	$\boldsymbol{\beta_{M1}}$ **[10^{-4}fm^3]**
Lensky	[46]	—	BχPT	10.8 ± 0.7	4.0 ± 0.7
Olmos de Léon	[67]	[63, 64, 66, 67]	DR	$12.1 \pm 0.3 \mp 0.4$	$1.6 \pm 0.4 \pm 0.4$
McGovern	[52]	[58, 60, 62–67][a]	HBχPT	$10.65 \pm 0.35 \pm 0.3 \pm 0.2$	$3.15 \mp 0.35 \mp 0.3 \pm 0.2$
Lensky	[74]	[58, 60, 62–67][a]	BχPT	$10.6 \pm 0.25 \pm 0.4 \pm 0.2$	$3.2 \mp 0.25 \mp 0.4 \pm 0.2$
Pasquini	[11]	[58–67, 69]	DR	$12.03^{+0.48}_{-0.54}$	$1.77^{+0.52}_{-0.54}$
PDG	[55]	[49, 52, 66, 67, 76]	—	11.2 ± 0.4	2.5 ± 0.4

[a] One single point was excluded from both Refs. [63, 67]

the fit could have had an even stronger impact on the final results. Another factor that can partially explain this disagreement is the value of the spin polarizabilities used in the model for the fit. In the work of Ref. [11], the authors used for the spin polarizabilities the experimental values published by the A2 collaboration [18], which was the first experimental extraction of these parameters. However, in the effective field theories the values of these parameters are predicted by the theory and not given as an input. To estimate the impact of these ingredients, namely the selection of the database and the spin polarizabilities values, to the fit of the scalar polarizabilities, Pasquini and colleagues [11] performed the fits using both the full and the "selected" database and both the experimental and the predicted spin polarizabilities values from Refs. [18] and [45], respectively. The results can be seen in Table 3.3 taken from Ref. [11], where the values in brackets are obtained using the spin polarizabilities predicted in HBχPT. It can be seen that the different inputs for the spin polarizabilities can affect the central value of β_{M1} up to a $\sim$ 30%, while the use of the "selected" database leads to a $\sim$ 50% increase. Furthermore, a fit within a DR framework using both the "selected" database and the spin polarizability values predicted in HBχPT (brackets in the right column in Table 3.3) seems to be in good agreement with the values extracted using χEFT-based models. Despite this being a simplistic test, it gives strong motivations in support of the experimental program conducted at the MAMI facility for both a first precise extraction of the spin polarizabilities and for a new precise measurement of the unpolarized Compton scattering cross-

Table 3.3: Extraction of the proton scalar polarizabilities using a bootstrap-based fit method within fixed-t subtracted DRs. The values on the left are obtained using all the datasets available below pion photoproduction threshold, while the ones on the right are obtained using the "selected" database described in Ref. [45]. In both cases, two different sets of spin polarizabilities were used: the experimental results from Ref. [18] and the values predicted in HBχPT [45]. The results for the latter case are reported in brackets. All the values are in units of 10^{-4} fm^3. The table is reproduced from Ref. [11].

	Full		**"Selected"**	
α_{E1}	11.99 ± 0.31	(11.47 ± 0.30)	11.02 ± 0.33	(10.46 ± 0.32)
β_{M1}	1.81 ± 0.31	(2.33 ± 0.30)	2.78 ± 0.33	(3.34 ± 0.32)

section.

3.4 Lattice QCD calculations of nucleon scalar polarizabilities

In the recent years Lattice Quantum ChromoDynamics (LQCD) with background magnetic fields was used to perform the first calculations of the nucleon magnetic polarizability β_{M1}. This so-called background-field method consists of measuring the mass shift of the nucleon placed in an external classical electromagnetic field [78], and it was successfully used in the past to compute the nucleon magnetic moment [79]. Unfortunately, the implementation of such a calculation for the proton, the case of interest for this dissertation, is very challenging due to the Landau quantization levels. A first result was obtained by the NPLQCD collaboration [80] at the unphysical pion mass $m_\pi \sim 806$ MeV. They obtained for the proton magnetic polarizability a value

$$\beta_{M1} = 5.22 \left(^{+0.66}_{-0.45}\right) (0.23) \times 10^{-4} \text{ fm}^3 \tag{3.18}$$

which is of the same order of magnitude as the experimental one presented in Eq. (3.16), even if they are not in full agreement. In Eq. (3.18), the first uncertainty is the combination of the statistical and systematic errors from the extraction of the energy shift, and the systematic error from the fit to the magnetic field strength. The second uncertainty accounts for discretization and finite volume effects. Very recently, a first extrapolation of the nucleon magnetic polarizability down to the physical region was published [81], using HBχPT framework and different lattice calculations at several pion masses. The resulting theoretical

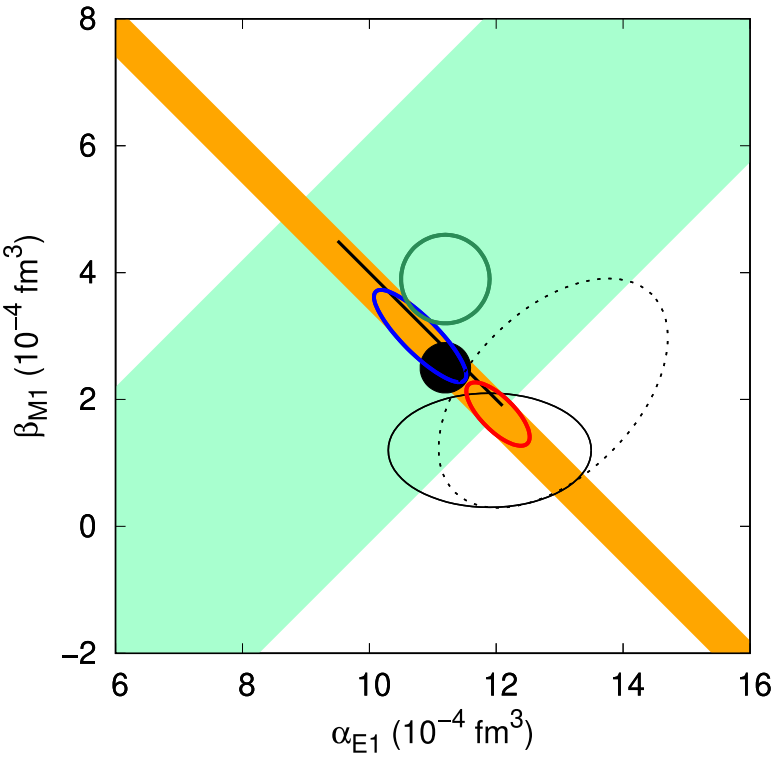

Figure 3.4: Results of α_{E1} vs β_{M1} for the proton, obtained from different experiments and theories. The light-green band shows the experimental results for $\alpha_{E1} - \beta_{M1}$ from Zieger *et al.* [64], the orange band represents the Baldin sum rule constraint average [12]. From the experimental side: the straight black line is Federspiel *et al.* [63] (obtained fitting $\alpha_{E1} - \beta_{M1}$ with the constraint $\alpha_{E1} + \beta_{M1} = 14.0 \times 10^{-4}$ fm^3), the short-dashed black curve is MacGibbon *et al.* [66] (unconstrained fit), and the solid black curve is Olmos de Léon *et al.* [67] (unconstrained fit). From the theoretical side: the green solid curve is the BχPT prediction [46], the blue solid curve is the extraction within HBχPT [52] (using the "selected" database, with the constraint $\alpha_{E1}+\beta_{M1} = (13.8\pm0.4)\times10^{-4}$ fm^3), the solid red curve is the bootstrap-based fit using fixed-t subtracted DRs [11] (using the full database, with the constraint $\alpha_{E1} + \beta_{M1} = (13.8 \pm 0.4) \times 10^{-4}$ fm^3). The solid black circle shows the global average quoted by the PDG [55]. The figure is reproduced from Ref. [11].

Table 3.4: Predictions for proton spin polarizabilities. HDPV is a subtracted fixed-t DR calculation [28]. DPV is a hyperbolic (fixed-angle) DR calculation [39]. $\mathcal{O}(p^n)$ are χEFT calculations at different orders [82–84]. ϵ^3 is a Small Scale Expansion calculation [82]. HBχPT is a heavy baryon chiral perturbation calculation [52]. BχPT is covariant baryon chiral perturbation calculation [74]. K-matrix is a combined K-matrix and DR calculation [85]. $\gamma_{E1} \equiv \gamma_{E1E1}$, $\gamma_{M1} \equiv \gamma_{M1M1}$, $\gamma_{M2} \equiv \gamma_{E1M2}$, and $\gamma_{E2} \equiv \gamma_{M1E2}$. All the values are in units of 10^{-4} fm^4.

	HDPV	**DPV**	$\mathcal{O}(p^3)$	$\mathcal{O}(p^4)_a$	$\mathcal{O}(p^4)_b$	$\mathcal{O}(\epsilon^3)$	**HBχPT**	**BχPT**	**K-Matrix**
γ_{E1}	-4.3	-3.8	-5.7	-1.3	-1.9	-5.4	$-1.1 \pm 1.8_{\text{th}}$	-3.3 ± 0.8	-4.8
γ_{M1}	2.9	2.9	-1.1	3.3	0.4*	1.4	$2.2 \pm 0.5 \pm 0.7_{\text{th}}$	2.9 ± 1.5	3.5
γ_{M2}	-0.02	0.5	1.1	0.2	0.7	1.1	$-0.4 \pm 0.4_{\text{th}}$	0.2 ± 0.2	-1.8
γ_{E2}	2.2	1.6	1.1	1.8	1.9	1.1	$1.9 \pm 0.4_{\text{th}}$	1.1 ± 0.3	1.1
γ_0	-0.8	-1.1	4.6	-3.8	-1.1	1.9	-2.6	-0.9 ± 1.4	2.0
γ_π	9.4	7.8	4.6	6.1	3.5	6.8	5.6	7.2 ± 1.7	11.2

prediction of

$$\beta_{M1} = 2.79(22)\,\binom{+13}{-18} \times 10^{-4}\ \text{fm}^3, \tag{3.19}$$

is in a very good agreement with the experimental results of Eq. (3.16). The numbers in parentheses describe the statistical and systematic uncertainties, respectively, that turned out to be competitive with the ones from experimental extractions.

3.5 Proton spin polarizabilities predictions and extractions

The present experimental knowledge of the proton spin polarizabilities is much poorer than the scalar one. This is mainly because the most clean observables that allow to access the spin polarizabilities are measurable with polarization experiments, in which both a polarized beam and a polarized target are required, considerably increasing the experimental complexity. Until recently, only two linear combination of these parameter — γ_0 and γ_π, introduced in Eqs. (2.9) and (2.10) — have been directly inferred from other reaction channels, still with unsatisfactory precision. The first results on this side have been recently published by the A2 collaboration [18, 19] as part of a massive Compton scattering experimental program, of which this dissertation covers the low-energy part. To counterbalance the lack of experimental data, a strong theoretical interested has resulted in a large set of theoretical predictions, mainly from dispersion relation and chiral perturbation calculations. These different predictions are summarized in Table 3.4. There are two different dispersion relation calculations. As briefly explained in Section 2.1.3, fixed-t subtracted DRs produce a set of parameters a_i

Table 3.5: Experimental extraction of the proton spin polarizabilities [19] from the fit of Σ_{2x}, Σ_{2z} and Σ_3 asymmetries, using either a HDPV [28, 39, 40] or a BχPT [47] calculation. All the values are in units of 10^{-4} fm^4.

	HDPV	**BχPT**	**Average**
γ_{E1E1}	-3.18 ± 0.52	-2.65 ± 0.43	-2.87 ± 0.52
γ_{M1M1}	2.98 ± 0.43	2.43 ± 0.42	2.70 ± 0.43
γ_{E1M2}	-0.44 ± 0.67	-1.32 ± 0.72	-0.85 ± 0.72
γ_{M1E2}	1.58 ± 0.43	2.47 ± 0.42	2.04 ± 0.43

that are directly related to the scalar and the spin polarizabilities. Rather than fixing the Mandelstam variable t, it is also possible to define dispersion relations at a fixed angle. These are known as fixed-angle or hyperbolic DRs. Both these predictions are shown in Table 3.4: HDPV, the fixed-t once-subtracted DR [28], are more accurate at forward $\theta_{\gamma'}$; DPV, the fixed-angle DR [39], are more accurate at backward $\theta_{\gamma'}$. The effective field theories, as briefly outlined in Section 2.1.4, can be used to study the low-energy region of QCD, where the perturbative approach is no longer usable. In this region, QCD is dominated by confinement and so pions and nucleons, instead of gluons and quarks, can be considered as the only relevant degrees-of-freedom. A so-called effective Lagrangian is constructed, that consists of an infinite number of terms that are organized subsequently according to the contribution of each term to the resulting amplitude. A breakdown is then defined, which is normally the mass of the lightest omitted degree-of-freedom. This provides a power counting scheme that allows to consider a calculation up to a given order. Table 3.4 shows EFT predictions at different orders: $\mathcal{O}(p^3)$ is a third order (p-expansion) calculation, $\mathcal{O}(p^4)$ are two fourth order calculations, $\mathcal{O}(\epsilon^2)$ is a small scale (ϵ-expansion) calculation [82–84]. HBχPT is a heavy baryon chiral perturbation calculation [52], and BχPT is a covariant baryon chiral perturbation calculation [74]. Finally, K-matrix is a calculation from a "dressed" K-matrix model, where a traditional K-matrix formalism is combined with dispersion relation [85]. The K-matrix formalism is derived from S-matrix scattering and provides an elegant method to build a unitary T-matrix in the two-body scattering processes. It was first introduced by Wigner and Eisenbud [86, 87] to study the resonances in nuclear reactions. A comprehensive review on the argument can be found in Ref. [88].

The wide range of values given in Table 3.4 clearly shows how a precise experimental extraction of these parameters is absolutely necessary. The experimental program on Compton scattering undertaken by the A2 collaboration, which this dissertation is a part of, has already led to the publication of the first mea-

surements of the double polarized observables Σ_{2x} [18] and Σ_{2z} [19] introduced in Section 2.3.3. An extraction of the proton spin polarizabilities was also performed by fitting these data from the A2 collaboration, together with the results on the beam asymmetry Σ_3 above the pion photoproduction threshold published by the LEGS collaboration [76]. The fit was performed using both HDPV [28, 39, 40] and BχPT [47] calculations. The results are summarized in Table 3.5.

Chapter 4

Experimental Setup

The following chapter introduces the experimental apparatus used to carry out the measurement discussed in this dissertation. The experiment was composed of two different data taking periods between February and July 2018 performed at the MAMI tagged photon facility located in the A2 Collaboration hall [89] at the *Institute für Kernphysik* of the *Johannes Gutenberg-Universität* in Mainz, Germany.

An overview of the setup is showed in Fig. 4.1. A photon beam was produced via bremsstrahlung on a thin radiator from the 883 MeV electron beam provided by the MAMI accelerator. The outgoing electrons were then bent using a dipole magnet and detected by the new tagger spectrometer, while the main electron beam was absorbed by a beam dump. From simple constraints on the kinematics, the energy of the generated photons is then determined. The resulting photon beam was collimated and impinged on a 10 cm liquid hydrogen target. The resulting particles were detected using the Crystal Ball/TAPS detector system, described in the next sections. This detector apparatus covers $\sim$ 97% of the solid angle around the target, providing a large angular acceptance together with an excellent angular and energy resolution, essential for the study of Compton scattering.

4.1 MAMI accelerator

The Mainz Microtron (MAMI) is a cascade of several different accelerating stages capable of providing an unpolarized or polarized Continuous Wave (CW) electron beam, with energies up to 1.6 GeV. The use of CW beam is an essential prerequisite for coincidence experiments in order to reduce the background due to random coincidences and to improve the beam luminosity.

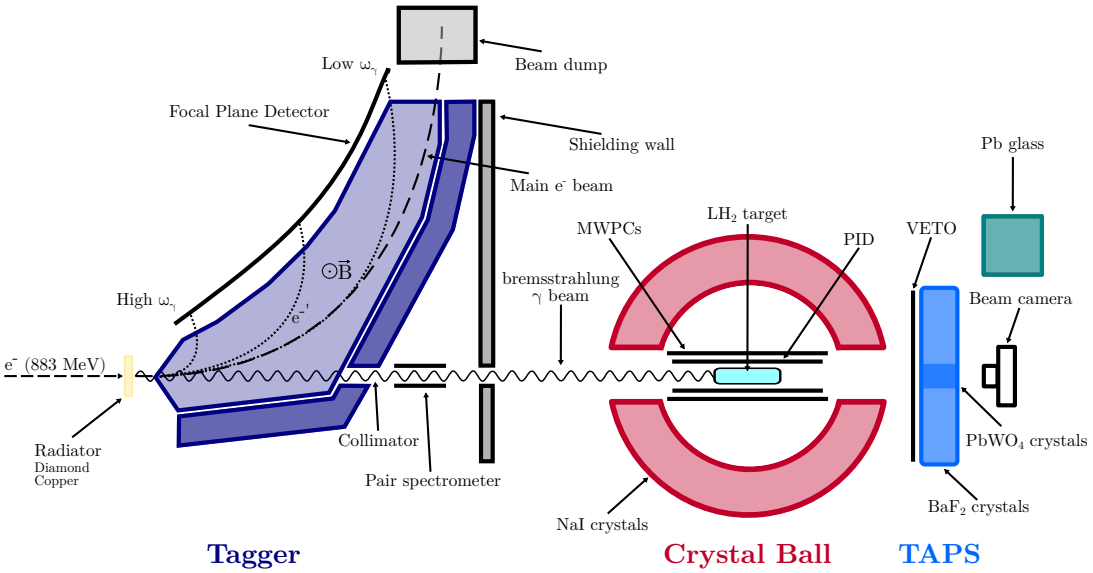

Figure 4.1: Overview of the experimental apparatus in the A2 Collaboration hall. The electron beam comes from the left and hits the radiator producing bremsstrahlung photons. Electrons are bent by the tagger spectrometer in blue, while the photon beam passes through a collimator and hits the LH_2 target. The particles in the final state are detected by the Crystal Ball and the TAPS apparatuses in red and light blue, respectively.

Figure 4.2 shows the floor plan of the MAMI facility, together with the new, still under construction, Mainz Energy-recovering Superconducting Accelerator (MESA) facility [90]. The MAMI accelerator is composed of four individual microtrons: three RaceTrack Microtrons (RTMs), divided into a MAMI-A (RTMs 1 and 2) and a MAMI-B (RTMs 1-3) stage, described in Section 4.1.1, and an Harmonic Double Sided Microtron (HDSM), constituting the MAMI-C (RTMs 1-3 and HDSM) stage, and described in Section 4.1.2. The initial injector linac provides an electron beam with an energy of 3.97 MeV, which can then be increased up to 14.86 MeV with RTM1, to 180 MeV with RTM2, to 883 MeV with RTM3 and, the maximum energy of 1604 MeV can finally be reached with the HDSM. These four stages can provide either a polarized electron beam having a degree of polarization of about 80% and a current up to 20 μA, or an unpolarized electron beam with a current up to 100 μA. The electron beam position is maintained with a precision of less than 200 μm via a complex control mechanism, while the beam diameter is roughly 0.1 mm. The energy resolution is less than 13 keV [91].

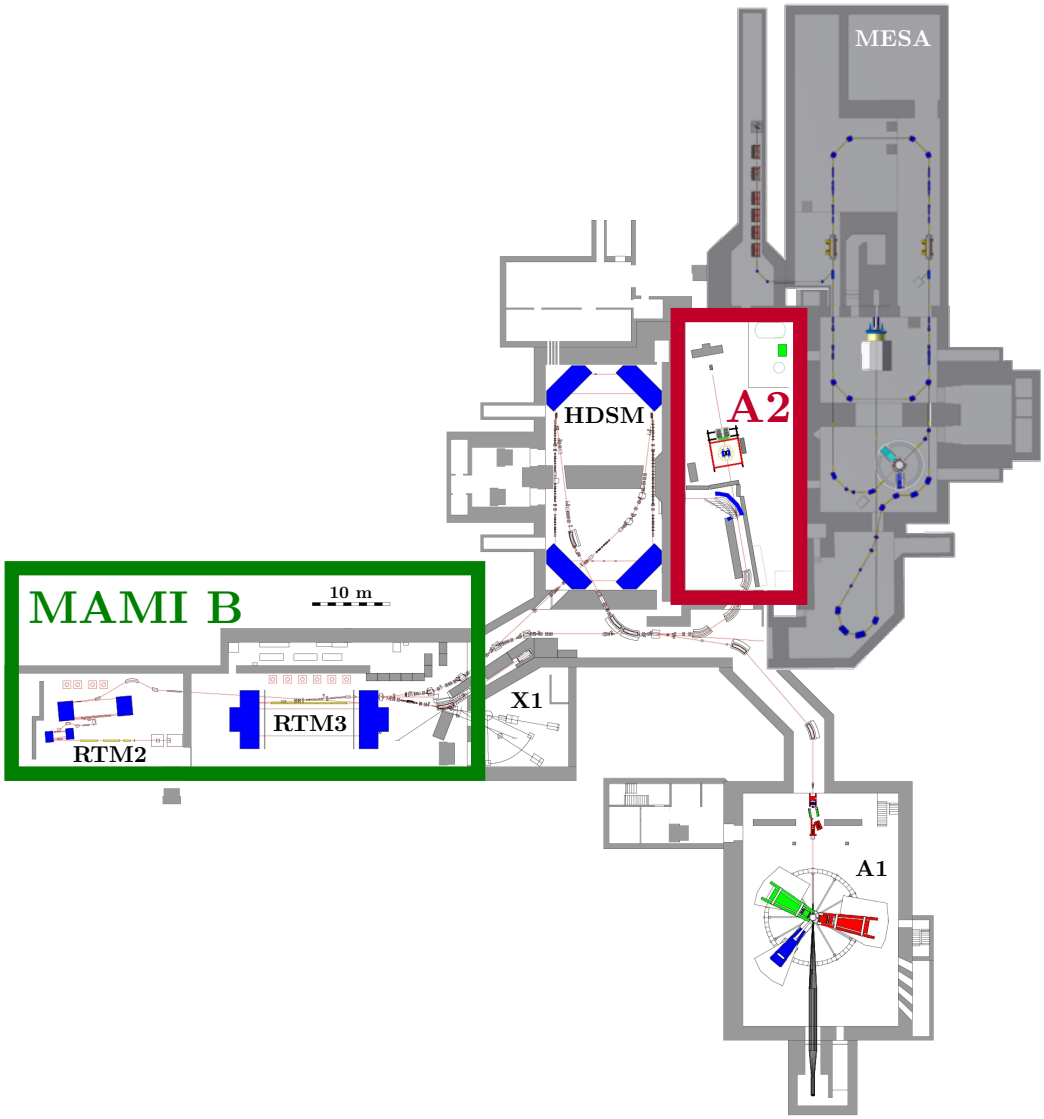

Figure 4.2: Floor plan of the MAMI and the new MESA facilities. The experiment described in this dissertation took place in the hall of the A2 Collaboration (in red) using the electron beam coming from the MAMI-B stage (in green) of the accelerator.

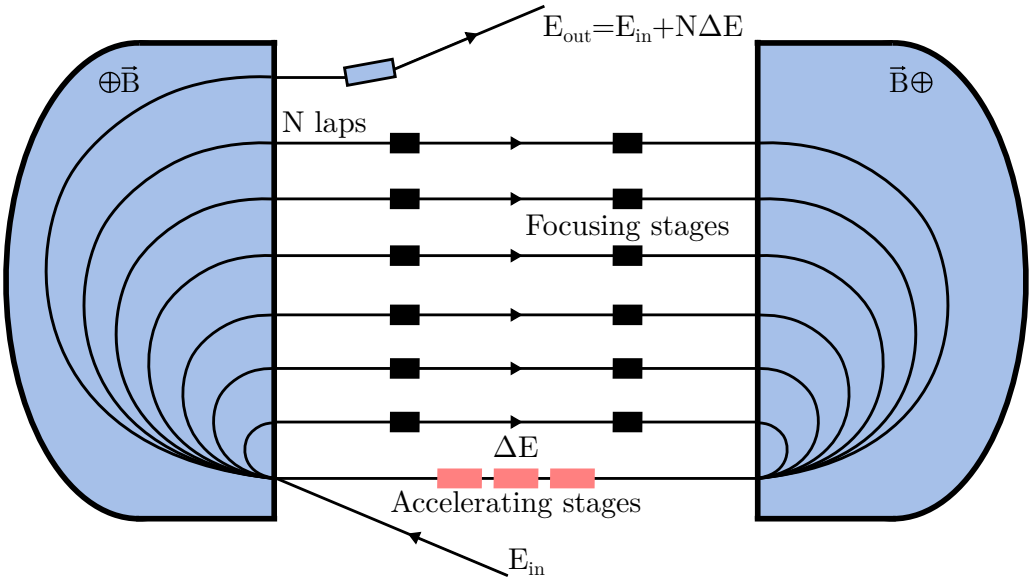

Figure 4.3: Scheme of a racetrack microtron (RTM).

4.1.1 Racetrack Microtron

A microtron is an accelerator in which the beam is guided many times through the same linac, and a particular version of this is the RTM, so-called because of its shape shown in Fig. 4.3. It consists of a single linac placed between two big dipole magnets, and the magnetic field B is chosen in such a way that the electrons, after each passage inside the linac, are bent by 180°. Then, the beam is focused and it travels into the second dipole where it is bent back into the accelerating stages, following the same radius of curvature since both magnets have the same magnetic field. The linac uses a radio frequency 50 kW klystron with a frequency $\nu_{fr} = 2.4495$ GHz to alternate the potentials of a series of standing wave cavities, accelerating a well timed bunch of electrons in each section. The energy gain after each passage in the linac can be calculated as [92]:

$$\Delta E = \frac{ec^2 B}{2\pi\nu_{rf}}, \tag{4.1}$$

where e is the electron charge and c is the speed of light. With the increase in the energy, also the radius of curvature in the dipole increases, up to the extracting stage. The maximum energy at the extraction can be easily calculated for each RTM as:

$$E_{out} = E_{in} + N\Delta E, \tag{4.2}$$

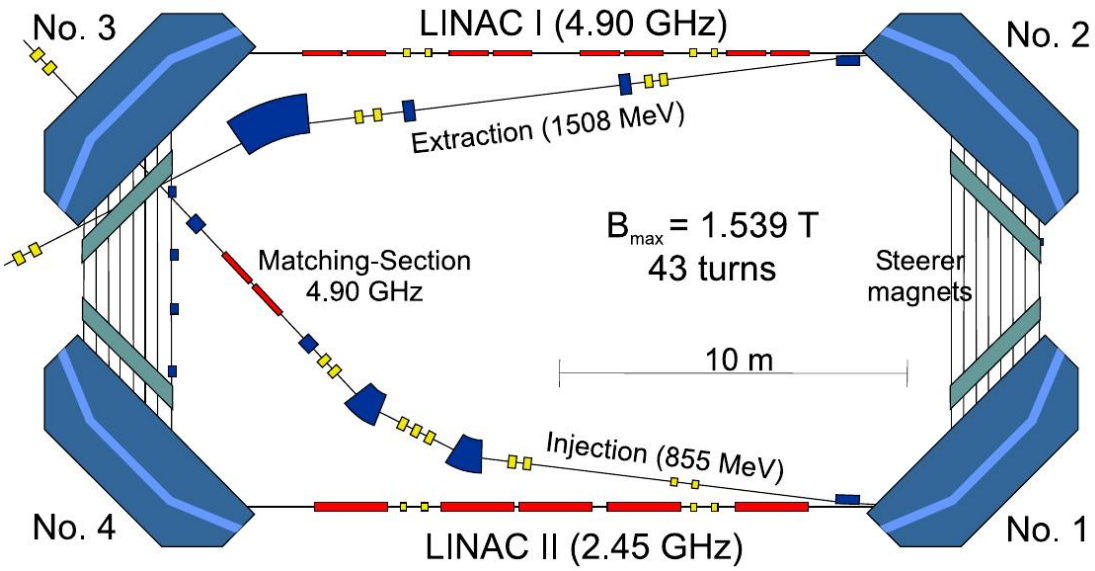

Figure 4.4: Sketch of the HDSM at MAMI facility [93].

where E_{in} is the injection energy (from a previous stage) and N is the total number of turns.

4.1.2 Harmonic Double Sided Microtron

The three RTMs composing MAMI-A and MAMI-B allow for a nominal maximum electron energy of 883 MeV, which is enough for the experiment described in this thesis. To provide electrons with higher energy, an additional accelerator stage was planned. The idea of a hypothetical fourth RTM to reach the energy of 1.6 GeV would have not been possible due to the large magnetic field required to bend the higher energy electron beam 180°. In particular, an hypothetical additional RTM stage would have had a magnet with an unrealistic weight of 3000 t. This would have had extremely technical complexities considering that a precision of $\Delta B/B \leqslant 10^{-4}$ is required.

Therefore, the possibility of modifying the RTM-principle by using more than two deflection dipoles, so-called polytron, was explored. The best option for the MAMI facility was found to be a polytron with four deflection dipoles, called Harmonic Double Sided Microtron (HDSM) [93]. As shown in Fig. 4.4, in the final design the HDSM consists of four dipole magnets at 90° and two linac accelerators, operating at two different radio frequencies: ν_{rf} and $2\nu_{rf}$. In this setup, each dipole has to bend the beam by only 45°, reducing the size and the intensity of each of them. Table 4.1 gives an overview of the parameters of each stage of the MAMI facility.

Table 4.1: MAMI parameters. The energy values can vary accordingly to the maximum energy needed. These are the parameters used for this experiment [92–94].

	Injector	**RTM1**	**RTM2**	**RTM3**	**HDSM**
E_{in} [MeV]	0.611	4.10	15.35	185.9	883.11
E_{out} [MeV]	4.10	15.35	185.9	883.11	1557.4
σ_E [keV]	1.2	1.2	2.8	13	110
Number of cycles	–	18	51	90	43
B [T]	–	0.106	0.573	1.326	1.428
Weight of the magnet [t]	–	4.2	92.3	911.6	1030
Length of linac [m]	4.93	0.80	3.55	8.87	8.57 – 10.10

4.2 Photon beam

Starting from the unpolarized electron beam produced by MAMI, either an unpolarized or a linearly polarized photon beam was produced via an incoherent or a coherent bremsstrahlung process, on an amorphous or a crystalline radiator, respectively.

4.2.1 Bremsstrahlung process

Bremsstrahlung (German word for *"braking radiation"*) is electromagnetic radiation produced by the deceleration of a charged particle deflected by another charged particle [95], in this specific case an electron deflected by an atomic nucleus. The process is obviously regulated by energy and momentum conservation. Considering an incoming electron with initial state $(E, \vec{p})$ and final state $(E', \vec{p'})$, the outgoing photon $(k, \vec{k})$ and the recoiling nucleus $(T, \vec{q})$ are related by:

$$E = E' + k + T, \tag{4.3}$$

$$\vec{p} = \vec{p'} + \vec{k} + \vec{q}. \tag{4.4}$$

Since the nucleus is extremely heavy compared to the electron, the recoil kinetic energy

$$T = \frac{|\vec{q}|^2}{2M} \tag{4.5}$$

is negligible. The transfer momentum $\vec{q}$ is limited both by kinematics, which set a lower limit, and by the fact that the bremsstrahlung cross-section drops off rapidly with the increasing of $\vec{q}$, setting an effective upper limit. By introducing,

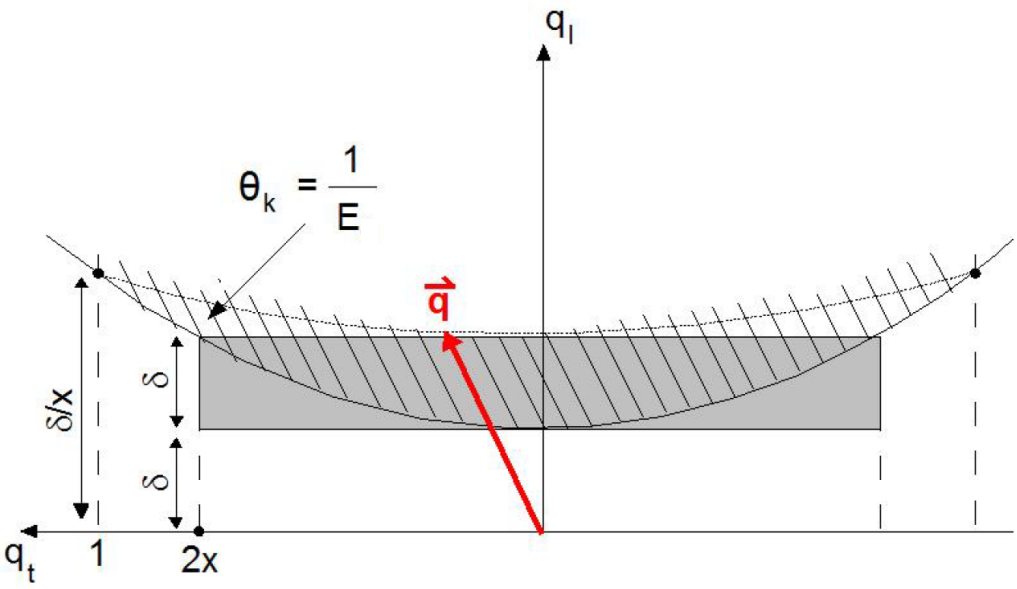

Figure 4.5: Sketch of the allowed kinematic region for bremsstrahlung in the transverse momentum space. The "pancake" shape is clearly visible. Figure taken from Ref. [97]

for convenience, the fractional energy

$$x = \frac{k}{E} \tag{4.6}$$

and by splitting the momentum $\vec{q}$ in terms of the transverse q_t and the longitudinal q_l component, one can define the allowed range as [96]:

$$0 \leq q_t \leq 2x, \tag{4.7}$$

$$\delta(x) \leq q_l \leq 2\delta(x), \tag{4.8}$$

where $\delta(x)$ is the minimum of q_l, defined as:

$$\delta(x) = \frac{x}{2E(1-x)}. \tag{4.9}$$

In momentum space these limits define a so-called pancake region, showed in Fig. 4.5: a shallow volume that is normal to, and centered on, the $\vec{p}$ direction [96].

4.2.2 Incoherent bremsstrahlung

Incoherent bremsstrahlung happens when the electron beam impinges on an amorphous radiator, for example a thin copper foil as in this experiment. The electrons interact with the Coulomb field of the atomic nucleus and in this case each point of the pancake region in momentum space can be the end point of the recoil vector $\vec{q}$. The cross-section for incoherent bremsstrahlung is described by a Bethe-Heitler distribution, which rapidly decreases as the photon energy increases (almost an $1/E$ behavior).

4.2.3 Coherent bremsstrahlung

An electron beam impinging upon a thin crystal will produce both incoherent and coherent radiation. In the latter case, the incident electron interacts with the whole crystal, and not with a single nucleus. This allows for a greatly enhanced bremsstrahlung cross-section at discrete values of $\vec{q}$. These enhancements show up as broad peaks superimposed upon the normal incoherent bremsstrahlung spectrum, with intensity comparable to or greater than the incoherent part.

Generally speaking, a crystalline radiator is a material whose atoms are arranged in a highly ordered structure. This pattern, the crystal's unity cell, repeats at a point known as a lattice point and extends in all directions, forming a crystal lattice. This unity cell is represented in terms of the three primitive lattice vectors ($\vec{a}$, $\vec{b}$, $\vec{c}$). It is possible to define a reciprocal crystal lattice, that is correlated to the direct one. The corresponding reciprocal lattice vectors ($\vec{a}^*$, $\vec{b}^*$, $\vec{c}^*$) are then related to the direct ones by:

$$\vec{a}^* = 2\pi \frac{(\vec{b} \times \vec{c})}{(\vec{a} \times \vec{b}) \cdot \vec{c}}, \tag{4.10}$$

$$\vec{b}^* = 2\pi \frac{(\vec{c} \times \vec{a})}{(\vec{a} \times \vec{b}) \cdot \vec{c}}, \tag{4.11}$$

$$\vec{c}^* = 2\pi \frac{(\vec{a} \times \vec{b})}{(\vec{a} \times \vec{b}) \cdot \vec{c}}. \tag{4.12}$$

Vectors and planes in a crystal lattice can be described introducing the Miller indices (h, k, l) [98], these indices can be used to define a reciprocal lattice vector $\vec{g}$ as:

$$\vec{g} = h\vec{a}^* + k\vec{b}^* + l\vec{c}^*. \tag{4.13}$$

While the constraints on the momentum transfer $\vec{q}$ given in Eqs. (4.8) and (4.9) are still valid, the coherent bremsstrahlung process places an additional constraint.

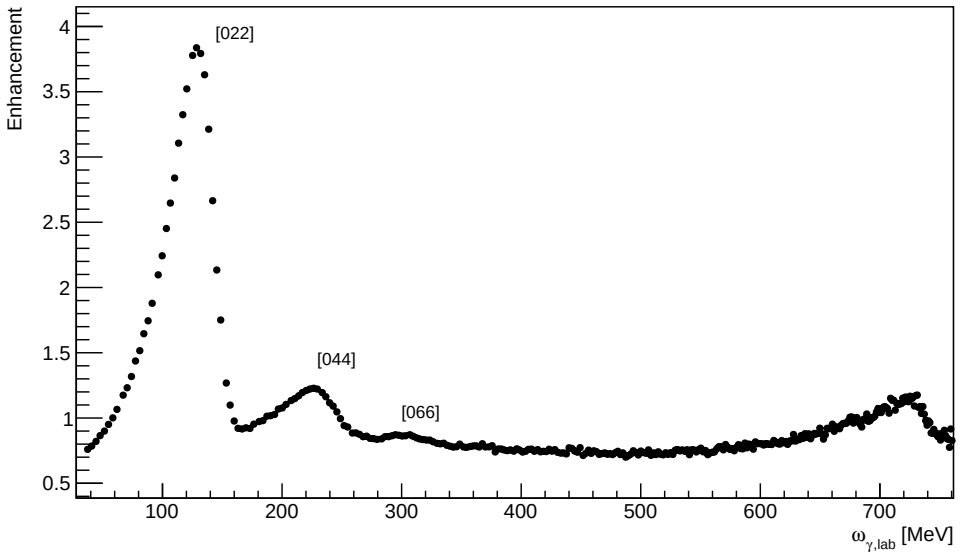

Figure 4.6: Example of the enhancement spectrum taken in March 2018, obtained from coherent bremsstrahlung on a thin diamond radiator. The three main peaks are indicated using the Miller indices of the reciprocal lattice vectors.

In particular, the recoil vector $\vec{q}$ must have its end point within the pancake region and, at the same time, be equal to a multiple n of the reciprocal lattice vector $\vec{g}$:

$$\vec{q} = n\vec{g}. \tag{4.14}$$

Equation (4.14), known as Laue condition, fixes the plane of the electron deflection and consequently the emitted photons are linearly polarized with the electric field vector oscillating in the plane given by the incoming electron momentum $\vec{p}$ and the lattice vector $\vec{g}$ [99]. These additional constraints result in a peak in the photon spectrum with a sharp discontinuity as soon as the fraction energy x is high enough for the reciprocal lattice vector $\vec{g}$ to exit the pancake region. This upper limit is given by,

$$x_d = \frac{2E\delta}{1 + 2E\delta}, \tag{4.15}$$

where δ is defined in Eq. (4.9), and the consequent discontinuity is known as coherent edge [96].

4.2.4 Linear polarization

The enhancement, R, in the bremsstrahlung cross-section due to coherent production can be found as

$$R = \frac{\sigma^{crystal}}{\sigma^{incoh}}, \tag{4.16}$$

where $\sigma^{crystal} = \sigma^{coh} + \sigma^{incoh}$.

An example of the enhancement spectrum taken during the March 2018 beamtime is shown is Fig. 4.6. The plot shows the coherent peak around $\omega_\gamma \sim 140$ MeV with a sharp drop right after it, known as coherent edge. This enhancement corresponds to the coherent bremsstrahlung off the [022] reciprocal lattice vector. A second polarization peak is also visible around $\omega_\gamma \sim 230$ MeV, corresponding to the [044] reciprocal lattice vector, as well as a third one at higher energies related to the [066] reciprocal lattice vector. The enhancement spectrum is obtained detecting the distribution of the electrons in the focal plane detector, described in Section 4.3.1. The incoherent contribution σ^{incoh} in the enhancement spectrum is estimated by detecting the same electron distribution using an amorphous radiator, a 10 μm copper radiator. Finally, the plot shown in Fig. 4.6 is obtained by dividing the crystal distribution $\sigma^{crystal}$ with the incoherent one.

The coherent part σ^{coh} of the bremsstrahlung production can be expressed in terms of the parallel and perpendicular components,

$$\sigma^{coh} = \sigma^{\parallel} + \sigma^{\perp}, \tag{4.17}$$

whose photon polarization vectors are parallel ($\sigma^{\parallel}$) and perpendicular ($\sigma^{\perp}$) to the orientation of a reference plane defined by the incoming electron and the lowest reciprocal lattice vector $\vec{a}^*$ of the crystal [99]. The degree of linear polarization of the photon beam, P, can be calculated as

$$P = \frac{\sigma^{\perp} - \sigma^{\parallel}}{\sigma^{crystal}}, \tag{4.18}$$

or, in terms of the enhancement R,

$$P = \left(1 - \frac{1}{R}\right) \frac{\sigma^{\perp} - \sigma^{\parallel}}{\sigma^{coh}}. \tag{4.19}$$

4.2.5 Stonehenge technique

The orientation of the crystal with respect to the electron beam is crucial to produce a linearly polarized photon beam, as discussed in Section 4.2.3. The coherent peak is produced by scattering off one specific set of reciprocal lattice vectors which have to lie inside the allowed momentum pancake region.

A correct alignment of the crystal is therefore critical to obtain the desired coherent spectrum for the experiment. A manual alignment could be performed by laser measurements and a careful mounting of the crystal on a goniometer [100].

However, this would need an extremely precise knowledge of the orientation of the beam and of the orientation of the lattice planes inside the crystal. To overcome these technical difficulties, the so-called Stonehenge technique was developed [101], and it is now commonly used in all the bremsstrahlung facilities around the world. It was applied at the beginning of this experiment to align the diamond radiator.

To perform the alignment, the crystal was mounted on a five-axis goniometer that can be controlled in order to vary the crystal orientation. The Stonehenge technique consists of rotating the crystal on its horizontal and vertical axes, θ_h and θ_v respectively, and to study how the level of enhancement varies with orientation. During this scan, the two orientations, θ_h and θ_v, are varied sinusoidally by moving the crystal axis in a cone of a given radius, and after each step a bremsstrahlung enhancement spectrum is taken. The intensity of the enhancement is then plotted as a function of the photon energy and the two orientation coordinates, θ_h and θ_v. An example of the resulting plot, known as Stonehenge plot is shown in Fig. 4.7. The color intensity indicates the intensity of the enhancement. The areas with the strongest intensity indicate the scattering from the sets of planes defined by the reciprocal lattice vector [022], and the points where they converge at $\omega_\gamma = 0$ (inner part of the colorful disk in the plot), indicate where the set of planes is parallel to the beam. Using those points, it is possible to obtain a complete set of coordinates to correctly align the crystal. A complete discussion of this technique and a step-by-step guide to use it can be found in the original paper in Ref. [101].

4.2.6 Collimation

The collimation of the photon beam is of primary importance to keep the beam from impinging on the beam pipe or on the target structure instead of on the target itself, creating undesired background. Furthermore, in the case of coherent bremsstrahlung, the collimation can be used to increase the degree of the linear polarization of the photons since the angular distribution of coherent and incoherent bremsstrahlung have different behaviors.

The photons produced via incoherent bremsstrahlung are emitted in a cone with an opening angle given by [102]

$$\theta_\gamma = \frac{m_e c^2}{E}, \tag{4.20}$$

from which it is clear that the distribution depends only on the incoming elec-

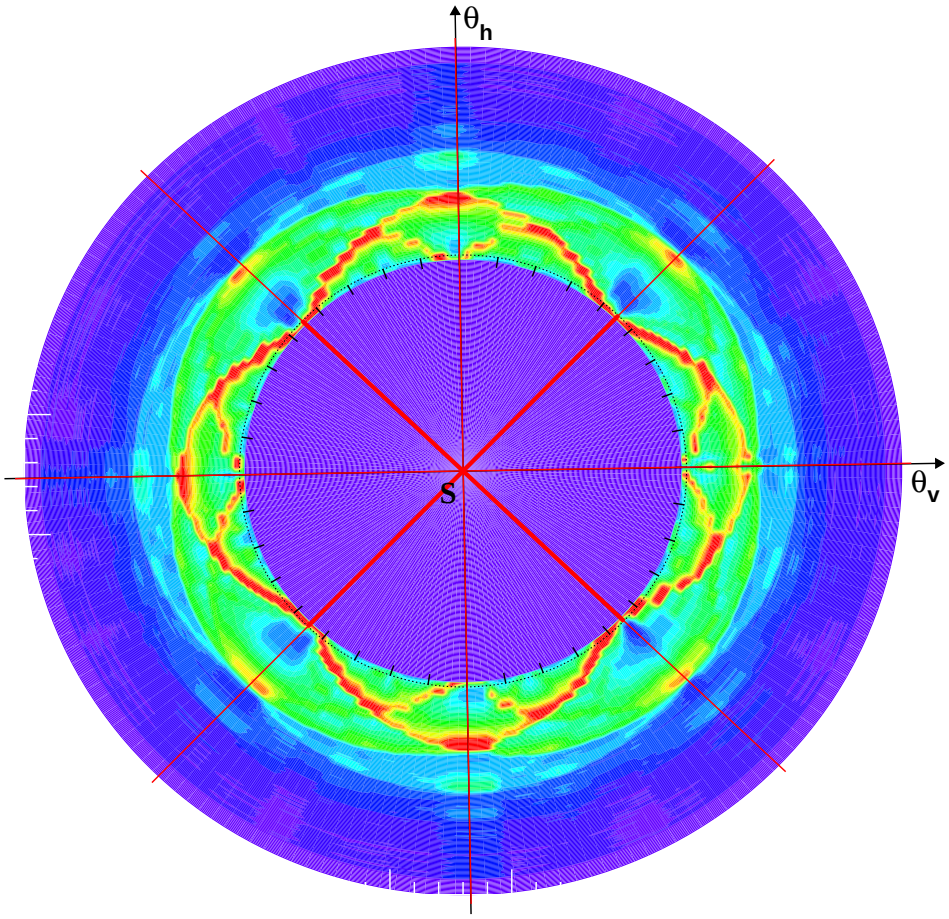

Figure 4.7: Example of a Stonehenge plot produced during the setup of the experiment. It was made by rotating the crystal about horizontal and vertical axes by varying the coordinates θ_h and θ_v, respectively. After each step an enhancement spectrum is acquired. These enhancement spectra are shown in the plot, where the radial axis corresponds to the beam energy and the color gradient to the level of enhancement.

tron beam energy E. Thus, the collimation of incoherent bremsstrahlung photons stops a fraction of the total photons that is independent of the photon energy. On the other hand, the angular distribution of the coherent bremsstrahlung depends on the photon energy. In particular, the emission angle θ_γ becomes smaller when the photon energy approaches the coherent edge x_d [96]. This causes two different effects. The collimation suppresses polarized photons more in the energy region further above and below the coherent edge, leading to a reduction of the polarization degree far from the peak and hence a narrowing of the peak itself. On the other hand, in the peak region where the emission angle is smaller for polarized photons, it stops more unpolarized radiation, increasing the maximal polarization degree.

It is therefore clear that a small collimator can enhance the degree of linear polarization, but it also reduces the number of photons that reach the target, namely the beam flux. It is therefore important to balance these two different effects. After different tests performed in a dedicated test beam, a 3-mm lead collimator was found to be the best solution for this experiment.

4.3 A2 Apparatus

4.3.1 Photon tagging spectrometer

The energy of the photons created via bremsstrahlung (Section 4.2.1) is inferred using the Glasgow Photon Tagging Spectrometer (or simply Tagger). It uses a large dipole magnet to bend the trajectory of the electrons. The magnetic field is chosen depending on the electron beam energy E, such that the electrons that do not emit a photon passing through the radiator are bent into the beam dump, as shown in Fig. 4.1. However, those electrons that radiate and lose part of their energy due to bremsstrahlung are bent with a radius of curvature given by the simple equation,

$$r = \frac{p'}{eB}. \tag{4.21}$$

For a fixed value of the magnetic field B, the radius of the curvature depends only on the momentum p' of the electron, as is clear from equation Eq. (4.21). Most of the bent electrons are then recorded by a focal plane detector composed of 328 plastic scintillators, each coupled to a Silicon PhotoMultiplier (SiPM). The physical position of the scintillator hit by the electron provides information on its energy, E_{tagg}. By knowing this information and the energy of the electron beam coming from MAMI E, it is straightforward to calculate the energy of the photon

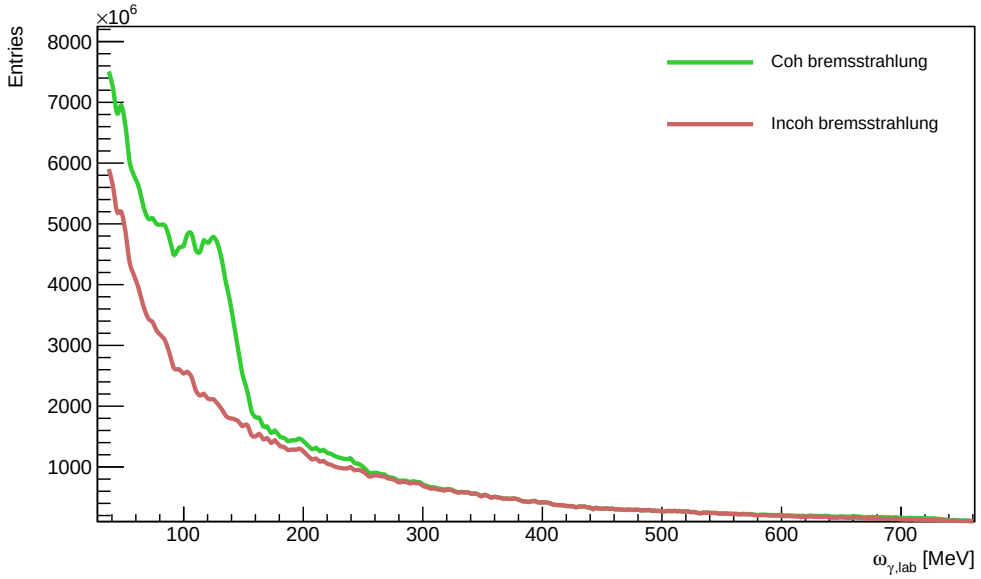

Figure 4.8: Sample distribution of the hit in the tagging spectrometer. The brown curve is obtained using an amorphous radiator and it shows a clear $1/\omega_\gamma$ incoherent bremsstrahlung distribution. The green curve is obtained using a diamond radiator and it shows the enhancement due to the peak of the coherent bremsstrahlung.

emitted via bremsstrahlung through the energy conservation:

$$\omega_\gamma = E - E_{tagg}, \tag{4.22}$$

where the tiny contribution from the energy of the recoil nucleus was neglected. The distribution of the hits in the tagging system follows the expected bremsstrahlung distribution, as shown in Fig. 4.8. The main detectors of the tagging spectrometer underwent a major upgrade in 2017. The new version has an extremely flexible modular design and in the configuration used for this experiment (the first one after the upgrade) it had 41 modules with 8 channels each, for a total of 328 channels. In the spring of 2019, an additional 10 modules were added to extend the coverage in the high photon energy region, bringing the total to 51 modules and 408 channels. Each channel is composed of a plastic scintillator (EJ200) rod, 30 mm long with a 6×6 mm base, read out by a 6×6 mm SensL-SiPM with a bias voltage of 25 mV. The signal is then guided using long Ethernet cables outside the region with intense radiation and is fed to a Constant Fraction Discriminator (CFD). This configuration assures a single-counter time resolution $\delta_t = 0.1$ ns [103]. The new faster detector also allows for a consistent increase in the electron rate, and so in the beam intensity, up to a certain point

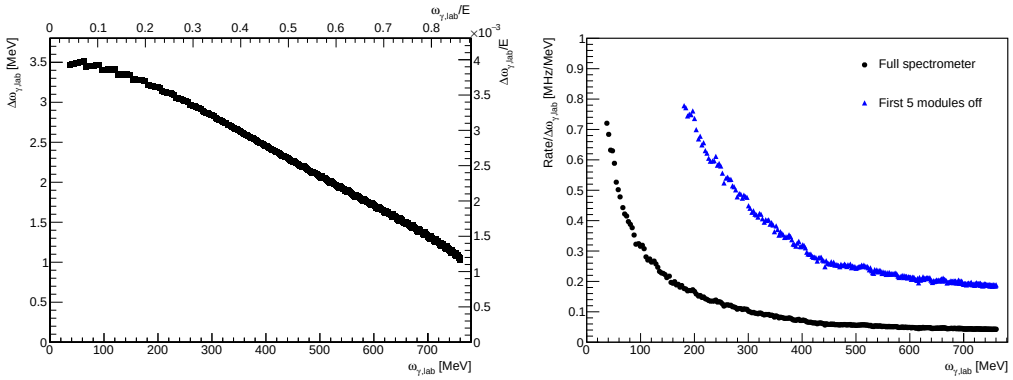

(a) Tagger energy resolution. (b) Tagger rates.

Figure 4.9: (a) Tagger channel resolution as a function of the tagged photon energy ω_γ. The right and top axes shows these values as fraction of the electron beam energy $E = 883$ MeV. (b) Example of rates in the tagging spectrometer in MHz per MeV. The black curve represent the situation of this experiment, with first channel running at ~ 2.5 MeV, the blue curve illustrates a case with the first 5 modules off.

after which the loss of signals due to pile-up starts to become relevant. A single counter rate limit of 2.5 MHz was employed to keep the pile-up below 5%. This is a significant improvement by a factor 2.5 compared to the old setup and it was crucial to obtain the high statistics needed to make this measurement competitive. In the configuration with 41 modules, photons can be tagged in a range of momentum from 4.3% to 86.1% (from 4.3% to 93.0% with 51 modules) of the incoming electron beam energy E. The energy resolution relative to E varies over the energy spectrum, from low to high photon energies, from 0.4% to 0.11%, and hence the total resolution varies from 3.47 MeV to 1.03 MeV, respectively. This performance is well illustrated in Fig. 4.9a.

The modular design, clearly visible in Fig. 4.10, is extremely convenient since it permits one to easily remove some modules that are not used, for example in the low photon energy region where the radiation is more intense, without making any changes to the readout or to the data acquisition system. This can allow for much higher rates in the central part of the tagging spectrometer, as shown by the red curve in Fig. 4.9b. Moreover, it gives easy access to each single module allowing for maintenance operations and swapping of damage components.

4.3.2 Liquid hydrogen target

The linearly polarized photons, after being collimated, travel down the beam line for 4.5 meters to the experimental area, where they impinge on an unpolarised

Figure 4.10: Picture of the new modular detector of the tagging spectrometer [104].

Figure 4.11: Liquid hydrogen target cell [105].

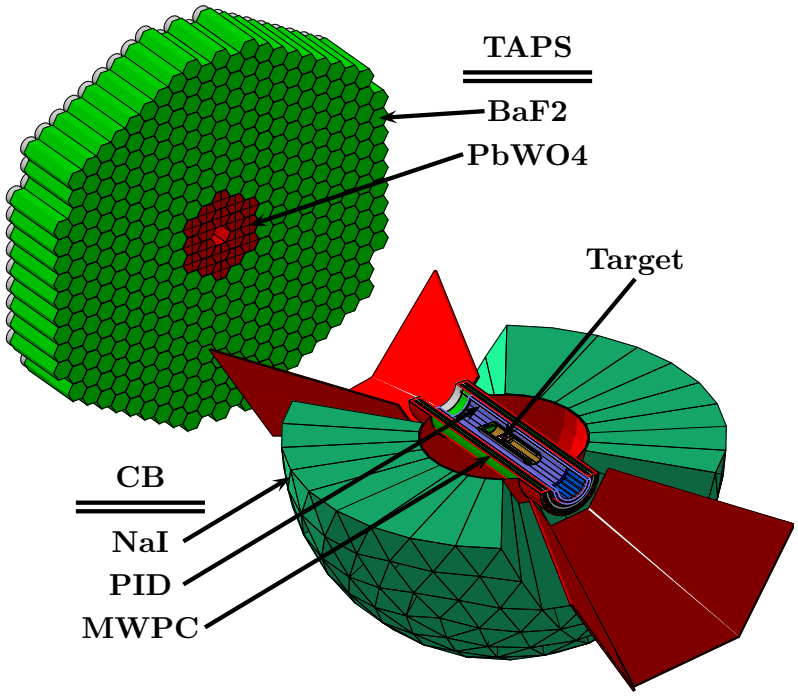

Figure 4.12: Sketch of the detector system in the A2 Collaboration hall. The photon beam comes from lower right and hits the target at the center of the Crystal Ball (CB). The different detectors are visible: the Particle Identification Detector (PID), two Multi Wire Proportional Chambers (MWPCs) and the CB, around the target from the innermost, and TAPS in the upper left corner, covering the forward region.

liquid hydrogen (LH_2) target. The target system consists of five different components: the target cell, located in the center of the detector apparatus, the liquid H_2 supply line, a 2 m^2 gas storage tank, the gas liquefier and the gas compressor. The cylindrical target cell (showed in Fig. 4.11), made of 125 μm Kapton surrounded by 8 layers of superisolation foil (each made of 8 μm Mylar and 2 μm aluminum), has a diameter of 4 cm and a length of (10.0 ± 0.1) cm [105]. During normal operation mode, about 25% of the gas is liquid and the temperature of the target nose is approximately 20 K. The pressure is automatically kept stable at (1080 ± 2) mbar by a dedicated system, leading to a density of $(70.548 \pm 0.01) \times 10^{-3}$ g/cm^3, which corresponds to 4.249×10^{23} protons/cm^2 [105].

4.3.3 Detectors

The apparatus used for the detection of the outgoing particles created in the scattering processes is shown in Fig. 4.12. Starting from the inner part, the system includes a thin segmented barrel of scintillator, two cylindrical multi-wire proportional chambers and an highly segmented calorimeter called the Crystal

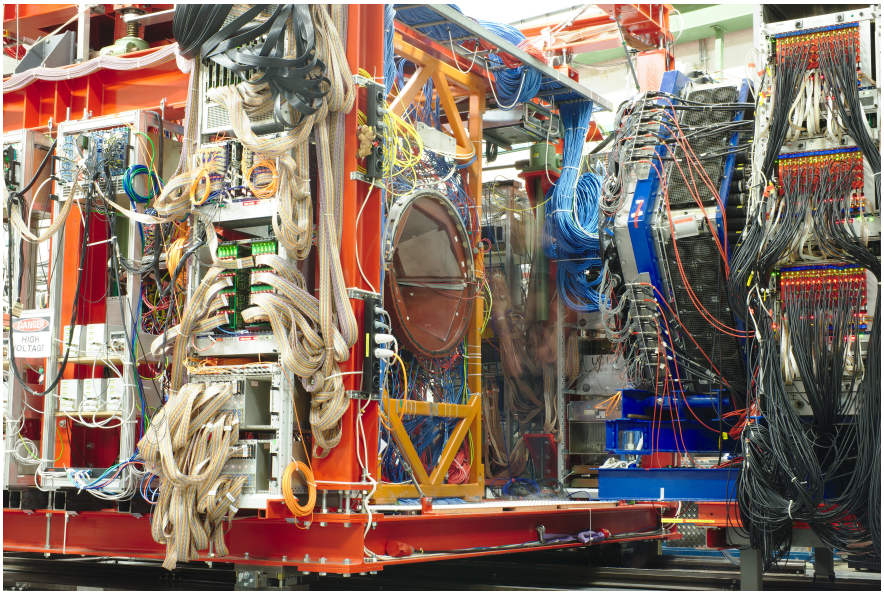

Figure 4.13: Crystal Ball detector installed in the A2 Collaboration experimental hall. The photon beam comes from the left, outside the figure, and hits the target in the center of the CB. TAPS, covering the forward region, is also visible on the right. Figure taken from Ref. [106].

Ball. These detectors together can cover a big part of the solid angle: $\phi \in [0, 2\pi)$ and $\theta \in [21°, 159°]$. A wall of scintillators, called TAPS, is used to cover the very forward polar angles. All this apparatus together covers 97% of 4π solid angle.

4.3.3.1 Crystal Ball

The Crystal Ball (CB) is a highly segmented spherical calorimeter built in the 1970's at the Stanford Linear Accelerator Center (SLAC). It ran at SLAC for eight years, playing a crucial role in many of the first measurements of the J/ψ. In the past years, it was used in other laboratories between USA and Europe, such as DESY in Hamburg and Brookhaven National Laboratory (BNL) in the state of New York. Finally, in 2002, its mechanical set-up was improved and the detector was relocated to the experimental hall of the A2 Collaboration at MAMI [107]. Its current location can be seen in Fig. 4.13.

The CB is an icosahedron, with 672 NaI crystals each shaped as a tapered truncated triangular pyramid. Each of its 20 faces (called "major triangles") is divided into 4 smaller triangles (called "minor triangles") and each of these triangles is again divided into 9 smaller triangles, for a total of 720 different sectors, as shown in Fig. 4.14. Considering that 48 sectors are unoccupied to make space for the entrance and the exit of the beam, 24 in the front and 24 in the back, respectively, we have in total 672 crystals. For technical and practical

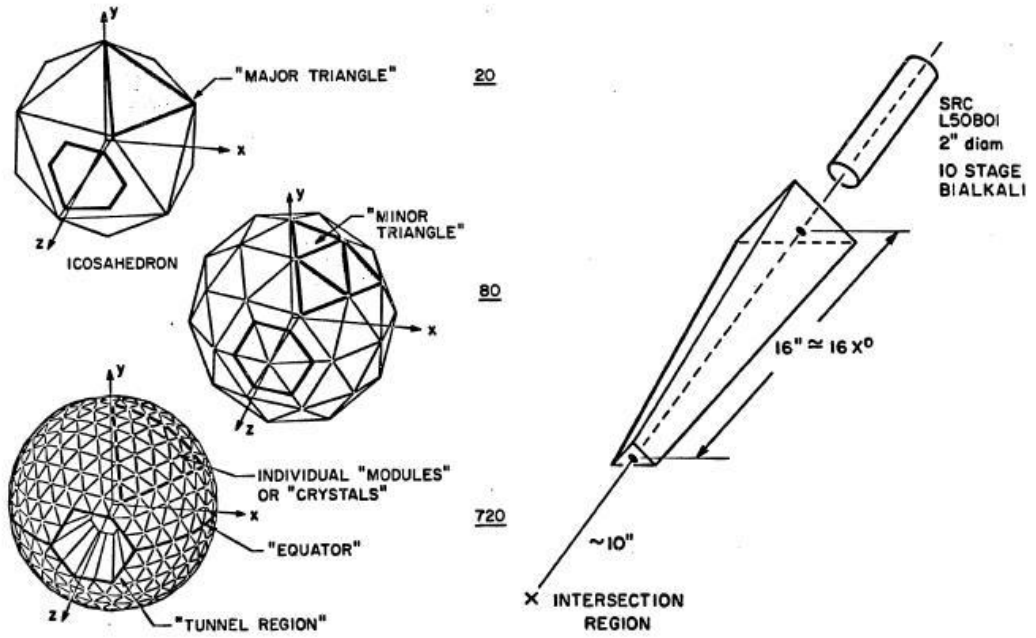

Figure 4.14: Sketch of the geometry of CB and of its crystals [108].

reasons, the detector is divided into two different hemispheres, with inner and outer radii of 25 cm and 66 cm, respectively. Each crystal, as show in Fig. 4.14, is 40.6 cm long. The triangular sides at the top of the pyramid (that corresponds to the inner surface of the detector) are 5.1 cm wide, while the ones at bottom of the pyramid (outer surface of the detector) are 12.7 cm wide. All crystals are optically isolated, individually wrapped in reflector paper and Mylar and they are also coupled to individual PhotoMultiplier Tubes (PMTs). Note that 27 of them were replaced with a new model a couple of months before the run periods used in this dissertation.

This detector is perfectly suited for measuring photon energy and the high granularity improves the resolution. The photons normally released their energy in a cluster of $3-4$ crystals, for the energy ranges relevant in this work. Furthermore, $\mu^{\pm}$ can be stopped up to a kinetic energy of $\sim$ 233 MeV, $\pi^{\pm}$ up to $\sim$ 240 MeV, $K^{\pm}$ up to $\sim$ 341 MeV and p up to $\sim$ 425 MeV. The energy resolution is $\frac{\sigma_E}{E} = \frac{2\%}{\sqrt[4]{E}}$ ($3-4\%$ in the region of interest), the time resolution $\sigma_t = 50$ ns, and the polar and the azimuthal angular resolutions are $\sigma_p = 3^\circ$ and $\sigma_a = \frac{\sigma_p}{\sin\theta}$ [107].

4.3.3.2 Particle Identification Detector

The PID is a cylindrical detector with an inner diameter of 116.5 mm and is made of 24 plastic scintillators. The scintillators are 500 mm long, 15 mm wide and 4 mm thick and they have a trapezoidal shape in order to minimize the empty

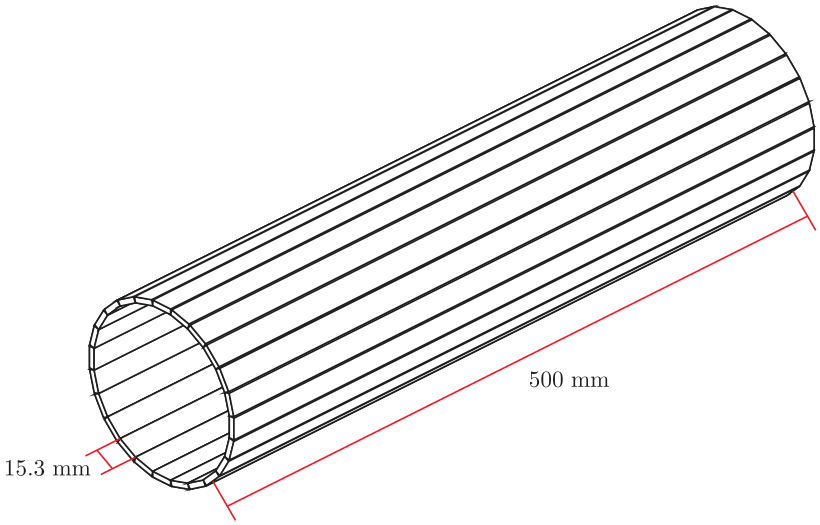

Figure 4.15: A sketch of the PID [23].

space between them, as seen in Fig. 4.15. Each element is individually wrapped in a Mylar foil and coupled to a PMT. The PID covers the full solid angle of CB and each of its element covers 15° of the azimuthal angle.

The PID was built and developed by the group of colleagues from the Edinburgh University at the beginning of 2000's, as an additional tool for charged particles identification. Due to the limited time resolution of CB and to its small inner radius and long crystal length, it is not possible to use the Time-of-Flight (ToF) technique to distinguish among the different types of charged particles. The charged particle identification is instead done using the $\Delta E/E$ method, based on the Bethe-Bloch formula. The small thickness of the scintillators causes a charged particle to deposit only a small fraction of its energy in the PID, before leaving all the rest inside CB. In particular, pions and electrons deposit a rather small part of their energy in the PID, being minimal ionizing particles. On the other hand, protons tend to release a higher fraction of their energy before leaving the PID scintillator, especially if they have low kinetic energy. These different behaviors allows for a clear separation of these three different types of charged particles, as is evident from a typical $\Delta E/E$ plot showed in Fig. 4.16.

4.3.3.3 Multi Wire Proportional Chambers

The two MWPCs in the apparatus of the A2 Collaboration, shown in Fig. 4.17, were developed and built by the group of colleagues from the National Institute of Nuclear Physics (INFN) in Pavia using the old MWPCs of the DAPHNE experiment as a prototype [71]. They are used for the charged-particle tracking

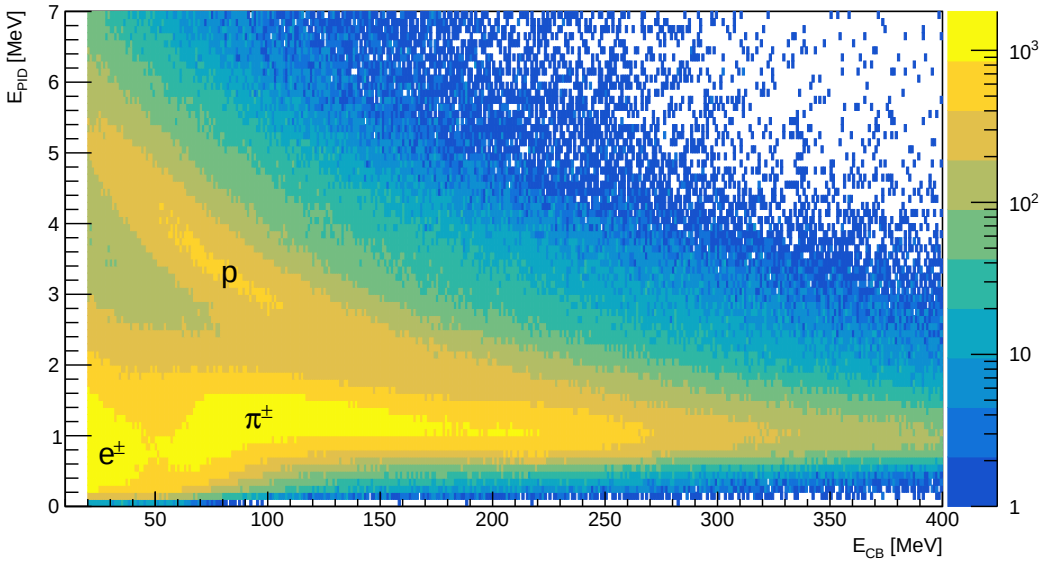

Figure 4.16: Example of a typical $\Delta E/E$ plot based on the Bethe-Bloch formula. The energy deposited in the PID is plotted on the y-axis as function of the total energy deposited in the CB. Electrons and pions are visible in the bottom of the plot, since they deposit a rather small amount of their energy in the PID, being minimal ionizing particle. The protons, especially the low-energy ones, tend to release a higher fraction of their energy, and so they distribute in the typical banana-shaped region visible in the middle left part of the plot.

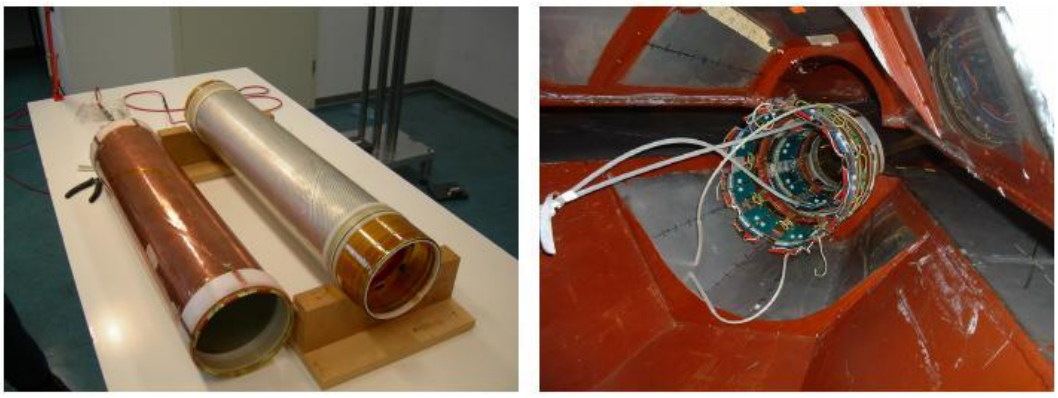

(a) (b)

Figure 4.17: (a) Picture of the inner and outer cathodes during repair of the MWPCs. (b) Picture of the MWPCs installed inside the CB.

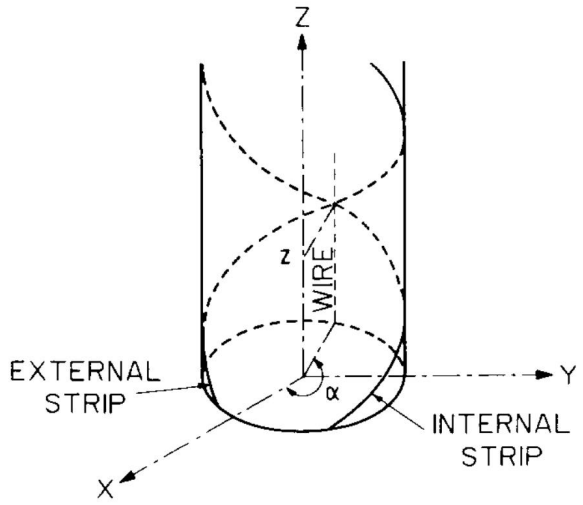

Figure 4.18: Coordinate system used in the MWPCs analysis. The photon beam comes from the bottom and travels along the z-axis. Within each chamber the azimuthal α and longitudinal *zeta* coordinates are evaluated from the charge distribution induced on the cathode strips. Since each pair of inner and outer strips cross each other twice, the position of the hit wires is needed to resolve the ambiguity. Figure taken from Ref. [71].

and they normally sit between the PID and CB, as shown in Fig. 4.12, covering the same solid angle fraction. This configuration was necessitated by the spatial constraints inside CB and it is not optimal since the trajectory of the particle may be affected by the interaction with the PID. Nevertheless, due to the small thickness of the scintillators the loss in tracking resolution is small and can be corrected. Each chamber is composed of two coaxial 1 mm thick Rohacell cylinders, with a gap of 8 mm in between filled with a mixture of gas composed of 69.5% of argon, 30% of ethane and 0.5% of Freon [109]. At the center of the gap between the two cylinders there is a layer of anode wires, parallel to the beam. The 20 μm diameter wires are made of tungsten plated with gold and they are equidistantly placed at 2 mm from each other, with the exception of the very last of each chamber that is slightly closer to the previous one, due to small mechanical imperfections. As shown in Fig. 4.18, a layer of cathode aluminum strips, 0.1 mm thick and 4.0 mm long, is placed on the outer and inner surface of the smaller and the bigger cylinders, respectively. These strips are spiraled around the cylinder, in opposite directions, at $\pm 45°$ respect to the wires and 90° with respect to each other. In total, the inner chamber has 232 wires, 69 inner strips and 77 outer strips; the outer chamber, instead, has 296 wires, 89 inner strips and 97 outer strips.

During the data taking, a positive voltage of 2500 V is applied to the wires

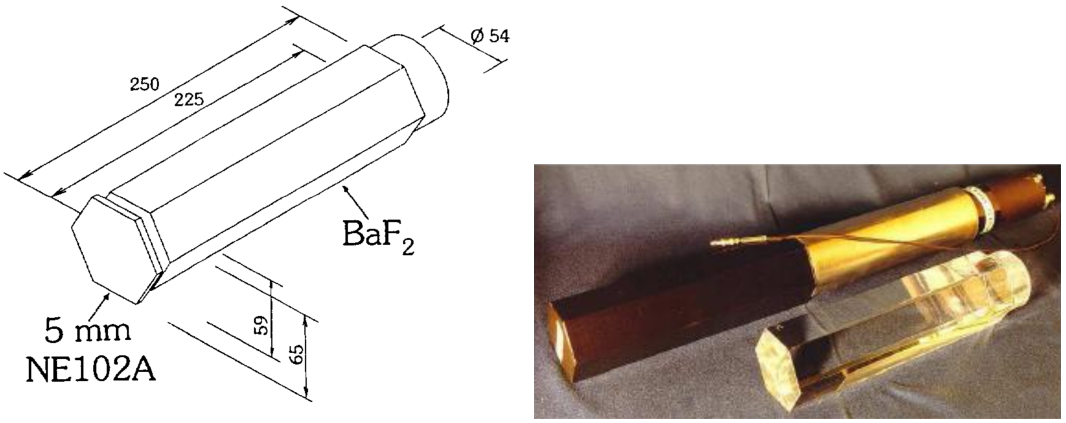

(a) Design [110]. (b) Picture.

Figure 4.19: (a) Design and (b) picture of a single BaF_2 crystal.

while the strips are connected to ground. A charged particle that goes through a wire chamber ionizes the gas inside it, producing a number of electron/hole pairs that is proportional to the quantity of deposited energy. Thanks to the voltage applied, the generated electrons (holes) drift in direction of the anode (cathodes) and due to the inverse proportionality of the electrical field to the distance, when they get closer to the wire ($10-20$ μm), they start producing more electron/hole pairs, generating a usable signal that is still proportional to the initial deposited energy.

The signals coming from the wires (electrons) and the strips (positive ions) can be used to reconstruct the track of a charged particle with a better angular resolution compared to the CB. In particular, by requiring two signals per chamber per track, it is possible to obtain an angular resolution of 2° for both the polar and azimuthal angles [71].

4.3.3.4 Two-Armed Photon Spectrometer

The Two-Arm Photon Spectrometer (TAPS) [110, 111] is a versatile calorimeter that can be used for the detection of high energy photons coming from neutral meson decays at forward polar angle ($\theta < 20°$), the region not covered by CB. Since it is the only detector in this spatial region, it is also used to reconstruct the tracks and to measure the energies of charged particles.

As showed in Fig. 4.1, it is placed downstream of the CB, approximately 1.8 m from the target. The detector consists of 366 BaF_2 and 72 $PbWO_4$ crystals placed to create a "wall" of scintillators. This scheme is reproduced in Fig. 4.20, where the inner smaller elements are the $PbWO_4$ crystals. Each BaF_2 element is 250 mm long, corresponding to approximately 12 radiation lengths, and it has a hexagonal

section with an inner diameter of 59 mm, as shown in Fig. 4.19a. Charged pions stop inside the crystal up to an energy of $\sim$ 185 MeV and protons up to $\sim$ 380 MeV. BaF_2 has the peculiarity of having both a fast and a slow scintillation light component. The former provides an excellent time resolution needed for the ToF technique, while the latter allows for a precise energy resolution. Together they can be use for Pulse Shape Analysis (PSA).

The $PbWO_4$ crystals, instead, are smaller with a trapezoidal shape so that four of them combined together have the same shape of a single BaF_2 crystal. They are placed in the two innermost section of TAPS to improve the high rate capabilities in the very forward angle. Each $PbWO_4$ is 20 cm long, corresponding to 22.5 radiation lengths thanks to the high density. Unfortunately, during the experiment, this section of TAPS was not working properly. Nevertheless, as it will be discussed later, this issue did not affect the data taking.

Each BaF_2 and $PbWO_4$ crystal is individually isolated and wrapped in Teflon and aluminum, and it is coupled to a PMT. In front of each crystal, there is also an additional 5 mm thick plastic scintillator paddle, called VETO, readout by a wavelength shifting fiber coupled to a PMT, which provides both particle identification and veto abilities. Similar to what happens in the PID, a charged particle deposits a part ΔE of its energy in the paddle, before leaving the rest, E, in the crystal. Besides identifying the track as charged, plotting the $\Delta E/E$ allows one to perform charge particle identification, as discussed in Section 4.3.3.2 for the CB-PID system.

Thanks to the unique properties of BaF_2 and $PbWO_4$, TAPS has an energetic resolution of:

$$\frac{\sigma}{E} = 1.8\% + \frac{0.8\%}{E\ [\mathrm{GeV}]}, \tag{4.23}$$

and an angular resolution of $\sim 1^\circ$ [110].

4.3.3.5 Lead Glass detector

The lead glass detector shown in Fig. 4.21 is a Cherenkov detector with a 100% efficiency for photon detection. It is essential for the determination of the tagging efficiency, namely the fraction of photons that pass the collimation, which is crucial for a precise extraction of cross-sections and asymmetries.

It is a squared box with sides that are approximately 20 cm long made of lead glass, corresponding to about 20 radiation lengths [55]. Considering that the photon beam spot at this point has diameter in the order of $3-4$ cm, one can assume that it can collect all the energy released by photons impinging on it. Each

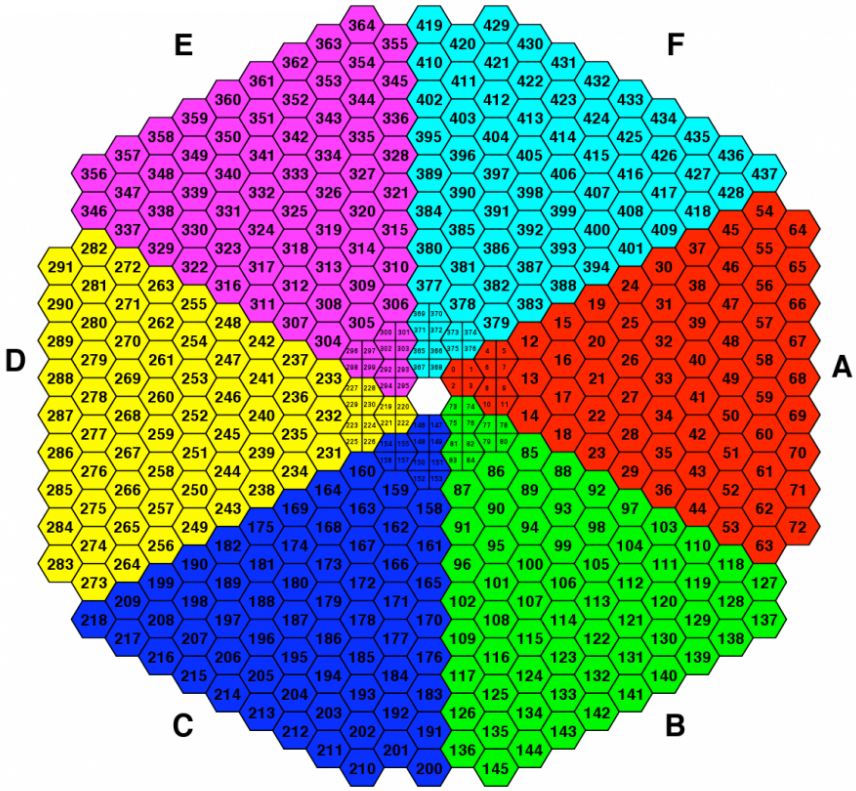

Figure 4.20: Scheme of the TAPS crystal distribution. In the first two innermost rings each BaF_2 crystal is replaced by four $PbWO_4$ crystals. The different colors correspond to different sections of electronic acquisition system [112].

Figure 4.21: Picture of the lead glass detector during maintenance work [113].

photon converts into an electron-positron pair that produces, via bremsstrahlung, a cascade of charged particles, which emit Cerenkov light that is detected by a PMT. The lead glass is wrapped in a layer of Mylar to assure optical isolation.

During the production runs, the lead glass detector is not placed inside the beam line (as shown in Fig. 4.1) and its PMT is off to protect it from the high photon rate. Usually once per day, the normal data taking is stopped and three dedicated 30 minutes runs at very low intensity with the lead glass in beam are collected, two with the diamond (one with the parallel and one with the perpendicular orientation) and one with the amorphous radiator. Due to the very high efficiency of this detector, a 10 minute background measurement without the beam is collected before and after the real measurement. This allows for a precise subtraction of the noise and of the environmental background. The measurement is performed with a beam intensity corresponding to a rate of 10 kHz in the lead glass. These data are used to evaluate the tagging efficiency as explained in Section 6.1.1.1.

4.3.3.6 Pair Spectrometer

The pair spectrometer is a simple detector installed in the beam line right after the collimator, as shown in Fig. 4.1. It is mainly dedicated to monitoring the

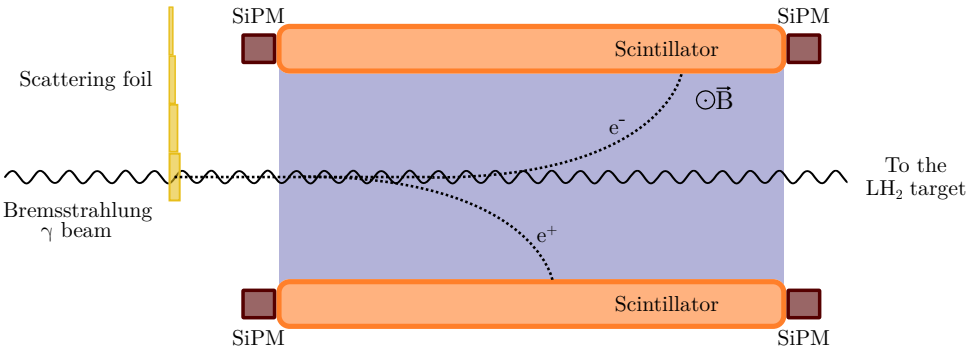

Figure 4.22: Sketch of the internal structure of the pair spectrometer.

photon flux during the production runs (see Section 6.1.1.2). Figure 4.22 shows a scheme of how it works. The photons coming from the collimator impinge on a thin retractable scattering foil. There are four different molybdenum targets with different thicknesses from 5 to 20 μm. During this experiment the 20 μm was used in order to maximize the number of e^+e^- pairs produced and detected by the spectrometer. It causes the conversion of a photon into a e^+e^- pair with a $\sim$ 0.1% efficiency. This is enough to perform a precise measurement of the photon flux, without interfering with the experiment. A strong magnetic field of 1 T bends both particles into opposite directions and they are then detected by the two 30 cm long scintillators [114]. If the two particles are detected in coincidence, the pair spectrometer sends a gating signal to the tagger scalers (prompt signal). It also provides a delayed gating signal (random signal), which makes it possible to perform a subtraction of the random coincidences in the tagging spectrometer. This is necessary, considering that the absolute count rate of the pair spectrometer is very low compared to the tagger rate.

4.4 Data acquisition

All the detectors forming the apparatus of the A2 Collaboration are read by PMTs, except for the MWPCs which are read by preamplifiers. The signal coming from the PMTs must be converted and stored in useful digital information that can be analyzed, as it will be explained in the next chapter. This process should be fast enough to keep up with the high rate of events and it is performed by a complex Data AcQuisition (DAQ) system.

Within a common layout of the front end electronics of a DAQ system, the analog output of a detector is typically split into two different branches: one is used to create a trigger for the event and to get a timing information, and the

other one instead is analyzed to get the energy information. The former branch usually runs into a discriminator that gives as an output a square signal (with a predefined width) only if the input is above a given threshold. This allows one to remove both the electronic noise and the events below the energy range of our interest. The output of the discriminator is normally then split again into two new branches: the first can be combined with the signals coming from the other detectors to form the trigger; while the second is typically sent to a Time-to-Digital Converter (TDC). This module compares the arrival time of the detector pulse with the reference one coming from the total experimental trigger, and gives as an output a digital number corresponding to this time interval. The second branch of the analog signal coming from the PMTs is sent directly to an Analog-to-Digital Converter (ADC), which gives as output a digital number corresponding to the integral (or to the amplitude) of the analog signal. The ADC normally also takes in input a trigger signal that gives instructions on if and when to analyze the signal.

4.4.1 Event readout

After an event is detected and the analog signals coming from the different detectors are digitized as explained in the previous paragraph, they have to be read out. In the A2 Collaboration system this is done in different ways and with different components, depending on the detector.

Concerning the timing signals, these are read out in the same way for tagger, CB, PID and MWPCs. They are fed into a Compass, Accumulation, Transfer and Control Hardware (CATCH) TDCs [115], electronic modules originally developed for the COmmon Muon and Proton Apparatus for Structure and Spectroscopy (COMPASS) [116] and the Large Hadron Collider beauty (LHCb) [117] experiments at Conseil Européen pour la Recherche Nucléaire (European Organization for Nuclear Research) (CERN). While a conventional TDC is started with a signal from a detector and stopped by a pulse coming from a trigger, the CATCH TDC does not use start/stop signals, allowing also for time determination of multiple hits. It uses a constantly running internal oscillator with a frequency of 8.55 GHz [23]. All the CATCH TDCs are synchronized by a CERN-standard Trigger Control System (TCS), with only one reference TDC connected to the experimental trigger providing a reference for the oscillator. When the TDC registers a timing signal coming from a PMT, the corresponding oscillator count is stored in a buffer. To determine the timing of the hit, the number in the reference TDC is then subtracted from the oscillator count and the result is divided

by the oscillator frequency. In addition, both the tagger and all the detectors in the Crystal Ball apparatus (CB, PID, MWPCs) have their own reference TCS to constantly check that they are still synchronized. The timing information from TAPS instead, is read by a normal TDC.

The energy signal is fed into traditional ADCs for TAPS and PID, while it is not used for the tagger since the energy is determined by the channel of the tagging spectrometer that detected the electron. For the CB and MWPCs, the analog energy signals are read into Sampling ADCs (SADCs). These ADCs sample their inputs at a given rate and integrate each sample in three predefined time windows: a section before a pulse, the larger part of the pulse and a section of the tail after the pulse. The integral of the first time interval allows for automatic pedestal suppression, by subtracting the baseline from the peak and requiring the remaining signal to be above threshold. The last temporal region provides a check for potential pile-up of two or more consecutive events.

4.4.2 Scalers

In addition to the event readout described in Section 4.4.1, the logic outputs of the discriminators of some detectors are sent into scalers modules, that simply count the number of pulses. These scalers are then read out only once every 10k events, a so-called "scaler read", which means typically every $\sim 1-2$ seconds. While during the readout of ADCs and TDCs, the DAQ system is inhibited to digitize and export the information, the scalers are always counting. This allows for a precise measurement of both the number of hits in each detector and the total number of trigger events.

To determine the livetime, which is the percentage of time in which the system is ready to acquire signal, a 1 MHz pulse generator is used. Its signal is split into two branches: one runs into a free running scaler which counts the total number of pulses and the other is sent into a scaler that is inhibited whenever the DAQ system is also inhibited. The ratio between the two scalers gives the livetime.

4.4.3 Trigger

The DAQ system used in every nuclear physics experiment cannot record and store data continuously because a given time interval is needed to readout, digitize and store the signal from all the detectors. For this reason, it is of primary importance to use a well-developed trigger system, in order to reduce the event rate by discarding the background — namely all the events in which we are not

interested — without losing any good events. This trigger system performs an online pre-selection of the events, so that only the potentially interesting events are registered and saved.

The first level of the trigger for this apparatus, called "CB Energy Sum", is built starting from the analog CB signal. The outputs from the PMTs of CB are sent into fan-in/fan-out splitting modules in groups of 16 channels. These modules, in addition to splitting the signal for energy and timing branches, sum up the 16 analog signals into one. The summed signals from all the 42 fan-in/fan-out modules are then summed together, providing a single analog signal representing the total energy deposition in all the NaI crystals. This signal is split and sent to two different discriminators with two different thresholds, the higher of them defines the first level trigger. For this experiment, a threshold of about 40 MeV was applied to cut the electronic noise and most of the cosmic events, without losing the low energy photons in which we are interested. In the second discriminator, a threshold of few MeV was set, which improves the timing performance of the trigger. The output of both the discriminators is put into a logical AND, creating the first level trigger.

Even if the "CB Energy Sum" was the only trigger used in this experiment, the A2 Collaboration system has also the possibility to implement more complicated second level triggers. For instance, it is possible to apply a threshold to each single group of 16 channels, and to count the number of these 42 clusters above threshold, giving a "multiplicity", and accept only events with multiplicity bigger than a given threshold.

Chapter 5

Event reconstruction and calibration

During the data taking, the raw digital ADC and TDC values from the different detectors are collected and stored. These signals need to be decoded and converted into usable energy and time information, to be then used to reconstruct the particle tracks involved in each event. This is done using two different parts of software, both being sets of C++-based classes built on top of the ROOT framework and developed internally by and for the A2 Collaboration: AcquRoot and GoAT. In order to correctly interpret the raw information coming for the DAQ system, a precise calibration of each single detector is of crucial importance. This is done separately for each data taking period using an additional set of C++ classes developed to work with AcquRoot, called CaLib. The first part of this chapter will be devoted to the description of the event reconstruction and of the software used for it. In the second part, the methods used to perform the detector calibrations will be briefly explained.

5.1 Software

5.1.1 ROOT

ROOT is an object-oriented program and library developed at CERN by René Brun and Fons Rademakers [118, 119]. It is mainly written in C++, but integrated with other languages, such as python. Its development was started back in 1994, and since then it has continuously grown hand in hand with the increasing demands for software efficiency and reliability of the modern nuclear and particle physics experiments. In fact, its main strength is the high computing efficiency

required for the online and offline analysis of the huge amount of data collected in such experiments. This is possible thanks to its key feature, a versatile data container called *tree*. The data in the file can be then retrieved entry by entry by advancing the index of such *tree*, avoiding memory allocation problems while handling buffering invisibly. In addition to this, ROOT offers many useful features, among them the possibility to produce and save in different formats highly-customized histograms and graphs, as well as highly-performing algorithms and routines for Monte Carlo generation, curve fitting and minimization of functional. For these reasons, ROOT is nowadays used by almost every nuclear and particle physics experiment around the world.

The most recent version of ROOT is the 6.20/04 [120], released in April 2020. It was used to create most of the plots showed in this thesis. Unfortunately, the analysis framework of the A2 Collaboration is still not fully compatible with ROOT 6, since the latter introduced some major changes, among the others a new C++ interpreter. For this reason, the data analysis was performed using ROOT 5.34/36 [121]. Despite this version was released four years ago, it is until now supported by the authors since it is still widely used in the community.

5.1.2 AcquRoot

AcquRoot [122] is the main acquisition and analysis framework of the A2 Collaboration. It contains a hierarchy of classes which decode the ADC and TDC information from the experimental apparatus to create hits in each individual detector elements. These hits contains energy and timing information, and they are then combined using cluster algorithms in CB and TAPS separately. The resulting clusters are then combined with the hits in PID, MWPCs and VETO to create tracks. All the information about detector hits and tracks are conveniently stored in ROOT trees. ready to be used by GoAT.

5.1.2.1 Decode hits

As discussed in Section 4.4, each individual element of each detector of the experimental apparatus is coupled to a PMT, whose signals are read both by an ADC and a TDC. These two electronic modules register a digital value that is proportional to the energy and time of the analog signal, respectively. AcquRoot, while running, reads each event separately from a data file, and goes through all the detector elements, converting all the ADC and TDC digital signals into readable

energy and time information. This can be done using the following equations:

$$E = g_E(C - P) + q_E(C - P)^2, \tag{5.1}$$

and

$$T = g_T(C - O), \tag{5.2}$$

respectively. In Eq. (5.1) (Eq. (5.2)) $g_{E(T)}$ is the gain, C is the ADC (TDC) channel value, P is the pedestal, O is the offset and q_E is a quadratic factor. These six parameters (with the exception of C) are specific for each detector element, and can slightly vary from data taking period to data taking period. For this reason, they have to be determined through the calibration process described later on in this chapter, and they are stored in an SQL database from where AcquRoot can retrieve them at the beginning of each analysis. Moreover, for each ADC and TDC element, a low and a high software threshold is applied. A hit information is stored in the output ROOT tree only if both the ADC and TDC values pass simultaneously both the thresholds. Table 5.1 gives a set of typical parameter values for an individual CB element. As can be seen, it is not necessary to extract the pedestal for the CB elements, since this is done automatically by the sampling ADCs during the data taking as described in Section 4.4.1. Moreover, the value of g_T reported in the table is constant for all the detector elements since this is the intrinsic gain of the CATCH TDCs used [123].

In addition to these parameters, information about the geometrical position of each element is passed to AcquRoot via a configuration file. In particular, for CB and TAPS, the (x, y, z)-position of the center of each element is given, together with a list of neighbor crystals used to create clusters, as described below. For the PID, instead, the position of each element is given in spherical coordinates: r (mm), θ (°), and ϕ (°).

The tagging system works slightly differently. While the TDC information is treated similarly as for the other detector, the energy information is given by which channel detects the electron, as described in Section 4.3.1. The energy calibration is strongly dependent on the value of the magnetic field, which slightly varies from data taking period to data taking period. The central energy value and the width of each channel are then calculated via a script that uses a complicated function with magnetic field and beam energy as input. This function does not change over time, but since the measurements described in this dissertation were the first one performed using the new tagging spectrometer, it had to be tuned using a complicated procedure. Once the energy calibration is produced,

Table 5.1: Example set of ADC and TDC parameter for a single CB element, used by AcquRoot to decode the hits information. For the specific case of CB, the ADC pedestal is provided by the sampling ADC and hence it is not needed to extract it during the calibration procedure

ADC	Physical channel	3014M1	channel
	Gain g_E	0.068	MeV/channel
	Quadratic factor q_e	1.005	$(\text{MeV/channel})^2$
	Pedestal P	0.0	channel
	Low threshold	2.0	MeV
	High threshold	2000.0	MeV
TDC	Physical channel	2033M0	channel
	Gain g_t	0.117	ns/channel
	Offset O	-2779.4	channel
	Low threshold	-100	ns
	High threshold	100	ns

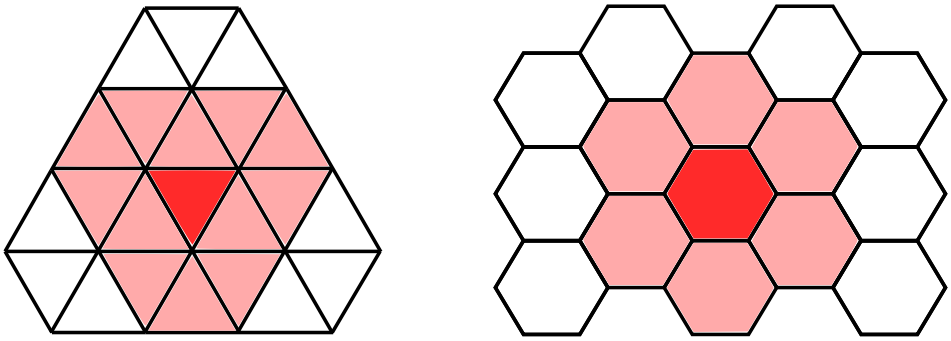

(a) NaI cluster. (b) BaF_2 cluster.

Figure 5.1: Cluster structure of (a) Crystal Ball and (b) TAPS. The central crystal is colored in red, together with the nearest neighbors — 12 and 6 for CB and TAPS, respectively — colored in pink.

it is passed to AcquRoot via a configuration file, together with the number of the scaler and TDC of each single channel.

5.1.2.2 Clustering

The two calorimeters of the experimental apparatus — CB and TAPS — are highly segmented detectors. This high segmentation causes particles to release their energy across multiple elements. This is especially true for photons, the particles of interest for this thesis, since they produce an electromagnetic shower at the interaction with the crystals. For this reason, the individual hits need to be reconstructed into one cluster resulting from the interaction of a single particle. The first step to create a cluster is to find the crystal with the highest energy

deposit. This will be the central element of the cluster. The cluster algorithm then goes through all the crystals surrounding the central one, so called neighbor elements. All the hits within these elements are then included into the cluster. Figure 5.1 shows the cluster structure of CB and TAPS. As can be seen, typically CB and TAPS elements have 12 and 6 neighbors, respectively. The size of a cluster, namely the number of hits included in it, is an important characteristic that helps in the particle identification. A photon is expected to create bigger clusters — $4-6$ hits each in the energy range $80-140$ MeV — if compared to neutron — $1-2$ hits per cluster. The maximum cluster size can be 13 for CB and 7 for TAPS.

There are particular cases where the number of neighbors element is smaller, and so the maximum cluster size. The atypical case for CB is due to its icosahedral shape. As can be seen in Fig. 4.14, each of the three points of each of the 20 "major triangles" loses one neighbor. The situation for TAPS is even more complicated due to the presence of the $PbWO_4$ crystals. As described in Section 4.3.3.4, in the two most inner rings of the calorimeter each BaF_2 crystal was replaced with a group of four smaller $PbWO_4$ crystals with the same shape. This creates cases where each crystal can have 6, 12, 18, 21, or 23 neighbors, as depicted in Fig. 4.20.

The total energy of the cluster E_{tot} is defined as the sum of the energy deposited in all the crystals included in it as:

$$E_{tot} = \sum_{i}^{size} E_i. \tag{5.3}$$

The cluster position $\vec{r}_{tot}$ is calculated as

$$\vec{r}_{tot} = \frac{\sum_{i}^{size} \vec{r}_i \sqrt{E_i}}{\sum_{i}^{size} \sqrt{E_i}}, \tag{5.4}$$

where $\vec{r}_i$ is the position of each single crystal inside the cluster. The total energy E_{tot} is compared to a software threshold. If it is above this value the cluster is accepted and all the hits composing it are removed from the list of the hits in that event. The remaining hits are fed again in the cluster algorithm to search for new clusters. This procedure is iterated until all the hits are used to form clusters.

AcquRoot has two additional clustering features that could be used in particular cases. One is important when treating very high energetic photons that

could release energy beyond the nearest neighbors. In such a case, one can ask to the algorithm to search for energy deposit in any elements within a given distance from the most energetic one. The other feature is useful to deal with split-offs, namely when one particle released its energy in what appear to be two separate clusters. In such cases, the algorithm can try to recombine two separate but close clusters into one. After Monte Carlo simulation of Compton events in the energy range of interest for this thesis, namely around the pion photoproduction threshold, it was decided to not use any of these additional features for this analysis. In fact the photons released all their energy in cluster of $4-6$ hits each, and a split-off was observed in less than 2% of the events. This can be easily taken into account with a Monte Carlo simulation correction, without introducing any additional error.

5.1.2.3 Tracking

Once the cluster algorithms combined all the hits in the two calorimeters, particle tracks are created by checking for possible correlations between the clusters, both in CB and TAPS, and the hits in the charged particle detectors — namely PID and MWPCs for CB, and VETO for TAPS.

For the Crystal Ball, the tracking algorithm checks for links between all the three detectors, or any possible pairs. The MWPCs can provide rather precise polar and azimuthal angular information. Therefore, a link between a hit in the MWPCs and a cluster in CB is defined using the vector-angle

$$\sphericalangle_{MWPCs-CB} = \cos^{-1}\left(\frac{\vec{r}_{MWPCs}\cdot\vec{r}_{CB}}{\|\vec{r}_{MWPCs}\|\|\vec{r}_{CB}\|}\right), \tag{5.5}$$

where $\vec{r}_{MWPCs}$ and $\vec{r}_{CB}$ are the 3D-vectors of the hit in the MWPCs and the cluster in CB, respectively. A correlation between the two requires $\sphericalangle_{MWPCs-CB} = [0°, 20°]$, as shown in Fig. 5.2a. The PID detector can only provide ϕ-information. Thus, a correlation between a hit in PID and a cluster in CB or between one hit in PID and another in MWPCs requires the difference between the two azimuthal angles to be within a selected region. In these cases, as shown in Figs. 5.2b and 5.2c, typical cuts used are $\Delta\phi_{PID-NaI} = [-15°, +15°]$ and $\Delta\phi_{PID-MWPCs} = [-50°, +50°]$. A correlation between all three detectors requires all these cuts to be satisfied.

The tracking procedure for TAPS is much simpler. As explained in Section 4.3.3.4, a VETO crystal is shaped to match the BaF_2 crystal, or the four $PbWO_4$ crystals, to which it is placed in front of. Therefore, there is a one-to-one

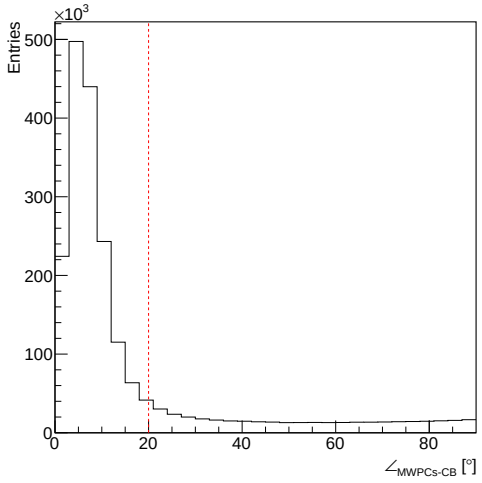

(a) $\sphericalangle_{MWPCs-CB}$.

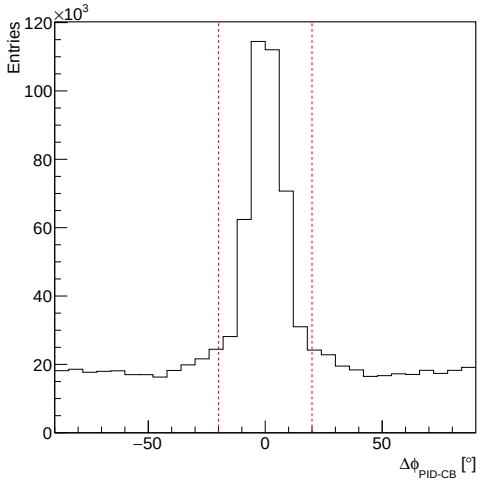

(b) $\Delta\phi_{PID-NaI}$.

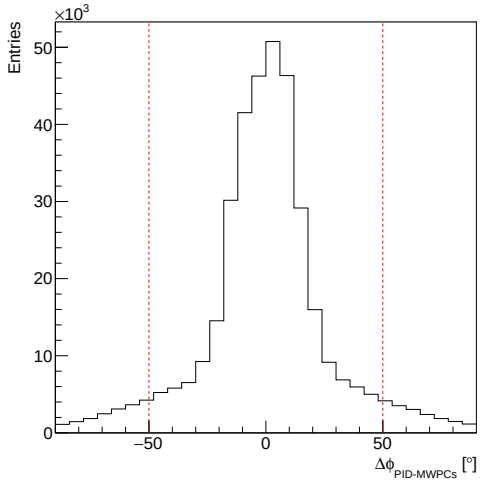

(c) $\Delta\phi_{PID-MWPCs}$.

Figure 5.2: Example of angular correlations between MWPCs hits, PID hits and CB clusters. The dotted red lines indicates the selections used to correlate this information into a track.

correlation between a hit in the VETO and the central crystal of a cluster. To form a particle track in TAPS, these two hits are linked together.

The particle tracks are then stored in a dedicated ROOT tree in the output file. The energy of the particle track is defined to be the cluster energy of Eq. (5.3). The time is defined to be the one of the central crystal of the cluster. Both these values are set to 0 in case of PID-MWPCs correlation without CB. The angular information θ and ϕ are normally defined to be the one calculated using the MWPCs, because of the better resolution if compared to the one from the cluster algorithm. For the particle tracks without MWPCs hits, the cluster angular information from Eq. (5.4) is used.

5.1.3 GoAT

Generation of Analysis Trees (GoAT) is a C++-based analysis framework developed internally to the A2 Collaboration [124, 125]. It uses as input the ROOT trees from AcquRoot containing event-by-event tracks and hits information, and it provides methods and algorithms for particle identification and meson reconstruction. Finally, it allows for an event pre-selection based on specific particle types, and energy or angular range. The information of the selected events are then conveniently stored event-by-event in ROOT trees ready for the final physical analysis described in the next chapters.

5.1.3.1 Particle identification

The first step of the data-sorting procedure operated by GoAT is the particle identification. The software runs over all the tracks reconstructed by AcquRoot and it tries to identify what type of particle created each track. A first separation between charged and neutral tracks is done by checking the presence of hits associated to the tracks in the PID, MWPCs and VETO. A track is defined as neutral if there is no hits in any of those detectors. Among the neutral tracks, a separation between photons and neutrons in CB can be done by cutting on the cluster size. As explained in Section 5.1.2.2, when photons interact with the detector they create an electromagnetic shower, which releases their energy across multiple crystals. On the other hand, neutrons tend to release all the energy in 1-2 crystals. Therefore, a cut on the dimension of the cluster can be a powerful way to distinguish among these two neutral particles. In TAPS the neutral identification can be done more easily using ToF and PSA methods. The latter uses the two different pulses provided by hits in the BaF_2 to distinguish between particles of

different mass, for more information see Ref. [97]. The identification of charged particle, instead, is done using the $\Delta E/E$ method explained in Section 4.3.3.2 for tracks created both using cluster in CB and TAPS.

5.1.3.2 Meson reconstruction

Once the individual tracks are identified, GoAT provides an algorithm for meson reconstruction and identification. Mesons are unstable particles and they decay within a very short time, definitely too fast to be detected by the apparatus. Thus, they have to be inferred by their detected decay products. For beam energy $\omega_\gamma < 1.6$ GeV, the maximal energy reachable by MAMI, four mesons are mainly generated: π^0, η, ω and η'. GoAT provides a method to reconstruct all of them.

A meson is normally inferred by calculating the invariant mass of the sum of the detected daughter particles. In particular, the invariant mass m of a system of N particles with energies E_i and momentum $\vec{p_i}$ (with $i = 1, \ldots, N$) is defined as:

$$m = \sqrt{\left(\sum_i^N E_i\right) - \left(\sum_i^N \vec{p}\right)}. \tag{5.6}$$

A similar method is used by GoAT to search for the presence of possible mesons. The invariant mass is calculated using some of the particles detected by the apparatus. In particular, to reconstruct the π^0 only the particles identified as photons are used, while to reconstruct η and η' also charged pions and electrons are considered. If the calculated invariant mass agrees with the nominal mass value of the meson, within a given range, the information about the reconstructed meson are saved in a dedicated ROOT tree. A detailed description of this feature can be found in Section 5.1.2.2 of Ref. [124].

5.1.3.3 Pre-selection of events

After particle identification and meson reconstruction, all the event-by-event information are stored in ROOT trees. At this point, GoAT allows for a first event selection by cutting on the number and the type of reconstructed particles/mesons in the final state. This is very useful in order to reduce the amount of events to be accessed in the next steps, discarding clear background events and saving time during the physics analysis.

For the Compton scattering analysis described in this thesis, a simple identification among neutral and charged particles was used. In fact, in the energy

range of our interest ($\omega_\gamma \sim 80 - 140$ MeV), only the scattered photon is detected while the recoil proton stops inside the target. For this reason, a strict selection of events with exactly 1 neutral and 0 charged tracks was applied. Nevertheless, to study possible systematic error introduced by this strict selection, the analysis was also performed allowing more than one neutral particle. The result of this test is described in Section 8.1.

5.1.4 A2Geant4

A2Geant4 [126] is a simulation package built to simulate the interaction of particles with the detection apparatus of the A2 Collaboration. It uses the Geant4 simulation toolkit [127–129], first developed in the mid 90s at CERN. Its development, maintenance and user support are taken care by the international Geant4 Collaboration [130] and it is nowadays widely used by many collaborations and experiments to simulate the passage of particles through matter. All the Monte Carlo simulations reported in this thesis were done using the Geant4 version 10.04 (patch-02) [131] released in May 2018.

The A2Geant4 package uses as input a ROOT file containing particles 4-momenta generated using AcquMC, a Monte Carlo event generator included in the AcquRoot package. AcquMC allows for Monte Carlo generation of simple physics reactions, such as proton Compton scattering, with a given beam position and energy distribution. The 4-momenta of the particle in the initial and final states are stored in ROOT trees, and their interaction within the experimental apparatus is simulated by the A2Geant4 package. It includes the two main calorimeters, CB and TAPS, as well as the three charged particle detectors — PID, MWPCs, VETO. It gives as output a ROOT file with the deposited energies and the time information in each detector. It can then be analyzed using AcquRoot and GoAT as a normal data file. A detailed description of the simulations done for this analysis in give in Section 7.4.

5.1.5 CaLib

CaLib [123, 132] is a software developed internally to the A2 Collaboration and used to calibrate the experimental data. CaLib is based on an SQL database system. It has an SQL table for each calibration parameter, containing columns for all the detector elements. It is also possible to add multiple rows, specifying different sets of parameter valid for specific sets of runs. These parameters are accessed and read by AcquRoot during the analysis, allowing for the use of

different calibration sets depending on the run number.

As described in the next session, the raw data are firstly analyzed using AcquRoot with a dedicated class that produces all the necessary histograms for the calibration. These plots are used by CaLib to perform the fits necessary to the calibration procedure. It also provides a user-friendly Graphical User Interface (GUI) to display the relevant spectra and to check the goodness of the fit for each detector element. Moreover, using the GUI it is possible to select among the different calibration sets, as well as to calculate and write the new parameters on the SQL database.

5.2 Calibration

The first step of the analysis performed using AcquRoot is the decoding of the raw digital signals coming from the ADC and TDC modules, as described in Section 5.1.2.1. This is done using different parameters reported in Table 5.1. Some of these parameters are fixed, such as the physical address of the modules of the software thresholds, while others, mainly gains, offsets and pedestals, are sensitive to environmental conditions and may vary from data taking period to data taking period. For this reason, it is extremely important to perform a precise calibration of these parameters before any analysis. The calibration of the data used in this analysis was performed using CaLib (see Section 5.1.5) following a precise order, since some parameters may be dependent on some others that need to be calibrated first. Moreover, in some cases the procedure was iterated multiple times in order to get a precise result, using every time the new parameters to re-analyze the data.

5.2.1 Crystal Ball

CB is the main calorimeter of the experimental apparatus. As described in Section 4.3.3.1, it is composed of 672 NaI crystals, each read by an SADC and a TDC. For each element, an energy and time calibration is needed, as well a correction for the energy dependence of the time, know as time walk.

5.2.1.1 Time calibration

The gain of the CATCH TDC modules used to read the time signal from the NaI crystals is fixed to $g_t = 0.117$ ns/channel. The TDC offset are instead adjusted for each channel to eliminate possible differences in cable length or hardware timing.

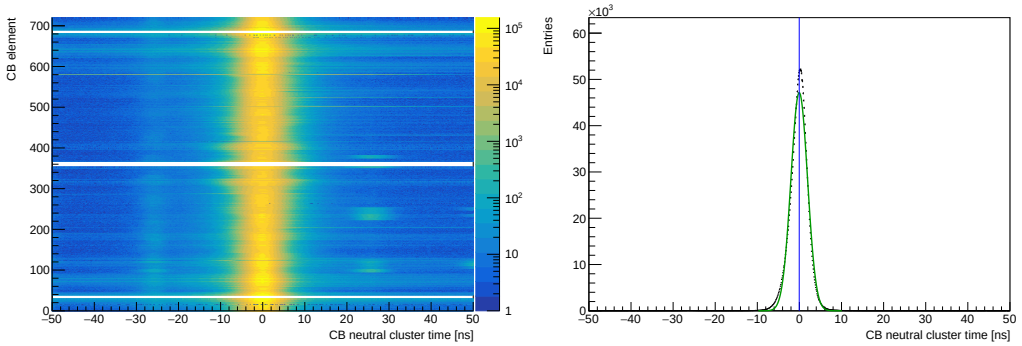

(a) 2-D distribution.

(b) Single element fit.

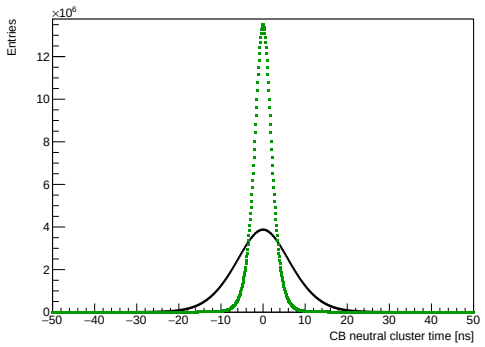

(c) CB time distributions: black and green lines are obtained pre and post calibration.

Figure 5.3: Example of the spectra used to perform the calibration of CB TDCs offset. (a) The NaI element is plotted versus the difference in time of two neutral hits in CB. (b) The time distribution is projected for each CB element, and the resulting distribution is fitted with a Gaussian function, to get the new offset. (c) The calibration procedure is iterated multiple times to get the final results.

To perform this calibration, the NaI element is plotted versus the difference in time of two neutral hits in CB, obtaining the spectra in Fig. 5.3a. Since this is done for each element, the histogram is filled twice for each couple of hits: the first element is filled at its time minus the second hit's time, and the second element is filled as its time minus the time of the first hit. In the case of two correlated hits, such as two photons from a π^0 decay, this difference should be zero. The 2-D histogram is projected onto the x-axis for each bin on the y-axis (corresponding to each NaI crystal), and the resulting plot is fitted with a Gaussian function, as shown in Fig. 5.3b. The new offset for the i-th crystal O_i' is calculated as

$$O_i' = O_i + \frac{\mu_i}{g_t}, \tag{5.7}$$

where O_i it the old offset used to create the calibration plot and μ_i is the mean of the Gaussian fit.

This procedure was iterated several times, using always the new offset to create the new calibration spectra. Finally, the mean value of the time difference for each element converged to zero, as can be seen in Fig. 5.3c.

5.2.1.2 Energy calibration

The calibration of the energy response of the NaI crystals is done using two different procedures. The first one is performed by placing a ^{241}Am^{9}B source in the center of the Crystal Ball. The source emits 4.438 MeV photons that are homogeneously detected by all the elements. The high voltage supplied to each single PMT is then adjusted until the responses from each tube result in approximately the same ADC channel. This first hardware calibration is done regularly once per year by the person responsible for the maintenance of the detector. Nevertheless, such a calibration done with extremely low energetic photons cannot be easily extrapolated to the few hundreds MeV energy range in which we are interested.

The second calibration procedure, which is done for every data production period, uses the single pion photoproduction reaction, $\gamma p \to \pi^0 p \to \gamma\gamma p$. In particular, the invariant mass of the two γ, $m_{\gamma\gamma}$, calculated using Eq. (5.6) is expected to be peaked at $m_{\gamma\gamma} = m_{\pi^0} = 134.9$ MeV. Using all the neutral clusters in CB, the invariant mass $m_{\gamma\gamma}$ is calculated for every cluster pair, and the result is plotted as a function of the central crystal of each of the two clusters. This results in the 2-D histogram showed in Fig. 5.4a, and again, as for the time calibration, each couple fills the histogram twice, once per cluster. Similarly to

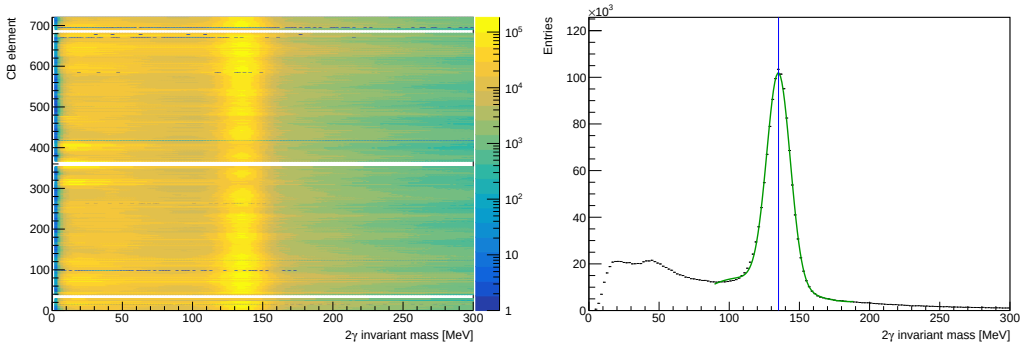

(a) 2-D distribution.

(b) Single element fit.

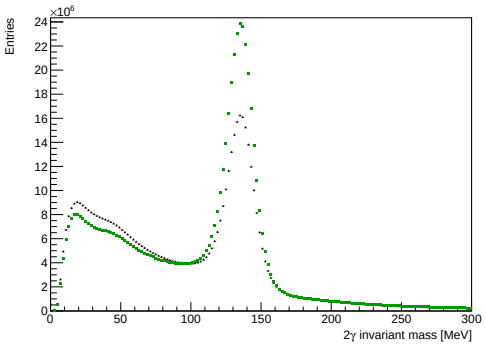

(c) $m_{\gamma\gamma}$ distribution in CB: black and green lines are obtained pre and post calibration.

Figure 5.4: Example of the spectra used to perform the calibration of CB ADCs gain. (a) The NaI element is plotted versus the invariant mass $m_{\gamma\gamma}$ calculated for every neutral cluster pair in CB. (b) The invariant mass distribution is projected for each CB element, and the resulting distribution is fitted with the sum of a Gaussian and a polynomial function, to get the new gain correction. (c) The calibration procedure is iterated multiple times to get the final results.

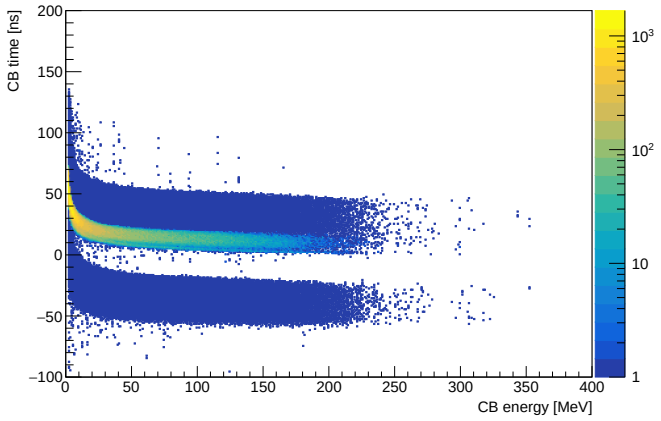

Figure 5.5: Example of the spectrum used to extract the parameters for the correction of the time walk effect. The time difference between a hit in CB and a hit in the tagger is plotted versus the energy deposited in CB, for each element. The distribution is fitted using the function in Eq. (5.9) to get the parameters needed for the time walk correction.

what happened for the time calibration, the 2-D histogram is projected into the x-axis for each bin on the y-axis, and the resulting plot (see Fig. 5.4b) is fitted using the sum of a Gaussian and a polynomial function, to describe the signal and the background, respectively. The new gain for the i-th element $g'_{E,i}$ is calculated as:

$$g'_{E,i} = g_{E,i} \frac{m^2_{\pi^0}}{m^2_{\gamma\gamma}}, \tag{5.8}$$

where $g_{E,i}$ is the old gain used to produce the calibration spectra. This procedure was iterated several times, until the peak of the invariant mass distribution for each channel turn out to be located at the mass of the π^0, as shown in Fig. 5.4c.

As reported in Eq. (5.1), there is an additional quadratic energy factor used in the conversion of the energy information. This factor accounts for the lack of linearity in the NaI response for the higher energetic photons. The effect of this is that after performing the energy calibration using the π^0 meson, the invariant mass of heavier mesons, such as the η, is wrongly reconstructed. To correct for this, a procedure similar to the one described above is done using higher energetic neutral clusters to reconstruct the η, and the resulting invariant mass is compared and centered to $m_\eta = 547.8$ MeV.

5.2.1.3 Time walk calibration

Due to the slow rise time of the signal in the NaI crystal, the time of the signal is affected by time walk. This causes a low-energy signal to have a later time trigger

if compared to a concomitant high energy signal. A correction of this effect is essential to improve the time resolution of the detector.

To perform such a calibration, the time difference between a hit in CB and a hit in the tagger is plotted versus the energy deposited for every detector element. An example for one of the 684 channels is seen in Fig. 5.5. Each plot is then fitted using the function:

$$t(E) = a + \frac{b}{(E+c)^d}, \tag{5.9}$$

where E is the energy deposited in the crystal and a, b, c, d are free parameters. These parameters are determined for each individual element, and during the analysis they are used to correct the cluster time information as:

$$t' = t - \left(a + \frac{b}{(E+c)^d}\right), \tag{5.10}$$

where t and t' are the uncorrected and the corrected time information, respectively.

5.2.2 PID

The PID is mainly used for the charged particle identification, as described in Section 4.3.3.2. The analysis described in this thesis deals with neutral particles only, and the PID was simply used to distinguish between charged and neutral cluster, without using the energy information. Among all the detectors in the experimental apparatus, the PID is the only one whose position can occasionally change, in particular its azimuthal orientation in respect to CB. For this reason, in addition to the energy and the time calibration, a calibration of the ϕ-alignment is usually performed. This is of crucial importance to correctly link a hit in the PID with a cluster in CB.

5.2.2.1 Time calibration

The time information of the PID is read using TDC modules similar to the ones used for CB and tagger. For this reason, also the calibration procedure works in the same way as described for CB in Section 5.2.1.1. The time difference between two hits in the PID is plotted as function of one of the two elements, giving the 2-D plot showed in Fig. 5.6a. For each element, a projection is created and the obtained distribution is fitted with a Gaussian function (see Fig. 5.6b), and the new offset is calculated using Eq. (5.7). After one single iteration, the time difference for all the PID elements was already well peaked at 0.

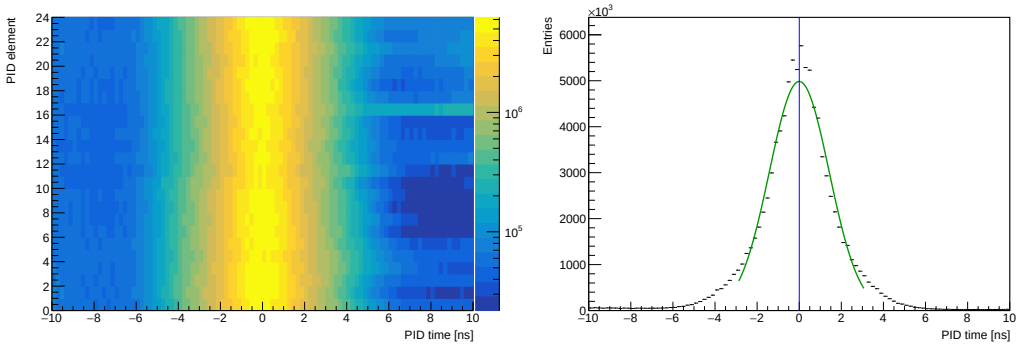

(a) 2-D distribution.

(b) Single element fit.

Figure 5.6: Example of the spectra used to perform the calibration of PID TDCs offset. (a) The PID element is plotted versus the difference in time of two neutral hits in the PID. (b) The time distribution is projected for each PID element, and the resulting distribution is fitted with a Gaussian function, to get the new offset.

5.2.2.2 Energy calibration

Due to the small thickness of the PID, charged particles release only a small fraction of their energy in it. This makes a direct calibration almost impossible. The idea then is to extrapolate the energy release in the PID for different cluster energies from a Monte Carlo simulation. In particular, with real data, the PID ADC channel is plotted as function of the cluster energy for protons only. The result is a $\Delta E/E$ plot showing only the proton band, with the raw ADC information on the y-axis, as in Fig. 5.7a. Projections of this histogram onto the y-axis are created for different ranges of cluster energy, giving the distribution of the proton signal over the raw ADC channel (see Fig. 5.7b). Such a distribution is fitted using a Gaussian function, and the mean ADC channel for each cluster energy range is found. A similar procedure is done using a Monte Carlo simulation of protons interacting with the experimental apparatus. For the same cluster energy ranges, the simulated energy deposition in the PID is evaluated. By plotting the raw ADC channel value from the Gaussian fit as a function of the expected energy deposition from the simulation, a linear relation can be extracted performing a fit, as shown in Fig. 5.7c.

5.2.2.3 ϕ calibration

The ϕ parameter of each single element of the PID is found with respect to CB. To obtain this calibration, for each charged cluster the PID element is plotted versus the ϕ information of the correlated cluster, obtaining the 2-D histogram showed in Fig. 5.8a. A projection for each element is created, and the distribution

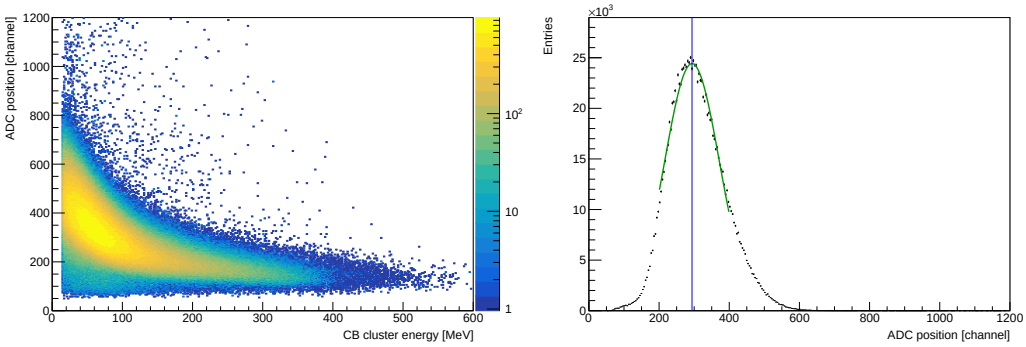

(a) $\Delta E/E$ distribution for one PID element.

(b) PID ADCs channel distribution from proton in a given cluster energy range.

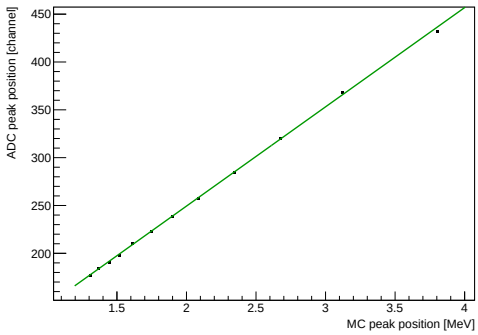

(c) Linear fit to find PID energy calibration.

Figure 5.7: Example of the spectra used to perform the calibration of the PID ADCs gain. (a) The PID ADC channel is plotted as function of the cluster energy for protons only. (b) The distribution of the proton signal over the raw ADC channel is projected for different ranges of cluster energy, and the obtained plots are fitted with a Gaussian function to get the mean channel. (c) The same procedure is repeated for Monte Carlo generated data where the energy deposition in the PID is calculated using the simulation. By plotting the raw ADC channel value from the Gaussian fit as a function of the expected energy deposition from the simulation, a linear relation can be extracted.

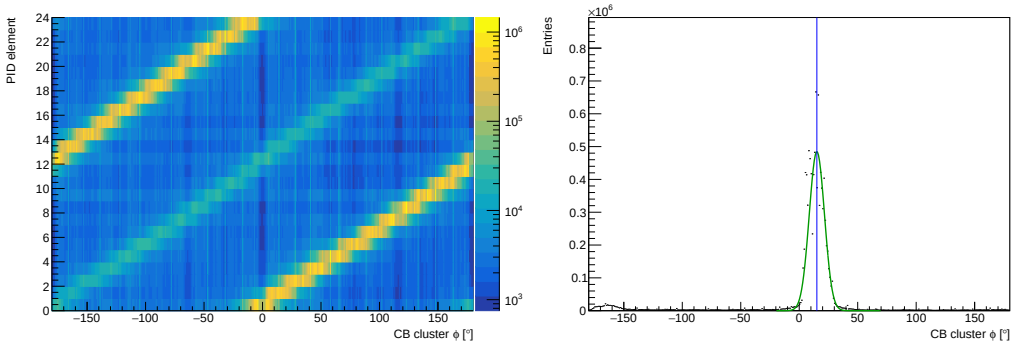

(a) 2-D distribution.

(b) Single element fit.

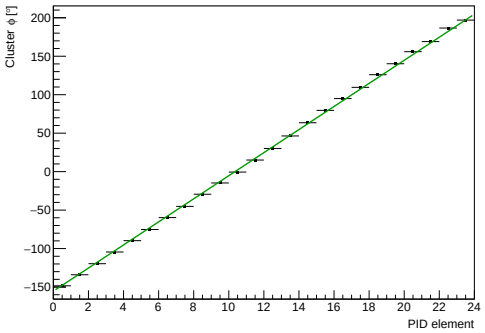

(c) Linear fit to find PID ϕ calibration.

Figure 5.8: Example of the spectra used to calibrate the ϕ offset between the PID and CB. (a) For each charged cluster, the PID element is plotted versus the ϕ of the correlated cluster. (b) For each element, the distribution is projected and fitted using a Gaussian function to find the mean ϕ value. (c) The PID elements is plotted as function of the mean cluster ϕ, and the resulting distribution is fitter to find the correlation.

is fitted with a Gaussian function, as shown in Fig. 5.8b. The mean value of the i-th Gaussian fit gives a ϕ_i parameter for the i-th element of the detector. Finally, the correlation between CB and the PID elements is found with a linear fit of the distribution of the ϕ parameters as a function of the 24 different elements, as shown in Fig. 5.8c.

5.2.3 TAPS

TAPS is the forward calorimeter of the experimental apparatus. As described in Section 4.3.3.4, it is composed of 366 BaF_2 and 72 $PbWO_4$ crystals. Unfortunately, the latter were not working properly during all the data taking period and it was decided to turn them off. In front of each BaF_2 crystal, as well as in front of each group of 4 $PbWO_4$ crystals, is placed a thin scintillator paddle, called VETO. The calibration of the signal coming from the crystals is similar to the one done for CB. Thanks to the fast response of BaF_2 crystals, the time walk calibration is not needed. Nevertheless, the energy calibration is slightly more complicated due to the two components of the energy response. Furthermore, the signal coming from the VETO paddles is calibrated similarly to the PID.

5.2.3.1 BaF_2 time calibration

TDC gains are usually determined by the persons in charge of the maintenance of the detector right before the start of the data taking period. This is done by using different delay cables of known length, to increase the time of the TDC stop signal. With every cable a short run with cosmics is taken, and from the analysis of these data, using a dedicated software, it is possible to determine the gain for each single detector element.

The calibration of the offset is performed similarly to what is described in Section 5.2.1.1. The time difference of two neutral hits in TAPS is plotted as function of one of the two elements, producing the plot in Fig. 5.9a. For each element, the distribution if fitted using a Gaussian function (Fig. 5.9b) and the new offset is calculated to center the Gaussian in zero. This procedure required multiple iterations to reach a final satisfying result, showed in Fig. 5.9c.

5.2.3.2 BaF_2 energy calibration

As previously mentioned, the BaF_2 has the peculiarity of having a fast and a slow signal component. For this reason, the analog signal coming from each TAPS crystal is fed into two different ADCs: one with a short integration gate,

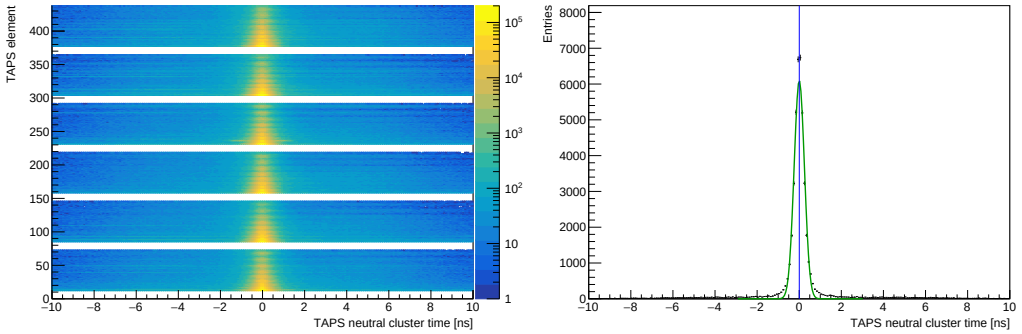

(a) 2-D distribution.

(b) Single element fit.

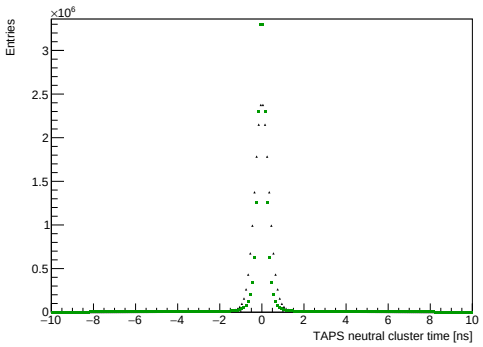

(c) TAPS time distributions: black and green lines are obtained pre and post calibration.

Figure 5.9: Example of the spectra used to perform the calibration of TAPS TDCs offset. (a) The BaF_2 element is plotted versus the difference in time of two neutral hits. (b) The time distribution is projected for each TAPS element, and the resulting distribution is fitted with a Gaussian function, to get the new offset. (c) The calibration procedure is iterated multiple times to get the final results.

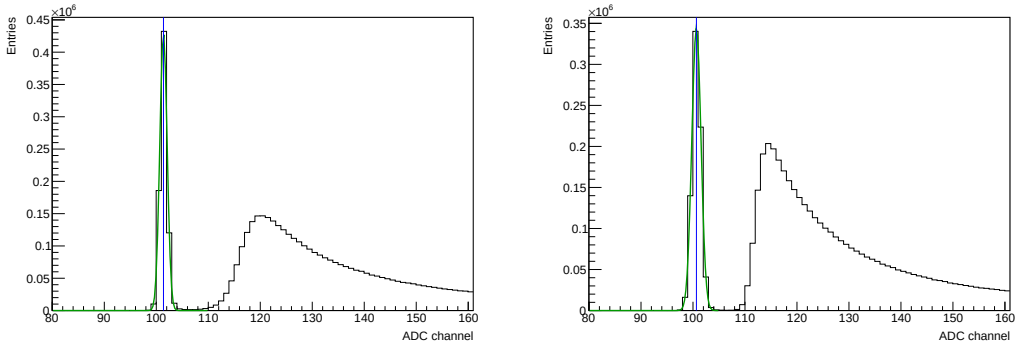

(a) Long gate ADC. (b) Short gate ADC.

Figure 5.10: Calibration of TAPS ADCs pedestal.

called Short Gate (SG), and one with a long integration gate, called Long Gate (LG). The LG modules integrate over the full signal, in a similar way to what happens for the signal from CB. The SG ADCs integrate only the first part of the signal, the fast component, which is essentially the full signal in case of a photon, or only a small part of it in case of a nucleon. Combining the SG and the LG response, the PSA can be performed to distinguish among photons and neutrons.

The two different sets of ADCs require separate gain calibrations. Since the LG signal is used to calibrate the SG one, its calibration comes first. The pedestal calibrations, instead, are performed in the same way for both the ADC sets. The raw ADC spectra are scanned to find the pedestal, as showed in Fig. 5.10.

LG calibration The LG ADCs gain is calibrated using the procedure described in Section 5.2.1.2. The invariant mass of 2 neutral clusters is plotted as function of the central crystal of each cluster, giving the spectra in Fig. 5.11a. Due to the generally low statistics in TAPS, the invariant mass is reconstructed using also the events with one neutral cluster in TAPS and one in CB. For this reason, this energy calibration was performed after the CB one. For each element, a fit to the distribution is performed (Fig. 5.11b) and the new gain is calculated to center the invariant mass distribution to the π^0 mass. Also this procedure was iterated multiple times to reach the result in Fig. 5.11c.

SG calibration By definition, the SG ADCs integrate only the fast component of the BaF_2 signal, leaving out the slow part. This causes a direct calibration to be complicated to performed. It is instead convenient to combine the two signal components, and to perform the calibration making use of the PSA. This is done

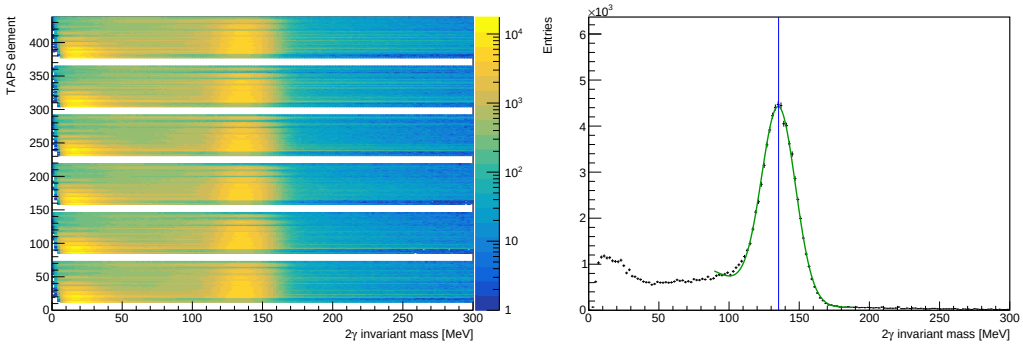

(a) 2-D distribution.

(b) Single element fit.

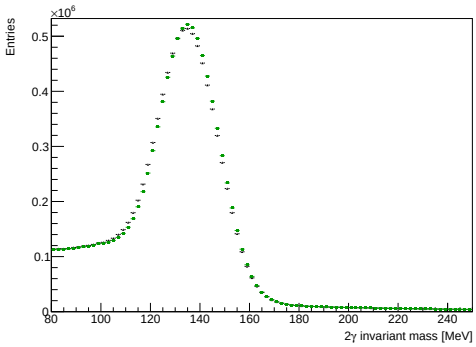

(c) $m_{\gamma\gamma}$ distribution in TAPS: black and green lines are obtained pre and post calibration.

Figure 5.11: Example of the spectra used to perform the calibration of TAPS LG ADCs gain. (a) The BaF_2 element is plotted versus the invariant mass $m_{\gamma\gamma}$ calculated for every pair of neutral cluster in TAPS and in TAPS+CB. (b) The invariant mass distribution is projected for each TAPS element, and the resulting distribution is fitted with the sum of a Gaussian and a polynomial function, to get the new gain correction. (c) The calibration procedure is iterated multiple times to get the final results.

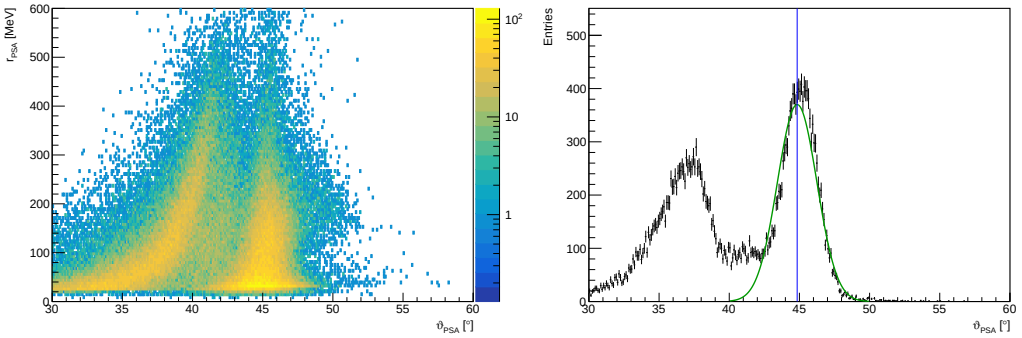

(a) PSA distribution. (b) Projection for a given r_{PSA} range.

Figure 5.12: Example of the spectra used to calibrate the TAPS SG ADCs gains. (a) The PSA radius is plotted versus the PSA angle, defined in Eqs. (5.11) and (5.12), respectively. (b) The PSA angle distribution is projected for different ranges of the PSA radius. The right peak of the obtained distribution is fitted and the ADC gain is adjusted to center the peak at 45°.

by computing the PSA radius (r_{PSA}) and the PSA angle (ϑ_{PSA}), respectively as

$$r_{PSA} = \sqrt{E_{SG}^2 + E_{LG}^2}, \tag{5.11}$$

and

$$\vartheta_{PSA} = \tan^{-1}\left(\frac{E_{SG}}{E_{LG}}\right). \tag{5.12}$$

The r_{PSA} is then plotted versus ϑ_{PSA}, giving the spectra in Fig. 5.12a. Since photons have a fast energy deposition, their SG and LG components are very close. Therefore, for photons, ϑ_{PSA} should be 45°, especially at higher energies. On the other hand, for low energetic hadrons ϑ_{PSA} should clearly deviate from this value. To calibrate the SG ADCs gain, such a plot is created for every single element. A projection of this plot on the x-axis is done, giving a characteristic two peaks distribution showed in Fig. 5.12b. The right hand peak is fitted and the ADC gain is adjusted to center this peak at 45°.

5.2.3.3 Veto time calibration

The VETO TDCs gain is fixed to 0.05 ns/channel [23]. The offset is calibrated in the same way as it is done for all the other detectors. The difference in time between two elements is plotted as a function of the element number (Fig. 5.13a), a projection for each element is created and the resulting distribution is fitted (Fig. 5.13b). The offsets are adjusted to set such a difference to zero (Fig. 5.13c).

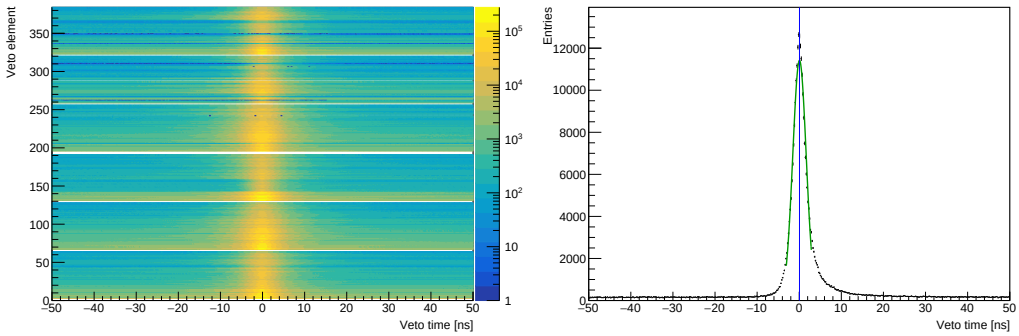

(a) 2-D distribution.

(b) Single element fit.

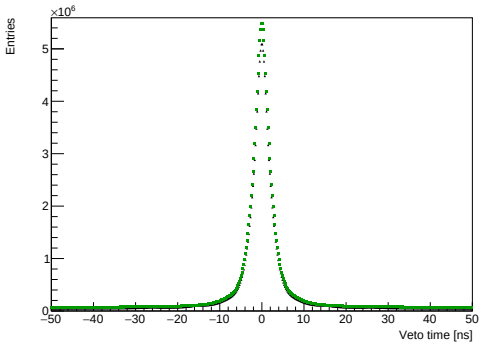

(c) VETO time distributions: black and green lines are obtained pre and post calibration.

Figure 5.13: Example of the spectra used to perform the calibration of VETO TDCs offset. (a) The VETO element is plotted versus the difference in time of two neutral hits. (b) The time distribution is projected for each VETO element, and the resulting distribution is fitted with a Gaussian function, to get the new offset. (c) The calibration procedure is iterated multiple times to get the final results.

5.2.3.4 Veto energy calibration

The VETO ADCs gain is calibrated in the same way as described in Section 5.2.2.2 for the PID. The idea again is to compare the $\Delta E/E$ from the data and from the Monte Carlo simulation, and to adjust the gains to match the former with the latter.

5.2.3.5 Veto correlation check

To correctly tag a cluster in TAPS as charged (or neutral), it is important to check that each VETO paddle is correctly linked to the corresponding BaF_2 to which it is placed in front of. This can be easily done by plotting the BaF_2 element versus the VETO hit for each charged cluster. If the two elements are correctly linked in the configuration file, there should be a one-to-one correspondence. If this is not the case, CaLib automatically corrects the links in the configuration file.

5.2.4 Tagger

The tagging spectrometer, in the configuration used for this experiment, is composed of 328 channels. Each channel is read by a TDC, while the energy information is determined based on the position of each channel, as explained in Section 4.3.1. The energy calibration depends on the electron beam energy and on the magnetic field and it is normally calculated for each beamtime using a simple software called "ugcal". Nevertheless, as already stated, this was the first experiment after a major upgrade of the tagger and the old "ugcal" was not valid anymore. For this reason, a huge effort was made inside the A2 Collaboration to create an updated version of this software, using a complicated calibration procedure similar to the one described in Section 6 of Ref [103].

5.2.4.1 Tagger time calibration

As already mentioned before, the CATCH TDCs gain is fixed at 0.117 ns/channel. The only parameter that needs to be adjusted is the offset. As for the other detectors, the idea is to align to zero the time difference between hits, in order to have the same time information regardless of which element detected the electron. Since each electron is detected by one single element, the difference in time is calculated using neutral hit in TAPS as a reference. This is a natural choice since TAPS has a better timing resolution compared to CB. The time difference between a hit in the tagger and a neutral hit in TAPS is plotted as function of the tagger channel, creating the 2-D spectra showed in Fig. 5.14a. For each

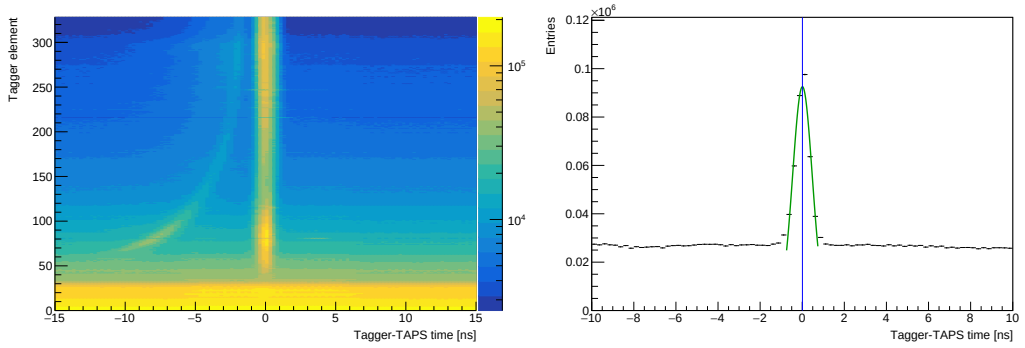

(a) 2-D distribution.

(b) Single channel fit.

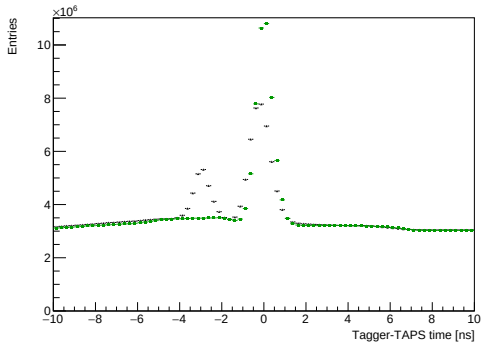

(c) Tagger time distributions: black and green lines are obtained pre and post calibration.

Figure 5.14: Example of the spectra used to perform the calibration of tagger TDCs offset. (a) The tagger channel is plotted versus the difference in time between the hit in the tagger and a hit in TAPS. (b) The time distribution is projected for each tagger channel, and the resulting distribution is fitted with a Gaussian function, to get the new offset. (c) The calibration procedure was iterated multiple times to get a precise calibration.

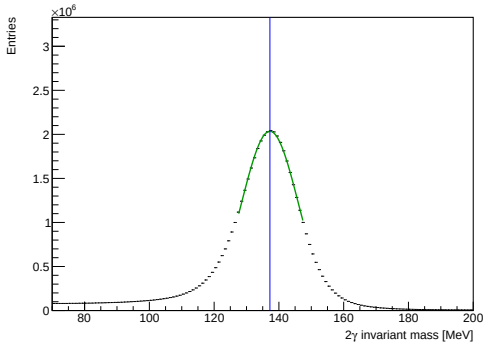

(a) $m_{\gamma\gamma}$ distribution without any shift.

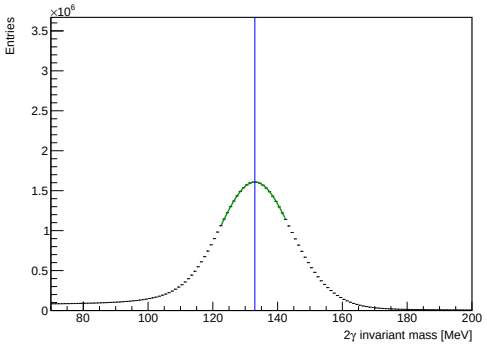

(b) $m_{\gamma\gamma}$ distribution with a -8.0 mm shift.

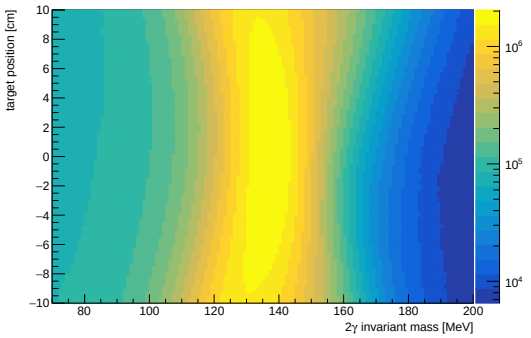

(c) 2-D distribution.

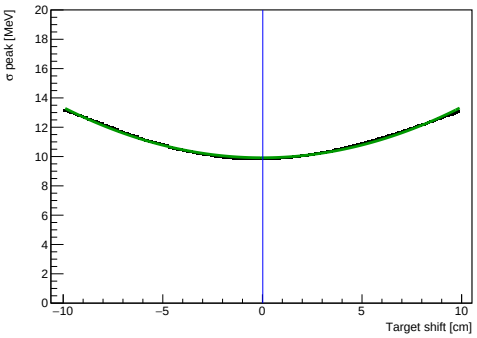

(d) Fit of $\sigma_{m_{\gamma\gamma}}$ versus the vertex shift.

Figure 5.15: Example of the spectra used to calibrate the target position along the z-axis. (a) and (b) show the 2γ invariant mass distribution calculated assuming two different offset of the target position with respect the CB. (c) The 2γ invariant mass is plotted as a function of the shift in target position. The invariant mass distribution is projected for different shift values and the resulting plot is fitted to get the width of the distribution. The minimum in the width distribution gives the real shift in the position of the target respect to the CB.

element, a projection on the x-axis in produced, and the resulting distribution is fitted using a Gaussian function, as showed in Fig. 5.14b. The offset is then adjusted to center this time difference to zero, as visible in Fig. 5.14c. In this particular spectrum, the importance of these calibrations is clear. It can be seen how, before the calibration (black curve), the time distribution had an additional peak at -3 ns. Without a proper correction, this would have caused the loss of the $\sim 30 - 40\%$ of the prompt events.

5.2.5 Target position

The position of the target with respect to the Crystal Ball can vary from data taking period to data taking period, in particular along the z-axis. In fact,

between each experiment, the experimental apparatus can be moved to change the target or to perform maintenance operations. It is therefore important to check the target position before the starting of an experiment. This is done during the first day of data taking using the MWPCs. By selecting events with two charged tracks that released signal in both wire chambers, it is possible to reconstruct the event vertex with a good resolution. This allows for a precise check of the position of the target in respect to the apparatus. If the center of the target is considerably off ($\gtrsim 0.5$ cm) compared to the center of CB, the apparatus can be moved to re-aligned everything.

A similar check can be performed also using CaLib. In this case, the position of the target in respect to CB is checked using the invariant mass $m_{\gamma\gamma}$. In this procedure, the invariant mass of each couple of neutral clusters $m_{\gamma\gamma}$ is calculated by shifting the vertex position, and the result is plotted as function of the altered position used. This produces the 2-D histogram showed in Fig. 5.15c. A projection of the $m_{\gamma\gamma}$ distribution for each shift in the vertex position is created and the resulting spectra is fitted using a Gaussian function. The effect on the $m_{\gamma\gamma}$ value of a shift in the vertex position is clearly visible in Figs. 5.15a and 5.15b: the latter plot is obtained by shifting the vertex by 8.0 mm on the z-axis in the negative direction, while the former is obtained without any shift. The sigma $\sigma_{m_{\gamma\gamma}}$ resulting from the Gaussian fit is plotted as function of the vertex position, and the minimum of the distribution corresponds to the actual target position, as showed in Fig. 5.15d. The resulting value can be used in the Monte Carlo simulation to adjust the center position of the target. The minimum of the $\sigma_{m_{\gamma\gamma}}$ distribution resulted to be very close to 0, as indicated by the blue line in Fig. 5.15d. This confirms the good alignment done at the beginning of the data taking period using the MWPCs.

Chapter 6

Photon beam analysis

A precise knowledge of the number of photons that reach the target is crucial for the measurement of a cross-section. The photon flux enters at the denominator of the cross-section equation, as explained in Chapter 8, and so it directly affects the final results. In a tagged photon facility, as the one used for this experiment, this measurement is quite challenging since it depends both on the number of electrons that interact in the radiator emitting a bremsstrahlung photon, and on the number of such photons that pass the collimator. While the former number can be easily measured by counting the number of electrons in the photon tagging spectrometer, the latter needs dedicated measurements and a constant monitoring since it depends on the beam conditions. Moreover, as discussed in Section 4.2, the use of a linearly polarized photon beam — needed for the extraction of the beam asymmetry Σ_3, but also useful to increase the statistics — enhances the number of photons that pass the collimator only in specific energy regions, making it even more challenging to precisely estimate the total photon flux. In fact, a relatively small change in the beam position can cause a not negligible change in the instantaneous photon rate. The first half of this chapter will be devoted to a detailed discussion of the analysis performed to ensure a precise measurement of the photon flux. In the second part, the analysis used to extract the degree of linear polarization will be presented. This information is needed to correctly extract the beam asymmetry Σ_3 from the data.

6.1 Photon flux

The photon flux, namely the number of photons reaching the target, can be calculated as the number of detected electrons in the tagger spectrometer scaled

with the probability of a photon to pass the collimator, know as tagging efficiency:

$$\Phi(i) = N_{e^-}(i)\epsilon_{tagg}(i), \tag{6.1}$$

where $\Phi(i)$ and $\epsilon_{tagg}(i)$ are the number of photons reaching the target that were produced by electrons detected in the i-th tagger channel and their tagging efficiency, respectively, and $N_{e^-}(i)$ is the total number of electrons detected in that given tagger channel. Ideally, the tagging efficiency should be constant over time and, in the case of an unpolarized photon beam, it should not depend on the tagger channel where the electron is detected, or in other words it should not be photon energy dependent. In the case of a polarized photon beam, as already mentioned, ϵ_{tagg} is strongly energy dependent and it becomes very sensitive to small variation in the beam quality and position. For this reason, it is very important to keep the tagging efficiency monitored during the whole experiment. This was done in two ways: once per day with dedicated measurements using the lead glass detector, and constantly using a pair spectrometer. The two methods are complementary: the former is more precise but it accounts for changes only every 24 hours, the latter is less precise but it provides for a real-time measurement of the tagging efficiency. A combination of these two methods would allow for an extremely precise photon flux calculation. Nevertheless, as shown in the next paragraphs, a precise analysis of the pair spectrometer data was unfortunately not possible. To try to remedy for this and to improve the analysis of the lead glass data, a new method was implemented and used. Thanks to it, it was possible to carefully control the systematic errors on the flux normalization.

6.1.1 Tagging efficiency evaluation

6.1.1.1 Lead glass

A precise measurement of the tagging efficiency was done daily using the lead glass detector (see Section 4.3.3.5). During these measurements, this extremely efficient detector is placed in the beamline behind TAPS and the electron beam current is reduced so that only a rate of 10^5 photons per second is recorded by it. A 30 minutes tagging efficiency run was collected for each orientation of the diamond radiator (parallel and perpendicular), as well as for the amorphous radiator. Moreover, at the beginning and at the end of each tagging efficiency set, a background measurement without the beam was also performed. With the old tagger spectrometer, the contribution of the background was almost negligible and constant in time. So, the tagging efficiency for the i-th channel given in

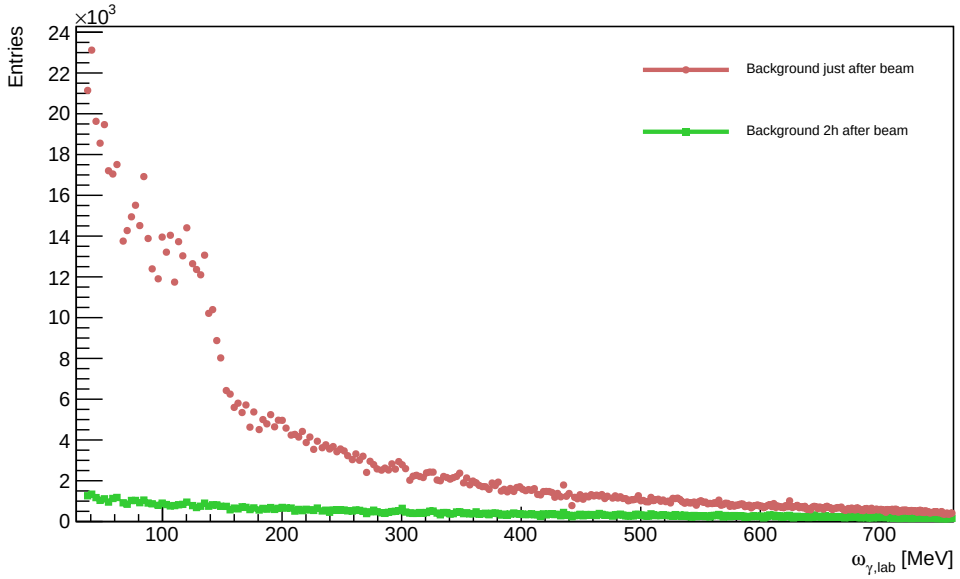

Figure 6.1: Sample of the scalers distribution of two different background measurements taken immediately (brick circles) and two hours after (green squares) the beam was stopped.

Eq. (6.1) was simply calculated as:

$$\epsilon_{tagg}(i) = \frac{N_{PbG}(i)}{N_{e^-}(i) - 0.5(t_1 N_{e^-}^{bkg_1} + t_2 N_{e^-}^{bkg_2})}, \tag{6.2}$$

where $N_{PbG}(i)$ is the number of electrons detected in the i-th tagger channel with an associated trigger in the lead glass, $N_{e^-}(i)$ is the number of electron registered in the scalers for that given channel, $N_{e^-}^{bkg_1}$ and $N_{e^-}^{bkg_2}$ are the number of electrons registered in the scalers in the initial and final background measurement, respectively. The two factors t_1 and t_2 account for the different duration of the background runs and they are defined as the ratio between the time duration of the run with beam and the time duration of the first and second background run, respectively. This equation works fine in the case of time independent background, where one can assume that an average of the background before and after the run is a good estimate of the background contamination during the actual measurement with the beam. Unfortunately, this is not true anymore with the new tagger spectrometer. In fact, in the scaler distribution from the first background measurement shown in Fig. 6.1 (brick circles), one can clearly see a nonuniform distribution that looks like the sample with beam shown in Fig. 4.8. Moreover, a repetition of the background measurement after two hours without beam shows a completely different scalers distribution, as shown in green in

Fig. 6.1, where in the same time span almost 20 times less electrons were collected. This strong time dependency of the scalers background indicates some activation inside the tagger, most likely in the aluminum structure surrounding each module. In this situation, a simple average of the two background measurements as in Eq. (6.2) would underestimate the background in the first measurement of the set and overestimate it in the last one. To correct for this issue, a new method for the subtraction of the background in the tagging efficiency calculation was implemented in GoAT.

The idea behind this method is to find the function $f_i(t)$ that describes the background rate in the i-th tagger channel at a given time t. Since most of this background comes from the activation of parts of the tagger, one can assume that:

$$f_i(t) = b_i + a_i e^{-\Delta_i t}, \tag{6.3}$$

where Δ_i is the decay constant, and a_i and b_i are two factors. Due to the homogeneity in the tagger structure, the decay constant can be safely assumed to be the same for every tagger channel $\Delta_i \equiv \Delta$. To determine it, the background rate averaged over tagger channels was plotted as function of the time passed after the starting of the first background measurement, and this distribution was fitted using the function in Eq. (6.3). The result is visible in Fig. 6.2a. To determine the two factors a_i and b_i, the same distribution was calculated using the background rate in each tagger channel, and the same fit was repeated with the decay constant Δ fixed to the value found in the fit to the averaged distribution (examples for two different tagger channels are reported in Figs. 6.2b and 6.2c). This allows for a precise calculation of the background rate in the i-th channel at any given time t'. In particular, the tagging efficiency can be now calculated correctly for every scaler read sr as:

$$\epsilon_{tagg}(i, sr) = \frac{N_{PbG}(i, sr)}{N_{e^-}(i, sr) - N_{e^-}^{bkg}(i, sr)}. \tag{6.4}$$

During a tagging efficiency measurement a scaler read occurs every 2 s, so this method can really correct for any time-dependency of the background rate. The final tagging efficiency is the averaged value over all the scaler reads. Figure 6.3 shows a comparison between a tagging efficiency calculated using the old and the new method. In Fig. 6.4 a typical set of tagging efficiency is shown: blue and red are the tagging efficiency for the parallel and perpendicular orientation of the diamond radiator, black is the tagging efficiency for the amorphous one. The last one is almost constant around 34%, while for the diamond radiator the

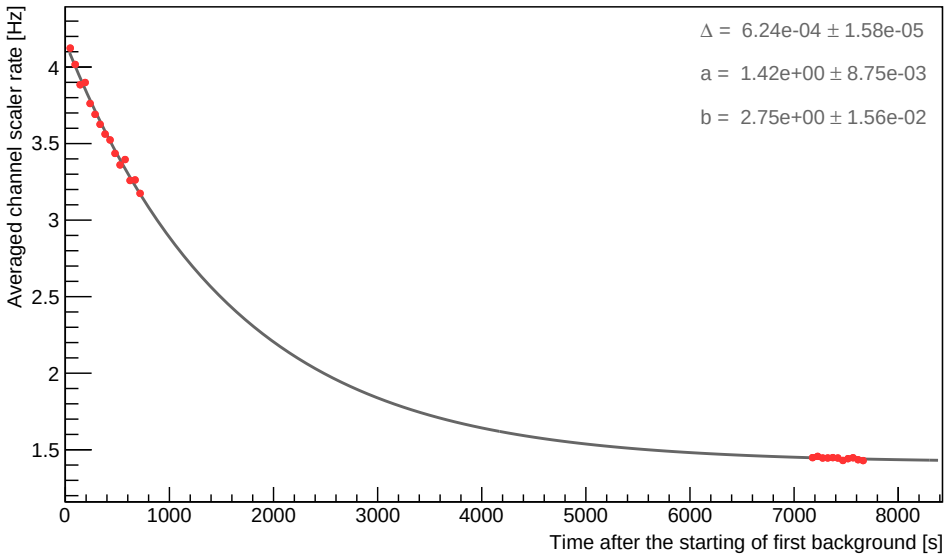

(a) Averaged rate over all tagger channel.

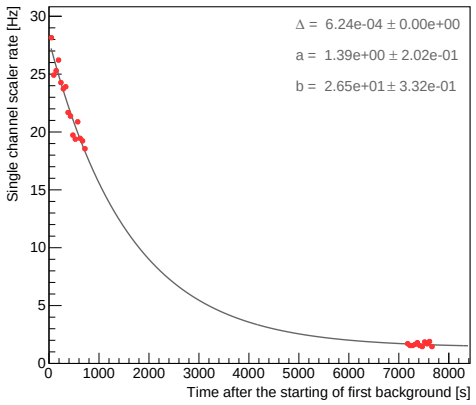

(b) Rate for tagger channel n. 2.

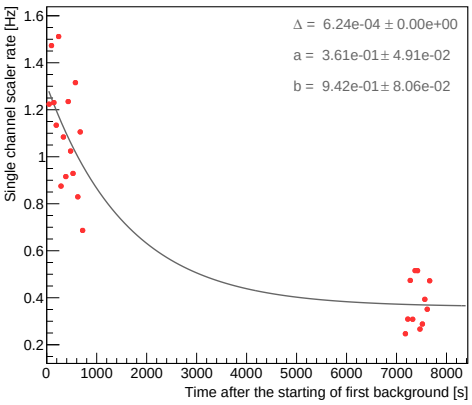

(c) Rate for tagger channel n. 150.

Figure 6.2: Background rate distributions as a function of time after the beam was stopped. (a) Averaged rate over all the tagger channel. The fit is used to determine the decay constant Δ, which is then used in the fit of the single channel distributions. (b) and (c) represent the typical distribution for two different tagger channels at low and high photon energy, respectively. In all the three distributions, the strong exponential decrease of the background in time is clearly visible.

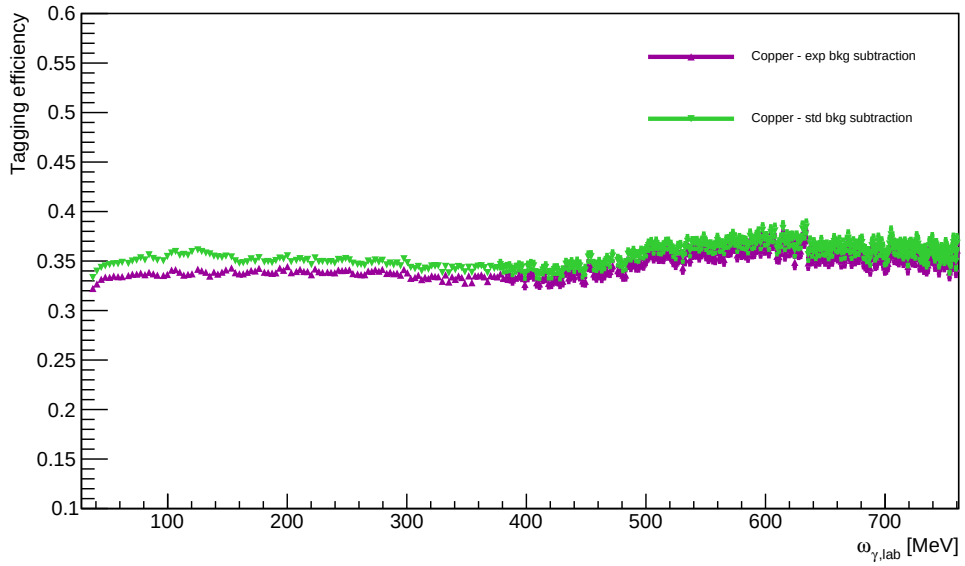

Figure 6.3: Comparison of the same amorphous tagging efficiency run analyzed using the two different methods for the scalers background subtraction. The green tagging efficiency obtained using the "standard" method (Eq. (6.2)) is constantly higher than the magenta one obtained using the new method (Eq. (6.4)).

enhancement due to the coherent peak is clearly visible around 140 MeV.

6.1.1.2 Pair spectrometer

In addition to the daily measurements using the lead glass, it is also possible to have a constant monitoring of the tagging efficiency using the pair spectrometer. Since it is placed behind the collimator in the experimental apparatus (see Section 4.3.3.6), it measures only the beam that is actually impinging on the target. The tagging efficiency using the pair spectrometer can be calculated as:

$$\epsilon_{tagg}^{PS}(i) = \frac{N_{prt}^{PS}(i) - N_{rnd}^{PS}(i)}{N_{e^-}(i)} \frac{1}{\epsilon_{PS}(i)}, \tag{6.5}$$

where $N_{prt}^{PS}(i)$ and $N_{rnd}^{PS}(i)$ are the number of hits in the i-th tagger channel with an associated trigger in the pair spectrometer that can be correlated (*prompt*) or uncorrelated (*random*) in time, respectively, and $N_{e^-}(i)$ is the number of electrons registered in the tagger scaler for that given channel. $\epsilon_{PS}(i)$ is the intrinsic pair spectrometer efficiency and it depends on the thickness of the scattering foil and on the incoming photon energy, hence its tagger channel dependency.

The intrinsic pair spectrometer efficiency ϵ_{PS} of Eq. (6.5) can ideally be calculated. It depends on the thickness of the scattering foil, the energy dependent

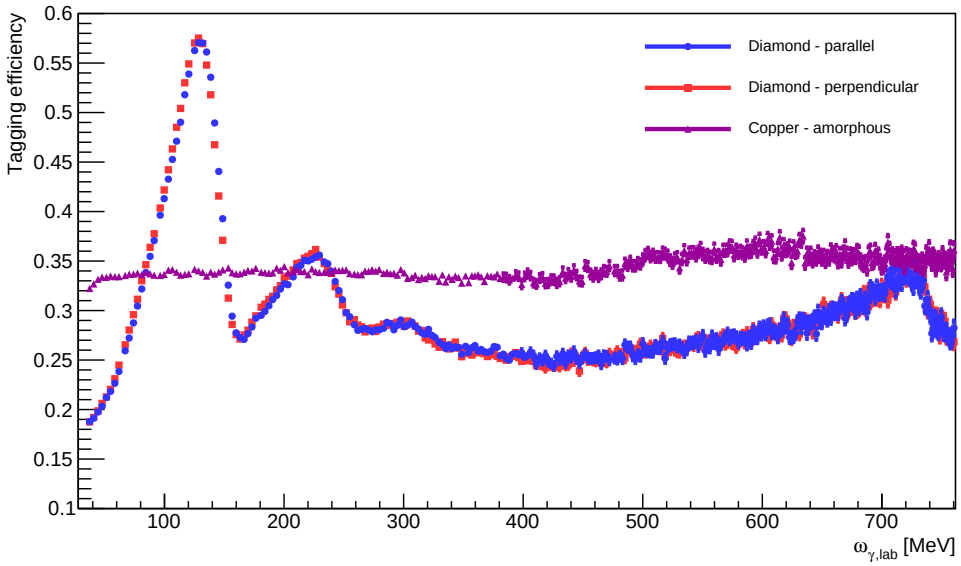

Figure 6.4: Example of a typical tagging efficiency set. Blue circles and red squares are the polarized tagging efficiencies as functions of the photon energy for the parallel and the perpendicular orientation of the diamond radiator, respectively. The unpolarized tagging efficiency obtained using the amorphous radiator is shown in magenta triangles.

cross-section for e^+e^- pair production, the dimension and the detection efficiency of the detector as well as on the magnetic field of the bending magnet. The first two parameters give the pair conversion rate $R(\omega_\gamma)$ at the scattering foil as

$$R(\omega_\gamma) = 1 - \frac{\Phi(x)}{\Phi_0} = 1 - \exp\left[-\mu(\omega_\gamma)x\right], \tag{6.6}$$

where x is the thickness of the scattering foil, Φ_0 and $\Phi(x)$ are the incident and the outgoing photon flux, respectively. The attenuation coefficient $\mu(\omega_\gamma)$ is given by:

$$\mu(\omega_\gamma) = \sigma_{e^+e^-}(\omega_\gamma)\frac{\rho N_A}{A}, \tag{6.7}$$

where $\sigma_{e^+e^-}(\omega_\gamma)$ is the e^+e^- photoproduction cross-section, N_A is the Avogadro constant, ρ and A are the density and the atomic mass of the scattering foil (molybdenum in this case). Unfortunately, the detector parameters — such as efficiency and magnetic field map — depend on many variables and cannot be calculated precisely in an easy way. Therefore, the intrinsic pair spectrometer efficiency was determined experimentally, exploiting the fact that the tagging efficiencies obtained with the lead glass detector and the pair spectrometer should be exactly equal for the same tagging efficiency run. Imposing $\epsilon^{PS}_{tagg}(i) = \epsilon_{tagg}(i)$,

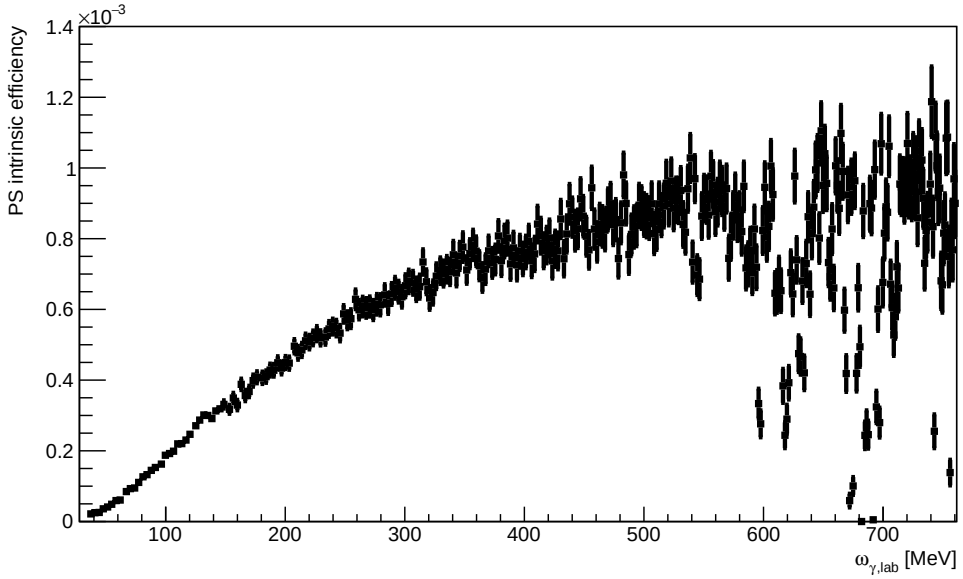

Figure 6.5: Average intrinsic pair spectrometer efficiency as function of the photon energy.

since the denominator is the same for both the tagging efficiency method, one can easily find the relation:

$$\epsilon_{PS}(i) = \frac{N^{PS}_{prt}(i) - N^{PS}_{rnd}(i)}{N_{PbG}(i)} \frac{1}{\epsilon_{tagg}(1)}. \tag{6.8}$$

Equation (6.8) could ideally be used to calculate the intrinsic pair spectrometer efficiency for each tagging efficiency run. Nevertheless, the scattering foil of the pair spectrometer was chosen as thin as possible, in order to not interfere with the photon beam, and during the tagging efficiency measurement the photon flux is kept very low in order to avoid pile up in the lead glass and to have a 100% efficiency in photon detection. The combination of these two factors causes the rate in the pair spectrometer to be extremely low, so to maximize the precision of the intrinsic pair spectrometer efficiency all the tagging efficiency runs were summed together and one single averaged value $\bar{\epsilon}_{PS}(i)$ was obtained per each tagger channel. The results are reported in Fig. 6.5 as a function of the photon energy. This approximation is valid under the reasonable assumption that the intrinsic pair spectrometer efficiency does not depend on the radiator used and it is constant over time for the duration of the beamtime.

The averaged intrinsic efficiency $\bar{\epsilon}_{PS}(i)$ was then used to extract the pair spectrometer tagging efficiency for each data production run. An example of three pair spectrometer tagging efficiencies, one for each different radiator setting,

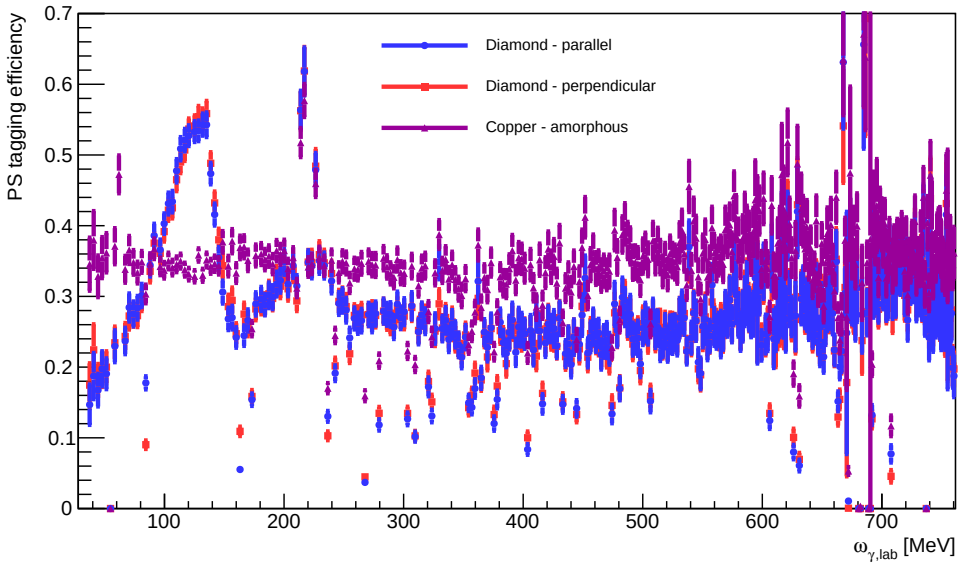

Figure 6.6: Example of three typical tagging efficiencies extracted from normal data runs using the pair spectrometer. Blue circles and red squares are extracted from two diamond runs with parallel and the perpendicular orientation, respectively. The magenta triangles show an amorphous tagging efficiency extracted from a run with the copper radiator.

can be seen in Fig. 6.6. Ideally, these tagging efficiencies could be directly used in Eq. (6.1) to calculate the photon flux run-by-run. Unfortunately this would lead to an imprecise result due to the poor statistics of these tagging efficiency measurements. Instead, the information from the pair spectrometer and the lead glass could be combined to get the best photon flux estimation possible.

6.1.2 Photon flux correction

The pair spectrometer tagging efficiency distributions in Fig. 6.6 fluctuate too much to be directly applied to the data. By comparing them with the lead glass tagging efficiencies in Fig. 6.4, it is clear that especially at high energy the pair spectrometer results are not fully reliable. This is probably due to a not perfect hardware timing coincidence between the tagger spectrometer and the pair spectrometer. For this reason, for the current analysis only the lead glass tagging efficiencies were used.

Figure 6.7 shows all the different lead glass tagging efficiencies — from now on, unless otherwise specified, all the tagging efficiencies have to be intended as measured with the lead glass. The nice agreement among the different sets is an indication of the excellent beam stability throughout the experiment, nevertheless

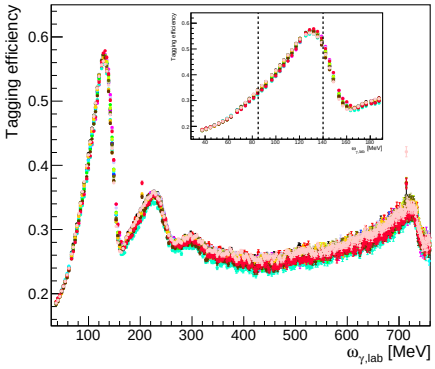

(a) March 2018 beamtime, diamond radiator with parallel orientation.

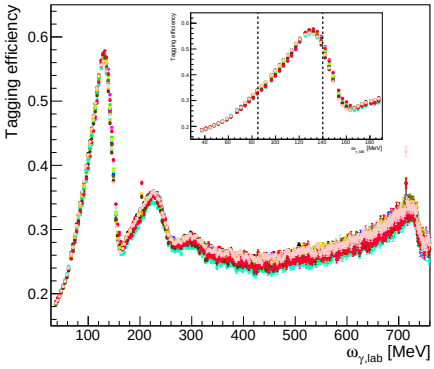

(b) July 2018 beamtime, diamond radiator with parallel orientation.

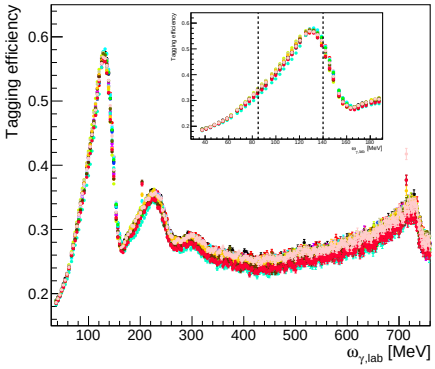

(c) March 2018 beamtime, diamond radiator with perpendicular orientation.

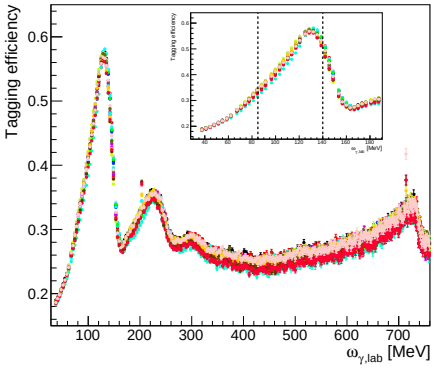

(d) July 2018 beamtime, diamond radiator with perpendicular orientation.

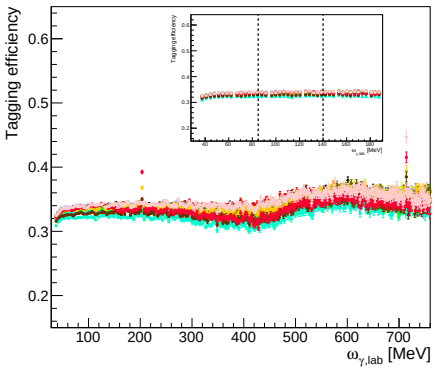

(e) March 2018 beamtime, amorphous radiator.

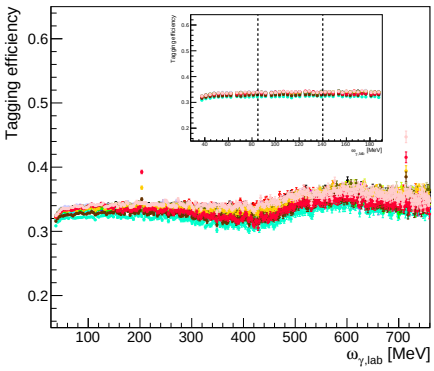

(f) July 2018 beamtime, amorphous radiator.

Figure 6.7: All the tagging efficiencies collected for this experiment in the March and in the July data taking period on the left and on the right, respectively. They are plotted separately for the three different radiator settings: (a) and (b) diamond in the parallel orientation, (c) and (d) diamond in perpendicular orientation, (e) and (f) copper radiator. Different colors correspond to different tagging efficiency sets. In the small canvas, the energy region around the coherent peak, that is also the one of interest for this analysis, is shown.

a $\sim 2\%$ absolute variation is still visible in the peak region. This is a normal fluctuation that can occur during a long experiment, and it is important to select for each production run the tagging efficiency that best represents the flux situation at that moment. In the analyses of the A2 Collaboration, the standard procedure is to select for each production run the tagging efficiency set right after in time. This is a valid approach since a beam optimization is generally performed once per day after the tagging efficiency measurement and, if the beam turns out in a slightly different position after the optimization, the tagging efficiency can be affected by it. On the other hand, it could happen that a second beam optimization was required or that the beam slightly drifted by itself during the day. These changes can affect the tagging efficiency and so the next measurement in time will no longer be the best choice. To correct for this, an improved method was implemented for this analysis, based on the fact that the best choice for each production run is the tagging efficiency with the same, or closest, tagger scaler distribution. This is particularly true for the linearly polarized data, where a small shift in the beam, and so in the coherent edge position, can cause a big shift in the tagging efficiency, and so in the photon flux.

The procedure to find the tagging efficiency set that best represent each production run can be described step-by-step as:

- for each diamond tagging efficiency run, the enhancement in the tagger scaler distribution due to the linear polarization is fitted to find the exact position of the coherent edge. This procedure is described in Section 6.2;
- this fit is done every 100 scaler reads, giving about 8 edge positions per run. The weighted average of these edge positions gives the final coherent edge position for each tagging efficiency run;
- a similar analysis is performed for the data taking runs;
- for each production run, the tagging efficiency(ies) with the same coherent edge position (± 0.5 MeV) is (are) selected. If more than one matching tagging efficiency is found, the closest one in time is selected, and the tagger scalers for that specific production run are corrected using Eq. (6.1);
- if no matching tagging efficiencies are found, this happens for the $\sim 5\%$ of the runs, the tagging efficiency next in time is used, as for the standard procedure.

This method has the drawback of not taking into account possible changes in the magnitude of the tagging efficiency during the beamtime. In fact, it selects the

best tagging efficiency set for each production run just based on the coherent edge position. The best way to correct for this would be to use the pair spectrometer information. It would allow for finding an overall scaling factor to adjust the magnitude of the chosen tagging efficiency set to the one at the moment when the data production run was taken. The scaling factor can be simply defined as

$$S = \frac{\bar{\epsilon}^{PS}_{tagg}(k)}{\bar{\epsilon}^{sel}_{tagg}}, \tag{6.9}$$

where $\bar{\epsilon}^{PS}_{tagg}(k)$ is the average over all the tagger channels of the pair spectrometer tagging efficiency for the k-th production run, and $\bar{\epsilon}^{sel}_{tagg}$ is the average over all the tagger channels of the lead glass tagging efficiency for the selected set. Unfortunately, as it can be seen in Fig. 6.8, this scaling factor seems to be systematically lower than 1, meaning that the pair spectrometer tagging efficiency is systematically smaller than the selected tagging efficiency. A possible explanation could be that the real intrinsic pair spectrometer efficiency $\epsilon_{PS}(i)$ (defined in Eq. (6.8)) is lower than what we extracted. We calculated it using the tagging efficiency runs as the ratio between the pair spectrometer and the lead glass signals, so with an extremely low beam intensity. On the other hand, during the data taking a high intensity photon beam was used to maximize the statistics, and it is possible than the pair spectrometer efficiency is intensity dependent. Since it was not possible to model this dependency, and to find an intensity-dependent correction factor for the intrinsic pair spectrometer efficiency, this scaling factor was not applied for the rest of the analysis. A systematic study of this new method together with a comparison with the standard method can be found in Section 8.1.2.

6.2 Determination of the photon linear polarization

The linearly polarized photon beam used in this experiment was produced via coherent bremsstrahlung on the diamond radiator as explained in detail in Section 4.2. Two different polarization settings were used — parallel (para) and perpendicular (perp) — whose polarization planes are separated by 90°. The degree of linear polarization, essential to extract the beam asymmetry Σ_3, is a complex function of photon energy and crystal structure and it can be extracted from data. For this analysis, a fitting routine described in Ref. [133] was used for this purpose.

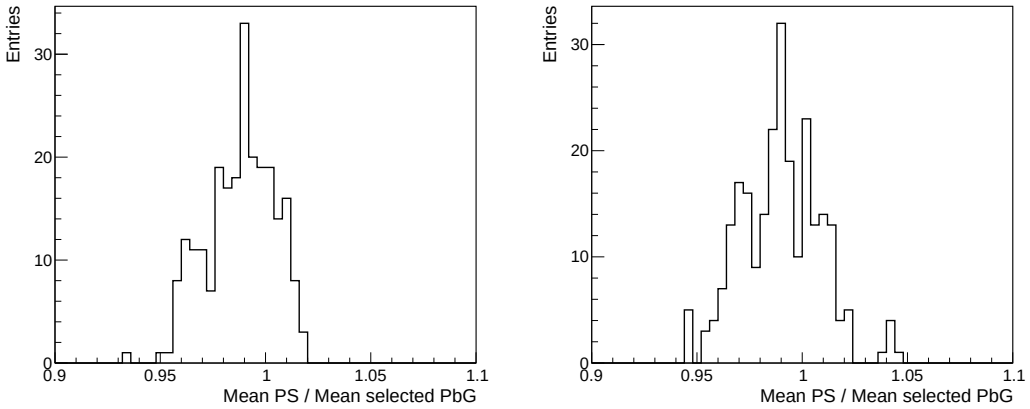

(a) Parallel. (b) Perpendicular.

Figure 6.8: Distribution of the pair spectrometer scaling factor to correct the tagging efficiency magnitude for a sample of the total dataset obtained with the two orientations of the diamond radiator.

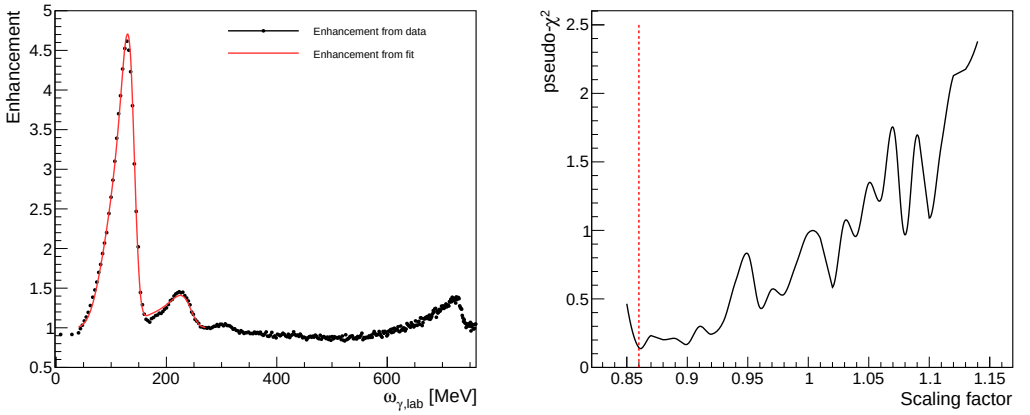

(a) Enhancement fit distribution. (b) Pseudo-χ^2 distribution.

Figure 6.9: Fit of the enhancement together with the pseudo-χ^2 distribution as function of the scaling factor. The red dotted line indicates the scaling factor corresponding to the minimum pseudo-χ^2.

The degree of linear polarization was determined once per day using the tagging efficiency measurement described in Section 6.1.1.1. For each tagging efficiency set, an enhancement R can be calculated for both the parallel and the perpendicular polarization setting as:

$$R(i) = \frac{N_{e^-}^{\text{para(perp)}}(i)}{N_{e^-}^{\text{amo}}(i)}, \tag{6.10}$$

where $N_{e^-}^{\text{para(perp)}}(i)$ and $N_{e^-}^{\text{amo}}(i)$ are the number of electrons registered in the tagger scaler for the i-th channel using the diamond parallel (perpendicular) configuration and the copper radiator, respectively. An example of the enhancement distribution can be found in Fig. 4.6. The shape of the enhancement distribution is directly related to the position of the coherent edge x_d introduced in Eq. (4.15), which is strongly sensitive to small variation in how the beam hits the diamond lattice structure. For this reason, the enhancement distribution can slightly vary from tagging efficiency to tagging efficiency.

Each enhancement distribution is then fitted using the fitting routine. It attempts to model the coherent contribution from the two primary reciprocal lattice vectors — [022] and [044] introduced in Section 4.2.3 — using some experimental parameters, such as incident electron beam energy, collimator diameter as well as its distance to the radiator, as fixed input. The enhancement distribution is then normalized to 1 in an energy region where there should be no contribution from the coherent part, and it is finally fitted using a MINUIT minimization function. A Gaussian smearing accounts for the parameters which cannot be easily measured, such as beam divergency and multiple scattering in the radiator. The parameters of the smear are determined by the fit to the data. This fit is repeated 20 times by slightly changing the overall scaling of the enhancement distribution, and the results of the fit with the best χ^2 are saved. This accounts for an imperfect normalization of the enhancement distribution and helps to keep the systematic errors as low as possible. An example of a fit to the coherent enhancement distribution obtained from a tagging efficiency run and the χ^2 distribution as function of the scaling factor, are reported in Fig. 6.9. A complete description of this method can be found in Ref. [133].

Using the output parameters from the fit, it is possible to determine the degree of linear polarization (see Eq. (4.19)). It is important to note that the degree of linear polarization distribution is dependent on the position of the coherent edge. Nevertheless, once an enhancement is fitted the degree of linear polarization can be calculated for any given coherent edge position. Figure 6.10a

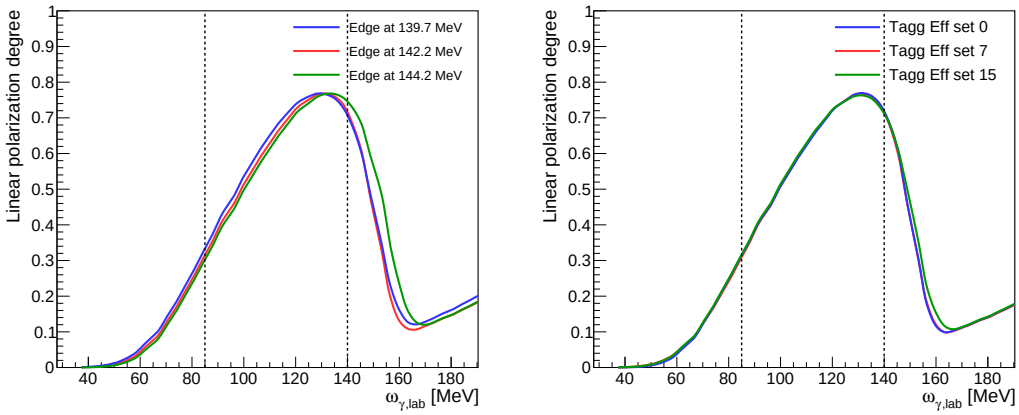

(a) Same tagging efficiency, different edge position.

(b) Same edge position, different tagging efficiencies.

Figure 6.10: Example of distributions of the degree of linear polarization for different coherent edge positions and different tagging efficiency sets.

shows the degree of linear polarization as function of the photon energy for three different positions of the coherent edge, using the same tagging efficiency set. On the other hand, for a given fixed coherent edge position, the polarization distribution is relatively independent of the tagging efficiency set used to produce it, as shown in Fig. 6.10b. During the data taking, the coherent edge position was conveniently set at 141 MeV. As already explained, it is sensitive to small variations in how the beam hits the diamond radiator, and so it is normal that the coherent edge position slightly varies during the beamtime. Figure 6.11 shows the edge position distribution for about half of the full dataset for the parallel and perpendicular runs, respectively. For a precise determination of the degree of linear polarization, during the analysis the enhancement distribution is fitted every 1000 events and the coherent edge position is determined. To create the enhancement distribution using Eq. (6.10), the incoherent contribution has to be known. For this reason, two 30 minutes runs with the copper radiator were collected each day. For each polarized run, the amorphous run after in time was used as incoherent normalization to create the enhancement for the determination of the edge position, and this information was used for a precise calculation of the degree of linear polarization using the fitting parameters extracted from the tagging efficiency set after in time. This method allows for best control of possible systematic errors in the extraction of the degree of linear polarization. Despite this, different sources of error are still present, such as approximations in the function used for modeling the enhancement and in the fit for the determination of the coherent edge position, or errors due to the choice of the tagging efficiency

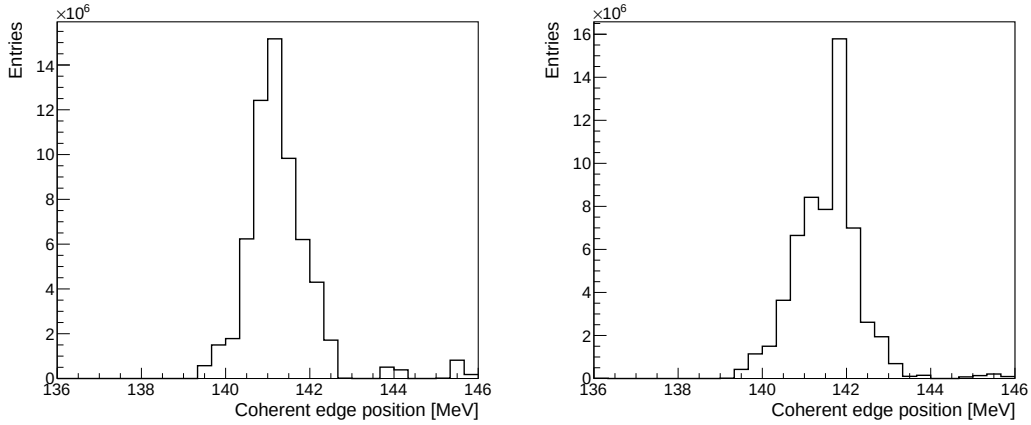

(a) Parallel. (b) Perpendicular.

Figure 6.11: Distribution of the coherent edge position for a sample of the total dataset obtained with the two orientations of the diamond radiator.

sets used for the extraction of the fit parameters. For this reason, as intensively studied in Ref. [97] and also confirmed by Ken Livingston [134], a systematic uncertainty of 5% should be considered for the degree of linear polarization.

Chapter 7

Data analysis

This chapter is devoted to the analysis procedure performed to select the final sample of events used for the extraction of the unpolarized proton Compton scattering cross-section and the beam asymmetry Σ_3. The analysis was performed using some of the classes already present in GoAT together with a few additional ones specifically written for this work.

In the first section, a short description of the beamtimes forming the data sample used for this work is given. In the second section, the procedure for the selection of Compton events is described with a particular focus on the missing mass studies. The third section will be devoted to the subtraction of the contribution from the empty target. In the last part, the Monte Carlo simulation used to estimate the detection and reconstruction efficiency is discussed.

7.1 Datasets

The data used for this experiment were collected in two three-week beamtimes in March and July 2018. The experimental conditions were kept identical in both periods, in order to assure a one to one comparison between the results. An unpolarized electron beam with a nominal energy of 883 MeV was provided by MAMI with a beam current of 3 nA or 9 nA when using the diamond or amorphous radiator, respectively. Even though it would be ideal to use a beam current as high as the accelerator can deliver, this value has to be carefully chosen as a compromise among many different factors: the performance of the DAQ, the deadtime of the single CPUs, the time resolution of the detectors and of course the need to collect as much data in the shortest time possible. Furthermore, the choice of a different electron beam current based on the type of radiator used is due to the differences in the Bremsstrahlung distribution between the unpolarized and

Table 7.1: Overview of the data collected in the two different beamtimes used in this dissertation.

Beamtime	**# runs**	**hours**	**radiator**	**target**
March 2018	409	240	Diamond	Full
	140	105	Diamond	Empty
	32	32	Copper	Full
	7	7	Copper	Empty
July 2018	352	205	Diamond	Full
	135	100	Diamond	Empty
	20	20	Copper	Full
	7	7	Copper	Empty

the polarized cases, as well as to the different tagging efficiencies. As previously discussed (see Figs. 4.8 and 6.4), the use of a crystalline radiator can enhance the number of produced photons, and their probability to pass the collimator. For the same electron beam current, the photon flux at the target when using an amorphous radiator is much lower compared to the diamond case. The two values of electron beam current were chosen to result in similar trigger rates in the CB. An overview of the data collected in the two beamtimes is reported in Table 7.1.

Two additional beamtimes were completed for this experiment, but unfortunately the data cannot be used due to major issues in the apparatus. A two-week long beamtime was done in December 2017. This was the first data taking period ever with the new tagging spectrometer and it was extremely useful to study the new detector. On the other hand, almost half of the CB channels were not triggering properly due to a problem in the front-end electronics. This is an issue in particular for a Compton analysis, where the majority of the events have one single cluster in the CB caused by the photon. When the photon ended up in one of the non-triggering crystals, the event was completely lost. This is evident when looking at the angular distribution of the single cluster events in the CB in Fig. 7.1. The central spot without events are the non-triggering channels. The relatively large number of the problematic channels makes it very difficult to use this data for a precise measurement of an unpolarized cross-section, therefore it was decided to not include those data in this dissertation nor in the final results. A shorter one-week beamtime was done in February 2018, after the triggering problem was solved. Unfortunately, in this new data taking period there

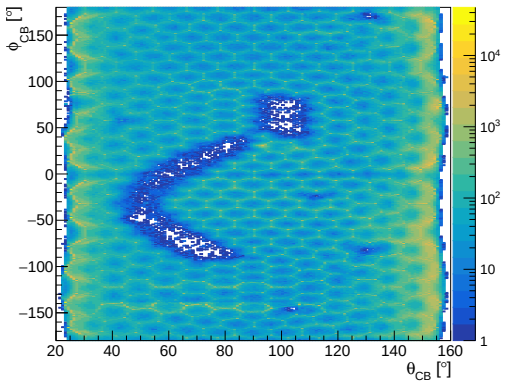

Figure 7.1: Sample of the angular distribution in the CB of single cluster events from the two-week beamtime in December 2017. The hole due to the non-triggering channel is clearly visible in the central region.

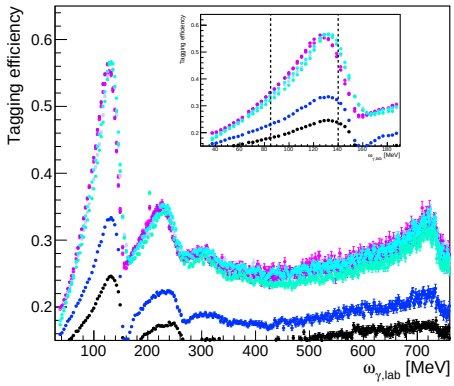

Figure 7.2: Example of tagging efficiencies collected during the February 2018 beamtime. The disagreement among the different runs is clearly evident. In the small canvas, the energy region around the coherent peak, which is also the one of interest for this analysis, is shown.

were issues with the tagger electronic modules during the tagging efficiency runs. In particular, the integral of both scalers and TDC hits for some scaler reads dropped to zero. This caused most of the tagging efficiencies from this beamtime to be completely off, as visible in Fig. 7.2 if compared to the good data shown in Fig. 6.7. As explained in Section 6.1, a reliable tagging efficiency is essential for a correct calculation of the photon flux and therefore also for a precise measurement of a cross-section. Considering also that this is just a small part of the full data sample, it was decided not to include this data in the analysis nor in the final results.

As reported in Table 7.1, the total data sample used for this thesis is composed of 821 runs with full target and 287 with empty target, corresponding to more than 700 hours of actual data taking. These data comprise more than 4.3 billions events, that were analyzed to select just the Compton scattering ones in the relevant kinematic region.

7.2 Event selection

The final goal of this experiment is to provide a high-precision Compton scattering dataset best suited for the extraction of the two proton scalar polarizabilities α_{E1} and β_{M1} by measuring the unpolarized proton Compton scattering cross-section

and the beam asymmetry Σ_3. To select the desired reaction $\gamma\vec{p} \to \gamma p$ and to reduce the background as much as possible a strict event selection was applied. The selection criteria applied are:

- one single neutral cluster in the CB in the final state;
- a time coincidence between the cluster in CB and the electron in the tagging spectrometer $\Delta t = \pm 3$ ns;
- an incoming beam energy $\omega_\gamma = 86.3 - 140.4$ MeV;
- a Compton missing mass $M_{miss} = 920 - 955$ MeV.

These criteria were carefully studied using both data and Compton scattering Monte Carlo simulations. The effects of small changes in any of them are discussed in Sections 8.1 and 9.1.

7.2.1 Number of particles in the final state

Two particles are present in the final state of proton Compton scattering: one charged, the recoil proton, and one neutral, the scattered photon. In the energy region of interest for this work $\omega_\gamma \lesssim 150$, the recoil proton never has enough momentum to exit the liquid H_2 target, and therefore is not detectable in our apparatus. Due to this, for this analysis only events with one neutral particle were considered. A neutral particle is defined as a cluster in the CB without any associated hits either in the PID or in the MWPCs. Figure 7.3 shows the distribution of the number of reconstructed particles in a Compton scattering Monte Carlo simulation. The vast majority of events (98%) have exactly one particle in the final state, showing the validity of the applied selection. In an almost negligible amount of events (1.8%), there are more than one reconstructed tracks, and this is probably due to a wrong cluster reconstruction, giving additional clusters — mainly two — instead of a single one. Since these split Compton events are difficult to disentangle from π^0 decays, which result in two photons, it was not possible to recover such events. Instead, it was decided to account for them in the Monte Carlo efficiency correction (see Section 7.4).

7.2.2 Photon tagging

The incident photon energy ω_γ is inferred from the energy E_{tagg} of the electron detected in the tagging spectrometer. This process is complicated by the relatively high electron beam current, which results in an average of 140 electrons detected

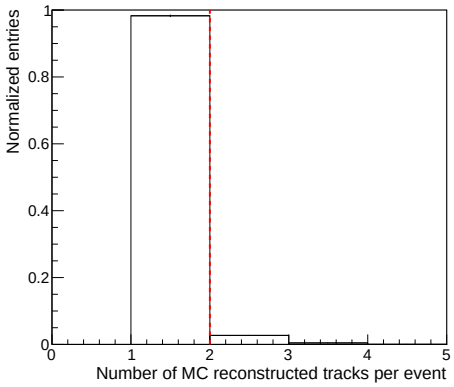

Figure 7.3: Number of reconstructed Monte Carlo tracks per event. The red dashed line indicates the selection used in the analysis.

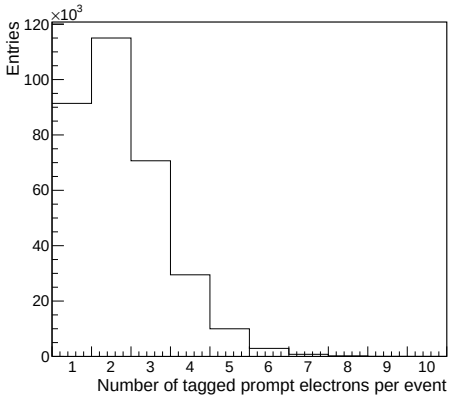

Figure 7.4: Example of the distribution of the number of prompt tagged electrons per event. In most of the events more than one prompt electron is registered, making it necessary to perform a random timing background subtraction.

within the same trigger window. For each selected event, the time difference Δt between each hit in the tagger and the neutral cluster in CB was calculated. A typical time distribution, shown in Fig. 7.5, has a sharp peak around zero, known as a "prompt peak", on top of a flat background distribution. An electron was considered linked to the event if the time difference $\Delta t_p \in [-3, 3]$ ns, and these events are known as "prompt" events. The energies of these electrons are used to infer the energy of the incident photon. On the other hand, the prompt window also includes the background underneath the peak, which is associated with random electrons. In particular, Fig. 7.4 shows that in most of the events more than one prompt electron is found. To model this random contribution within the prompt region and enable its subtraction, two random samples were defined: one on the left $\Delta t_{r1} \in [-180, -80]$ ns and one on the right $\Delta t_{r2} \in [100, 500]$ ns of the prompt peak. In Fig. 7.5, the prompt and random time regions are shown in green and gray, respectively. It is important to note that the number of random coincidences in the tagger spectrometer is higher in the first channels, the ones associated with low electron energy. This is due to the typical shape of the bremsstrahlung distribution. It is visible in the comparison between the two time distributions shown in Fig. 7.6, representing the hits from the first and the last tagger channel included in this analysis, respectively. In the latter the prompt/random ratio is ~ 0.70, while in the former it is ~ 0.87.

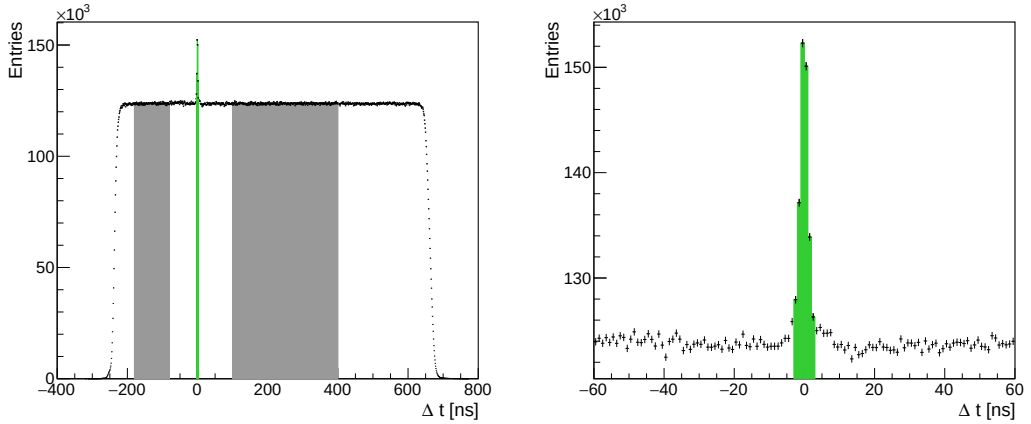

(a) Full time window. (b) Zoom around the prompt peak.

Figure 7.5: Sample of the time difference distribution between each hit in the tagger and the scattered photons in the CB. In the left panel, the full time interval registered by the tagger TDCs is shown. On the right, the distribution is zoomed around the prompt peak. The random sample and the prompt peak are shown in gray and green, respectively.

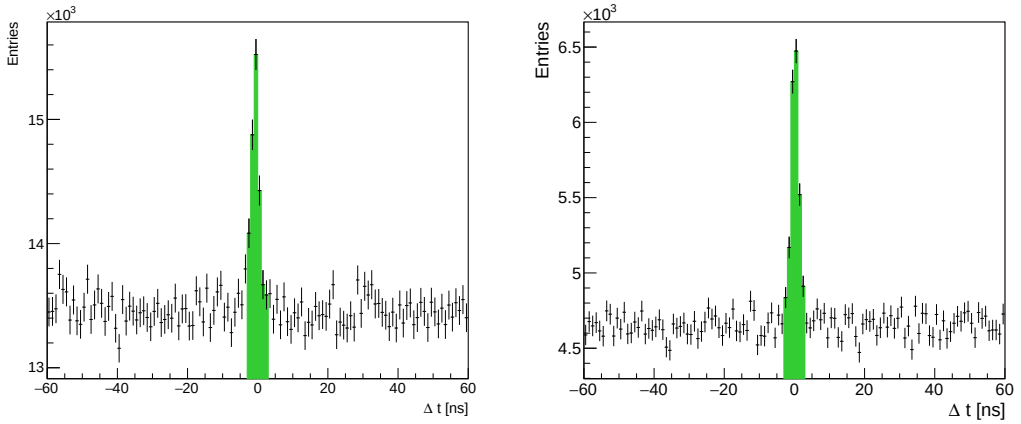

(a) Time distribution for tagger ch. 14. (b) Time distribution for tagger ch. 28.

Figure 7.6: Example of the time distribution for the scattered photons using only the first (left) and the last (right) tagger channels included in the analysis. The differences in the prompt over background ratio is visible.

7.2.3 Beam energy

As discussed in the theoretical introduction to this dissertation (see Section 2.1.2), the Compton scattering cross-section starts to be sensitive to the proton internal structure, and so to the scalar polarizabilities, at an incoming photon energy $\omega_\gamma \sim 60$ MeV, and this sensitivity increases with the energy. Unfortunately, as ω_γ reaches the threshold for pion photoproduction, the spin polarizabilities start to play a role in the description of Compton scattering, making it more difficult to disentangle the non-spin dependent contribution. On the other hand, due to experimental constraints such as the high level of random coincidences in the tagger spectrometer and the presence of an unknown source of low-energetic background (explained later in Section 8.1.5), it was not possible to precisely measure either the unpolarized cross-section or the beam asymmetry Σ_3 at incoming photon energies $\omega_\gamma < 85$ MeV. For these reasons, despite the fact that the tagger spectrometer can cover a photon energy range $\omega_\gamma = 35.8 - 760.9$ MeV, a much smaller range $\omega_\gamma = 86.3 - 140.4$ MeV was used for this analysis. In this incoming photon energy region, each tagger channel is ~ 3.4 MeV wide giving a total of 15 tagger channels in the selected energy range. These 15 channels were equally divide in 5 energy bins: $\omega_\gamma = 86.3 - 98.2$ MeV, $\omega_\gamma = 98.1 - 108.4$ MeV, $\omega_\gamma = 108.5 - 118.7$ MeV, $\omega_\gamma = 118.7 - 130.2$ MeV, and $\omega_\gamma = 130.3 - 140.4$ MeV.

7.2.4 Missing mass

In Compton scattering, the initial state can be defined as the sum of the incident photon's and target proton's four momenta k and q, respectively. The final state can be similarly defined as the sum of the scattered photon's and recoil proton's four momenta k' and q', respectively. Energy and momentum conservation for the reaction requires

$$k + q = k' + q'. \tag{7.1}$$

The energy of the incoming photon ω_γ is inferred using the tagging technique, while the free protons of the target have negligible momenta and can be assumed to be at rest. Therefore, the left term in Eq. (7.1) is fully determined. At these energies, as already explained, it was not possible to detect the recoil proton and so its four momentum cannot be measured. By defining it as "missing four-momentum" $q' \equiv P_{miss}$, Eq. (7.1) can be rearranged as

$$P_{miss} = k + q - k'. \tag{7.2}$$

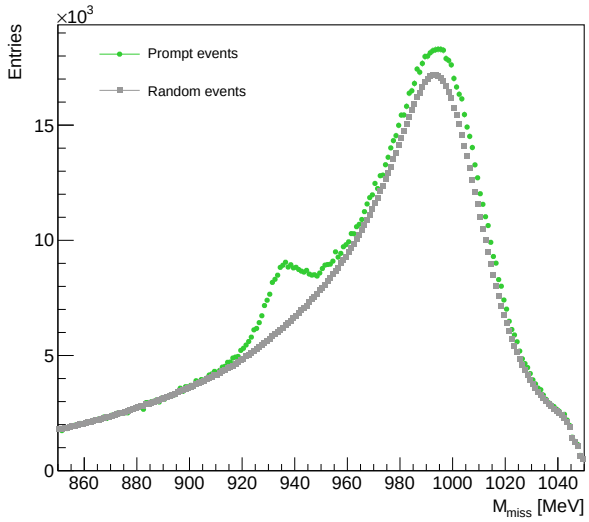

(a) Events from the prompt and random windows.

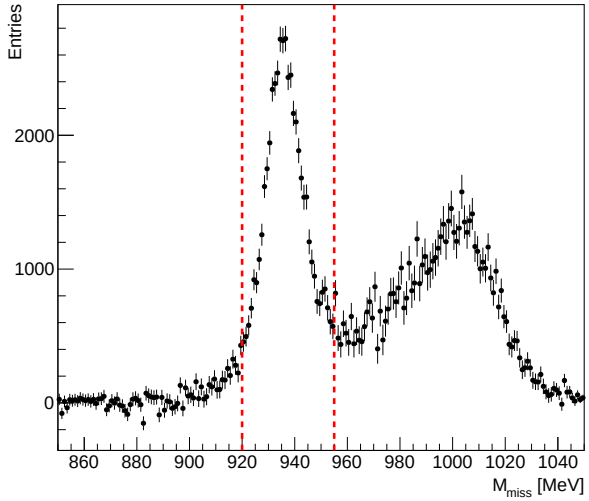

(b) Events from the prompt peak after the subtraction of the random contribution.

Figure 7.7: Example of the missing mass distribution using events from the prompt and random time windows in green and gray, respectively. The prompt and random distributions are scaled accordingly to the size of the time windows defined in Section 7.2.2. The Compton missing mass peak centered at the proton mass is clearly visible. On the right, the missing mass distribution is shown after subtracting the prompt and the random components. The red dotted lines show the missing mass selection applied in the analysis. The additional background contribution on the right of the distribution does not come from the liquid hydrogen inside the target and it is subtracted later in the analysis.

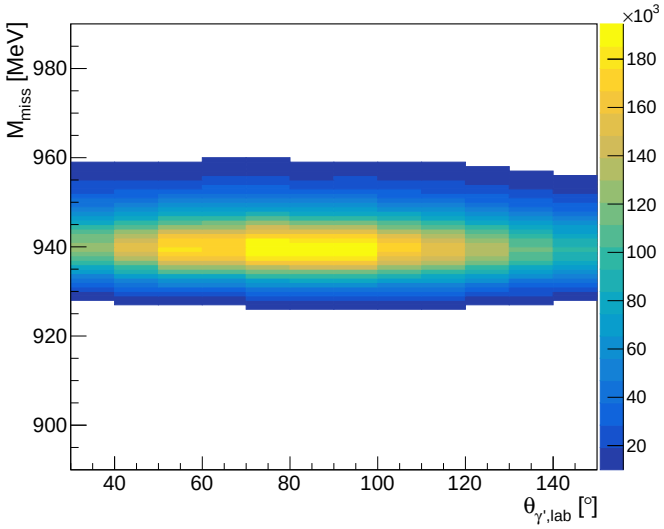

Figure 7.8: Simulated Monte Carlo missing mass distribution as function of the scattering angle $\theta_{\gamma'}$. The missing mass distribution peaks around the proton mass value.

Consequently, a "missing mass" can be defined as $M_{miss} = \sqrt{E_{miss}^2 - \vec{P}_{miss}^2}$. If the missing particle is the recoil proton, M_{miss} should be equal to the proton mass m_p:

$$M_{miss} = \sqrt{(\omega_\gamma + m_p - \omega_{\gamma'})^2 - (\vec{k} - \vec{k}')^2} \equiv m_p = 938.27 \text{ MeV}. \tag{7.3}$$

Due to the detector resolution, the experimental missing mass in real data is a Gaussian distribution centered around the proton mass with a tail on the right due to energy losses. The missing mass was calculated for both the prompt and random events and two separate histogram were filled. An example of the missing mass distribution for prompt and random events is shown in Fig. 7.7a in green and gray, respectively. The prompt and random distributions were then subtracted to get the missing mass distribution from only the events in the prompt peak. An example of the subtracted distribution is shown in Fig. 7.7b.

In a two-body reaction, as Compton scattering is, the missing mass provides a powerful variable for the optimization of the event selection and the consequent reduction of the background events. To find the best cut to be applied to the data to select the interesting events, the missing mass distribution on Monte Carlo Compton scattering events was studied. As it is obvious, applying Eq. (7.3) to generated Monte Carlo data would give a δ distribution peaked on the proton mass. For this reason, the interactions of the generated data with the detector apparatus of the A2 Collaboration were simulated using the A2Geant4 software

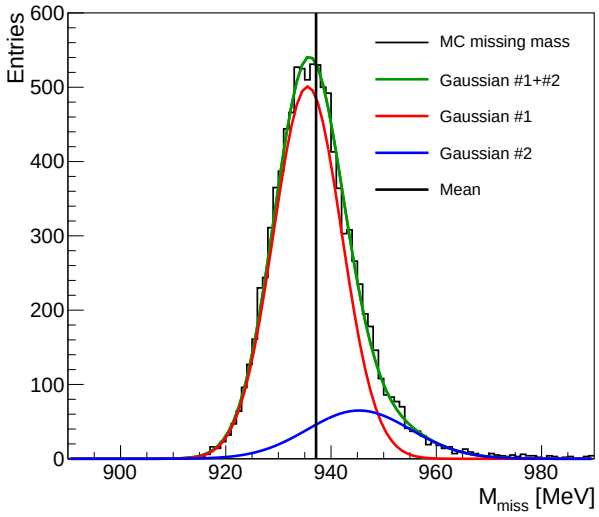

Figure 7.9: Example of the fit to the simulated Monte Carlo missing mass distribution for a given bin in ω_γ and $\theta_{\gamma'}$. The double Gaussian fit function together with the two separate contribution are shown in green, red and blue, respectively. The vertical black line indicates the mean value $\bar{\mu}_i$ calculated using Eq. (7.6).

described in Section 5.1.4. The simulated data were then analyzed using AcquRoot and GoAT as for the real data, and the missing mass was calculated. An example of the simulated missing mass distribution as a function of the scattered angle $\theta_{\gamma'}$ is reported in Fig. 7.8. This distribution was fitted using a double Gaussian function, defined as:

$$f(x) = h\left[e^{-\frac{1}{2}(\frac{x-\mu}{\sigma})} + h' e^{-\frac{1}{2}(\frac{x-\mu-\mu'}{\sigma\sigma'})}\right], \tag{7.4}$$

for different bins in $\theta_{\gamma'}$. In Eq. (7.4), μ', σ' and h' are the relative mean, width and height of the second Gaussian with respect to the first one. The usage of a double Gaussian function allows for a better fit of the tail on the right of the distribution compared to a single Gaussian fit [23]. The fit was performed for the 5 bins in photon beam energy and for 12 bins in the scattering angle range $\theta_{\gamma'} = 30° - 150°$, each 10° wide, yielding 60 bins in total. An example of a fitted distribution can be seen in Fig. 7.9. For every fit a missing mass selection was chosen according to:

$$\bar{\mu}_i - 2.5\bar{\sigma}_i < M_{miss} < \bar{\mu}_i + 2.5\bar{\sigma}_i, \tag{7.5}$$

with

$$\bar{\mu}_i = \mu_i w_{1,i} + \mu'_i w_{2,i} \tag{7.6}$$

$$\bar{\sigma}_i = \sigma_i w_{1,i} + \sigma'_i w_{2,i}, \tag{7.7}$$

where $w_{1(2),i}$ is the weight of the first (second) Gaussian for the i-th bin, and $i = 1, \ldots, 60$ runs over all the energy and angular bins. The weight is defined as the integral of one of the two functions divided by the sum of the two. The average values over all the bins of the lower and upper limits were calculated and they were used for the selection of the Compton events in the analysis of the data. The limit values used are: $M_{miss}^{\min} = 920$ MeV and $M_{miss}^{\max} = 955$ MeV. To make sure that this selection is valid also in the analysis of the real data, the simulated data were carefully calibrated to match the real one, as discussed in Section 7.4.

The missing mass is the main, if not the only, variable on which a cut can reduce the background contamination inside the final Compton scattering sample. While the selection of a narrow range to get a cleaner sample can be beneficial for the measurement of the beam asymmetry Σ_3, it is not a valid approach for the unpolarized cross-section. For a precise measurement of this observable every Compton scattering event should be included in the final sample. While this is not realistic, it is crucial to minimize the possibility of rejecting good events. The final missing mass limits used in the analysis are a compromise between these two different approaches.

7.3 Empty target contribution

The liquid hydrogen used as a pure proton target for this experiment was contained inside a cylindrical target cell made of Teflon, described in Section 4.3.2. The target cell was also surrounded by layers of insulating material used to keep the hydrogen at a temperature of 20 K. All this material produced an additional contribution to the collected data other than the contribution of photon beam interactions on the liquid hydrogen. Additional background could come from the beam photons converting to e^+e^- pairs, as well as from the electron beam dump and other background sources inside the experimental hall. All this unwanted contribution needs to be subtracted out to isolate only the events coming from the liquid hydrogen.

To sample this background, a bit more than one third of the run period was devoted to collecting data using the empty target cell. During these runs, the experimental conditions were set as similar as possible to their state during data taking with a full target. This allows for a one to one comparison between the background contributions in the samples collected using the full and the empty

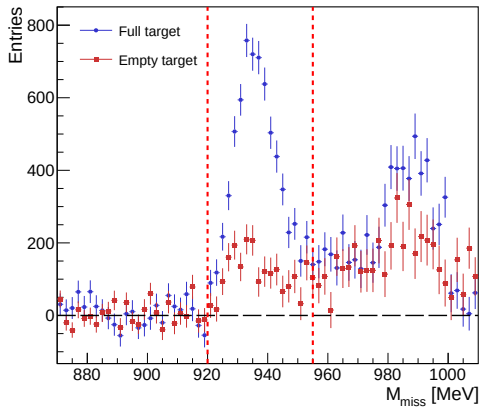

(a) $\theta_{\gamma'} = 55°$.

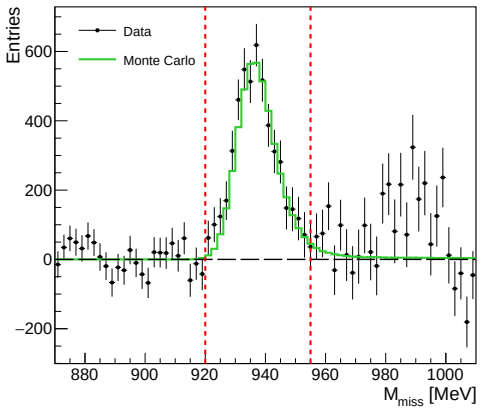

(b) $\theta_{\gamma'} = 55°$.

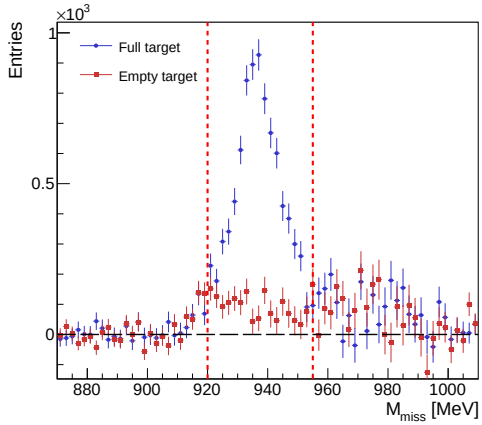

(c) $\theta_{\gamma'} = 85°$.

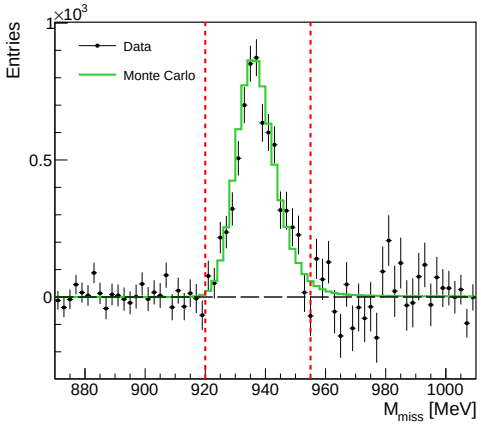

(d) $\theta_{\gamma'} = 85°$.

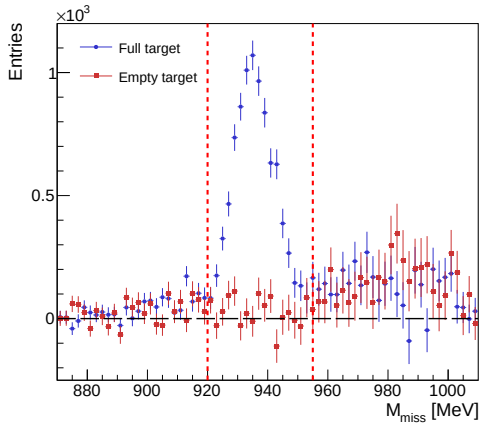

(e) $\theta_{\gamma'} = 135°$.

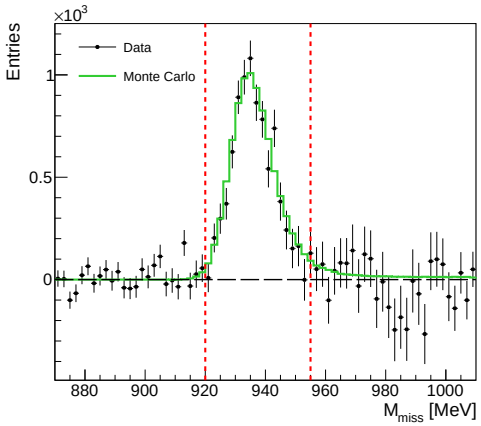

(f) $\theta_{\gamma'} = 135°$.

Figure 7.10: Example of missing mass distributions at three different scattering angles. The left panels show the full and empty target sample distributions in blue and red dots, respectively. The right panels show the empty target subtracted distribution together with the simulated Monte Carlo one, respectively in black and green. In all the panels, the red dashed lines show the selection applied in the analysis.

target cell. The empty target sample was analyzed using the same calibration and event selection described previously. It was then scaled accordingly to the photon beam flux and subtracted from the full target sample. Figure 7.10 shows examples of missing mass distributions for different values of the scattering angles $\theta_{\gamma'}$. Figures 7.10a, 7.10c and 7.10e show the full and empty target contributions separately in red and blue, respectively. The empty target background contribution is relevant and definitely cannot be neglected. It is interesting to note that in the forward region (Fig. 7.10a), the empty target sample seems to underestimate the background contribution on the right of the missing mass peak. The source of this additional background was intensively studied (see Section 8.1.5) without coming to a definite conclusion. Nevertheless, these background events seem to be generated by low energetic neutral particles and so they are excluded from the final sample by the missing mass selection. This is visible in Figs. 7.10b, 7.10d and 7.10f where the missing mass distributions after the empty target subtraction are shown together with the simulated Monte Carlo distribution. The remaining background is visible at $M_{miss} \sim 990$ MeV, well outside the accepted missing mass range given by the two red dashed lines.

7.4 Detection and reconstruction efficiency

The determination of the Compton scattering detection and reconstruction efficiency ϵ_{rec} is crucial for a correct measurement of the unpolarized cross-section. It allows for an estimate of the fraction of events that went undetected or were lost in the analysis process. ϵ_{rec} was calculated starting from a sample of 100 million Monte Carlo generated Compton scattering events. These are simply randomly generated four-momenta of particles in the initial and final state of Compton scattering that were then used to simulate physical interactions within the A2 experimental apparatus, using the A2Geant4 software described in Section 5.1.4. The simulated hits went through the same analysis procedure as the real data. The detection and reconstruction efficiency ϵ_{rec} was calculated as

$$\epsilon_{rec}(\omega_\gamma, \theta^{rec}_{\gamma'}) = \frac{N_{rec}(\omega_\gamma, \theta^{rec}_{\gamma'})}{N_{gen}(\omega_\gamma, \theta^{gen}_{\gamma'})}, \tag{7.8}$$

where $N_{rec}(\omega_\gamma, \theta^{rec}_{\gamma'})$ and $N_{gen}(\omega_\gamma, \theta^{gen}_{\gamma'})$ are the number of reconstructed and generated Compton scattering events, respectively. It is important to note that the former is considered as a function of the reconstructed scattering angle $\theta^{rec}_{\gamma'}$, while the latter is considered as a function of the generated scattering angle $\theta^{gen}_{\gamma'}$.

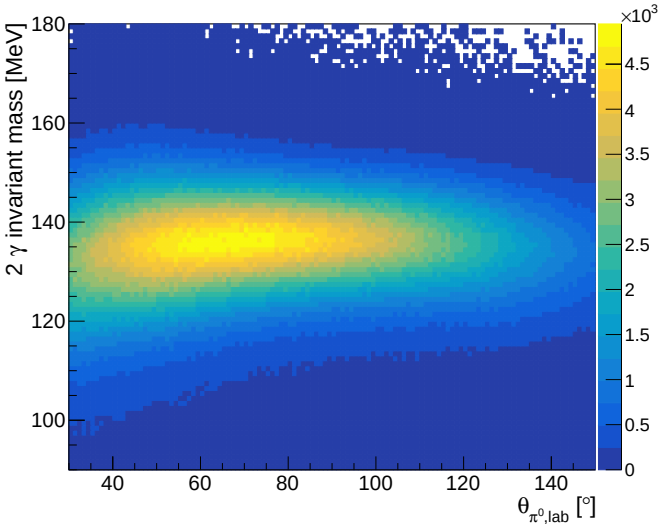

Figure 7.11: Simulated Monte Carlo 2-γ invariant mass distribution.

Due to the angular resolution of the experimental apparatus and of the clustering algorithm, these two values may be significantly different. The use of the reconstructed angular information for the reconstructed events, instead of the generated one, corrects for possible systematic shifts in the reconstruction of the angular information, since it should affect both the simulated and the real data in the same way.

For a precise estimate of the efficiency ϵ_{rec}, it is important that the simulated data emulates the real data as accurately as possible. In this way, the selection applied in the analysis affects the simulated and real data in the same way. Particularly important is the energy smearing of the simulated data, which is necessary to match the resolution of the experimental data For the NaI crystals of CB, the energy resolution in GeV was given by:

$$\Delta E_{CB} = 0.20 * (E_{CB}/GeV)^{0.7}. \tag{7.9}$$

Moreover, the simulated data were also calibrated using an overall scaling factor to match the calibration of the real data. The calibration and the smearing of the simulated data were checked using neutral pion photoproduction. Compared to Compton scattering, it has two main advantages: a 100 times higher cross-section, and the possibility to use the π^0 invariant mass as an energy calibration check. A Monte Carlo sample of $\gamma p \to p\pi^0$ events was generated and its interaction with the experimental apparatus was simulated. For the pion analysis, the events with exactly two neutral particles with energy $\omega_{\gamma'} < 150$ MeV in the final state were selected, both in the simulated and in the real data. This tight cut was chosen

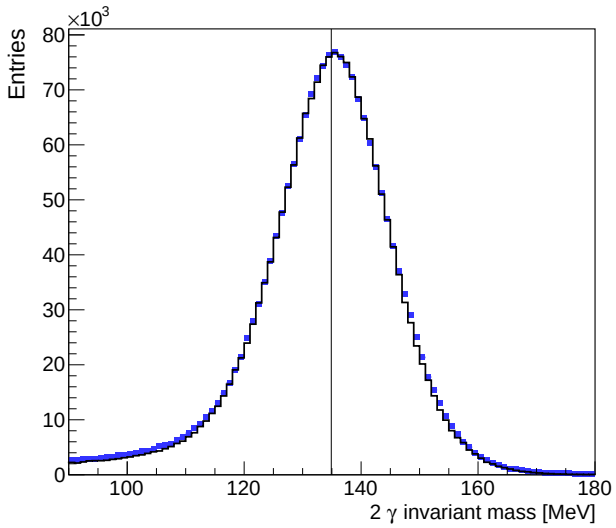

Figure 7.12: Example of 2-γ invariant mass distribution for a given $\theta_{\gamma'}$ bin. The simulated distribution in black is compared with the empty target subtracted distribution in blue. The nice agreement among the two distributions demonstrates an appropriate Monte Carlo calibration and smearing.

to select photons as similar as possible to the ones used in the main Compton analysis. The invariant mass of the two photons, $m_{\gamma\gamma}$, was plotted as a function of the scattering angle θ_{π^0} for both simulated and real data. The 2-D distribution for the simulated data can be seen in Fig. 7.11. To check the goodness of the energy smearing, the invariant mass distribution was projected in 10° wide θ_{π^0} bin, and the simulated and real distributions were plotted together. An example of these comparisons can be seen in Fig. 7.12. The agreement between the real and the simulated distributions indicates an appropriate energy calibration and smearing.

The final step towards ensuring that the simulated data imitates the real data as accurately as possible is the exclusion of the broken CB channels from the analysis. During the two data taking periods, a few of the 672 channels of the CB were not working properly, either giving no output or a signal lower than expected. It is important to account for these problematic channels in the simulation and to include them in the efficiency calculation. Since it is not possible to precisely simulate their level of inefficiency, these channels were completely excluded in the analyses of both simulated and real data. Figure 7.13 shows the angular distribution of simulated and real Compton events in CB in the left and right panel, respectively. The spots with fewer events are related to the ten missing channels reported in red. As it can be seen, the holes in the angular distribution of real data are well represented in the simulated distribution.

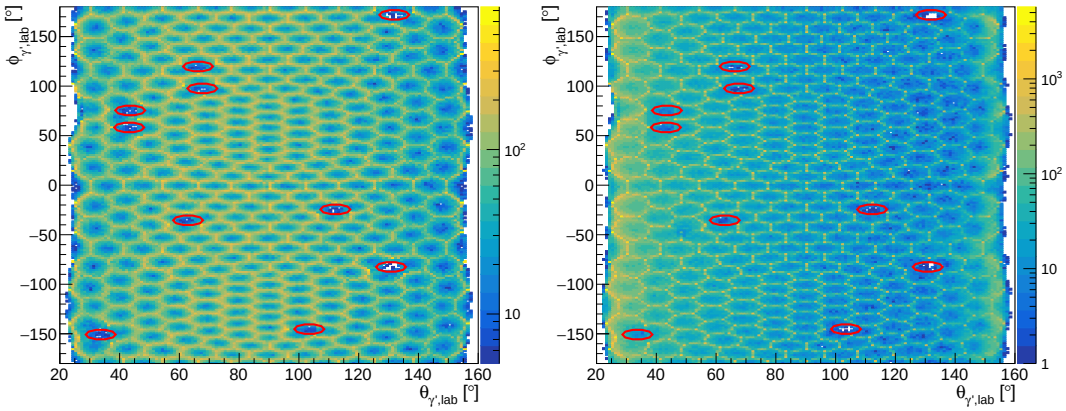

(a) Monte Carlo. (b) Real data.

Figure 7.13: Angular distribution in the CB of simulated and real Compton scattering events in the left and right panel, respectively. The red ellipses shows the ten problematic CB channels.

After all these checks, the detection and reconstruction efficiency ϵ_{rec} was calculated using Eq. (7.8). Figure 7.14 shows the distribution of ϵ_{rec} as a function of the photon beam energy ω_γ and the scattering angle $\theta_{\gamma'}$. Thanks to the experimental apparatus used being extremely suitable for the detection of photons, the overall efficiency is relatively high, $\epsilon_{rec} \sim 87\%$, and it shows a weak energy and angular dependency. The drop in efficiency visible at $\theta_{\gamma'} = 45°$ is caused by the the missing CB channels reported in Fig. 7.13.

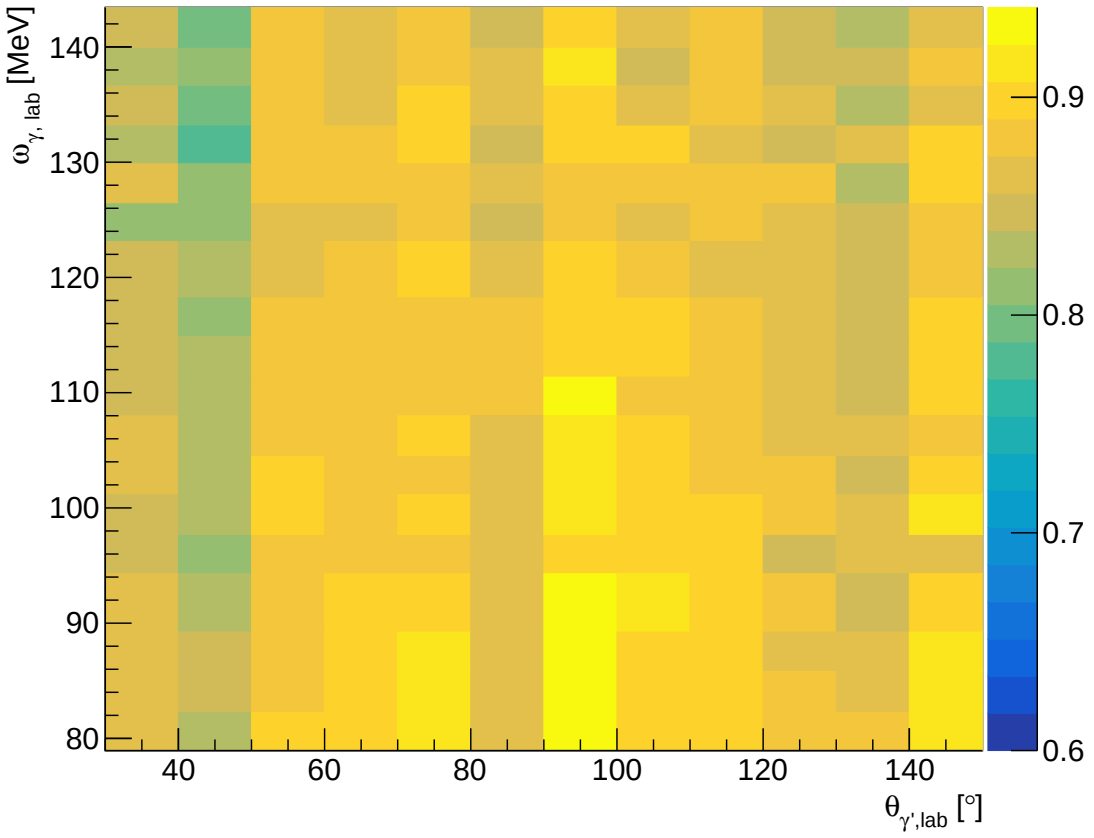

Figure 7.14: Compton scattering detection and reconstruction efficiency as a function of the photon beam energy ω_γ and the scattering angle $\theta_{\gamma'}$. The drop in efficiency visible at $\theta_{\gamma'} = 45°$ is due the the missing channels in the CB reported in Fig. 7.13.

Chapter 8

Determination of the unpolarized cross-section

The cross-section of a physical reaction is a measure of the probability that that specific process will take place. In the case of proton Compton scattering, the cross-section is a measure of the probability that a photon will interact with a proton and will be re-scattered at a given angle. It is expressed in units of area, and in nuclear physics the conventional unit is barn b ($1\text{b} = 10^{-28}$ m^2). It is one of the most useful measurable physical quantities and it can be accessed using the experiment described in this dissertation.

In the case of an incoming photon beam with energy ω_γ and flux Φ_γ impinging on a proton target at rest with a given density ρ_{LH_2} and length l_{LH_2}, the number of Compton scattering events N can be defined as

$$N = \sigma \Phi_\gamma N_p, \tag{8.1}$$

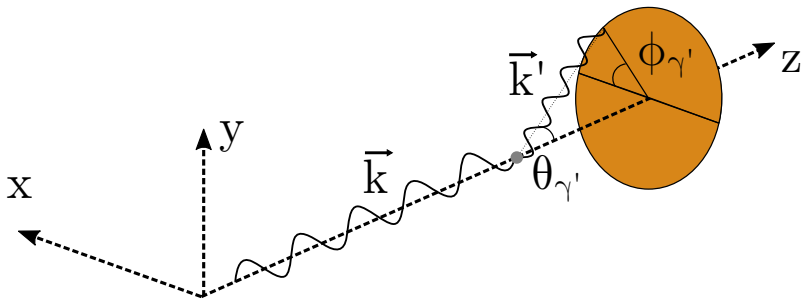

Figure 8.1: Scheme of the polar and azimuthal scattering angles $\theta_{\gamma'}$ and $\phi_{\gamma'}$, respectively. The interaction point is shown in gray.

where N_p is the number of protons in the target, and the proportionality constant σ is the cross-section. The photon flux Φ_γ can be calculated using Eq. (6.1), where the dependency on the tagging spectrometer channel indicates a dependency on the incoming photon beam energy ω_γ. The number of protons per unit area in the target can be calculated as:

$$N_p = \frac{N_A \rho_{LH_2} l_{LH_2}}{A_{H_2}} = 4.249 \times 10^{23} \text{ protons/cm}^2, \tag{8.2}$$

where $N_A = 6.022 \times 10^{23}$ mol^{-1} is the Avogadro constant, $\rho_{LH_2} = (70.548 \pm 0.01) \times 10^{-3}$ g/cm^3 is the target density, $l_{LH_2} = (10.0 \pm 0.1)$ cm is the target length, and $A_{H_2} = 1.007$ g/mol is the atomic weight of hydrogen [105]. Furthermore, to extract the real cross-section from the measured one, it is important to account for the reconstruction and detection efficiency ϵ_{rec} calculated in Section 7.4 and depicted in Fig. 7.14. In particular, given a number of experimentally observed Compton scattering events $N_{\gamma'}$, the real number of events is higher than the measured one, and it can be calculated as

$$N = \frac{N_{\gamma'}}{\epsilon_{rec}}. \tag{8.3}$$

Using Eqs. (6.1), (8.1) and (8.3), the energy dependent cross-section can be calculated as

$$\sigma(\omega_\gamma) = \frac{N_{\gamma'}(\omega_\gamma)}{N_{e^-}(\omega_\gamma)\epsilon_{tagg}(\omega_\gamma)\epsilon_{rec}(\omega_\gamma)N_p}. \tag{8.4}$$

More complete information can be obtained by studying the polar and azimuthal angular dependency of the cross-section. The two reaction angles are shown in Fig. 8.1. Defining the solid angle $d\Omega_{\gamma'} = \sin\theta_{\gamma'} d\theta_{\gamma'} d\phi_{\gamma'}$, the cross-section as a function of the solid angle — usually called differential cross-section — can be defined as

$$\frac{d\sigma}{d\Omega}(\omega_\gamma, \theta_{\gamma'}, \phi_{\gamma'}) = \frac{N_{\gamma'}(\omega_\gamma, \theta_{\gamma'}, \phi_{\gamma'})}{d\Omega} \frac{1}{N_{e^-}(\omega_\gamma)\epsilon_{tagg}(\omega_\gamma)\epsilon_{rec}(\omega_\gamma, \theta_{\gamma'}, \phi_{\gamma'})N_p}. \tag{8.5}$$

In the case of an unpolarized cross-section, the result is azimuthally symmetric, therefore there is no dependency on $\phi_{\gamma'}$ and the solid angle can be integrated over the full azimuthal angle:

$$\Delta\Omega = \int_0^{2\pi} d\phi_{\gamma'} \int_{\theta^i_{\gamma'}}^{\theta^f_{\gamma'}} \sin\theta_{\gamma'} d\theta_{\gamma'} = 2\pi(\cos\theta^i_{\gamma'} - \cos\theta^f_{\gamma'}), \tag{8.6}$$

where $\theta^i_{\gamma'}$ and $\theta^f_{\gamma'}$ are the lower and upper limits of each bin in the scattering angle $\theta_{\gamma'}$. The total cross-section $\sigma(\omega_\gamma)$ can then be extracted from the differential one by integrating over the angles

$$\sigma(\omega_\gamma) = \int d\Omega \frac{d\sigma(\omega_\gamma, \theta_{\gamma'}, \phi_{\gamma'})}{d\Omega} = \int_0^{2\pi} d\phi_{\gamma'} \int_0^{\pi} d\theta_{\gamma'} \sin\theta_{\gamma'} \frac{d\sigma(\omega_\gamma, \theta_{\gamma'}, \phi_{\gamma'})}{d\Omega}. \quad (8.7)$$

The unpolarized ϕ-independent Compton scattering cross-section measured in this thesis is finally given by:

$$\frac{\Delta\sigma}{\Delta\Omega}(\omega_\gamma, \theta_{\gamma'}) = \frac{N_{\gamma'}(\omega_\gamma, \theta_{\gamma'})}{2\pi(\cos\theta^i_{\gamma'} - \cos\theta^f_{\gamma'})} \frac{1}{N_{e^-}(\omega_\gamma)\epsilon_{tagg}(\omega_\gamma)\epsilon_{rec}(\omega_\gamma, \theta_{\gamma'})N_p}. \quad (8.8)$$

where $N_{\gamma'}(\omega_\gamma, \theta_{\gamma'})$ is the number of observed Compton scattering events within a given beam photon energy and scattering angle bin, with central values ω_γ and $\theta_{\gamma'}$, respectively.

8.1 Systematic studies

In addition to the statistical errors, the measurements of this thesis are also affected by systematic uncertainties. They quantify the effects of the different analysis steps, and they provide a measure of the robustness of the obtained results. Therefore, it is important to study all the sources of possible systematic effects and to provide a clear estimate of them. The sources of systematic uncertainties can be intrinsic to the experiment, such as the target density or the photon flux, or can be dependent on the analysis procedure, such as the cuts on the proton missing mass or on the number of particles in the final state. In this section, all the possible sources of systematic errors are discussed and their effects on the final unpolarized Compton scattering cross-section results are estimated.

To estimate the size of the systematic errors, changes to the different sources are applied, and the effects of these changes on the final results are calculated. In the following part of the text, the lower case δ and the upper case Δ are used to indicate a relative or an absolute error, respectively.

8.1.1 Target density

The number of protons per unit area in the target enters directly at the denominator in the calculation of the unpolarized cross-section, as shown in Eq. (8.8). This number is calculated using Eq. (8.2), where the sources of uncertainty are

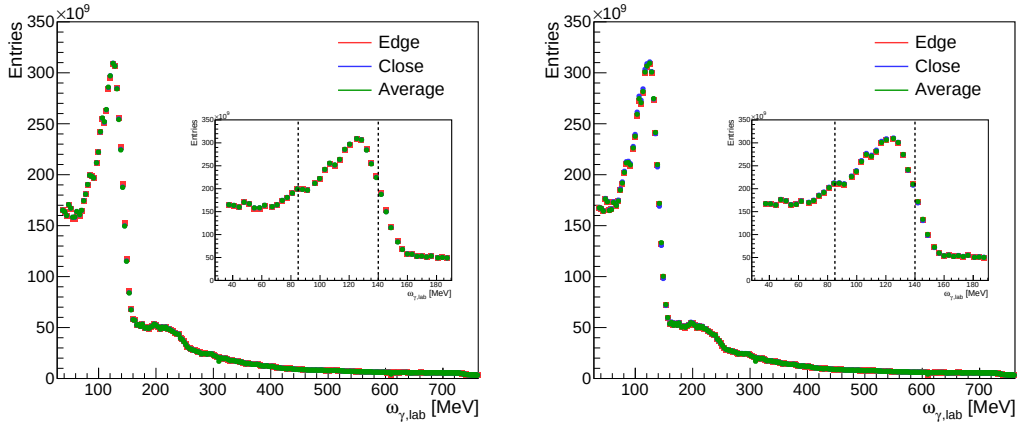

(a) Parallel (b) Perpendicular

Figure 8.2: Sample of the photon beam flux distributions obtained with the (a) parallel and (b) perpendicular orientation of the diamond. The three colors correspond to three different methods used to select the tagging efficiency measurement to be used to correct the photon flux for each production run. The red points correspond to the "edge" method, the one used for the final results. Blue and green points correspond to the "close" and "average" method, respectively, that were used for the estimation of the systematic uncertainty. In the small canvas, the beam energy region of interest for this analysis is shown, and the dashed lines show the cuts applied in the analysis.

the target length l_{LH_2} and the target density ρ_{LH_2}. During the measurement, the temperature of the target was kept stable and so the target density value is known with a negligible error ($< 0.1\%$). On the other hand, the target length is known with an error of 1% that should be taken into account in the final results.

8.1.2 Photon flux

The main source of systematic error in the determination of the photon flux is the tagging efficiency measurement. It was performed daily using the lead glass detector that is assumed to have a 100% efficiency for photon detection. The same tagging efficiency measurement is normally used in the analysis to calculate the photon flux in all the runs collected in the preceding 24 hours. This approach is mostly valid in the case of an unpolarized photon beam, while with a linearly polarized beam it does not account for possible variations in the position of the linear polarization edge from run to run. To partially compensate for this issue, a different approach was used in the analysis of this thesis, as described in Section 6.1.2. This method tries to find the tagging efficiency closest in shape to the tagger scaler distribution of each data taking run, independent on when it was

taken. The selection is based on the coherent edge position, and if more than one tagging efficiency with the same coherent edge position is found, the one closest in time to the production run is selected. To study the validity of this new method, as well as to estimate the systematic error in the tagging efficiency measurement, a sample of the total photon flux was calculated using three different methods:

- "edge" method, the one used in this analysis to calculate the photon flux for each production run (described in Section 6.1.2);
- "average" method, in which the weighted average $\bar{\epsilon}_{tagg}(i)$ over all the tagging efficiency sets was calculated for the i-th channel as

$$\bar{\epsilon}_{tagg}(i) = \frac{\sum_{s=1}^{n} \epsilon_{tagg}(i,s) w(i,s)}{\sum_{s=1}^{n} w(i,s)}, \tag{8.9}$$

  where $\epsilon_{tagg}(i,s)$ and $w = 1/\Delta_{\epsilon}(i,s)$ are the tagging efficiency measurement and the weight — given by the reciprocal of the variance — for the s-th set, respectively. $\bar{\epsilon}_{tagg}(i)$ was used to calculate the photon flux for every production run;
- "close" method, in which the tagging efficiency measurement next in time was used to calculate the photon flux for each production run.

Figure 8.2 shows a sample of the photon flux separately for the parallel and perpendicular dataset calculated using the three methods. The differences between the three methods are extremely small. To get a better estimate of the differences, the ratios between the outcome of the three different methods are shown in Fig. 8.3. As expected, the three methods give very similar results and inside the cuts applied in the analysis the difference between any two of them is never larger than 1.5%. A stronger difference is visible right after the selected region, where the coherent edge sits. This was expected since the tagging efficiency drops after the coherent edge, as visible in Fig. 6.4. Therefore, in that region a small oscillation of the beam can cause a significant change in the flux. This is the main reason why the coherent edge was set to be outside the beam energy cuts.

It is also interesting to note that the photon flux obtained with the "edge" method seems to be less in agreement with the other two. This highlights the fact that the coherent edge position can noticeably shift between runs and this is not perfectly represented by the tagging efficiency measurements performed closest in time. Fig. 8.4 shows a sample of the coherent edge positions for tagging efficiency

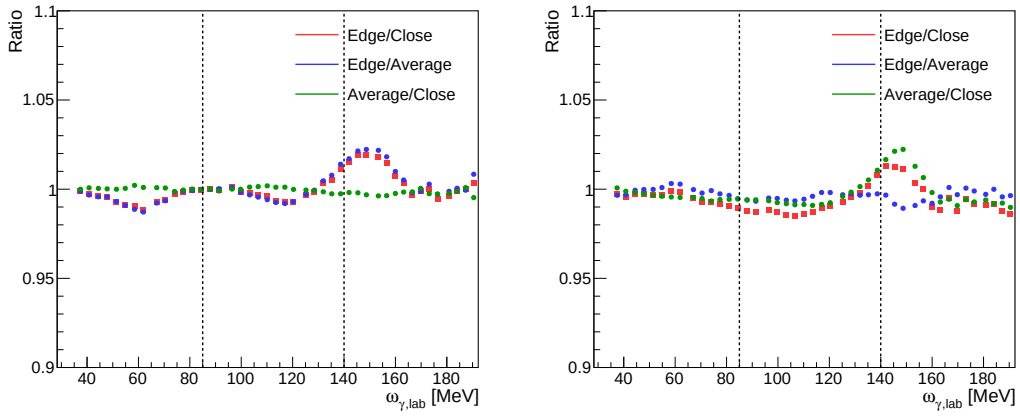

(a) Parallel (b) Perpendicular

Figure 8.3: Ratio between the photon beam flux distributions shown in Fig. 8.2. The red points show the ratio between the photon flux obtained using the "edge" and the "close" methods. The blue points show the ratio between the photon flux obtained using the "edge" and the "average" methods. The green points show the ratio between the photon flux obtained using the "average" and the "close" methods. The beam energy range is zoomed in on the region of interest for this analysis, and the dashed lines show the cuts applied.

and production runs. As can be seen, the two distributions have different shapes and this may indicate that it is more correct to select the tagging efficiency based on the shape, as it was done in the analysis of this thesis.

Since it was not possible to clearly determine which method was more correct, a systematic error in the order of 2% was determined based on the maximum difference between the results obtained using the different methods.

8.1.3 Analysis cuts

The different cuts applied in the selection of the final data sample have a strong influence on the quality of the final results. Variations in the strength of these conditions can be used to prove the reliability of the final results, as well as to get an estimate of the systematic uncertainties coming from them. The three main variables on which cuts were applied in this analysis are the number of particles in the final state, the prompt time window, and the proton missing mass (see Section 7.2).

8.1.3.1 Number of particles in the final state

In the beam energy range of interest for this work, the recoil proton is never detected. Therefore, the requirement of exactly one neutral particle in the final

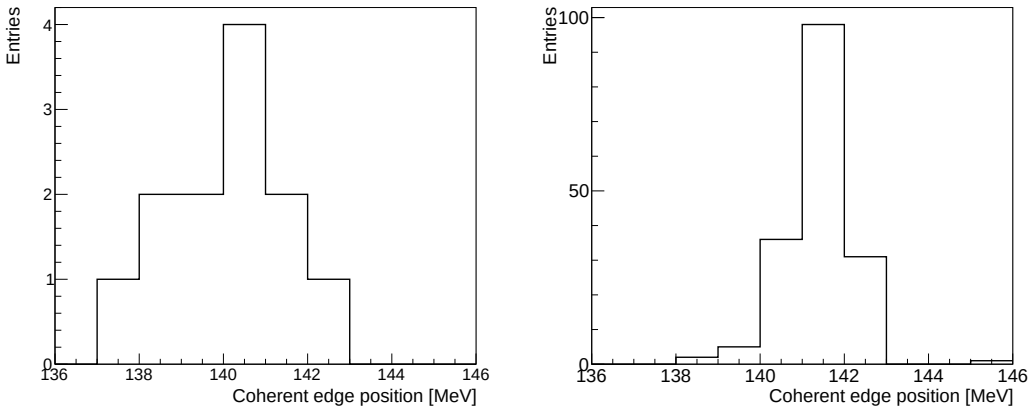

(a) Tagging efficiencies (b) Production runs

Figure 8.4: Sample of the average edge position distributions for tagging efficiencies and production runs in the left and right plot, respectively. The average edge position for the tagging efficiencies was obtained by fitting the coherent enhancement distribution every 100 scaler reads, giving around eight edge position values per run, and calculating the average of these values. For the production runs, the coherent enhancement distribution was fitted every scaler read, giving about 400 edge positions per run, and the plotted value is their average.

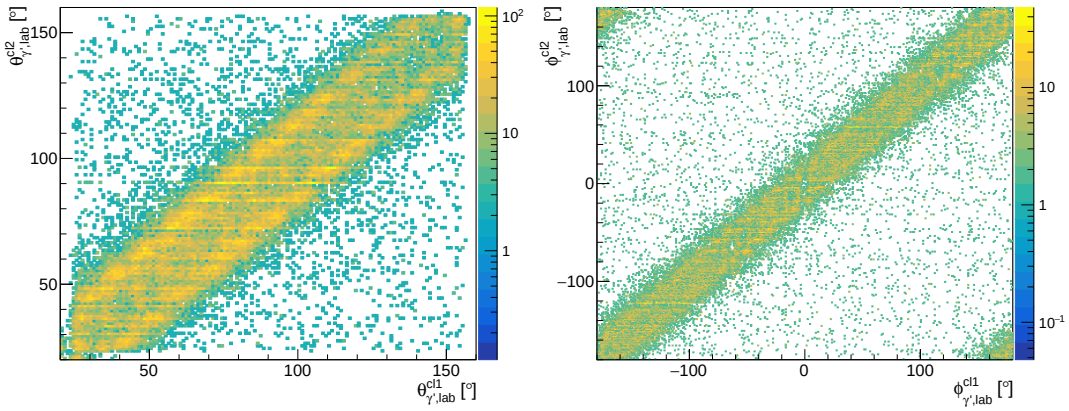

(a) Polar angle $\theta_{\gamma'}$. (b) Azimuthal angles $\phi_{\gamma'}$.

Figure 8.5: Angular distribution of the two-neutral-cluster Compton scattering Monte Carlo generated events. The y-axis gives the angular information of the lower energy cluster as a function of the same variable for the higher energy one. The two clusters tend to be very close, indicating a misconstructed single-cluster event.

state is the natural choice. Nevertheless, as shown in Fig. 7.3, in the analysis of Monte Carlo generated Compton scattering data around 1.5% of events were reconstructed with two neutral clusters. To study what these events are, the kinematic distribution of the two clusters was studied.

Fig. 8.5 shows the angular distribution of one cluster versus the other, for both the azimuthal $\phi_{\gamma'}$ and the polar $\theta_{\gamma'}$ angle. There is a clear correlation between the position of the two clusters, and in particular they seem to be very close to each other. This is an indication that they are produced by one single neutral particle that was misconstructed by the cluster algorithm. Unfortunately, in the analysis of production data it is extremely difficult to disentangle such events from a neutral pion decay, and thereby from $p\pi^0$ production in which the proton was not detected. Since neutral pion photoproduction has a three orders of magnitude higher cross-section, a small change in the selection to include Compton events with cluster splitting also caused the inclusion of a overwhelming number of $p\pi^0$ events with a random electron detected in the tagger spectrometer with an energy inside the cuts. Even though these events, being random, were eventually subtracted from the final sample leaving the results unchanged, the statistical errors increased. It was therefore decided to keep the strict selection of one neutral cluster event, since this small amount of lost events is reproduced in the Monte Carlo and should be corrected with the detection and reconstruction efficiency.

8.1.3.2 Timing random background subtraction

The subtraction of random timing coincidences in the tagger spectrometer is crucial in a tagged photon experiment. The conservative choice of considering a prompt electron if $\Delta t = t_{e^-} - t_{\gamma'} \in [-3, 3]$ ns minimized the errors after the subtraction as much as possible. To check if Compton events were excluded by this narrow cut, the analysis was repeated by doubling the prompt interval and considering $\Delta t_{sys} = t_{e^-} - t_{\gamma'} \in [-6, 6]$ ns. The two results were compared and no significant difference was found.

8.1.3.3 Missing mass cut

The most powerful cut that was applied in the analysis of the data is the one on the proton missing mass. All the analyzed events have exactly one particle in the final state, and the mass of the undetected particle (M_{miss}) was calculated using kinematics (see Section 7.2.4). If the event is actually a Compton scattering event, the missing particle is the recoil proton and M_{miss} should be equal to the

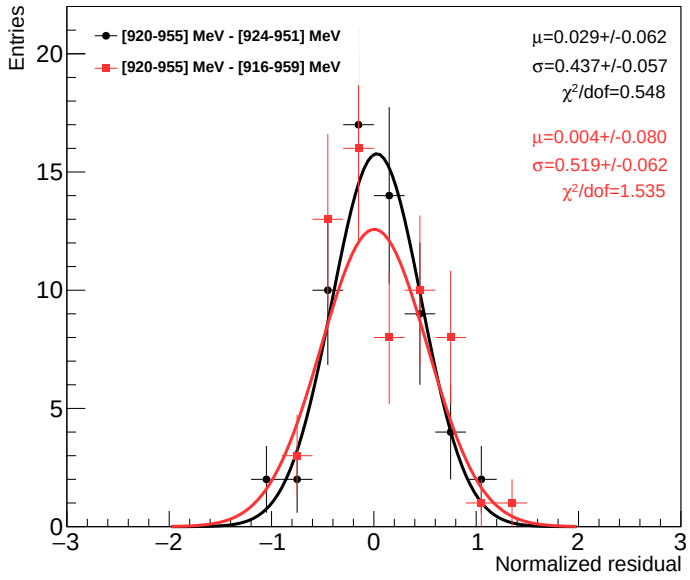

Figure 8.6: Normalized residual for unpolarized Compton scattering cross-section with different missing mass cuts. The cut used in the analysis was $M_{miss} = [920 - 955]$ MeV. Black and red points show the residual when considering a narrower ($M_{miss} = [924 - 951]$ MeV) and a wider ($M_{miss} = [916 - 959]$ MeV) missing mass cut. Gaussian fits were performed to each residual distribution (black and red line), and the results are also reported on the right.

proton mass. Using studies on Monte Carlo generated data, the missing mass cut for this analysis was set to be $M_{miss}^{\min} = 920$ MeV and $M_{miss}^{\max} = 955$ MeV.

The values set for the analysis were decided based on a double-Gaussian fit of the Monte Carlo simulated missing mass distribution. In particular, the final cuts were chosen to be $\mu \pm 2.5\sigma$ where μ and σ are the mean and the width of the fitting function (see Eqs. (7.5) and (7.6)). To test the stability of this selection, the analysis was also performed with a looser and a tighter cut defined as $\mu \pm 2.0\sigma$ and $\mu \pm 3.0\sigma$, respectively. To give an idea on the absolute variation of the cuts, this corresponds to narrowing or to widening the cut by 8 MeV, more than a 20% variation with respect to the nominal cut. The compatibility between the Compton scattering cross-section results obtained with the cuts used in the analysis and with the looser and tighter ones was evaluated with the normalized residual, defined as:

$$r = \frac{d\sigma - d\sigma_{sys}}{\sqrt{\Delta d\sigma + \Delta d\sigma_{sys}}}, \tag{8.10}$$

where $d\sigma$ and $\Delta d\sigma$ are the value and the error of the cross-section using the final cuts, respectively, and $d\sigma_{sys}$ and $\Delta d\sigma_{sys}$ are the value and the error of the cross-section obtained with one of the two cuts defined above, respectively. The distribution of the normalized residual is shown in Fig. 8.6, together with a Gaussian fit of the two distributions. The results of the fits are also reported in the canvas. The two obtained distributions have a mean compatible with zero, while the standard deviation is smaller than expected. This could reflect the fact that the two samples of points are not totally uncorrelated as they come from a different analysis of the same dataset.

As a further check to estimate a possible systematic error coming from the missing mass cut, the relative variation of each cross-section point was calculated as

$$v = \frac{d\sigma - d\sigma_{sys}}{d\sigma}, \tag{8.11}$$

and the average values over all bins was evaluated. The average value of the relative variation for the loose and tight cuts are 0.3% and 0.4%, respectively. Taken together, all these tests seem to indicate a strong stability of the results to sizable variation in the missing mass cut. This proves that the Monte Carlo efficiency correction works well in correcting for the additional Compton events cut out with the narrower cut, and it is also an indication of a low background contamination in the final sample. In fact, if this was not the case, one would expect more background events to be selected by the wider cut and therefore systematically higher cross-section results.

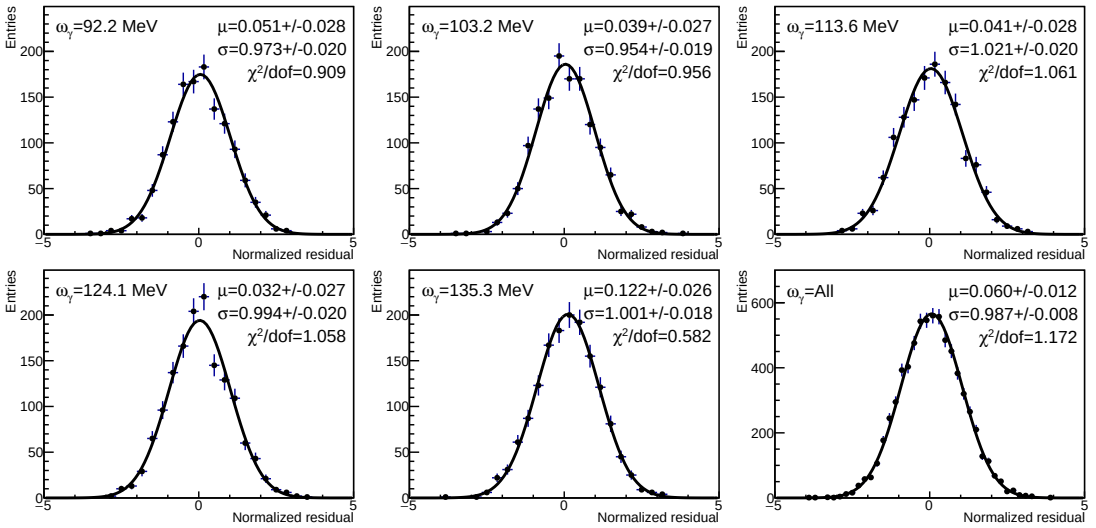

Figure 8.7: Normalized residual for missing mass distribution using different empty target samples. The first five canvases show the residual for the different beam energy bins, the bottom right one shows the residual for the whole energy region. Gaussian fits (black curves) were performed to each distribution and the results are reported in the canvases.

8.1.4 Empty target subtraction

Due to the low energy threshold set for this experiment, a relatively high background contamination coming mainly from the target cell passed the trigger cut and was recorded in the data sample. In the forward $\theta_{\gamma'}$ region, this contamination is particularly important, together with the background generated by beam photons converting into e^+e^- pairs. Therefore, a significant amount of beam time was used to sample this background by collecting data with an empty target. The liquid hydrogen target in the A2 setup can run in two different empty target configurations: a first one called cold gas, where a small quantity of hydrogen remains in the target ($\rho_{cgH_2}(1.419 \pm 0.01) \times 10^{-3}$ g/cm^3, about 50 times smaller than the LH_2), and a pumped configuration, where ideally no hydrogen is left in the target cell. The former empty mode is easier and quicker to obtain and it was used to collect all the empty target sample during March 2018 beamtime, and half of the one during July 2018 beamtime. The pumped mode is more time-consuming and delicate, and it was used to collect just a small sample in order to check for any appreciable difference between the two modes.

To compare the contribution of the empty target background in the two different modes, the missing mass distributions, normalized according to the flux, were compared for the different bins in beam energy. To check for possible discrepancies, the normalized residual for the two missing mass distributions were

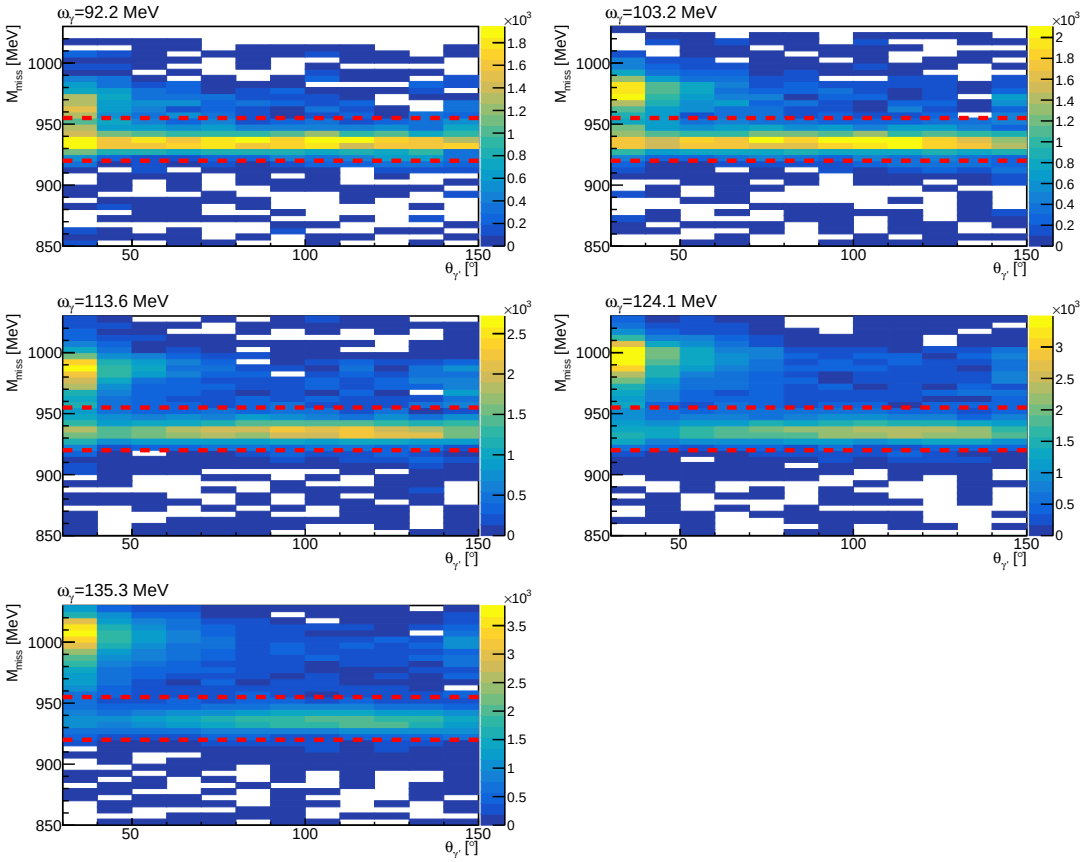

Figure 8.8: Missing mass distribution from the full target sample as a function of the scattering angle $\theta_{\gamma'}$ for the five different bins in beam energy. The red dotted lines show the missing mass cuts applied in the analysis. The background peak is clearly visible for $\theta_{\gamma'} < 50°$ and $M_{miss} > 960$ MeV.

calculated in a similar way to Eq. (8.10). The residual distributions for the five different bins in beam energy are reported in the first five canvases of Fig. 8.7. The bottom-right canvas shows the residual distribution for the whole energy and angular region. Gaussian fits were performed and the results are also reported in the canvases. They show a very nice agreement between the two empty target samples, indicating that the cold gas mode does not significantly overestimate the contribution of the empty target cell.

8.1.5 Background

The remaining background contamination in the final sample is difficult to estimate. At beam energies below the pion photoproduction threshold, there are no other prominent reaction channels that can be misidentified as Compton scattering. The main background contributions could come from the target cell and from the photon beam itself, and they were sampled and subtracted as already

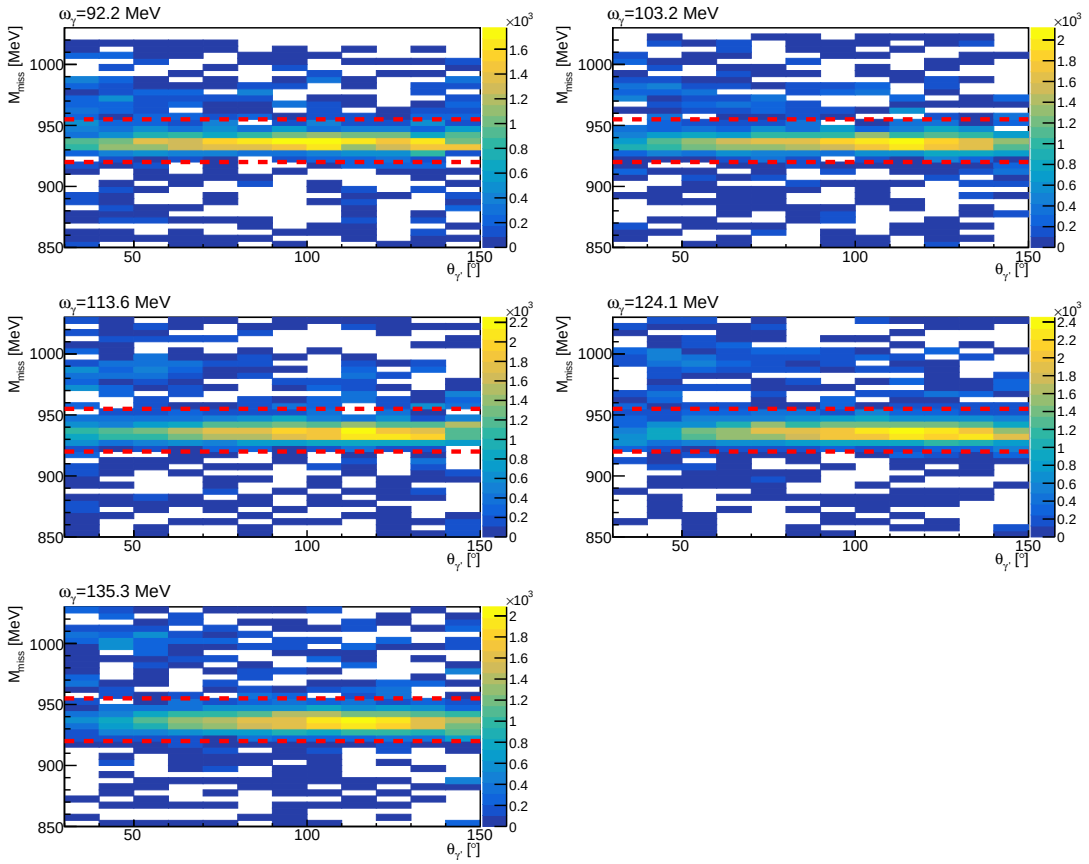

Figure 8.9: Missing mass distribution from the full target sample as a function of the scattering angle $\theta_{\gamma'}$ for the five different bins in beam energy, after the subtraction of the empty target contribution. The red dotted lines show the missing mass cuts applied in the analysis. Some remaining background is still visible for $\theta_{\gamma'} < 50°$ and $M_{miss} > 960$ MeV.

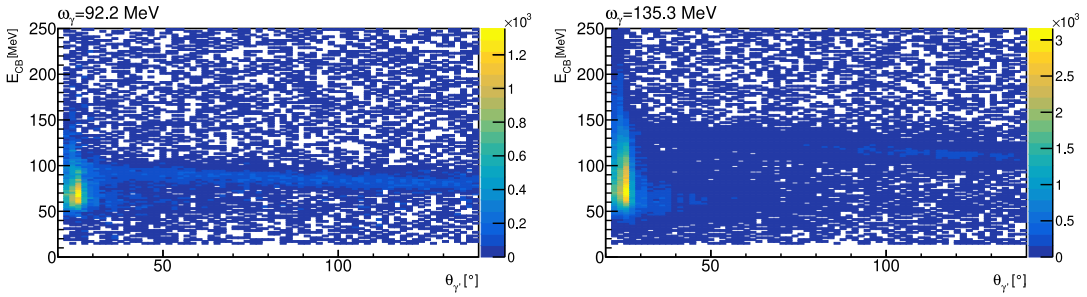

Figure 8.10: Energy distribution in the CB as a function of the scattering angle $\theta_{\gamma'}$ for two different bins in beam energy, from the full target sample. The background contribution is clearly visible at $E_{CB} \sim 60$ MeV for both beam energies.

explained. From the missing mass distributions in Fig. 7.10, the empty target contribution seems to be more important at forward angles (red points in Fig. 7.10a), and it does not fully describe the background peak on the right side in the full target (blue points in Fig. 7.10a). In fact, after the subtraction, there is still a small background peak on the right of the missing mass cuts (see Fig. 7.10b). This is not the case for larger values of $\theta_{\gamma'}$ (see Figs. 7.10c to 7.10e).

Fig. 7.10 shows a sample of the missing mass distribution for one bin in beam energy. To have a more complete overview, the missing mass was plotted as a function of the scattering angle $\theta_{\gamma'}$ for all five bins in beam energy. Fig. 8.8 shows the results for the full target sample, together with the cuts applied in the analysis indicated by the red dashed lines. A few different observations can be made from these spectra: (a) the background peak is mainly visible at forward scattering angle ($\theta_{\gamma'} < 50°$); (b) the background contribution is more important at higher beam energies, and for $\omega_\gamma = 135.3$ MeV the background peak is higher than the Compton missing mass peak at forward angle; (c) the background missing mass value shifts with the beam energy, in particular it moves ~ 10 MeV from one bin to the other from $M_{miss}^{bkg} \sim 965$ to 1005 MeV. This last point is the more interesting one to understand the nature of this additional background, and it indicates that its energy is independent of the beam energy. By looking at the energy released in the CB as a function of the scattered angle — two examples for the lower and higher beam energy are reported in Fig. 8.10 — the energy of the background seems to be ~ 60 MeV. Another interesting variable to look at is the size of the cluster created by these particles in the CB, meaning the number of crystals in which they deposited energy. As previously explained, hadrons tend to deposit all their energy in one or two crystals, while this is not true for photons and pions. Fig. 8.11 shows two examples of the missing mass distribution as function of the cluster size for the two extreme beam energies. The Compton events

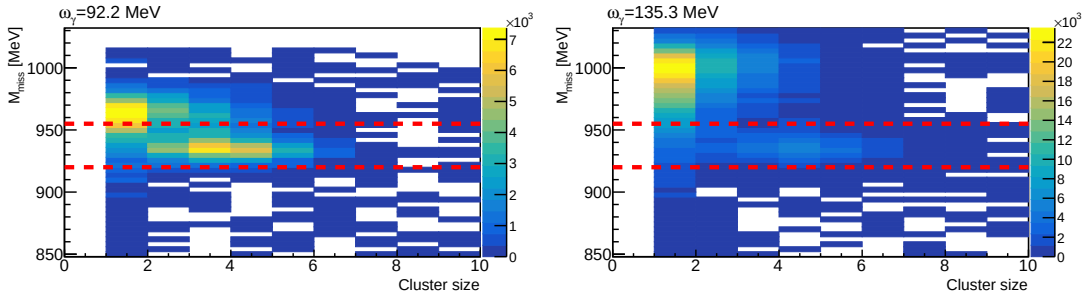

(a) Full target.

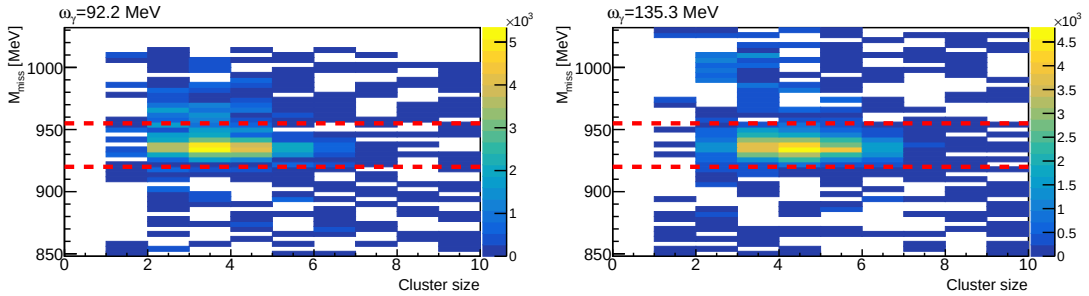

(b) Empty target subtracted.

Figure 8.11: Missing mass distribution as a function of the number of CB crystals in the cluster using the full target sample, before and after the subtraction of the empty target contribution, in the top and bottom canvas, respectively. The results are shown for the lower and higher energy bin on the left and on the right, respectively. The background contribution is clearly visible in the full target sample for cluster size equal to one and $M_{miss} > 960$ MeV. After the subtraction of the empty target contribution, there is only a small background left with cluster size equal to two and three.

within the missing mass cuts deposited their energy in average in three or four crystals as expected. The background peak, clearly visible at $M_{miss} > 955$ MeV, is composed of particles that deposited their energy in one or two crystals. This seems to indicates that they are probably neutrons. On the other hand, the same distributions after the subtraction of the empty target contribution no longer show the peak at cluster size equal to one, indicating that the small remaining background after the empty target subtraction — visible in Fig. 8.9 at $M_{miss} > 955$ MeV — is probably not composed of those neutrons. This was also proved by the fact that imposing a cut on the cluster size in the analysis did not change the final results significantly. Taken all together, these tests indicate a prominent background contamination mainly composed of neutrons with $E_{CB} \sim 60$ MeV in the full target sample that was correctly sampled and subtracted, even though a small part of this background with a cluster composition similar to a photon still remained in the final sample.

After the subtraction of the empty target contribution, the remaining background was cut away by the missing mass selection, with the exception of the lower beam energy bin. For this particular bin, the missing mass value of the background is just to the right of the applied cuts, as visible in the top-left panel of Fig. 8.9. Therefore, it was decided to estimate an additional systematic error for possible background contamination.

To estimate the systematic error, a few assumptions were made: (1) most of the background comes from the photon beam and the target cell; (2) this background should be described by the empty target sample; (3) the background peak still visible in the missing mass spectra after the empty target subtraction may be due to a non-perfect flux normalization, and consequently an underestimation, of the empty target sample. Taking these assumptions together, the remaining background contamination was estimated from rescaling the empty target sample. As first, a normalization factor ($f_{\mathrm{norm}}(\omega_\gamma)$) for each bin in beam energy was found so that the background peak to the right of the Compton scattering missing mass peak in the full target sample, was also fully described in the empty target sample. The factor was found to vary from 1.25 to 1.05 from the lower to the higher beam energy bin. The relative empty target contribution ($N_{\mathrm{empty}^{\mathrm{rel}}}(\omega_\gamma, \theta_{\gamma'})$) was then calculated for each bin in beam energy and scattering angle as:

$$N^{\mathrm{rel}}_{\mathrm{empty}}(\omega_\gamma, \theta_{\gamma'}) = \frac{N_{\mathrm{empty}}(\omega_\gamma, \theta_{\gamma'})}{N_{\mathrm{full}}(\omega_\gamma, \theta_{\gamma'})}, \tag{8.12}$$

where $N_{\mathrm{full}}(\omega_\gamma, \theta_{\gamma'})$ and $N_{\mathrm{empty}}(\omega_\gamma, \theta_{\gamma'})$ are the number of events for each bin in

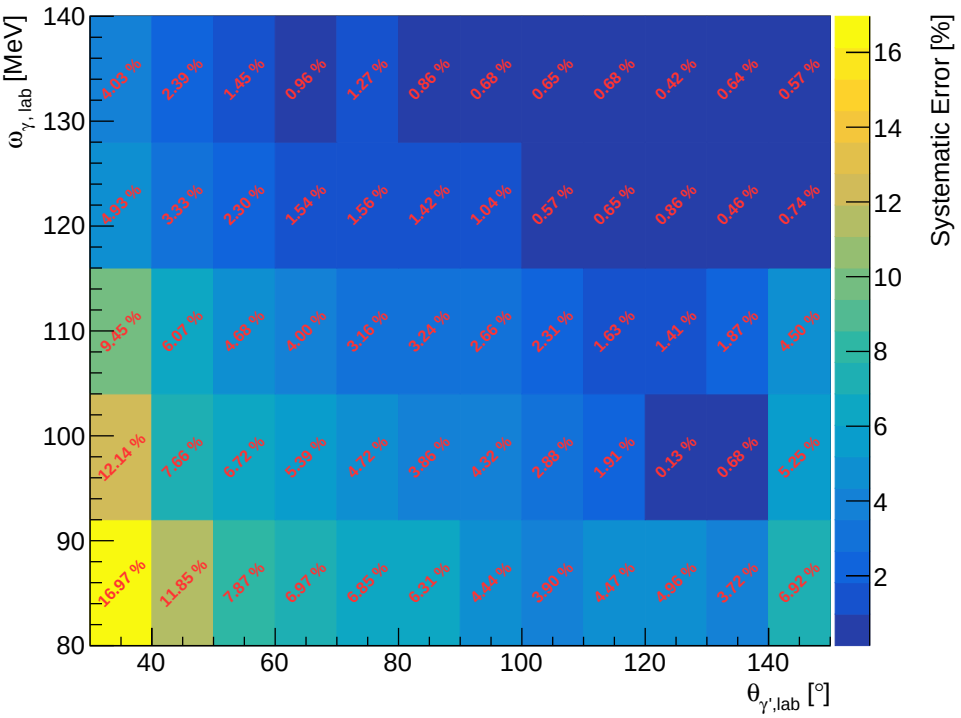

Figure 8.12: Systematic errors due to the background contamination as a function of the beam energy ω_γ and the scattering angle $\theta_{\gamma'}$. They are calculated as the relative empty target contribution to the full target sample scaled by a normalization factor. This factor is determined such that the background peak in the empty target fully describe the one in the full target.

energy and scattered angle for the full and empty target sample, respectively. The final systematic uncertainties for each bin were then defined as

$$\delta\sigma^{sys}_{bkg}(\omega_\gamma, \theta_{\gamma'}) = N^{\text{rel}}_{\text{empty}}(\omega_\gamma, \theta_{\gamma'})\,(1 - f_{\text{norm}}(\omega_\gamma))\,. \tag{8.13}$$

The results are reported in Fig. 8.12, and they vary in a wide range from 6% in the lower energy region to less than 1% in the higher energy region, with the exception of the most forward bin where the background contamination is higher.

8.1.6 Comparison of the two beamtimes

The dataset used for this experiment was collected in two separate beamtimes. Although the experimental conditions were kept identical for both periods, these can be considered as two (at least partially) independent measurements. The final results from the two individual beamtimes should be in agreement within

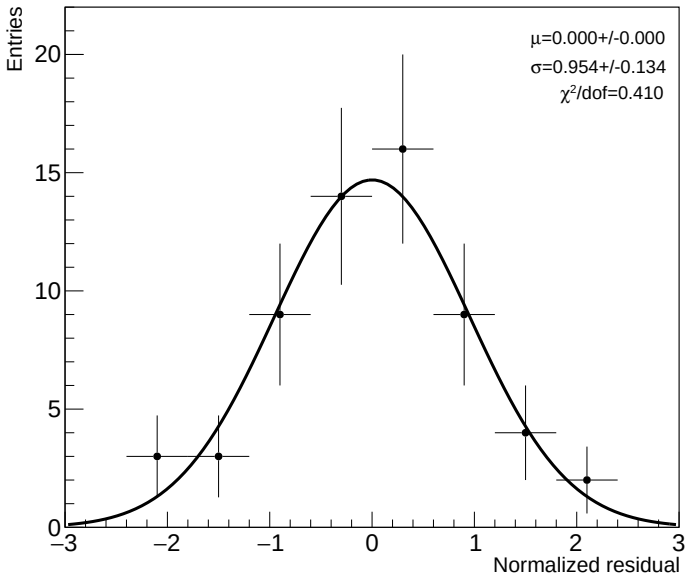

Figure 8.13: Normalized residual for the unpolarized Compton scattering cross-section obtained using March 2018 data with respect to the results obtained using July 2018 data. A Gaussian fit was also performed (black line), and the results are reported on the right.

their errors, in order to exclude systematic differences between them. To check this, the normalized residual for the two unpolarized cross-sections obtained using the two separated beamtimes were calculated, using Eq. (8.10). The results are reported in Fig. 8.13. As expected, the residuals are Gaussian distributed, with a mean compatible with zero. This indicates an absence of an overall systematic effect between the two beamtimes. It may be interesting to check the residual distributions for the different beam energy bins. Although the small number of points does not allow for a Gaussian fit to each beam energy bin (there are only twelve angular bins for each energy), the mean and Root Mean Square (RMS) of the twelve normalized residuals in each energy bin can give a good estimate of the agreement. The obtained results are:

$$\begin{aligned}
\omega_\gamma = 92.2 \text{ MeV} &: \mu = -0.63, \quad \text{RMS} = 0.77 \\
\omega_\gamma = 103.2 \text{ MeV} &: \mu = -0.03, \quad \text{RMS} = 1.14 \\
\omega_\gamma = 113.6 \text{ MeV} &: \mu = 0.08, \quad \text{RMS} = 0.75 \\
\omega_\gamma = 124.1 \text{ MeV} &: \mu = 0.24, \quad \text{RMS} = 0.93 \\
\omega_\gamma = 135.3 \text{ MeV} &: \mu = 0.21, \quad \text{RMS} = 0.83.
\end{aligned}$$

As a rule of thumb, the bias is negligible compared to the statistical uncertainty if the ratio mean/RMS < 0.25 [135], which is the case for all the bins but the first. For the low energy bin, there seems to be a significant discrepancy between the results obtained with the two different beamtimes. In particular, given the negative sign of the mean, the results of the July 2018 beamtime are higher than the March 2018 ones. In order to center the residual distribution to zero, the March 2018 results have to be increased by 6%, but this of course makes the results in all the other bins incompatible. To account for this possible discrepancy between the two results, a 3% systematic uncertainty — the half of the factor needed to resolve the discrepancy — was added to the total systematic error for the lower energy bin only.

8.1.7 Sum of systematic uncertainties

The different sources of systematic errors described above can be considered as independent, at least in the first approximation, therefore they can be added in quadrature to give the total systematic uncertainties that would be Gaussian. However, it is important to note that the different sources may affect the results in different ways, and so they should be treated differently. The systematic uncertainties on target density $\delta\sigma^{sys}_{\rho}$, photon flux $\delta\sigma^{sys}_{\Phi}$ and analysis cuts and Monte Carlo simulation $\delta\sigma^{sys}_{cuts}$ affect all the cross-section points in the same way, scaling the final results in one way or the other. The remaining sources of systematic errors — background contamination $\delta\sigma^{sys}_{bkg}$ and the comparison between the two beamtimes $\delta\sigma^{sys}_{beam}$ — may independently affect the different points. The last contribution in particular, $\delta\sigma^{sys}_{beam}$, affects only the points in the lower energy bin. The different systematic uncertainties are summarized in Table 8.1. The total systematic error can be calculated in RMS units as:

$$\begin{aligned} \delta\sigma^{sys}_{corr} &= \sqrt{\left(\delta\sigma^{sys}_{\rho}\right)^2 + \left(\delta\sigma^{sys}_{\Phi}\right)^2 + \left(\delta\sigma^{sys}_{cuts}\right)^2} = 3.0\% \\ \delta\sigma^{sys}_{uncorr}(\omega_\gamma, \theta_{\gamma'}) &= \sqrt{\left(\delta\sigma^{sys}_{bkg}(\omega_\gamma, \theta_{\gamma'})\right)^2 + \left(\delta\sigma^{sys}_{beam}\right)(\omega_\gamma, \theta_{\gamma'})^2}. \end{aligned} \tag{8.14}$$

where subscripts *corr* and *uncorr* indicates that the systematic errors are correlated and point-to-point uncorrelated, respectively.

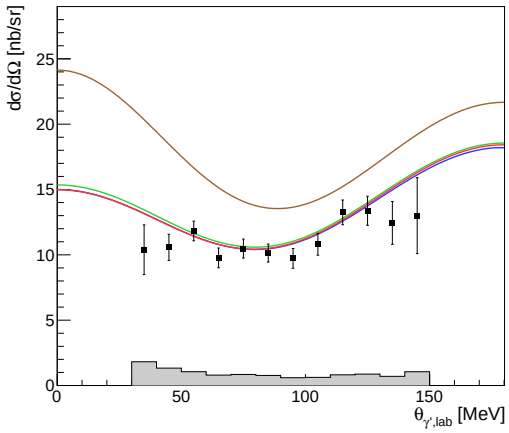

(a) 86.3 MeV $< \omega_\gamma <$ 98.2 MeV.

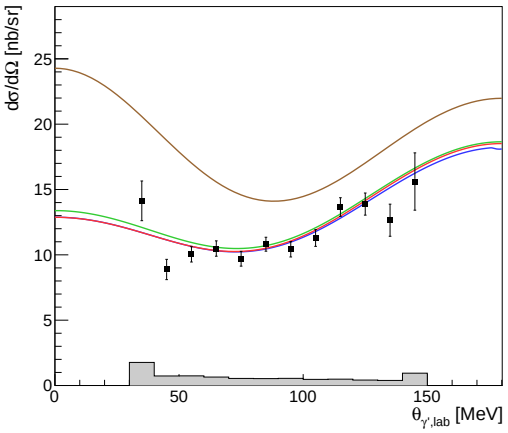

(b) 98.1 MeV $< \omega_\gamma <$ 108.4 MeV.

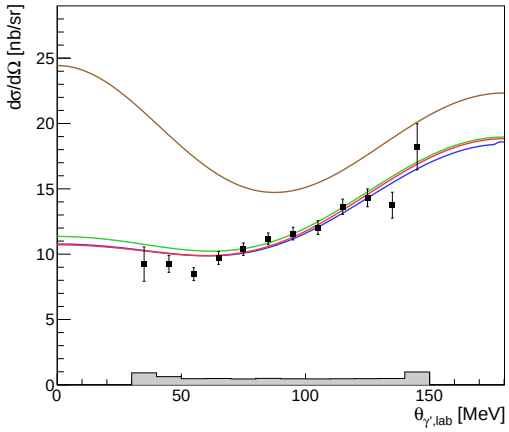

(c) 108.5 MeV $< \omega_\gamma <$ 118.7 MeV.

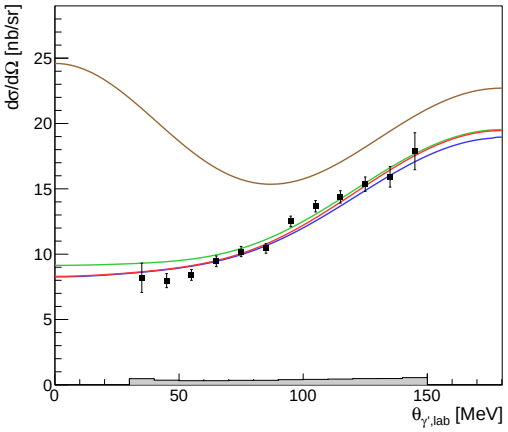

(d) 118.7 MeV $< \omega_\gamma <$ 130.2 MeV.

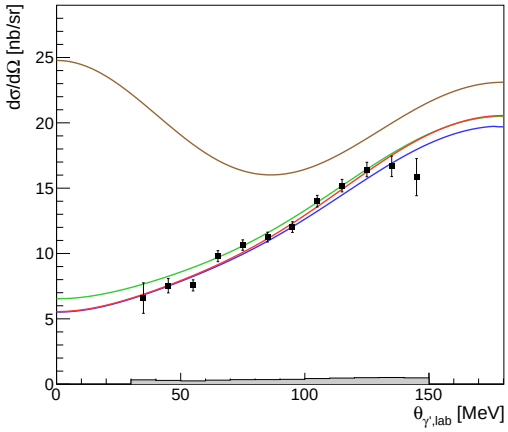

(e) 130.3 MeV $< \omega_\gamma <$ 140.4 MeV.

Figure 8.14: The new A2 Collaboration data on the proton Compton scattering unpolarized cross-section using the March 2018 data, for the five different beam energy bins. The errors are statistical only. The systematic uncertainties are depicted as gray bars. Brown curves represent the Born contribution only. Red, blue and green curves represent the theoretical calculation for fixed values of both scalar and spin polarizabilities within DR [40, 41], BχPT [47] and HBχPT [52] frameworks, respectively.

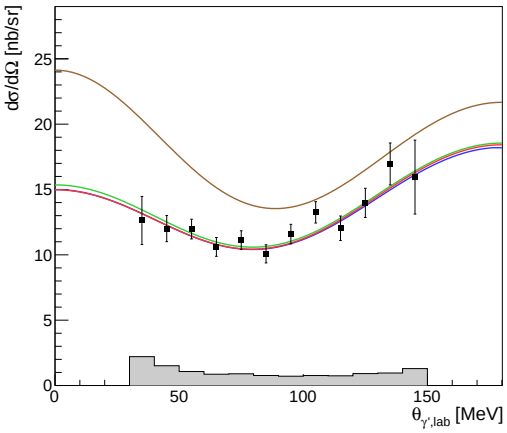

(a) 86.3 MeV $< \omega_\gamma <$ 98.2 MeV.

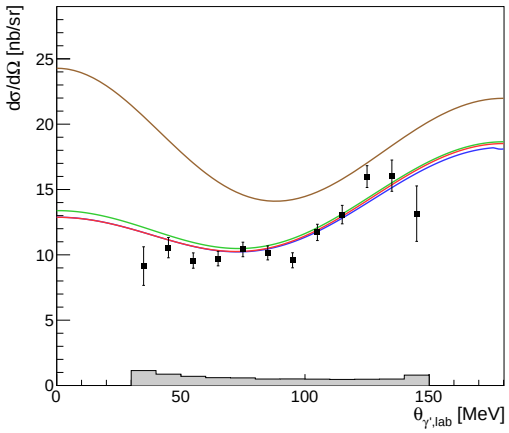

(b) 98.1 MeV $< \omega_\gamma <$ 108.4 MeV.

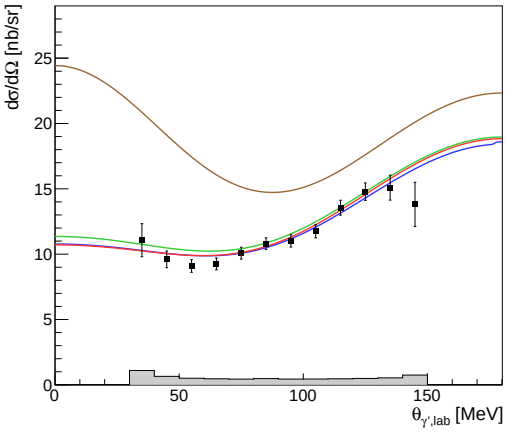

(c) 108.5 MeV $< \omega_\gamma <$ 118.7 MeV.

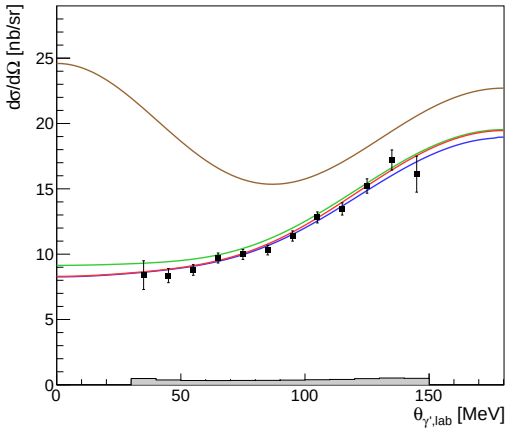

(d) 118.7 MeV $< \omega_\gamma <$ 130.2 MeV.

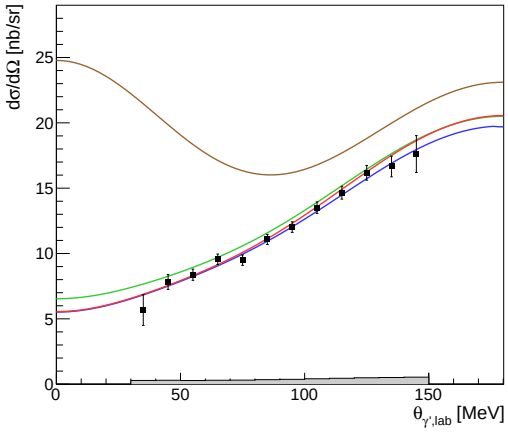

(e) 130.3 MeV $< \omega_\gamma <$ 140.4 MeV.

Figure 8.15: The new A2 Collaboration data on the proton Compton scattering unpolarized cross-section using the July 2018 data, for the five different beam energy bins. The errors are statistical only. The systematic uncertainties are depicted as gray bars. Brown curves represent the Born contribution only. Red, blue and green curves represent the theoretical calculation for fixed values of both scalar and spin polarizabilities within DR [40, 41], BχPT [47] and HBχPT [52] frameworks, respectively.

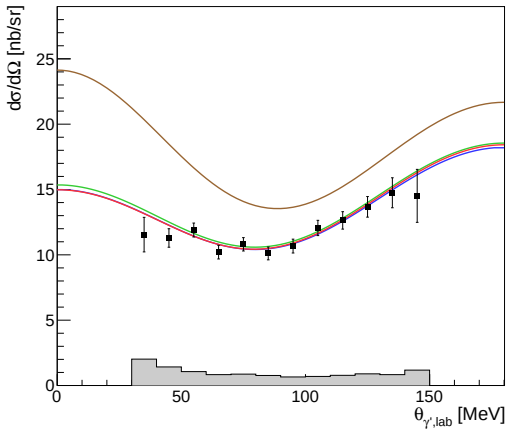

(a) 86.3 MeV $< \omega_\gamma <$ 98.2 MeV.

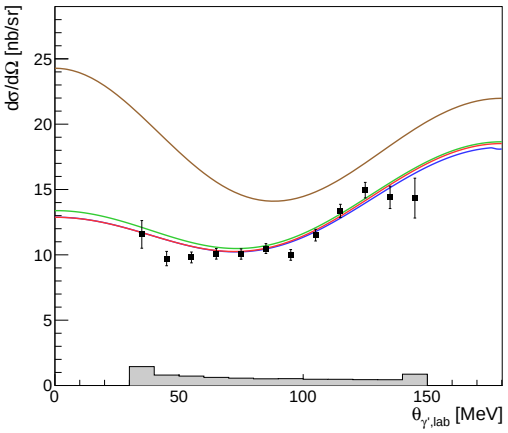

(b) 98.1 MeV $< \omega_\gamma <$ 108.4 MeV.

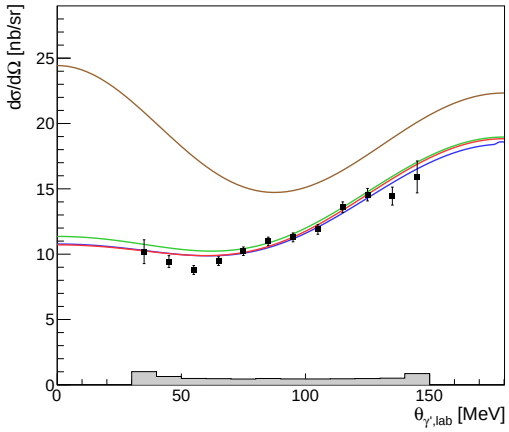

(c) 108.5 MeV $< \omega_\gamma <$ 118.7 MeV.

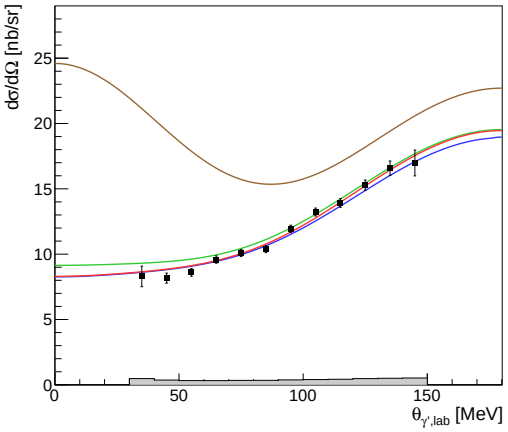

(d) 118.7 MeV $< \omega_\gamma <$ 130.2 MeV.

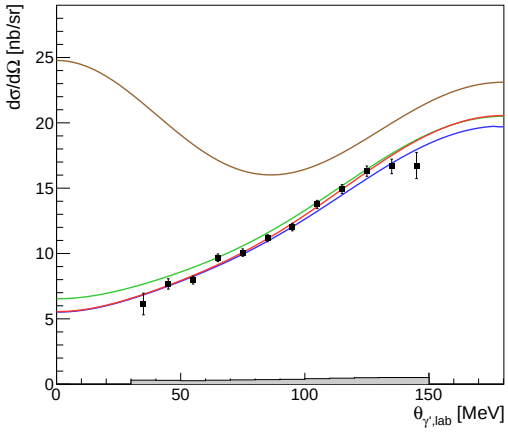

(e) 130.3 MeV $< \omega_\gamma <$ 140.4 MeV.

Figure 8.16: The new A2 Collaboration data on the proton Compton scattering unpolarized cross-section combining the results from the two different beamtimes, for the five different beam energy bins. The errors are statistical only. The systematic uncertainties are depicted as gray bars. Brown curves represent the Born contribution only. Red, blue and green curves represent the theoretical calculation for fixed values of both scalar and spin polarizabilities within DR [40, 41], BχPT [47] and HBχPT [52] frameworks, respectively.

Table 8.1: Relative systematic uncertainties on the unpolarized Compton scattering cross-section in RMS units.

$\delta\sigma_{\rho}^{sys}$	$\delta\sigma_{\Phi}^{sys}$	$\delta\sigma_{cuts}^{sys}$	$\delta\sigma_{bkg}^{sys}$	$\delta\sigma_{beam}^{sys}$
1%	2%	2%	see Fig. 8.12	$\begin{cases} 3\%, & \text{if } \omega_\gamma \leq 98.2 \text{ MeV} \\ 0, & \text{otherwise} \end{cases}$

8.2 Results

Figs. 8.14 to 8.16 show the new A2 Collaboration data on the proton Compton scattering unpolarized cross-section for the March and the July 2018 beamtime separately, and for the combined results, respectively. They cover a photon beam energy from 86.2 to 140.4 MeV, in five different bins. The error bars represent the statistical errors. The absolute systematic uncertainties are depicted as gray bars, and they were calculated as

$$\Delta\sigma_{tot}^{sys}(\omega_\gamma, \theta_{\gamma'}) = \sqrt{\left(\delta\sigma_{corr}^{sys}\right)^2 + \left(\delta\sigma_{uncorr}^{sys}(\omega_\gamma, \theta_{\gamma'})\right)^2}\,\sigma(\omega_\gamma, \theta_{\gamma'}), \tag{8.15}$$

where $\sigma(\omega_\gamma, \theta_{\gamma'})$ is the cross-section value in that bin. The brown curves represent the Born contribution to the unpolarized cross-section (see Section 2.1.2.1). The red, blue and green curves represent the theoretical calculations within DR [40,41], BχPT [47] and HBχPT [52] frameworks, respectively. In each of these calculations, the values for the different polarizabilities were fixed at: $\alpha_{E1} = 11.2$, $\beta_{M1} = 2.5$, $\gamma_{E1E1} = -2.87$, $\gamma_{M1M1} = 2.70$, $\gamma_{E1M2} = -0.85$, and $\gamma_{M1E2} = 2.04$, in the usual units. The values for the scalar polarizabilities are the ones quoted by the PDG [55], while the spin polarizabilities were taken from the last experimental paper by the A2 Collaboration [19]. Even though the χEFT based theories are able to predict the values for the spin polarizabilities, the choice of keeping them fixed at the most recent experimental values was done in order to have a direct comparison between the three theories using the same parameters.

Chapter 9

Determination of the beam asymmetry Σ_3

The use of a linearly polarized photon beam in combination with an unpolarized target introduces an azimuthal dependence to the Compton scattering cross-section, and allows for the determination of the single polarization observable Σ_3. Defining φ as the angle between the scattering plane and the photon polarization plane, the polarized cross-section modulation can be written as

$$\frac{d\sigma}{d\Omega}_{pol}(\omega_\gamma, \theta_{\gamma'}, \varphi) = \frac{d\sigma}{d\Omega}_{unpol}(\omega_\gamma, \theta_{\gamma'}) \left(1 + p_\gamma \Sigma_3 \cos(2\varphi)\right), \tag{9.1}$$

where $\frac{d\sigma}{d\Omega}_{pol}$ and $\frac{d\sigma}{d\Omega}_{unpol}$ are the polarized and unpolarized cross-section, respectively, and p_γ is the degree of linear polarization. The photon polarization plane (in green in the sketch in Fig. 9.1) is defined by the incoming photon momentum $\vec{k}$ and the polarization vector $\vec{\epsilon}$, while the scattering plane (in blue in Fig. 9.1) is defined by the particles in the final state. The angle φ between the two planes is related to the measured azimuthal angle $\phi_{\gamma'}$ of the scattered photon in the detector lab system by the relation

$$\varphi = \phi_{\gamma'} + \varphi_0, \tag{9.2}$$

where φ_0 gives the orientation of the photon polarization plane in the detector lab system.

The beam asymmetry Σ_3 can be determined from Eq. (9.1) by measuring the polarized Compton scattering cross-section. To minimize the systematic errors due to flux normalization and acceptance efficiency correction, an easier way to extract Σ_3 is by constructing an asymmetry. This can be done by measuring

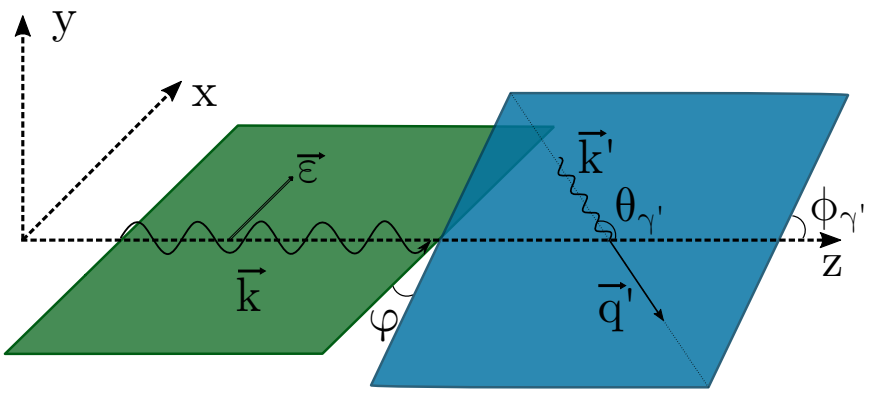

Figure 9.1: Scheme of the photon polarization and reaction scattering planes. The former, in green, is defined by the incoming photon momentum $\vec{k}$ and the polarization vector $\vec{\epsilon}$. The latter, in blue, is given by the scattered photon and the recoil proton momenta $\vec{k'}$ and $\vec{q'}$, respectively. Adapted from Ref. [97]

the polarized Compton scattering cross-section with two different orthogonal orientations of the photon polarization plane, usually called "parallel" (para) and "perpendicular" (perp). The two orthogonal orientations can be obtained by rotating the polarization vector $\vec{\epsilon}$ by 90°. The names of "parallel" and "perpendicular" refer to the fact that conventionally the diamond radiator is set to have the beam polarization plane parallel or perpendicular to the x-z plane in the detector lab system, namely $\varphi_0^{\parallel} = 0$ and $\varphi_0^{\perp} = 90°$. Nevertheless, these two values can be chosen arbitrarily as long as they remain orthogonal to each other. For the experiments in this dissertation, slightly different values were chosen for the two beamtimes. The actual values were obtained directly from the data by fitting the $\phi_{\gamma'}$ distributions. In order to maximize the statistics, the distributions were integrated over $\theta_{\gamma'}$ and ω_{γ}. The same distributions were calculated for the full and empty target samples; the latter was scaled with the ratio of the photon beam fluxes and subtracted from the former. The resulting distributions were fitted using the following function, derived from Eq. (9.1):

$$f(\phi_{\gamma'}) = a + b\cos(2(\phi_{\gamma'} + \varphi_0)), \tag{9.3}$$

where a and b are parameters accounting for the unpolarized cross-section, the beam asymmetry and the degree of linear polarization. The resulting distributions are reported in Fig. 9.2, and the values of φ_0 obtained are:

- March 2018: $\varphi_0^{\parallel} = 45°$ and $\varphi_0^{\perp} = -45°$
- July 2018: $\varphi_0^{\parallel} = 43°$ and $\varphi_0^{\perp} = -46°$.

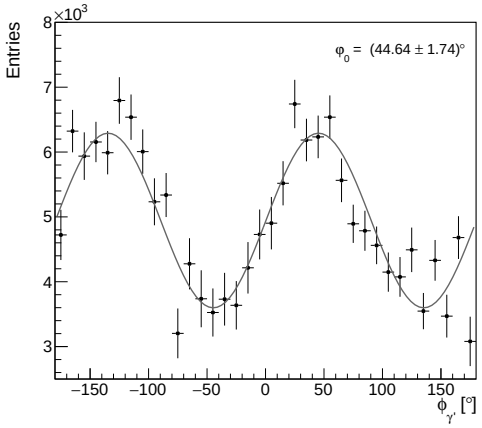

(a) March 2018 - Parallel.

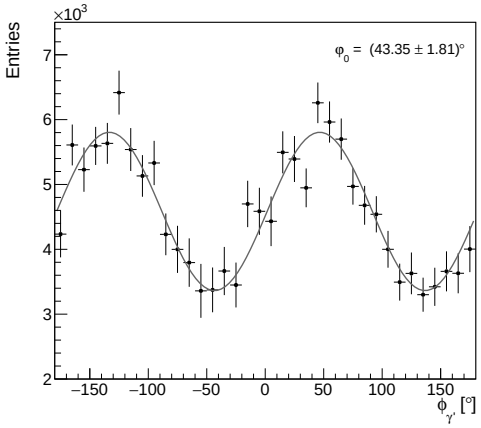

(b) July 2018 - Parallel.

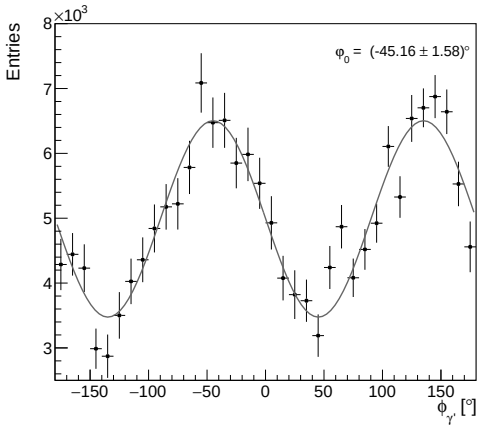

(c) March 2018 - Perpendicular.

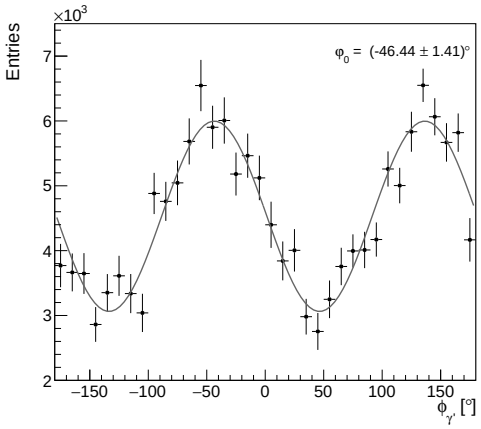

(d) July 2018 - Perpendicular.

Figure 9.2: Extraction of φ_0 by fitting $\phi_{\gamma'}$ distributions separated for the two beamtimes, for the parallel and perpendicular datasets. The gray curves are the fit functions defined in Eq. (9.3). The values of φ_0 obtained for each dataset are reported in the figures. The 90° shift in the cosine distribution between the parallel and perpendicular distributions is clearly visible.

From Eq. (9.1), the two polarized cross-sections with the two different orientations of the photon polarization plane can be defined as:

$$\sigma^{\parallel}(\omega_\gamma, \theta_{\gamma'}, \varphi) = \sigma_{unpol}(\omega_\gamma, \theta_{\gamma'}) \left(1 + p_\gamma^{\parallel} \Sigma_3 \cos(2\varphi)\right) \tag{9.4}$$

and

$$\begin{aligned} \sigma^{\perp}(\omega_\gamma, \theta_{\gamma'}, \varphi) &= \sigma_{unpol}(\omega_\gamma, \theta_{\gamma'}) \left(1 + p_\gamma^{\perp} \Sigma_3 \cos(2(\varphi + 90^\circ))\right) \\ &= \sigma_{unpol}(\omega_\gamma, \theta_{\gamma'}) \left(1 - p_\gamma^{\perp} \Sigma_3 \cos(2\varphi)\right) \end{aligned} \tag{9.5}$$

where $\sigma^{\parallel(\perp)} \equiv \dfrac{d\sigma}{d\Omega}^{\parallel(\perp)}$ and $p_\gamma^{\parallel(\perp)}$ are the cross-sections and the degree of linear polarization obtained with the two orthogonal orientations of the photon polarization plane, respectively. Using Eqs. (9.4) and (9.5), an asymmetry can be constructed as

$$\frac{\sigma^{\parallel} - \sigma^{\perp}}{\sigma^{\parallel} + \sigma^{\perp}} = \frac{\sigma_{unpol} \left(1 + p_\gamma^{\parallel} \Sigma_3 \cos(2\varphi)\right) - \sigma_{unpol} \left(1 - p_\gamma^{\perp} \Sigma_3 \cos(2\varphi)\right)}{\sigma_{unpol} \left(1 + p_\gamma^{\parallel} \Sigma_3 \cos(2\varphi)\right) + \sigma_{unpol} \left(1 - p_\gamma^{\perp} \Sigma_3 \cos(2\varphi)\right)}, \tag{9.6}$$

where the dependency from angles and energies are left out for convenience. The beam asymmetry Σ_3 in Eq. (9.6) can be isolated as

$$\begin{aligned} A(\varphi) = \Sigma_3 \cos(2\varphi) &= \frac{\sigma^{\parallel}(\omega_\gamma, \theta_{\gamma'}, \varphi) - \sigma^{\perp}(\omega_\gamma, \theta_{\gamma'}, \varphi)}{p_\gamma^{\perp} \sigma^{\parallel}(\omega_\gamma, \theta_{\gamma'}, \varphi) + p_\gamma^{\parallel} \sigma^{\perp}(\omega_\gamma, \theta_{\gamma'}, \varphi)} \\ &= \frac{N^{\parallel}(\omega_\gamma, \theta_{\gamma'}, \varphi) - N^{\perp}(\omega_\gamma, \theta_{\gamma'}, \varphi)}{p_\gamma^{\perp} N^{\parallel}(\omega_\gamma, \theta_{\gamma'}, \varphi) + p_\gamma^{\parallel} N^{\perp}(\omega_\gamma, \theta_{\gamma'}, \varphi)}. \end{aligned} \tag{9.7}$$

where $N^{\parallel(\perp)}$ is the number of events normalized for the photon flux for the two polarization settings used in the experiment, and $p_\gamma^{\parallel(\perp)}$ is the average degree of linear polarization obtained as:

$$p_\gamma^{\parallel(\perp)} = \frac{\sum_i^{N_e^{\parallel(\perp)}} p_{\gamma,i}^{\parallel(\perp)}}{N_e^{\parallel(\perp)}}, \tag{9.8}$$

where $N_e^{\parallel(\perp)}$ is the total number of events in the final sample for the two different polarization settings. The statistical errors of $A(\varphi)$ were calculated according to Gaussian error propagation.

The asymmetry $A(\varphi)$ defined in Eq. (9.7) was constructed from the data. At first, the asymmetry was integrated over the scattering angle $\theta_{\gamma'}$ and the beam energy ω_γ, and the resulting distribution was fitted using Eq. (9.3) to extract the value of φ_0 for the asymmetry. This should be equal to the one obtained for the

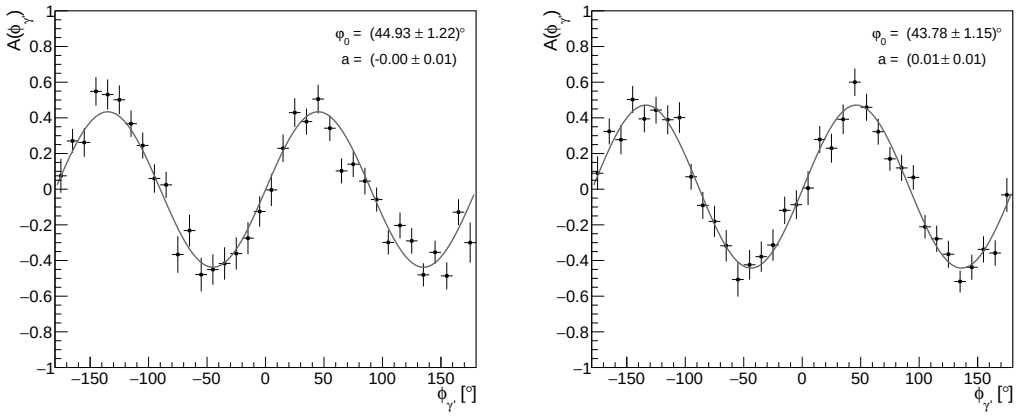

(a) March 2018. (b) July 2018.

Figure 9.3: Extraction of φ_0 from the $A(\phi_{\gamma'})$ distribution separated for the two main beamtimes. The gray curves are the fit functions defined in Eq. (9.3). The values of both φ_0 and a are reported in the canvas.

parallel distribution in Fig. 9.2. Moreover, the parameter a in Eq. (9.3) should be exactly zero if the event rates for the two different polarization settings are properly normalized. The results for the two different beamtimes are reported in Fig. 9.3. Following these results, the fitting function to be used for the extraction of the beam asymmetry Σ_3 from the data can be defined as:

$$f(\phi_{\gamma'}) = a + b\cos(2(\phi_{\gamma'} + \varphi_0)) \quad \text{where} \quad \varphi_0 = \begin{cases} (44.9 \pm 1.2) & \text{for March} \\ (43.8 \pm 1.2) & \text{for July} \end{cases} . \tag{9.9}$$

To account for the finite size of the $\phi_{\gamma'}$-binning in the $A(\varphi)$ distributions to be fitted, an additional prefactor should be added as

$$\sin(\phi_{\gamma',f} - \phi_{\gamma',i})/(\phi_{\gamma',f} - \phi_{\gamma',i}), \tag{9.10}$$

where $\phi_{\gamma',i}$ and $\phi_{\gamma',f}$ are the lower and upper limits of each bin, respectively. It can be derived from the integration over $\phi_{\gamma'}$ of the asymmetry $A(\varphi)$, where the $\cos(2\phi)$ modulation cancels out only in the sum in the denominator. Therefore, the integration of a finite bin damps the amplitude of the modulation in the numerator, causing the true-asymmetry at the mid-point to be higher than the average over the bin [136]. The final equation used to fit the experimental

asymmetry and to extract the beam asymmetry follows from Eq. (9.9):

$$f(\phi_{\gamma'}) = a + \frac{\sin(\Delta\phi_{\gamma'})}{\Delta\phi_{\gamma'}} b \cos(2(\phi_{\gamma'} + \varphi_0)) \quad \text{where} \quad \varphi_0 = \begin{cases} (44.9 \pm 1.2) & \text{for March} \\ (43.8 \pm 1.2) & \text{for July} \end{cases} \tag{9.11}$$

where $\Delta\phi\gamma' = \phi_{\gamma',f} - \phi_{\gamma',i}$ for each bin in $\phi_{\gamma'}$. A binning of 30° was chosen for this analysis, therefore the prefactor to be used for each bin can be calculated as $\sin(\phi_{\gamma',f} - \phi_{\gamma',i})/(\phi_{\gamma',f} - \phi_{\gamma',i}) = 3/\pi \approx 0.95493$. The selected photon beam energy range (see Section 7.2.3) was divided into three bins: $\omega_\gamma = 86.3{-}98.2$ MeV, $\omega_\gamma = 98.1 - 118.7$ MeV, and $\omega_\gamma = 118.7 - 140.4$ MeV. In each energy bin, the data were further divided into 12 scattering angle bins from $30 - 150°$, each 10° wide. A total of 36 $(\omega_\gamma, \theta_{\gamma'})$ bins were obtained for each of the two beamtimes. The distribution in each $(\omega_\gamma, \theta_{\gamma'})$ bin was fitted using Eq. (9.11), and the results are reported in Appendix C. In the fit, a was left as a free parameter even though it was found to be compatible with zero in the fit of the integrated distribution. The distribution of this parameter resulting from the fit of the single $(\omega_\gamma, \theta_{\gamma'})$ bins is shown in Fig. 9.4a. The distribution was fitted using a Gaussian function, and the results are reported within the figure. As expected, the mean of the distribution is consistent with zero. To examine the goodness of the fits to the data for the extraction of the beam asymmetry Σ_3, the reduced χ^2 distribution is reported in Fig. 9.4b. The average value of the distribution is very close to 1, showing an overall good quality of the fit results and a successful extraction of the beam asymmetry Σ_3 from the data.

9.1 Systematic studies

The calculation of an asymmetry is extremely convenient from the point-of-view of the systematic uncertainties, since many effects such as flux normalization, target density and Monte Carlo efficiency cancel out in the final results. The two sources of systematic uncertainties that dominate in the measurement of the beam asymmetry Σ_3 are the determination of the linear polarization degree and the background contamination.

9.1.1 Degree of linear polarization

As described in Section 6.2, the degree of linear polarization is extracted from the fit of the coherent enhancement distribution. It is not easy to estimate an error

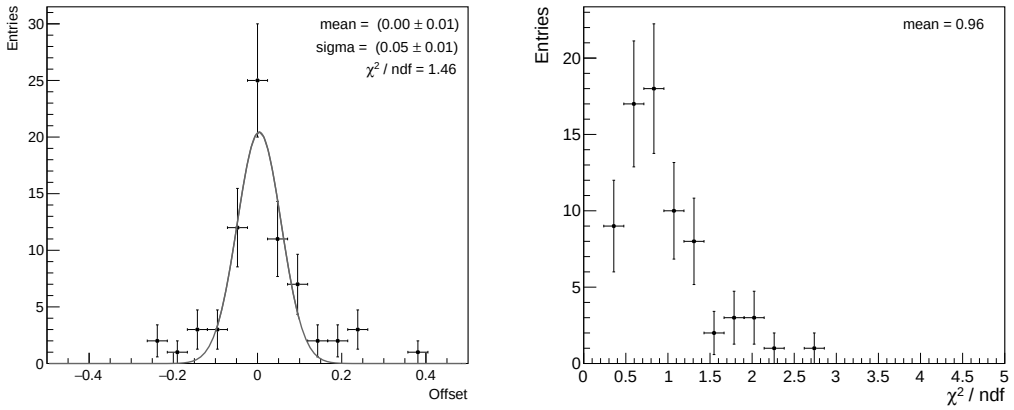

(a) Offset a in Eq. (9.11). (b) χ^2/ndf.

Figure 9.4: Distribution of the fit parameters resulting from the fit to the experimental asymmetry $A(\phi_{\gamma'})$. On the left, the offset parameter is plotted together for the two beamtimes. The Gaussian fit in gray confirms that the offset is compatible with zero. On the right, the reduced χ^2 distribution is shown. The average χ^2 value is 0.96.

due to this procedure, but an upper limit for this is estimated to be $\delta\Sigma_{pol}^{sys} = 5\%$, uniformly distributed. [97, 137].

9.1.2 Background contamination

The background contamination in the final sample can affect the beam asymmetry results. In particular, the measured asymmetry value Σ_3^{meas} can be decomposed into the real asymmetry value Σ_3^{real} and the background asymmetry Σ_3^{bkg} as:

$$\Sigma_3^{\text{meas}} = (1 - \delta_{bkg})\Sigma_3^{\text{real}} + \delta_{bkg}\Sigma_3^{\text{bkg}}, \tag{9.12}$$

where δ_{bkg} is the background contamination in the final sample. Since the background contamination is generally low as discussed in Section 8.1.5, it is difficult to properly determine the background asymmetry Σ_3^{bkg}, and different attempts of using a sideband analysis to calculate the background asymmetry led to an unreliable value with a very large systematic error. Therefore, it was not possible to extract the real asymmetry value from the measured one. It was decided, instead, to assign a systematic error to account for possible background contamination in the final sample. As an upper limit, it is safe to assume that the absolute systematic error due to the background contamination is of the same order as the relative background contamination left in the sample. This derives from the assumption that Σ_3^{bkg} can take any value from the physically allowed

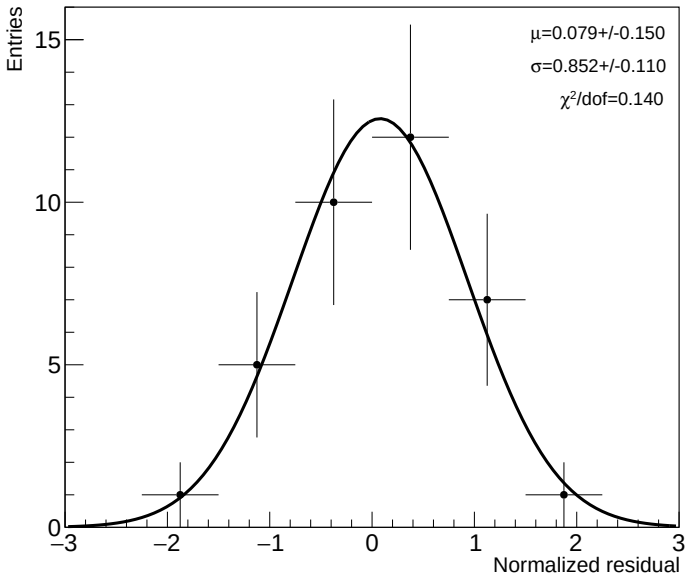

Figure 9.5: Normalized residual for the Compton scattering beam asymmetry Σ_3 obtained using the March 2018 data with respect to the results obtained using the July 2018 data. A Gaussian fit was also performed (black line), and the results are reported on the right.

interval $[-1, 1]$ and was discussed in details in Ref. [137]. Despite the fact that it may overestimate this source of systematic uncertainty, it was decided to take

$$\Delta\Sigma^{sys}_{bkg}(\omega_\gamma, \theta_{\gamma'}) = \delta_{bkg}(\omega_\gamma, \theta_{\gamma'})/100, \tag{9.13}$$

where $\delta_{bkg}(\omega_\gamma, \theta_{\gamma'})$ is the percentage of background contamination as reported in Fig. 8.12. The analysis for the extraction of the beam asymmetry was performed with a different beam energy binning, because of the larger statistical errors. As explained before, the same 15 tagger channels used for the unpolarized cross-section were divided in three asymmetrical bins: the first beam energy bin is the same for both unpolarized cross-section and beam asymmetry, while each of the other two bins of the Σ_3 analysis were obtained by merging two of the bins of the cross-section analysis. Therefore, the background contamination for the second and the third energy bins of the Σ_3 analysis was obtained as an average between the second and third, and the fourth and fifth energy bin in Fig. 8.12, respectively.

9.1.3 Comparison of the two beamtimes

The beam asymmetry results obtained using the two different beamtimes were compared and the distribution of the normalized residuals was checked, as it was done for the unpolarized cross-section in Section 8.1.6. The normalized residuals were calculated using Eq. (8.10) and the results are reported in Fig. 9.5. A Gaussian fit was also performed and the results are reported in the canvas. The fit results seem to exclude a possible systematic shift. However, due to the small number of points the fit may not be fully reliable. The mean and RMS of the 36 normalized residual were calculated, resulting in $\mu = 0.10$ and RMS $= 0.80$, respectively, confirming the fit results. The $\mu/\text{RMS} = 0.125$ indicates that the bias is negligible, considering also the sizable uncertainty on the degree of linear polarization. The normalized residual distributions for the three different bins in beam energy were also checked, and the means and RMS of the three groups of 12 residual were calculated as well. The obtained results are:

$$\begin{aligned}
\omega_\gamma = 92.2 \text{ MeV} : \mu = 0.26, \quad \text{RMS} = 0.80 \\
\omega_\gamma = 108.5 \text{ MeV} : \mu = 0.15, \quad \text{RMS} = 0.87 \\
\omega_\gamma = 129.5 \text{ MeV} : \mu = -0.16, \quad \text{RMS} = 0.84.
\end{aligned}$$

Similar to the unpolarized cross-section results, there seems to be a small offset in the first energy bin, but in this case it has the opposite sign because the beam asymmetries are negative. This bias can be corrected by increasing the March results by 6%, same as for the cross-section. It was therefore decided to account for an additional 3% systematic uncertainty for this first energy bin.

9.1.4 Sum of systematic uncertainties

For the beam asymmetry Σ_3, the relative systematic uncertainty in the extraction of the linear polarization $\delta\Sigma_{pol}^{sys}$ affects all the final points in the same way, scaling the final results up or down. The absolute systematic uncertainty due to the background contamination and the relative uncertainty due to the imperfect agreement of the low-energy points between the two different beamtimes may affect each point independently. The different systematic uncertainties are summarized in Table 9.1. The total systematic error in RMS units can be calculated as:

$$\delta\Sigma_{corr}^{sys} = \delta\Sigma_{pol}^{sys} = \left(5/\sqrt{3}\right)\% \approx 2.89\% \tag{9.14}$$

Table 9.1: Relative systematic uncertainties on the Compton scattering beam asymmetry Σ_3 in RMS units.

$\delta\Sigma^{sys}_{pol}$	$\Delta\Sigma^{sys}_{bkg}$	$\delta\Sigma^{sys}_{beam}$
2.89%	see Fig. 8.12	$\begin{cases} 3\%, & \text{if } \omega_\gamma \leq 98.2 \text{ MeV} \\ 0, & \text{otherwise} \end{cases}$

$$\Delta\Sigma^{sys}_{uncorr}(\omega_\gamma, \theta_{\gamma'}) = \sqrt{\left(\Delta\Sigma^{sys}_{bkg}(\omega_\gamma, \theta_{\gamma'})\right)^2 + \left(\delta\Sigma^{sys}_{beam}(\omega_\gamma, \theta_{\gamma'})\Sigma_3(\omega_\gamma, \theta_{\gamma'})\right)^2}.$$

where subscripts *corr* and *uncorr* indicates that the systematic errors are correlated and point-to-point uncorrelated, respectively. It is important to note here that the latter is given as an absolute error, as opposed to the former.

9.2 Results

Figs. 9.6 to 9.8 show the new A2 Collaboration data on the proton Compton scattering beam asymmetry Σ_3 for the March and July 2018 beamtimes separately, and for the combined results, respectively. They cover a photon beam energy from 86.2 to 140.4 MeV, in three different bins. The error bars represent the statistical errors. The absolute systematic uncertainties are depicted as gray bars, and they were calculated as

$$\Delta\Sigma^{sys}_{tot}(\omega_\gamma, \theta_{\gamma'}) = \sqrt{\left(\delta\Sigma^{sys}_{corr}\Sigma_3(\omega_\gamma, \theta_{\gamma'})\right)^2 + \left(\Delta\Sigma^{sys}_{uncorr}(\omega_\gamma, \theta_{\gamma'})\right)^2}. \tag{9.15}$$

The brown curves represent the Born contribution to the beam asymmetry Σ_3. The red, the blue and the green curves represent the theoretical calculations within DR [40, 41], BχPT [47] and HBχPT [52] frameworks, respectively. In each of these calculations, the values for the different polarizabilities were fixed at: $\alpha_{E1} = 11.2$, $\beta_{M1} = 2.5$, $\gamma_{E1E1} = -2.87$, $\gamma_{M1M1} = 2.70$, $\gamma_{E1M2} = -0.85$, and $\gamma_{M1E2} = 2.04$, in the usual units. The values for the scalar polarizabilities are the ones quoted by the PDG [55], while the spin polarizabilities were taken from the last experimental paper from the A2 Collaboration [19]. Also for the case of the beam asymmetry, the χEFT based theories could predict the values for the spin polarizabilities, but it was decided to keep them fixed at the most recent experimental values in order to have a direct comparison between the three theories using the same parameters.

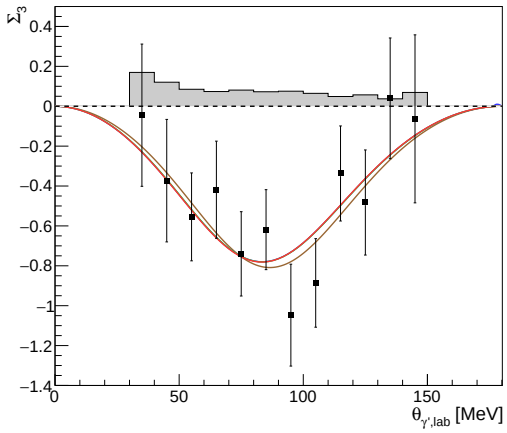

(a) 86.3 MeV $< \omega_\gamma <$ 98.2 MeV.

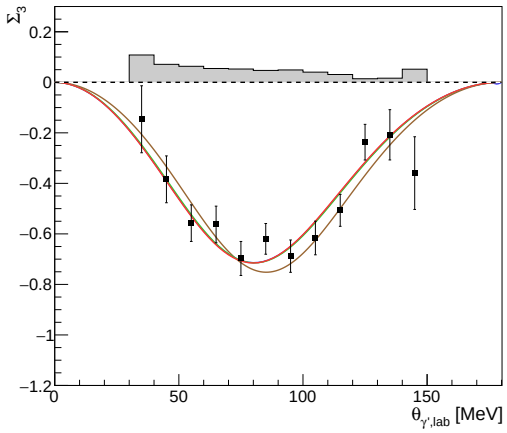

(b) 98.1 MeV $< \omega_\gamma <$ 118.7 MeV.

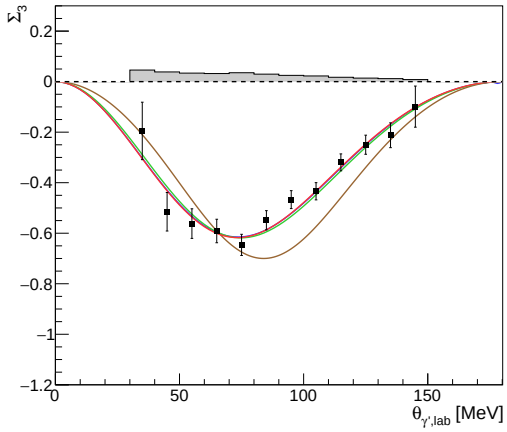

(c) 118.7 MeV $< \omega_\gamma <$ 140.4 MeV.

Figure 9.6: The new A2 Collaboration data on the proton Compton scattering beam asymmetry Σ_3 using the March 2018 data, for the three different beam energy bins. The errors are statistical only. The systematic uncertainties are depicted as gray bars. Brown curves represent the Born contribution only. Red, blue and green curves represent the theoretical calculation for fixed values of both scalar and spin polarizabilities within DR [40, 41], BχPT [47] and HBχPT [52] frameworks, respectively.

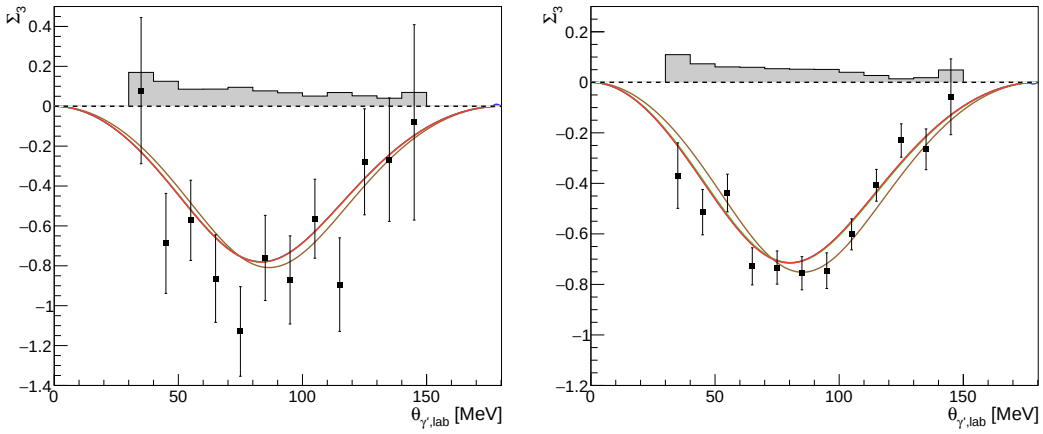

(a) 86.3 MeV $< \omega_\gamma <$ 98.2 MeV.

(b) 98.1 MeV $< \omega_\gamma <$ 118.7 MeV.

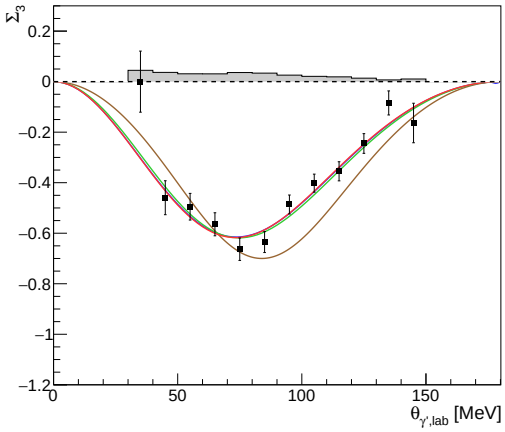

(c) 118.7 MeV $< \omega_\gamma <$ 140.4 MeV.

Figure 9.7: The new A2 Collaboration data on the proton Compton scattering beam asymmetry Σ_3 using the July 2018 data, for the three different beam energy bins. The errors are statistical only. The systematic uncertainties are depicted as gray bars. The brown curves represent the Born contribution only. Red, blue and green curves represent the theoretical calculation for fixed values of both scalar and spin polarizabilities within DR [40, 41], BχPT [47] and HBχPT [52] frameworks, respectively.

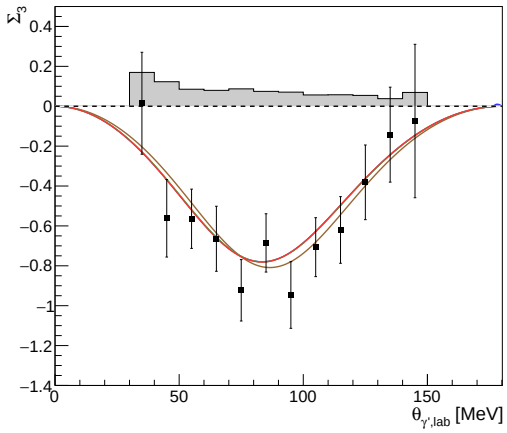

(a) 86.3 MeV $< \omega_\gamma <$ 98.2 MeV.

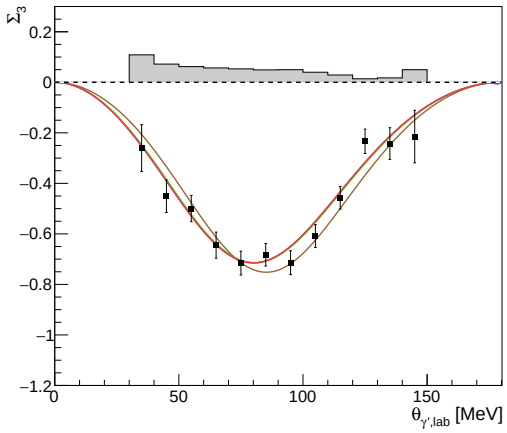

(b) 98.1 MeV $< \omega_\gamma <$ 118.7 MeV.

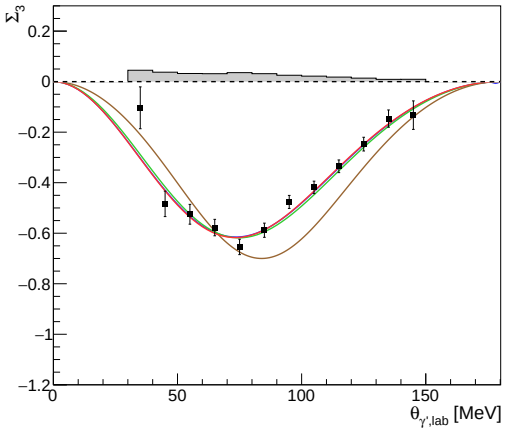

(c) 118.7 MeV $< \omega_\gamma <$ 140.4 MeV.

Figure 9.8: The new A2 Collaboration data on the proton Compton scattering beam asymmetry Σ_3 combining the results from the two different beamtimes, for the three different beam energy bins. The errors are statistical only. The systematic uncertainties are depicted as gray bars. The brown curves represent the Born contribution only. Red, blue and green curves represent the theoretical calculation for fixed values of both scalar and spin polarizabilities within DR [40, 41], BχPT [47] and HBχPT [52] frameworks, respectively.

Chapter 10

Results and discussion

The new A2 Collaboration data on the proton Compton scattering unpolarized cross-section $d\sigma/d\Omega$ and beam asymmetry Σ_3 were presented in Chapters 8 and 9, respectively. These results were obtained from the analysis of two different datasets taken in March and July 2018 at the MAMI tagged photon facility in Mainz, Germany. They provide new high-statistics measurements well suited for the study of the proton scalar polarizabilities α_{E1} and β_{M1}, two parameters that quantify the response of a proton to an applied external electromagnetic field. As discussed in the theoretical review at the beginning of this dissertation, these two scalar polarizabilities contribute to the second order of the effective Hamiltonian — as well as to the low-energy expansion of the cross-section — for Compton scattering. They can therefore be extracted by fitting the data using one of the different theoretical models available.

The fits to the new data presented in this thesis were performed with a routine that takes the polarizabilities as input parameters and varies them in order to find the values that best describe the data. This is done by minimizing a χ^2 distribution usually defined as:

$$\chi^2(\mathcal{P}) = \sum_{j}^{N_{sets}} \left(\sum_{i}^{N_{pt}^{j}} \left(\frac{O_{ij}^{exp} - O_{ij}^{thr}(\mathcal{P})}{\Delta O_{ij}^{exp}} \right)^2 \right), \tag{10.1}$$

where O_{ij}^{exp} are the experimental values of the measured observable, ΔO_{ij}^{exp} are their statistical uncertainties in RMS units and $O_{ij}^{thr}(\mathcal{P})$ are the predicted theoretical values for the given set of polarizabilities $\mathcal{P}$. The sums run over all the datasets $j = 1, \ldots, N_{sets}$ and the experimental points $i = 1, \ldots, N_{pt}^{j}$ in each dataset. The uncorrelated point-to-point systematic errors were added in quadrature to the statistical ones. The correlated systematic uncertainties, instead, were

included into the fit as common normalization factors, one for each dataset, and treated as additional fit parameters. The consequent χ^2 function to be minimized was obtained by modifying Eq. (10.1) as follows [138]

$$\chi^2(\mathcal{P}) = \sum_j^{N_{sets}} \left(\sum_i^{N_{pt}^j} \left(\frac{s_j O_{ij}^{exp} - O_{ij}^{thr}(\mathcal{P})}{s_j \Delta O_{ij}^{exp}} \right)^2 + \left(\frac{s_j - 1}{\Delta s_j} \right)^2 \right), \tag{10.2}$$

where s_j is the scaling factor for the j-th dataset. The χ^2 function was minimized using the MINUIT minimization routine [139] and the result of the fit is the set of polarizabilities $\bar{\mathcal{P}}$ that correspond to the minimum of the χ^2 function.

10.1 Data fitting with L'vov DR model

The first analyses were done using the dataset from the TAPS collaboration, presented in Section 3.1.5. It was fitted using the same conditions as in Ref. [67], using the L'vov DR model [68] with the pion photoproduction multipoles of Arndt *et al.* [42], solution SAID-SM99K, and by fixing the value of the backward spin polarizability $\gamma_\pi = -37.1$ [140]. The results obtained were identical to those reported in Table 3 in the original publication [67].

This analysis was simply used as a test for the validity of the fitter. The commonly accepted value for the backward polarizability is slightly different from what was used for the fitting of the TAPS dataset. The most recent value comes from a combined analysis of some existing datasets from MAMI [140], LARA [141] and Saskatoon [65], resulting in $\gamma_\pi = -38.7$ [26]. Moreover, more recent pion photoproduction multipoles are available, with the inclusion of the newer data. For the analyses of the new data, it was decided to use the MAID07 model [44]. The changes both in the value of the γ_π constraint and in the model used for the calculation of the multiple amplitudes may affect the results of the fit by shifting the central values of the two scalar polarizabilities, but they should not influence the final errors. The fits to the TAPS dataset were repeated with the new conditions, with and without the Baldin sum rule constraint $\alpha_{E1} + \beta_{M1} = 13.8 \pm 0.4$, and the minimum of the χ^2 function in Eq. (10.1) was obtained with the following polarizabilities:

$$\begin{aligned} &\text{with } \alpha + \beta = 13.8 \pm 0.4 && \text{with } \alpha + \beta = \text{free} \\ &\alpha_{E1} = 11.6 \pm 0.4 \pm 1.0 && \alpha_{E1} = 11.2 \pm 0.5 \pm 1.2 \\ &\beta_{M1} = 2.1 \mp 0.4 \mp 0.8 && \beta_{M1} = 1.5 \pm 0.7 \pm 0.3 \end{aligned} \tag{10.3}$$

$$\chi^2_{red} = 83.20/64 = 1.30 \qquad \chi^2_{red} = 82.30/63 = 1.31$$

where the quoted errors are statistical and systematic, respectively. The systematic errors are calculated as the difference in the values of α_{E1} and β_{M1} caused by a 3% scaling of the whole dataset. Comparing these values with the original ones reported in Section 3.1.5 and Table 3.1, the errors did not change, while the central values of β_{M1} slightly increased.

The same fit procedure was performed on the new data. The two different beamtimes were treated as independent datasets resulting in 192 points in total, divided in four different datasets: two cross-section datasets with 60 points each, and two beam asymmetry datasets with 36 points each. The uncorrelated point-to-point systematic uncertainties $\delta\sigma^{sys}_{uncorr}$ and $\Delta\Sigma^{sys}_{uncorr}$ of Eqs. (8.14) and (9.14) were added in quadrature to the statistical errors of the cross-section and the beam asymmetry values, respectively. The fit to the new A2 Collaboration data with and without the Baldin sum rule constraint resulted in:

$$\begin{array}{rr}
\text{with } \alpha+\beta = 13.8 \pm 0.4 & \text{with } \alpha+\beta = \text{free} \\
\alpha_{E1} = 11.67 \pm 0.17 \pm 1.00 & \alpha_{E1} = 11.78 \pm 0.18 \pm 1.10 \\
\beta_{M1} = 2.77 \mp 0.23 \mp 0.52 & \beta_{M1} = 3.02 \pm 0.26 \pm 0.33 \\
\chi^2_{red} = 155.01/191 = 0.81 & \chi^2_{red} = 150.96/190 = 0.79
\end{array} \tag{10.4}$$

where the quoted errors are statistical and systematic, respectively. The latter are calculated in the same way as for the TAPS results. The four datasets were scaled by their relative systematic errors in RMS units $\delta\sigma^{sys}_{corr} = 3\%$ and $\Delta\Sigma^{sys}_{corr} = 5/\sqrt{3}\%$ for the cross-section and the beam asymmetry, respectively. The fits were repeated with the scaled datasets and the differences in the central values of α_{E1} and β_{M1} were assigned as systematic errors.

To compare the polarizabilities extracted from the new data with the ones extracted from the TAPS dataset, reported in Eq. (10.3), the discrepancy in terms of RMS was calculated for each result using the squared sum of the statistical and systematic component as errors. When the Baldin sum rule constraint is considered, both α_{E1} and β_{M1} are in agreement well inside one sigma. In the unconstrained fit, the value of α_{E1} is still in perfect agreement, while the difference in the values of β_{M1} is larger but still consistent within two sigma. The results obtained with the new A2 Collaboration data are also in fair agreement with the values quoted by the PDG obtained from the fit of all the existing extractions ($\alpha_{E1} = 11.2 \pm 0.4$ and $\beta_{M1} = 2.5 \pm 0.4$) [55]. Since the main goal of this work was

the measurement of a new high-statistics dataset for the extraction of these two parameters, it is more interesting to compare the errors in Eqs. (10.3) and (10.4). There is an improvement by a factor two in the statistical errors, corresponding to about four times more statistics. Unfortunately, there was limited improvement in the systematic uncertainties. The two scalar polarizabilities are very sensitive to even small changes in the data, in particular to the overall scaling of the whole dataset. Therefore, this method of accounting for the correlated systematic errors by scaling all the datasets and checking the effects on the central values of α_{E1} and β_{M1} may not be the best one, since it can overestimate the systematic component to the final error.

Alternatively, correlated systematic errors can be taken into account by introducing in the fit a scaling factor for each dataset to be treated as an additional free parameter, and by changing consequently the χ^2 function as shown in Eq. (10.2). In this way, the fitter is free to scale the data to find the best χ^2, giving a more realistic estimate of the systematic errors. This is particularly useful when fitting more than one dataset simultaneously, as in the case of the new data. This approach was used to refit both TAPS and the new A2 data. The minimum χ^2 was obtained for the TAPS data with the following polarizabilities:

$$\begin{aligned}
\text{with } \alpha+\beta &= 13.8 \pm 0.4 && \text{with } \alpha+\beta = \text{free} \\
\alpha_{E1} &= 12.38 \pm 0.39 \pm 0.59 && \alpha_{E1} = 11.17 \pm 0.54 \pm 1.03 \\
\beta_{M1} &= 1.39 \mp 0.42 \mp 0.51 && \beta_{M1} = 1.33 \pm 0.70 \pm 0.24 \\
S_\sigma &= 0.975 \pm 0.019 && S_\sigma = 0.981 \pm 0.023 \\
\chi^2_{red} &= 81.50/63 = 1.29 && \chi^2_{red} = 81.45/62 = 1.31,
\end{aligned} \tag{10.5}$$

where S_σ is the scaling factor applied to the data. The fits to the new data with the inclusions of the scaling factor resulted in

$$\begin{aligned}
\text{with } \alpha+\beta &= 13.8 \pm 0.4 && \text{with } \alpha+\beta = \text{free} \\
\alpha_{E1} &= 11.08 \pm 0.17 \pm 0.45 && \alpha_{E1} = 11.76 \pm 0.18 \pm 0.63 \\
\beta_{M1} &= 3.10 \mp 0.23 \mp 0.24 && \beta_{M1} = 3.01 \pm 0.26 \pm 0.22 \\
S_{\sigma_M} &= 1.014 \pm 0.015 && S_{\sigma_M} = 0.997 \pm 0.019 \\
S_{\sigma_J} &= 1.023 \pm 0.015 && S_{\sigma_J} = 1.005 \pm 0.019 \\
S_{\Sigma_M} &= 1.006 \pm 0.019 && S_{\Sigma_M} = 1.000 \pm 0.019 \\
S_{\Sigma_J} &= 0.988 \pm 0.019 && S_{\Sigma_J} = 0.983 \pm 0.019 \\
\chi^2_{red} &= 151.59/187 = 0.81 && \chi^2_{red} = 149.07/186 = 0.80,
\end{aligned} \tag{10.6}$$

Table 10.1: Scalar polarizabilities extracted by fitting the new data using the HDPV DR code [40, 41]. When given, the errors are statistical and systematic, respectively. The spin polarizabilities were fixed or constrained to the values in Eq. (10.7), when their values are reported without and with the errors, respectively. S_{σ_M}, S_{Σ_M}, S_{σ_J}, and S_{Σ_J} are the scaling factors for the March and July 2018 datasets, for the unpolarized cross-section and the beam asymmetry points, respectively. The scalar and spin polarizability values are in units of 10^{-4} fm^3 and 10^{-4} fm^4, respectively.

$\alpha_{E1} + \beta_{M1}$	13.8 ± 0.4	Free	13.8 ± 0.4	Free
γ	Fixed	Fixed	Constrained	Constrained
α	$11.25 \pm 0.16 \pm 0.41$	$11.76 \pm 0.17 \pm 0.58$	$11.30 \pm 0.30 \pm 0.41$	$12.08 \pm 0.33 \pm 0.58$
β	$2.84 \mp 0.21 \mp 0.21$	$2.80 \pm 0.24 \pm 0.18$	$2.91 \mp 0.34 \mp 0.28$	$3.10 \pm 0.41 \pm 0.21$
γ_{E1}	-2.87	-2.87	-2.99 ± 0.50	-2.81 ± 0.51
γ_{M1}	2.7	2.7	2.99 ± 0.32	3.14 ± 0.32
γ_{M2}	-0.85	-0.85	-0.72 ± 0.64	-0.35 ± 0.67
γ_{E2}	2.04	2.04	1.76 ± 0.39	1.75 ± 0.39
S_{σ_M}	1.005 ± 0.015	0.991 ± 0.018	1.012 ± 0.016	0.995 ± 0.019
S_{σ_J}	1.014 ± 0.015	1.000 ± 0.018	1.022 ± 0.016	1.004 ± 0.019
S_{Σ_M}	1.008 ± 0.019	1.004 ± 0.019	1.006 ± 0.019	0.998 ± 0.020
S_{Σ_J}	0.989 ± 0.019	0.986 ± 0.019	0.988 ± 0.019	0.981 ± 0.020
χ^2/DOF	$153.56/187 = 0.821$	$152.15/186 = 0.818$	$151.54/187 = 0.810$	$148.08/186 = 0.796$

where $S_{\sigma_{M(J)}}$ and $S_{\Sigma_{M(J)}}$ are the scaling factors applied to the unpolarized cross-section and the beam asymmetry results obtained using the March (July) 2018 data, respectively. In both Eqs. (10.5) and (10.6) the errors on the polarizabilities are statistical and systematic, respectively. The latter are calculated as the squared difference between the final error reported by the fitter with and without the scaling factor. Comparing Eqs. (10.4) and (10.6), the central values were slightly changed by the introduction of the scaling factors, because the four new parameters changed the χ^2 distribution. It is interesting that the final values of the scaling factors reported in Eqs. (10.4) and (10.6) are always smaller than the input ones, 3% and $5/\sqrt{3}$% for the unpolarized cross-section and the beam asymmetry, respectively. This could indicate that the various systematic effects are more accurate than the estimated precision, and it is reflected in the smaller systematic uncertainties in the final values of α_{E1} and β_{M1}.

Taken all together, these first analyses on the new A2 Collaboration data show a big statistical improvement compared to the TAPS data, together with a clear understanding of the systematic uncertainties whose final effects on the experimental points may be slightly overestimated.

10.2 Data fitting with HDPV DR model

The fits described in the previous section were useful to directly compare the new data with the already published one. Nevertheless, the L'vov code does not allow for the fit and the control of each single spin polarizability. They are parameters that enter at the third order in the energy expansion of the Compton scattering effective Hamiltonian, and even though they start to significantly affect the cross-section only for beam energies above the pion photoproduction threshold, they can still play a role in the fitting of low-energy data. For this reason, the new data were fitted using more recent and complete models, within both DR and BχPT frameworks.

The fits described in this section were performed using a fixed-t dispersion relation code provided by Barbara Pasquini [40, 41]. As with the L'vov model used before, it can take the polarizabilities α_{E1}, β_{M1}, and γ_π as input. However, it can also take the individual spin polarizabilities as input, permitting the fitter to fix them (zero error), or allow them to vary within a constraint (non-zero error), or allow them to vary freely (no error). For all the fits described from now on, the spin polarizabilities were set to be equal to the most recent experimental values published by the A2 Collaboration [19]:

$$\begin{aligned} \gamma_{E1E1} &= -2.87 \pm 0.52 \\ \gamma_{M1M1} &= 2.70 \pm 0.43 \\ \gamma_{E1M2} &= -0.85 \pm 0.72 \\ \gamma_{M1E2} &= 2.04 \pm 0.43, \end{aligned} \tag{10.7}$$

where the errors were used to constrain the four parameters in the fit.

The first fits were performed combining all the new datasets, for a total of 192 points. The fits were performed both with and without the Baldin sum rule constraint and the spin polarizabilities were either fixed or allowed to vary within their experimental errors. The results are reported in Table 10.1. A few preliminary observations can be made from this analysis. There is a big improvement (of almost a factor of three) in both statistical and systematic errors compared to the previously published experimental extractions of the scalar polarizabilities summarized in Table 3.1. It is also interesting to note that the central values of α_{E1} and β_{M1} do not change significantly when the spin polarizabilities are allowed to vary within their experimental errors. This is an indication that the new datasets presented in this work are well suited for the study of the scalar

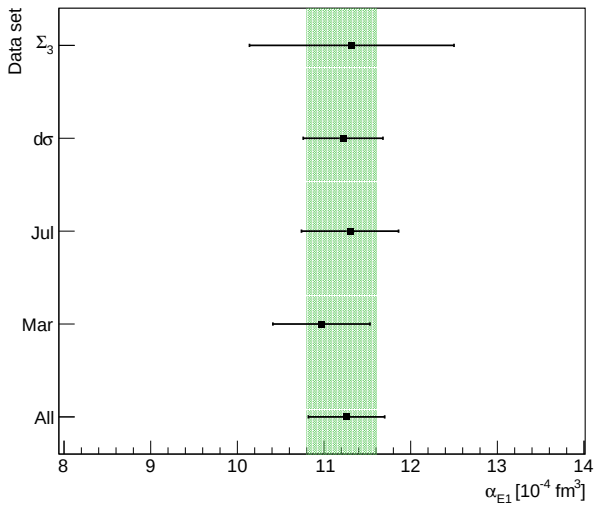

(a) α_{E1}.

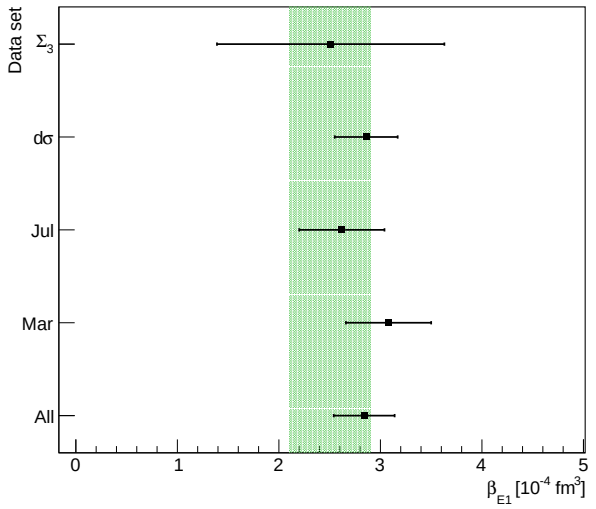

(b) β_{M1}.

Figure 10.1: Comparison of the scalar polarizabilities extracted by fitting different combinations of the new data using a DR model [40, 41]. "Mar" and "Jul" correspond to the fits using only March or July 2018 dataset, respectively. $d\sigma$ and Σ_3 correspond to the fits using only the unpolarized cross-section or the the beam asymmetry points, respectively. "All" indicates the results using all the new data. The fits were performed with the Baldin sum rule constraint $\alpha_{E1} + \beta_{M1} = 13.8$ and the spin polarizabilities were fixed at the values in Eq. (10.7). The light green band shows the polarizability value quoted by the PDG [55].

Table 10.2: Scalar polarizabilities extracted by fitting March and July 2018 datasets separately, using the HDPV DR code [40, 41]. When given, the errors are statistical and systematic, respectively. The spin polarizabilities were fixed to the values in Eq. (10.7). S_σ, S_Σ are the scaling factors for the unpolarized cross-section and the beam asymmetry points, respectively. The scalar and spin polarizability values are in units of 10^{-4} fm^3 and 10^{-4} fm^4, respectively.

$\alpha_{E1} + \beta_{M1}$	13.8 ± 0.4	Free	13.8 ± 0.4	Free
Beamtime	March	March	July	July
α	$10.96 \pm 0.22 \pm 0.51$	$11.84 \pm 0.25 \pm 0.83$	$11.30 \pm 0.22 \pm 0.51$	$11.68 \pm 0.25 \pm 0.83$
β	$3.08 \mp 0.27 \mp 0.32$	$3.01 \pm 0.34 \pm 0.26$	$2.62 \mp 0.27 \mp 0.32$	$2.60 \pm 0.34 \pm 0.25$
γ_{E1}	-2.87	-2.87	-2.87	-2.87
γ_{M1}	2.7	2.7	2.7	2.7
γ_{M2}	-0.85	-0.85	-0.85	-0.85
γ_{E2}	2.04	2.04	2.04	2.04
S_σ	1.014 ± 0.018	0.990 ± 0.025	1.012 ± 0.018	1.002 ± 0.025
S_Σ	1.010 ± 0.019	1.002 ± 0.020	0.991 ± 0.019	0.988 ± 0.020
χ^2/DOF	$83.03/93 = 0.893$	$81.40/92 = 0.885$	$70.16/93 = 0.754$	$69.82/92 = 0.759$

Table 10.3: Scalar polarizabilities extracted by fitting the unpolarized cross-section and the beam asymmetry separately, using the HDPV DR code [40, 41]. When given, the errors are statistical and systematic, respectively. The spin polarizabilities were fixed to the values in Eq. (10.7). S_M, S_J are the scaling factors for the March and July 2018 datasets, respectively. The scalar and spin polarizability values are in units of 10^{-4} fm^3 and 10^{-4} fm^4, respectively.

$\alpha_{E1} + \beta_{M1}$	13.8 ± 0.4	Free	13.8 ± 0.4	Free
Observable	$d\sigma/d\Omega$	$d\sigma/d\Omega$	Σ_3	Σ_3
α	$11.22 \pm 0.16 \pm 0.43$	$11.78 \pm 0.18 \pm 0.62$	$11.32 \pm 1.04 \pm 0.56$	$11.80 \pm 1.29 \pm 1.30$
β	$2.86 \mp 0.21 \mp 0.23$	$2.82 \pm 0.31 \pm 0.18$	$2.51 \mp 1.01 \mp 0.48$	$2.51 \pm 1.07 \pm 0.33$
γ_{E1}	-2.87	-2.87	-2.87	-2.87
γ_{M1}	2.7	2.7	2.7	2.7
γ_{M2}	-0.85	-0.85	-0.85	-0.85
γ_{E2}	2.04	2.04	2.04	2.04
S_M	1.006 ± 0.015	0.991 ± 0.019	1.008 ± 0.020	1.004 ± 0.023
S_J	1.015 ± 0.015	1.000 ± 0.019	0.991 ± 0.020	0.987 ± 0.023
χ^2/DOF	$101.03/117 = 0.864$	$99.63/116 = 0.859$	$52.53/69 = 0.761$	$52.42/68 = 0.771$

polarizabilities without much interference from higher order terms.

Instead of fitting all the new data together, the scalar polarizabilities were also extracted from various combinations of the new datasets. These analyses were performed keeping the values of the spin polarizabilities fixed to reduce the number of parameters in the fit. This was particularly useful for the fitting of the beam asymmetry data alone, since there are fewer points with larger statistical errors compared to the cross-section data. The results are reported in Tables 10.2 and 10.3. In the first one, the data of the two beamtimes were fit separately. Each fit includes 60 unpolarized cross-section and 36 beam asymmetry points. It is interesting to note that, although the results are in agreement within one sigma, β_{M1} extracted from the March 2018 data is higher compared to the results

from July 2018. Also, the results from the latter are almost independent from the $\alpha_{E1} + \beta_{M1}$ constraint, while this is not true for the former in which the central value of α_{E1} shifted to a higher value when the Baldin sum rule is not considered. A possible cause for this small difference in the results could be the difference in the empty target samples collected during the two beamtimes, as explained in Section 8.1.4. Even though a systematic shift in the two results was not observed, due to the high sensitivity of α_{E1} and β_{M1} to variations in the unpolarized cross-section, even small fluctuations in the results can cause noticeable changes in the extracted polarizabilities.

Table 10.3 shows the results obtained by fitting the two observables independently. All the results obtained are in good agreement among themselves. As expected, the results of the fit to the beam asymmetry data alone have much higher errors. Comparing the first two columns in Tables 10.1 and 10.3, it can be noted how the results are almost unaffected by the inclusion of the beam asymmetry points in the fit.

Fig. 10.1 shows a comparison between the scalar polarizabilities extracted using all the new data, the two beamtimes separately, or the two observables separately. All the fits were performed with the Baldin sum rule constraint and the spin polarizabilities were fixed to the values in Eq. (10.7).

10.3 Data fitting with BχPT model

The new data were also fitted using the BχPT code from Vadim Lensky and Vladimir Pascalutsa [47]. The same constraints as in the previous HDPV fits were used. The fits were performed using all the new data, for a total of 192 points. The results are reported in Table 10.4. Similar observations can be made as for the HDPV fits. Also in these cases, the values of α_{E1} and β_{M1} seem to be almost independent on whether the spin polarizabilities are fixed or just constrained. The errors on the scalar polarizabilities are practically identical to the ones obtained from the HDPV fits, but the central values of the magnetic polarizability are systematically higher in this case. This is not unexpected considering that in all the analyses published previously, there is always a discrepancy between the results obtained within DR and BχPT frameworks. Nevertheless, this difference can be thought of as a model-dependent uncertainty on the final results. Fig. 10.2 shows a comparison between the scalar polarizabilities extracted using the two different models, with the spin polarizabilities fixed at the values in Eq. (10.7).

Fits of the separate datasets were also performed with the BχPT code. The

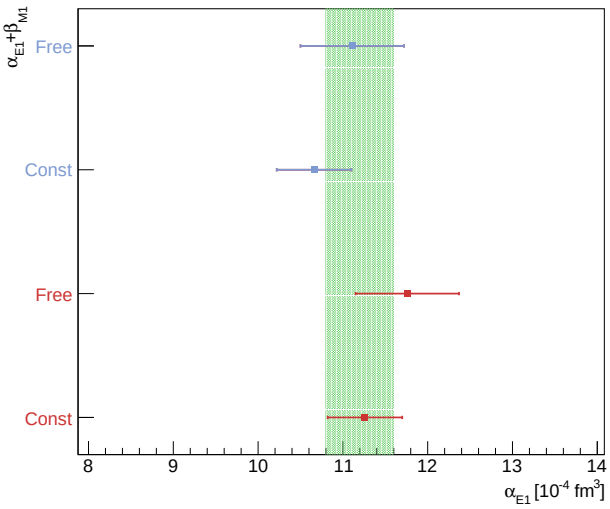

(a) α_{E1}.

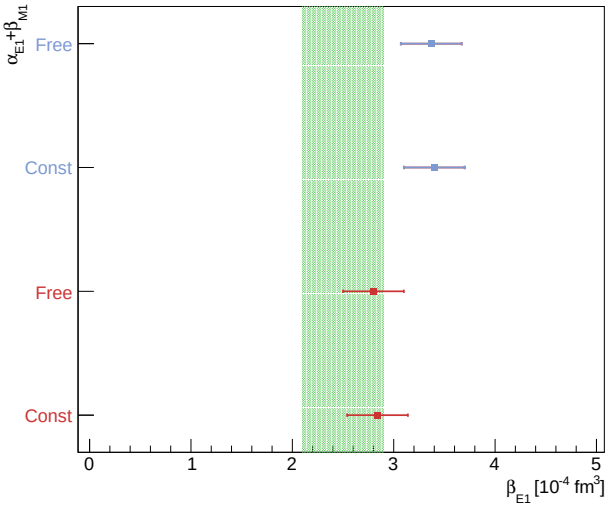

(b) β_{M1}.

Figure 10.2: Comparison of the scalar polarizabilities extracted using DR [40, 41] and BχPT [47] in red and light blue, respectively. The first and third points were obtained using the Baldin sum rule constraint $\alpha_{E1} + \beta_{M1} = 13.8$, while in the second and fourth the two scalar polarizabilities were free to vary. In all the fits the spin polarizabilities were fixed at the values in Eq. (10.7). The light green band shows the polarizability value quoted by the PDG [55].

Table 10.4: Scalar polarizabilities extracted by fitting the new data using the BχPT code [47]. When given, the errors are statistical and systematic, respectively. The spin polarizabilities were fixed or constrained to the values in Eq. (10.7), when their values are reported without and with the errors, respectively. S_{σ_M}, S_{Σ_M}, S_{σ_J}, and S_{Σ_J} are the scaling factors for the March and July 2018 datasets, for the unpolarized cross-section and the beam asymmetry points, respectively. The scalar and spin polarizability values are in units of 10^{-4} fm^3 and 10^{-4} fm^4, respectively.

$\alpha_{E1}+\beta_{M1}$	13.8 ± 0.4	Free	13.8 ± 0.4	Free
γ	Fixed	Fixed	Constrained	Constrained
α	$10.66 \pm 0.15 \pm 0.41$	$11.11 \pm 0.16 \pm 0.59$	$10.79 \pm 0.29 \pm 0.42$	$11.58 \pm 0.31 \pm 0.59$
β	$3.40 \mp 0.20 \mp 0.22$	$3.37 \pm 0.22 \pm 0.20$	$3.41 \mp 0.33 \mp 0.27$	$3.57 \pm 0.39 \pm 0.22$
γ_{E1}	-2.87	-2.87	-3.07 ± 0.50	-2.90 ± 0.51
γ_{M1}	2.7	2.7	3.09 ± 0.32	3.25 ± 0.32
γ_{M2}	-0.85	-0.85	-0.72 ± 0.65	-0.39 ± 0.67
γ_{E2}	2.04	2.04	1.80 ± 0.39	1.78 ± 0.38
S_{σ_M}	1.008 ± 0.015	0.996 ± 0.018	1.016 ± 0.016	0.999 ± 0.019
S_{σ_J}	1.016 ± 0.015	1.004 ± 0.018	1.025 ± 0.016	1.008 ± 0.019
S_{Σ_M}	1.012 ± 0.019	1.008 ± 0.019	1.009 ± 0.019	1.000 ± 0.020
S_{Σ_J}	0.995 ± 0.019	0.991 ± 0.019	0.982 ± 0.019	0.984 ± 0.020
χ^2/DOF	$154.64/187 = 0.83$	$153.72/186 = 0.83$	$151.86/187 = 0.81$	$148.50/186 = 0.80$

results show the same behaviors observed in the HDPV fits, and no further features were observed. For this reason, they are not reported in the thesis.

Chapter 11

Summary and outlook

The experiment described in this dissertation provides a new high-precision measurements of the proton Compton scattering unpolarized differential cross-section $d\sigma/d\Omega$ and beam asymmetry Σ_3. It was performed at the MAMI tagged photon facility using the A2 Collaboration experimental apparatus, in two beamtimes conducted in March and July 2018. A linearly polarized photon beam with energies from 85 to 140 MeV impinged on a liquid hydrogen target and the scattered photons were detected using the Crystal Ball/TAPS setup. The collected data were thoroughly reconstructed, calibrated and analyzed to select the final sample and to extract the two experimental observables. Particular effort was spent in the analysis of the photon flux, described in Chapter 6, to reduce as much as possible the systematic errors on the unpolarized cross-section data.

The obtained new results show a consistent improvement in statistics compared to the previously published data on both the unpolarized cross-section and the beam asymmetry below the pion photoproduction threshold, together with a careful study of the systematic uncertainties. These new data were used to extract the scalar polarizabilities in different conditions and by using two different theoretical approaches. The results are reported in Tables 10.1 to 10.4. The different datasets composing the results of this thesis give very similar results, as shown in Fig. 10.1. On the contrary, the extraction of the scalar polarizabilities — in particular of β_{M1} — exhibits a model dependence, as evident from Fig. 10.2. The best estimate of the central values for the two scalar polarizabilities was therefore calculated as the weighted average between the two theories, and the difference was used to estimate an additional error due to the model dependence. The best values for the unconstrained extraction of the scalar polarizabilities from the new

data are

$$\begin{aligned} \alpha_{E1} &= 11.43 \pm 0.17 \pm 0.59 \pm 0.33 \\ \beta_{M1} &= 3.08 \pm 0.24 \pm 0.20 \pm 0.28 \end{aligned} \tag{11.1}$$

where the errors are statistical, systematic and model dependent, respectively. The extraction using the Baldin sum rule constraint $\alpha_{E1} + \beta_{M1} = 13.8 \pm 0.4$ results in

$$\begin{aligned} \alpha_{E1} &= 10.95 \pm 0.16 \pm 0.41 \pm 0.30 \pm 0.20 \\ \beta_{M1} &= 3.12 \mp 0.20 \mp 0.22 \pm 0.28 \pm 0.20 \\ \rho_{\alpha_{E1}-\beta_{M1}} &= -0.71 \end{aligned} \tag{11.2}$$

where the additional error at the end comes from the Baldin sum rule. $\rho_{\alpha_{E1}-\beta_{M1}}$ is the correlation coefficient between the two scalar polarizabilities given by the fitter routine, and it was used to correctly draw the dark purple ellipse in Fig. 11.1. Both the results in Eqs. (11.1) and (11.2) were obtained with the spin polarizabilities fixed to the values in Eq. (10.7).

Figure 11.1 shows the new scalar polarizability extractions in purple together with some of the available results. The black circle shows the results from the TAPS collaboration [67], the highest statistic dataset published up to now. The improvement in the errors in the new data is clearly visible, proving the achievement of the main goal of the work described in this thesis. The light green circle shows the polarizability values quoted by the PDG [55]. As previously explained in Section 3.3.5, these values significantly changed in 2012 — both the central values and the errors — due to the inclusion in the average of the fit results obtained using HBChPT from McGovern *et al.* [52], without any new experimental dataset being published. The dark green circle is a full theoretical prediction within BχPT [46], while the red and the blue circles are global extractions within DR [11] and HBχPT [52]. The light gray and orange bands show the experimental results for $\alpha_{E1} - \beta_{M1}$ from Zieger *et al.* [64] and the Baldin sum rule constraint average [12], respectively.

Taken together, these tests show that the new A2 Collaboration data on the proton Compton scattering presented in this thesis provide a new high-statistics dataset perfectly suited for the extraction of the proton scalar polarizabilities. From the preliminary fits performed using only these new data, it was possible to achieve a level of precision which is comparable to the existing current global

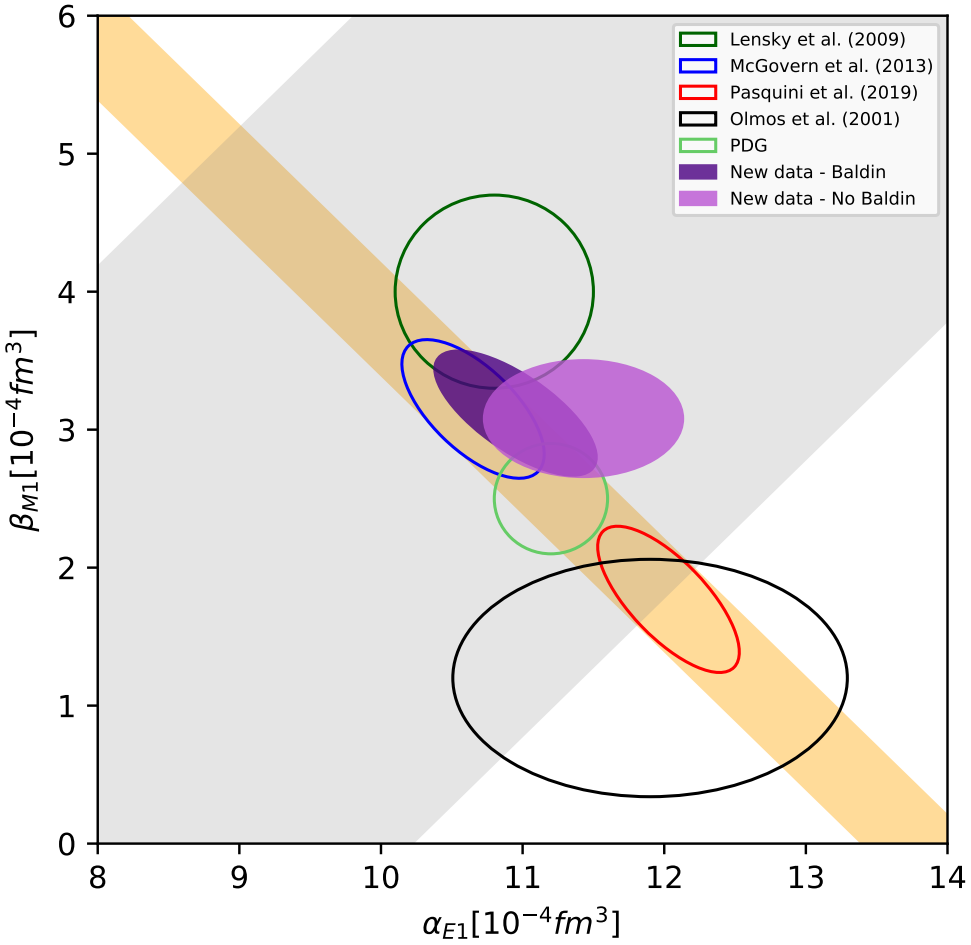

Figure 11.1: Results of α_{E1} vs β_{M1} for the proton, obtained from different experiments and theories. The extractions from the new data are depicted in light and dark purple full circles for the unconstrained and constrained fit, respectively. The final values are reported in Eqs. (11.1) and (11.2). The light gray and orange bands show the experimental results for $\alpha_{E1} - \beta_{M1}$ from Zieger *et al.* [64] and the Baldin sum rule constraint average [12], respectively. The black circle shows the results of the unconstrained fit from the TAPS collaboration [67]. The dark green curve is the BχPT prediction [46], the blue solid curve is the extraction within HBχPT [52], and the solid red curve is the bootstrap-based fit using fixed-t subtracted DRs [11]. The light green circle shows the scalar polarizabilities values quoted by the PDG [55].

extractions that combined all previous data. This indicates that these new results can be crucial in resolving the ambiguities in these existing extractions.

Moreover, the work presented provides an important contribution to the experimental Compton scattering program at MAMI. These new results can be used in combination with the already published ones on single and double spin observables to additionally improve the knowledge of the values of the spin polarizabilities, obtaining the first combined extraction of all the six proton polarizabilities from experimental data measured at the MAMI facility, and achieving a new important milestone in this program. However, to reach a satisfactory level of precision in spin polarizabilities, new precise data on the double spin polarizabilties in the $\Delta(1232)$ region are needed.

The A2 Collaboration has already planned to perform new measurements of the Σ_{2x} asymmetry. Unfortunately, the current level of precision is limited by the energy range kinematically accessible using the current experimental apparatus. To widen it, the detection of the recoil proton is needed in order to reconstruct the full events and to suppress the background contamination. This can be done by the use of an active polarized target that is currently under development. A successful test with a prototype was performed in 2016 [142].

Beyond these planned improvements on the proton data, the A2 Collaboration is also turning its focus onto studies of the polarizabilities for the neutrons, where the existing information is extremely fragmentary and limited [36], using active helium and active polarized deuterium targets in development [143].

Appendix A

Unpolarized cross-section values

A.1 March 2018

Table A.1: Unpolarized Compton scattering cross-section for $\omega_\gamma = 86.3 - 98.2$ MeV extracted using March 2018 data.

$\boldsymbol{\omega_\gamma}$ [MeV]	$\boldsymbol{\theta_{\gamma'}}$ [°]	$\boldsymbol{\frac{d\sigma}{d\Omega}}$ [nb/sr]	$\boldsymbol{\Delta\left(\frac{d\sigma}{d\Omega}\right)}$ (stat.) [nb/sr]	$\boldsymbol{\Delta\left(\frac{d\sigma}{d\Omega}\right)}$ (syst.) [nb/sr]	$\boldsymbol{\Delta\left(\frac{d\sigma}{d\Omega}\right)}$ (corr. 3%) [nb/sr]
92.2	35.0	10.391	1.902	1.802	0.312
92.2	45.0	10.572	1.000	1.304	0.317
92.2	55.0	11.826	0.751	0.998	0.355
92.2	65.0	9.766	0.757	0.751	0.293
92.2	75.0	10.481	0.726	0.792	0.314
92.2	85.0	10.136	0.688	0.707	0.304
92.2	95.0	9.726	0.754	0.554	0.292
92.2	105.0	10.808	0.835	0.579	0.324
92.2	115.0	13.249	0.947	0.694	0.397
92.2	125.0	13.372	1.114	0.785	0.401
92.2	135.0	12.444	1.641	0.687	0.373
92.2	145.0	13.000	2.907	1.018	0.390

Table A.2: Unpolarized Compton scattering cross-section for $\omega_\gamma = 98.1 - 108.4$ MeV extracted using March 2018 data.

ω_γ [MeV]	$\theta_{\gamma'}$ [°]	$\frac{d\sigma}{d\Omega}$ [nb/sr]	$\Delta\left(\frac{d\sigma}{d\Omega}\right)$ (stat.) [nb/sr]	$\Delta\left(\frac{d\sigma}{d\Omega}\right)$ (syst.) [nb/sr]	$\Delta\left(\frac{d\sigma}{d\Omega}\right)$ (corr. 3%) [nb/sr]
103.2	35.0	14.133	1.519	1.714	0.424
103.2	45.0	8.879	0.776	0.679	0.266
103.2	55.0	10.037	0.586	0.673	0.301
103.2	65.0	10.482	0.588	0.565	0.314
103.2	75.0	9.700	0.565	0.458	0.291
103.2	85.0	10.813	0.533	0.417	0.324
103.2	95.0	10.424	0.587	0.449	0.313
103.2	105.0	11.288	0.639	0.325	0.339
103.2	115.0	13.657	0.714	0.261	0.410
103.2	125.0	13.885	0.846	0.018	0.417
103.2	135.0	12.650	1.228	0.084	0.380
103.2	145.0	15.611	2.193	0.818	0.468

Table A.3: Unpolarized Compton scattering cross-section for $\omega_\gamma = 108.5 - 118.7$ MeV extracted using March 2018 data.

ω_γ [MeV]	$\theta_{\gamma'}$ [°]	$\frac{d\sigma}{d\Omega}$ [nb/sr]	$\Delta\left(\frac{d\sigma}{d\Omega}\right)$ (stat.) [nb/sr]	$\Delta\left(\frac{d\sigma}{d\Omega}\right)$ (syst.) [nb/sr]	$\Delta\left(\frac{d\sigma}{d\Omega}\right)$ (corr. 3%) [nb/sr]
113.6	35.0	9.237	1.314	0.873	0.277
113.6	45.0	9.257	0.648	0.561	0.278
113.6	55.0	8.469	0.492	0.396	0.254
113.6	65.0	9.711	0.490	0.388	0.291
113.6	75.0	10.381	0.472	0.328	0.311
113.6	85.0	11.175	0.446	0.361	0.335
113.6	95.0	11.577	0.486	0.308	0.347
113.6	105.0	12.035	0.529	0.278	0.361
113.6	115.0	13.630	0.584	0.222	0.409
113.6	125.0	14.312	0.684	0.200	0.429
113.6	135.0	13.748	0.990	0.256	0.412
113.6	145.0	18.215	1.766	0.820	0.546

Table A.4: Unpolarized Compton scattering cross-section for $\omega_\gamma = 118.7 - 130.2$ MeV extracted using March 2018 data.

ω_γ [MeV]	$\theta_{\gamma'}$ [°]	$\frac{d\sigma}{d\Omega}$ [nb/sr]	$\Delta\left(\frac{d\sigma}{d\Omega}\right)$ (stat.) [nb/sr]	$\Delta\left(\frac{d\sigma}{d\Omega}\right)$ (syst.) [nb/sr]	$\Delta\left(\frac{d\sigma}{d\Omega}\right)$ (corr. 3%) [nb/sr]
124.1	35.0	8.192	1.120	0.404	0.246
124.1	45.0	7.975	0.537	0.265	0.239
124.1	55.0	8.411	0.412	0.193	0.252
124.1	65.0	9.454	0.408	0.145	0.284
124.1	75.0	10.201	0.390	0.158	0.306
124.1	85.0	10.439	0.367	0.148	0.313
124.1	95.0	12.510	0.403	0.129	0.375
124.1	105.0	13.668	0.435	0.076	0.410
124.1	115.0	14.383	0.471	0.092	0.431
124.1	125.0	15.358	0.550	0.132	0.461
124.1	135.0	15.923	0.787	0.072	0.478
124.1	145.0	17.879	1.414	0.131	0.536

Table A.5: Unpolarized Compton scattering cross-section for $\omega_\gamma = 130.3 - 140.4$ MeV extracted using March 2018 data.

ω_γ [MeV]	$\theta_{\gamma'}$ [°]	$\frac{d\sigma}{d\Omega}$ [nb/sr]	$\Delta\left(\frac{d\sigma}{d\Omega}\right)$ (stat.) [nb/sr]	$\Delta\left(\frac{d\sigma}{d\Omega}\right)$ (syst.) [nb/sr]	$\Delta\left(\frac{d\sigma}{d\Omega}\right)$ (corr. 3%) [nb/sr]
135.3	35.0	6.589	1.168	0.265	0.198
135.3	45.0	7.534	0.549	0.179	0.226
135.3	55.0	7.561	0.425	0.110	0.227
135.3	65.0	9.798	0.421	0.093	0.294
135.3	75.0	10.645	0.399	0.135	0.319
135.3	85.0	11.256	0.377	0.096	0.338
135.3	95.0	12.021	0.407	0.082	0.361
135.3	105.0	14.004	0.444	0.090	0.420
135.3	115.0	15.194	0.477	0.103	0.456
135.3	125.0	16.426	0.553	0.067	0.493
135.3	135.0	16.672	0.785	0.107	0.500
135.3	145.0	15.843	1.421	0.089	0.475

A.2 July 2018

Table A.6: Unpolarized Compton scattering cross-section for $\omega_\gamma = 86.3 - 98.2$ MeV extracted using July 2018 data.

ω_γ [MeV]	$\theta_{\gamma'}$ [°]	$\frac{d\sigma}{d\Omega}$ [nb/sr]	$\Delta\left(\frac{d\sigma}{d\Omega}\right)$ (stat.) [nb/sr]	$\Delta\left(\frac{d\sigma}{d\Omega}\right)$ (syst.) [nb/sr]	$\Delta\left(\frac{d\sigma}{d\Omega}\right)$ (corr. 3%) [nb/sr]
92.2	35.0	12.629	1.840	2.175	0.379
92.2	45.0	12.012	1.002	1.468	0.360
92.2	55.0	11.972	0.756	1.008	0.359
92.2	65.0	10.606	0.720	0.804	0.318
92.2	75.0	11.124	0.719	0.832	0.334
92.2	85.0	10.076	0.695	0.703	0.302
92.2	95.0	11.590	0.744	0.620	0.348
92.2	105.0	13.252	0.817	0.651	0.398
92.2	115.0	12.033	0.939	0.648	0.361
92.2	125.0	13.975	1.117	0.810	0.419
92.2	135.0	16.956	1.605	0.809	0.509
92.2	145.0	15.948	2.828	1.201	0.478

Table A.7: Unpolarized Compton scattering cross-section for $\omega_\gamma = 98.1 - 108.4$ MeV extracted using July 2018 data.

ω_γ [MeV]	$\theta_{\gamma'}$ [°]	$\frac{d\sigma}{d\Omega}$ [nb/sr]	$\Delta\left(\frac{d\sigma}{d\Omega}\right)$ (stat.) [nb/sr]	$\Delta\left(\frac{d\sigma}{d\Omega}\right)$ (syst.) [nb/sr]	$\Delta\left(\frac{d\sigma}{d\Omega}\right)$ (corr. 3%) [nb/sr]
103.2	35.0	9.139	1.476	1.109	0.274
103.2	45.0	10.550	0.776	0.807	0.317
103.2	55.0	9.564	0.586	0.642	0.287
103.2	65.0	9.715	0.557	0.524	0.291
103.2	75.0	10.412	0.556	0.491	0.312
103.2	85.0	10.148	0.535	0.392	0.304
103.2	95.0	9.582	0.576	0.413	0.287
103.2	105.0	11.716	0.623	0.337	0.351
103.2	115.0	13.080	0.706	0.250	0.392
103.2	125.0	15.988	0.835	0.021	0.480
103.2	135.0	16.059	1.196	0.108	0.482
103.2	145.0	13.152	2.121	0.689	0.395

Table A.8: Unpolarized Compton scattering cross-section for $\omega_\gamma = 108.5 - 118.7$ MeV extracted using July 2018 data.

ω_γ [MeV]	$\theta_{\gamma'}$ [°]	$\frac{d\sigma}{d\Omega}$ [nb/sr]	$\Delta\left(\frac{d\sigma}{d\Omega}\right)$ (stat.) [nb/sr]	$\Delta\left(\frac{d\sigma}{d\Omega}\right)$ (syst.) [nb/sr]	$\Delta\left(\frac{d\sigma}{d\Omega}\right)$ (corr. 3%) [nb/sr]
113.6	35.0	11.070	1.264	1.046	0.332
113.6	45.0	9.601	0.639	0.582	0.288
113.6	55.0	9.095	0.483	0.425	0.273
113.6	65.0	9.255	0.456	0.370	0.278
113.6	75.0	10.078	0.454	0.318	0.302
113.6	85.0	10.809	0.441	0.349	0.324
113.6	95.0	11.013	0.469	0.293	0.330
113.6	105.0	11.754	0.508	0.272	0.353
113.6	115.0	13.556	0.571	0.221	0.407
113.6	125.0	14.782	0.668	0.207	0.443
113.6	135.0	15.094	0.956	0.281	0.453
113.6	145.0	13.806	1.690	0.621	0.414

Table A.9: Unpolarized Compton scattering cross-section for $\omega_\gamma = 118.7 - 130.3$ MeV extracted using July 2018 data.

ω_γ [MeV]	$\theta_{\gamma'}$ [°]	$\frac{d\sigma}{d\Omega}$ [nb/sr]	$\Delta\left(\frac{d\sigma}{d\Omega}\right)$ (stat.) [nb/sr]	$\Delta\left(\frac{d\sigma}{d\Omega}\right)$ (syst.) [nb/sr]	$\Delta\left(\frac{d\sigma}{d\Omega}\right)$ (corr. 3%) [nb/sr]
124.1	35.0	8.398	1.100	0.414	0.252
124.1	45.0	8.363	0.542	0.278	0.251
124.1	55.0	8.791	0.409	0.201	0.264
124.1	65.0	9.708	0.384	0.149	0.291
124.1	75.0	9.978	0.383	0.155	0.299
124.1	85.0	10.313	0.369	0.146	0.309
124.1	95.0	11.391	0.392	0.117	0.342
124.1	105.0	12.812	0.422	0.072	0.384
124.1	115.0	13.462	0.468	0.086	0.404
124.1	125.0	15.217	0.550	0.131	0.457
124.1	135.0	17.207	0.771	0.077	0.516
124.1	145.0	16.124	1.378	0.120	0.484

Table A.10: Unpolarized Compton scattering cross-section for $\omega_\gamma = 130.3 - 140.4$ MeV extracted using July 2018 data.

$\boldsymbol{\omega_\gamma}$ [MeV]	$\boldsymbol{\theta_{\gamma'}}$ [°]	$\boldsymbol{\frac{d\sigma}{d\Omega}}$ [nb/sr]	$\boldsymbol{\Delta\left(\frac{d\sigma}{d\Omega}\right)}$ (stat.) [nb/sr]	$\boldsymbol{\Delta\left(\frac{d\sigma}{d\Omega}\right)}$ (syst.) [nb/sr]	$\boldsymbol{\Delta\left(\frac{d\sigma}{d\Omega}\right)}$ (corr. 3%) [nb/sr]
135.3	35.0	5.677	1.177	0.229	0.170
135.3	45.0	7.819	0.570	0.186	0.235
135.3	55.0	8.377	0.428	0.121	0.251
135.3	65.0	9.558	0.402	0.091	0.287
135.3	75.0	9.493	0.400	0.121	0.285
135.3	85.0	11.073	0.386	0.094	0.332
135.3	95.0	12.023	0.406	0.082	0.361
135.3	105.0	13.509	0.442	0.086	0.405
135.3	115.0	14.651	0.488	0.100	0.440
135.3	125.0	16.176	0.562	0.066	0.485
135.3	135.0	16.660	0.790	0.107	0.500
135.3	145.0	17.612	1.411	0.099	0.528

Appendix B

Beam Asymmetry Σ_3 values

B.1 March 2018

Table B.1: Compton scattering beam asymmetry Σ_3 for $\omega_\gamma = 86.3 - 98.2$ MeV extracted using March 2018 data.

$\boldsymbol{\omega_\gamma}$ [MeV]	$\boldsymbol{\theta_{\gamma'}}[^\circ]$	$\boldsymbol{\Sigma_3}$	$\boldsymbol{\Delta\Sigma_3}$(stat.)	$\boldsymbol{\Delta\Sigma_3}$(syst.)	$\boldsymbol{\Delta\Sigma_3}$(corr. $5/\sqrt{3}\%$)
92.2	35.0	-0.045	0.357	0.170	0.001
92.2	45.0	-0.373	0.307	0.119	0.011
92.2	55.0	-0.555	0.220	0.080	0.016
92.2	65.0	-0.419	0.244	0.071	0.012
92.2	75.0	-0.740	0.211	0.072	0.021
92.2	85.0	-0.619	0.201	0.066	0.018
92.2	95.0	-1.047	0.255	0.054	0.030
92.2	105.0	-0.886	0.222	0.047	0.026
92.2	115.0	-0.337	0.238	0.046	0.010
92.2	125.0	-0.483	0.264	0.052	0.014
92.2	135.0	0.040	0.303	0.221	0.001
92.2	145.0	-0.063	0.421	0.057	0.002

Table B.2: Compton scattering beam asymmetry Σ_3 for $\omega_\gamma = 98.1 - 118.7$ MeV extracted using March 2018 data.

$\boldsymbol{\omega_\gamma}$ [MeV]	$\boldsymbol{\theta_{\gamma'}}[^\circ]$	$\boldsymbol{\Sigma_3}$	$\boldsymbol{\Delta\Sigma_3}$(stat.)	$\boldsymbol{\Delta\Sigma_3}$(syst.)	$\boldsymbol{\Delta\Sigma_3}$(corr. $5/\sqrt{3}\%$)
108.5	35.0	-0.146	0.133	0.108	-0.004
108.5	45.0	-0.384	0.093	0.068	-0.011
108.5	55.0	-0.558	0.072	0.057	-0.016
108.5	65.0	-0.563	0.073	0.047	-0.016
108.5	75.0	-0.697	0.067	0.039	-0.020
108.5	85.0	-0.620	0.061	0.035	-0.018
108.5	95.0	-0.688	0.064	0.035	-0.020
108.5	105.0	-0.616	0.067	0.026	-0.018
108.5	115.0	-0.507	0.063	0.018	-0.015
108.5	125.0	-0.237	0.071	0.008	-0.007
108.5	135.0	-0.208	0.100	0.013	-0.006
108.5	145.0	-0.359	0.144	0.049	-0.010

Table B.3: Compton scattering beam asymmetry Σ_3 for $\omega_\gamma = 118.7 - 140.4$ MeV extracted using March 2018 data.

$\boldsymbol{\omega_\gamma}$ [MeV]	$\boldsymbol{\theta_{\gamma'}}[^\circ]$	$\boldsymbol{\Sigma_3}$	$\boldsymbol{\Delta\Sigma_3}$(stat.)	$\boldsymbol{\Delta\Sigma_3}$(syst.)	$\boldsymbol{\Delta\Sigma_3}$(corr. $5/\sqrt{3}\%$)
129.5	35.0	-0.195	0.114	0.045	-0.006
129.5	45.0	-0.515	0.076	0.028	-0.015
129.5	55.0	-0.562	0.059	0.019	-0.016
129.5	65.0	-0.591	0.047	0.012	-0.017
129.5	75.0	-0.646	0.042	0.014	-0.019
129.5	85.0	-0.549	0.038	0.011	-0.016
129.5	95.0	-0.467	0.036	0.008	-0.013
129.5	105.0	-0.434	0.034	0.006	-0.013
129.5	115.0	-0.320	0.034	0.007	-0.009
129.5	125.0	-0.250	0.038	0.006	-0.007
129.5	135.0	-0.212	0.049	0.005	-0.006
129.5	145.0	-0.099	0.081	0.006	-0.003

B.2 July 2018

Table B.4: Compton scattering beam asymmetry Σ_3 for $\omega_\gamma = 86.3 - 98.2$ MeV extracted using July 2018 data.

$\boldsymbol{\omega_\gamma}$ [MeV]	$\boldsymbol{\theta_{\gamma'}}[^\circ]$	$\boldsymbol{\Sigma_3}$	$\boldsymbol{\Delta\Sigma_3}$(stat.)	$\boldsymbol{\Delta\Sigma_3}$(syst.)	$\boldsymbol{\Delta\Sigma_3}$(corr. $5/\sqrt{3}\%$)
92.2	35.0	0.078	0.366	0.170	0.002
92.2	45.0	-0.688	0.251	0.120	-0.020
92.2	55.0	-0.572	0.201	0.081	-0.017
92.2	65.0	-0.864	0.220	0.074	-0.025
92.2	75.0	-1.129	0.225	0.076	-0.033
92.2	85.0	-0.761	0.214	0.067	-0.022
92.2	95.0	-0.871	0.221	0.051	-0.025
92.2	105.0	-0.564	0.198	0.042	-0.016
92.2	115.0	-0.894	0.234	0.052	-0.026
92.2	125.0	-0.279	0.266	0.050	-0.008
92.2	135.0	-0.268	0.309	0.038	-0.008
92.2	145.0	-0.081	0.490	0.069	-0.002

Table B.5: Compton scattering beam asymmetry Σ_3 for $\omega_\gamma = 98.1 - 118.7$ MeV extracted using July 2018 data.

$\boldsymbol{\omega_\gamma}$ [MeV]	$\boldsymbol{\theta_{\gamma'}}[^\circ]$	$\boldsymbol{\Sigma_3}$	$\boldsymbol{\Delta\Sigma_3}$(stat.)	$\boldsymbol{\Delta\Sigma_3}$(syst.)	$\boldsymbol{\Delta\Sigma_3}$(corr. $5/\sqrt{3}\%$)
108.5	35.0	-0.369	0.130	0.108	-0.011
108.5	45.0	-0.514	0.090	0.068	-0.015
108.5	55.0	-0.438	0.075	0.057	-0.013
108.5	65.0	-0.729	0.073	0.047	-0.021
108.5	75.0	-0.733	0.066	0.039	-0.021
108.5	85.0	-0.756	0.066	0.035	-0.022
108.5	95.0	-0.746	0.071	0.035	-0.022
108.5	105.0	-0.602	0.061	0.026	-0.017
108.5	115.0	-0.408	0.063	0.018	-0.012
108.5	125.0	-0.230	0.066	0.008	-0.007
108.5	135.0	-0.265	0.081	0.013	-0.008
108.5	145.0	-0.057	0.150	0.049	-0.002

Table B.6: Compton scattering beam asymmetry Σ_3 for $\omega_\gamma = 118.7 - 140.4$ MeV extracted using July 2018 data.

$\boldsymbol{\omega_\gamma}$ [MeV]	$\boldsymbol{\theta_{\gamma'}}[^\circ]$	$\boldsymbol{\Sigma_3}$	$\boldsymbol{\Delta\Sigma_3}$(stat.)	$\boldsymbol{\Delta\Sigma_3}$(syst.)	$\boldsymbol{\Delta\Sigma_3}$(corr. $5/\sqrt{3}\%$)
129.5	35.0	0.000	0.121	0.045	0.000
129.5	45.0	-0.460	0.067	0.028	-0.013
129.5	55.0	-0.495	0.053	0.019	-0.014
129.5	65.0	-0.565	0.046	0.012	-0.016
129.5	75.0	-0.663	0.044	0.014	-0.019
129.5	85.0	-0.635	0.042	0.011	-0.018
129.5	95.0	-0.486	0.038	0.008	-0.014
129.5	105.0	-0.402	0.036	0.006	-0.012
129.5	115.0	-0.355	0.038	0.007	-0.010
129.5	125.0	-0.245	0.039	0.006	-0.007
129.5	135.0	-0.084	0.048	0.005	-0.002
129.5	145.0	-0.164	0.078	0.007	-0.005

Appendix C

Experimental asymmetry $A(\phi_{\gamma'})$

C.1 March 2018

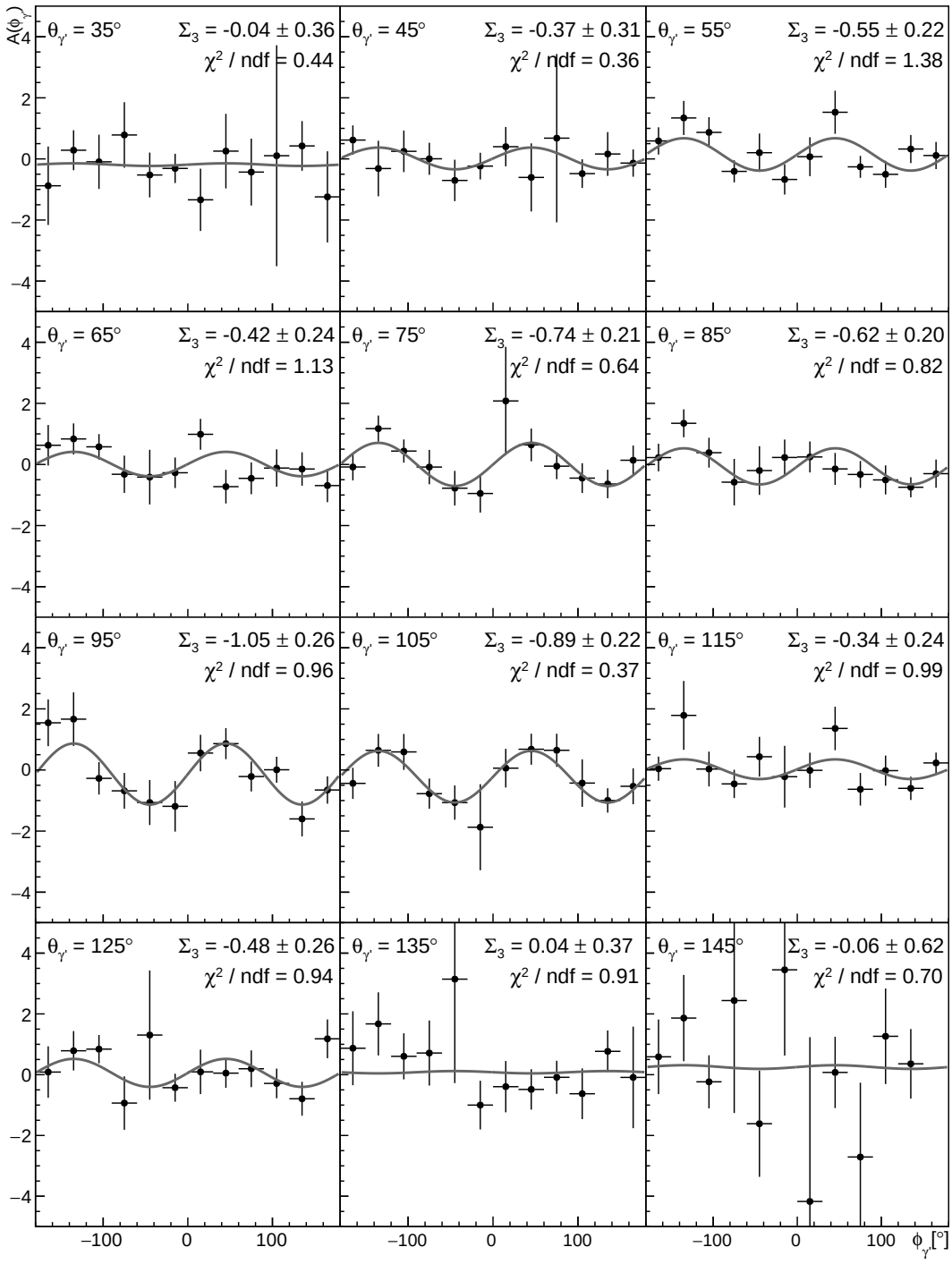

Figure C.1: Experimental asymmetry $A(\phi_{\gamma'})$ for the incoming beam energy $\omega_\gamma = 86.3 - 98.2$ MeV using the March 2018 dataset. The distributions were fitted using Eq. (9.11) and the results are shown within the plots.

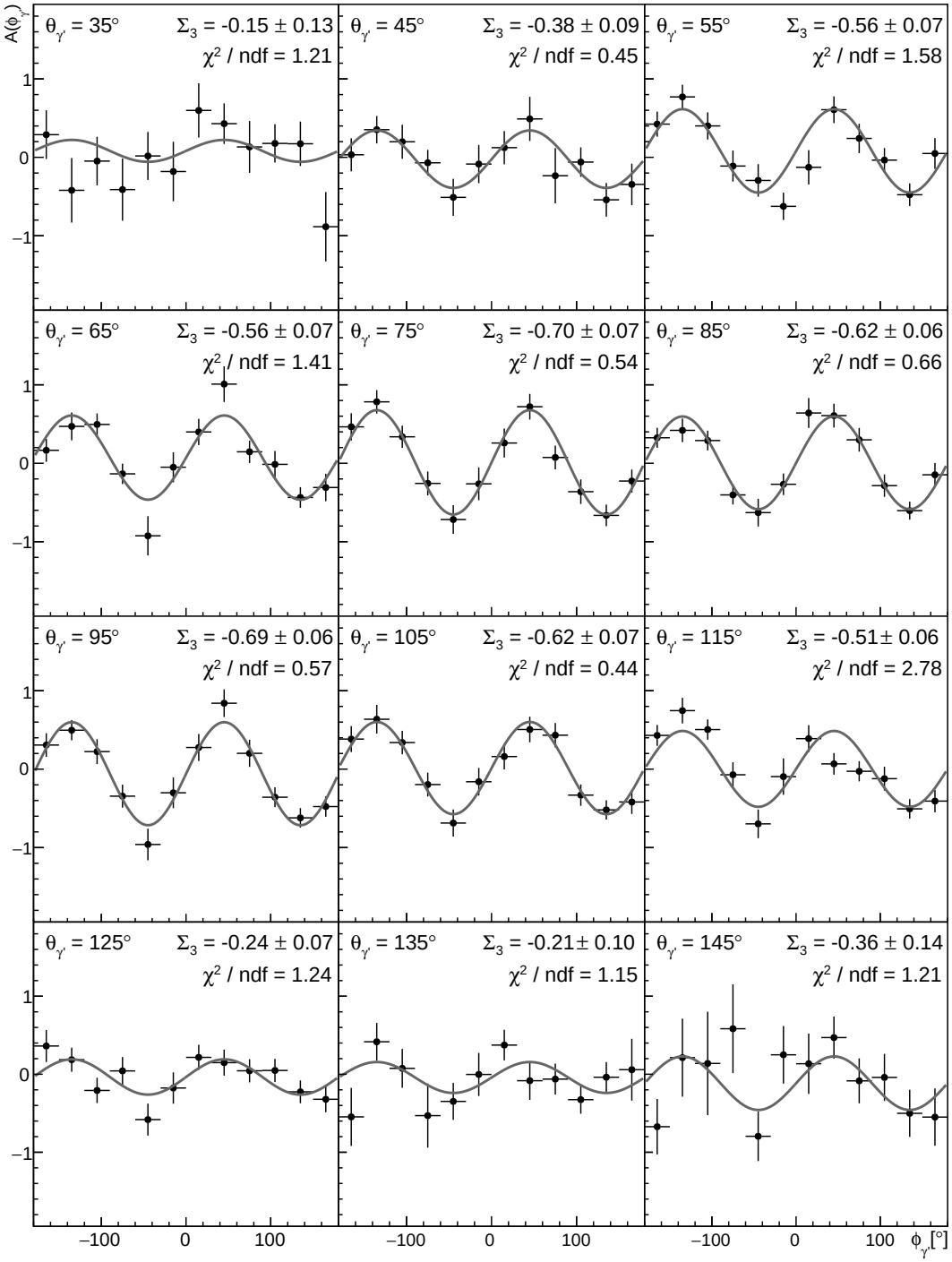

Figure C.2: Experimental asymmetry $A(\phi_{\gamma'})$ for the incoming beam energy $\omega_\gamma = 98.1 - 118.7$ MeV using the March 2018 dataset. The distributions were fitted using Eq. (9.11) and the results are shown within the plots.

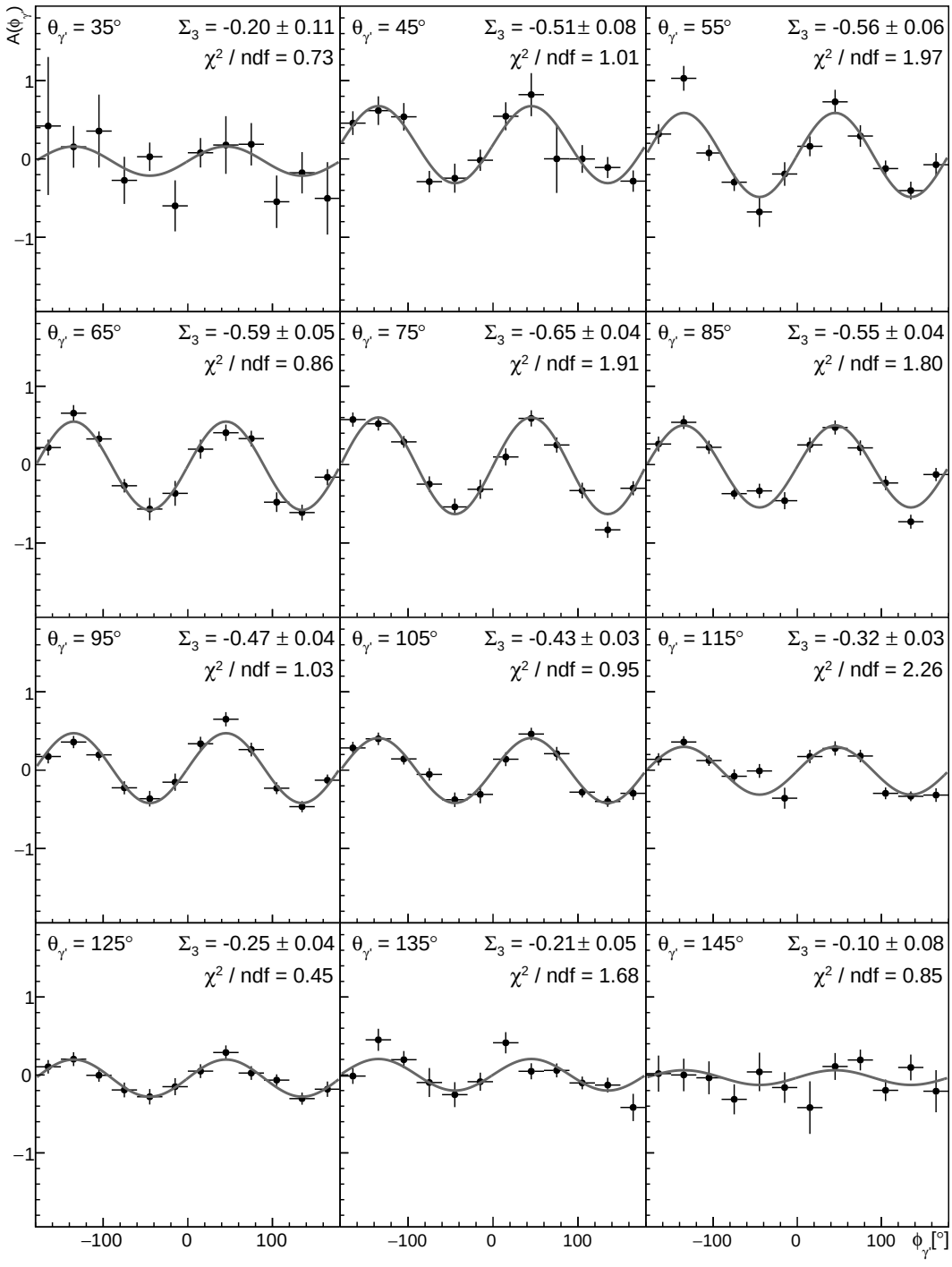

Figure C.3: Experimental asymmetry $A(\phi_{\gamma'})$ for the incoming beam energy $\omega_\gamma = 118.7 - 140.4$ MeV using the March 2018 dataset. The distributions were fitted using Eq. (9.11) and the results are shown within the plots.

C.2 July 2018

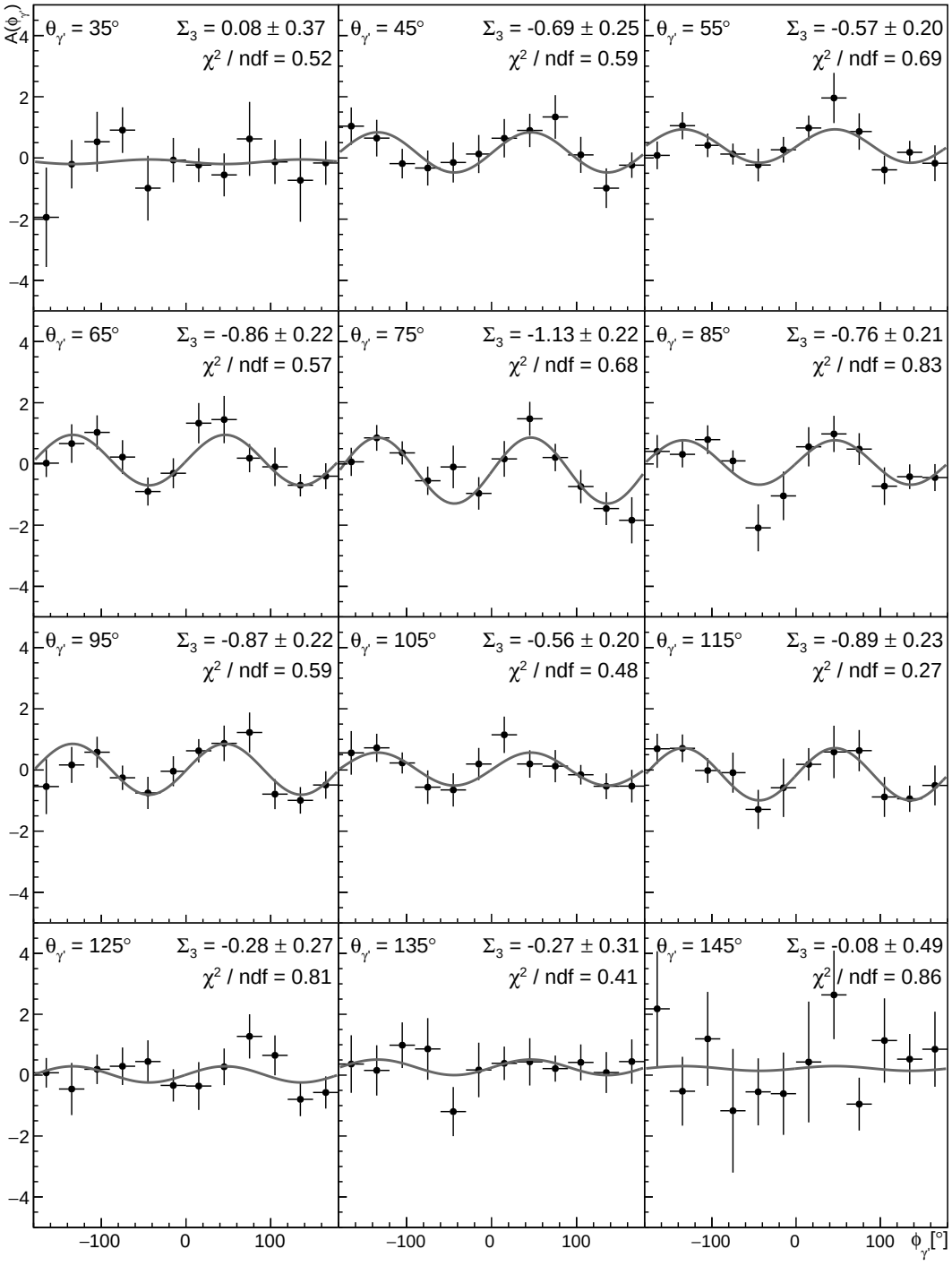

Figure C.4: Experimental asymmetry $A(\phi_{\gamma'})$ for the incoming beam energy $\omega_\gamma = 86.3 - 98.2$ MeV using the July 2018 dataset. The distributions were fitted using Eq. (9.11) and the results are shown within the plots.

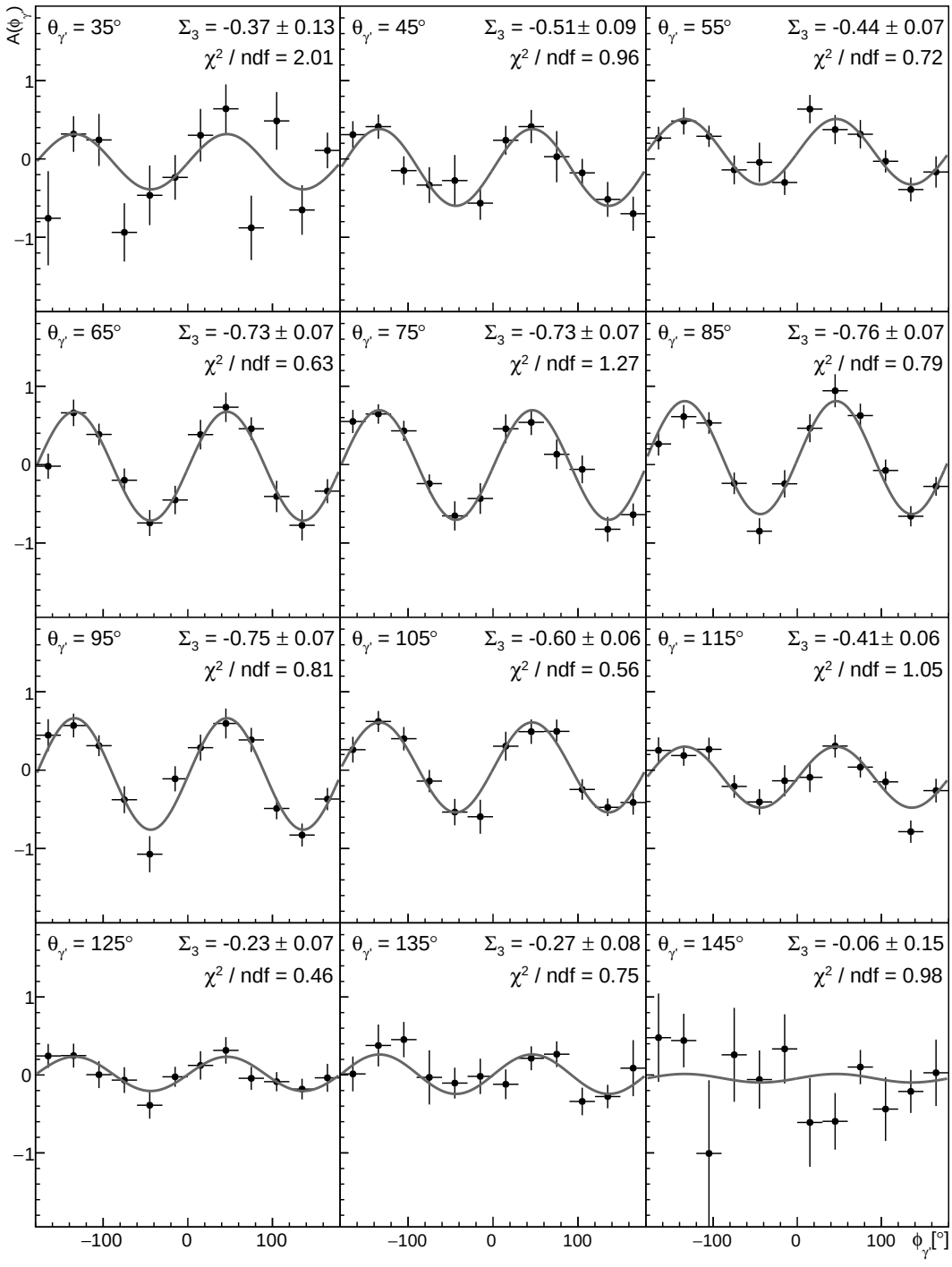

Figure C.5: Experimental asymmetry $A(\phi_{\gamma'})$ for the incoming beam energy $\omega_\gamma = 98.1 - 118.7$ MeV using the July 2018 dataset. The distributions were fitted using Eq. (9.11) and the results are shown within the plots.

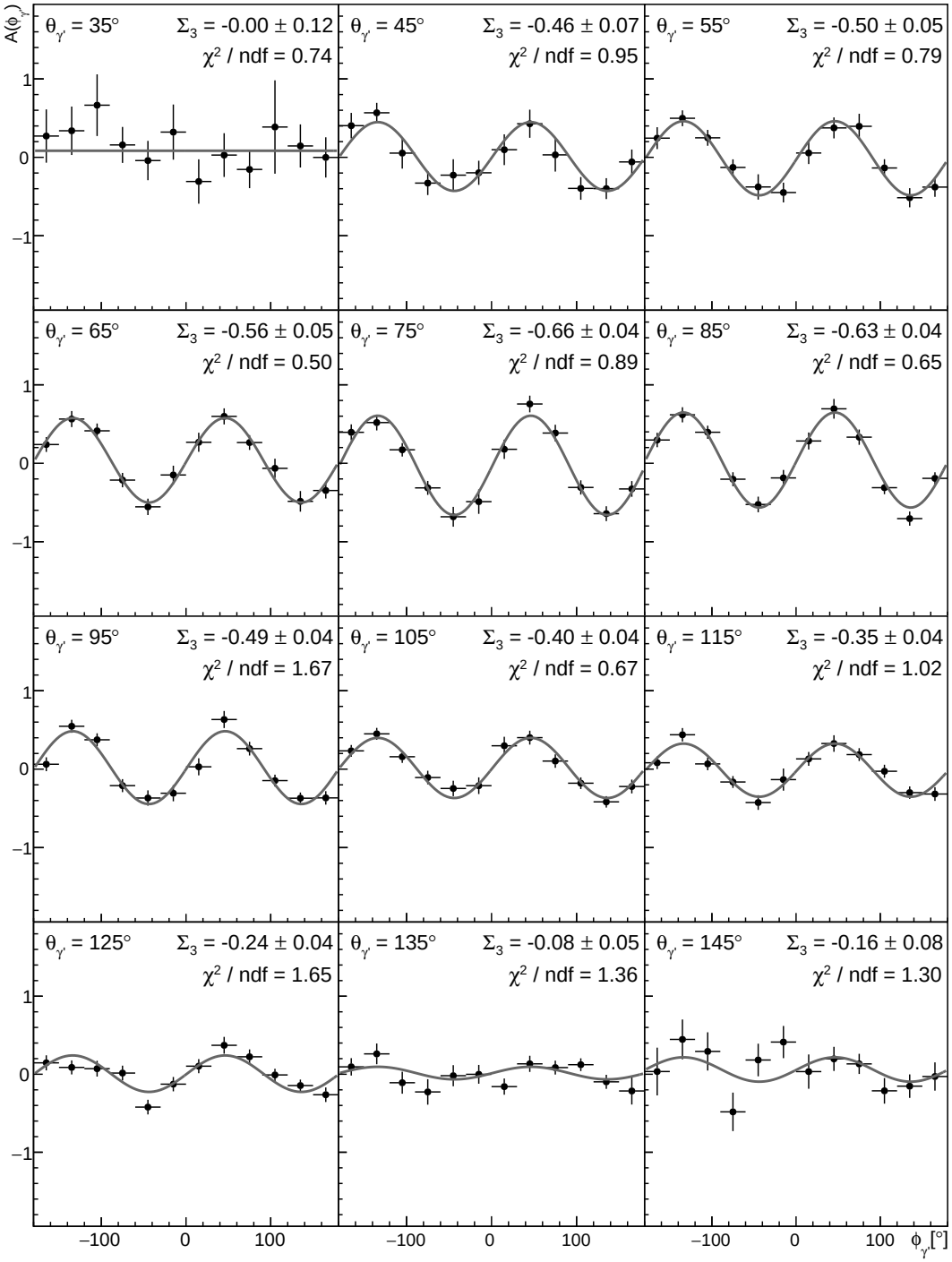

Figure C.6: Experimental asymmetry $A(\phi_{\gamma'})$ for the incoming beam energy $\omega_\gamma = 118.7 - 140.4$ MeV using the July 2018 dataset. The distributions were fitted using Eq. (9.11) and the results are shown within the plots.

Bibliography

[1] E. Rutherford, "The scattering of alpha and beta particles by matter and the structure of the atom", *Phil. Mag. Ser.6*, vol. 21, pp. 669–688, 1911.

[2] R. Pohl *et al.*, "The size of the proton", *Nature*, vol. 466, pp. 213–216, 2010.

[3] M. Gell-Mann, "A Schematic Model of Baryons and Mesons", *Phys. Lett.*, vol. 8, pp. 214–215, 1964.

[4] G. Zweig, "An SU_3 model for strong interaction symmetry and its breaking; Version 1", CERN, Geneva, Tech. Rep. CERN-TH-401, Jan 1964.

[5] G. Zweig, "An SU_3 model for strong interaction symmetry and its breaking; Version 2", no. CERN-TH-412, p. 80 p, Feb 1964.

[6] E. D. Bloom *et al.*, "High-Energy Inelastic e p Scattering at 6-Degrees and 10-Degrees", *Phys. Rev. Lett.*, vol. 23, pp. 930–934, 1969.

[7] M. Creutz, *Quarks, gluons and lattices*, ser. Cambridge Monographs on Mathematical Physics. Cambridge, UK: Cambridge Univ. Press, 1985.

[8] C. Gattringer and C. B. Lang, "Quantum chromodynamics on the lattice", *Lect. Notes Phys.*, vol. 788, pp. 1–343, 2010.

[9] A. H. Compton, "A Quantum Theory of the Scattering of X-rays by Light Elements", *Phys. Rev.*, vol. 21, pp. 483–502, 1923.

[10] B. Pasquini and M. Vanderhaeghen, "Dispersion Theory in Electromagnetic Interactions", *Ann. Rev. Nucl. Part. Sci.*, vol. 68, pp. 75–103, 2018.

[11] B. Pasquini, P. Pedroni, and S. Sconfietti, "Proton scalar dipole polarizabilities from real Compton scattering data using fixed-t subtracted dispersion relations and the bootstrap method", *Journal of Physics G: Nuclear and Particle Physics*, vol. 46, no. 10, p. 104001, sep 2019.

[12] F. Hagelstein, R. Miskimen, and V. Pascalutsa, "Nucleon Polarizabilities: from Compton Scattering to Hydrogen Atom", *Prog. Part. Nucl. Phys.*, vol. 88, pp. 29–97, 2016.

[13] H. W. Griesshammer, J. A. McGovern, and D. R. Phillips, "Comprehensive Study of Observables in Compton Scattering on the Nucleon", *Eur. Phys. J.*, vol. A54, no. 3, p. 37, 2018.

[14] A. Antognini *et al.*, "Proton Structure from the Measurement of $2S - 2P$ Transition Frequencies of Muonic Hydrogen", *Science*, vol. 339, pp. 417–420, 2013.

[15] R. Pohl *et al.*, "Laser spectroscopy of muonic deuterium", *Science*, vol. 353, no. 6300, pp. 669–673, 2016.

[16] A. Walker-Loud, C. E. Carlson, and G. A. Miller, "The Electromagnetic Self-Energy Contribution to M_p - M_n and the Isovector Nucleon Magnetic Polarizability", *Phys. Rev. Lett.*, vol. 108, p. 232301, 2012.

[17] V. Lensky, J. M. Alarcón, and V. Pascalutsa, "Moments of nucleon structure functions at next-to-leading order in baryon chiral perturbation theory", *Phys. Rev.*, vol. C90, no. 5, p. 055202, 2014.

[18] P. P. Martel *et al.*, "Measurements of Double-Polarized Compton Scattering Asymmetries and Extraction of the Proton Spin Polarizabilities", *Phys. Rev. Lett.*, vol. 114, no. 11, p. 112501, 2015.

[19] D. Paudyal *et al.*, "Extracting the spin polarizabilities of the proton by measurement of Compton double-polarization observables", *Phys. Rev. C*, vol. 102, no. 3, p. 035205, 2020.

[20] V. Sokhoyan *et al.*, "Determination of the scalar polarizabilities of the proton using beam asymmetry Σ_3 in Compton scattering", *Eur. Phys. J.*, vol. A53, no. 1, p. 14, 2017.

[21] M. I. Levchuk and A. I. L'vov, "Deuteron Compton scattering below pion photoproduction threshold", *Nucl. Phys.*, vol. A674, pp. 449–492, 2000.

[22] J. D. Jackson, *Classical Electrodynamics*. Wiley, 1998.

[23] P. P. Martel, "Measuring Proton Spin Polarizabilities with Polarized Compton Scattering", Ph.D. dissertation, University of Massachusetts - Amherst, 2013.

[24] J. Ahrens *et al.*, "First measurement of the Gerasimov-Drell-Hearn integral for Hydrogen from 200 to 800 MeV", *Phys. Rev. Lett.*, vol. 87, p. 022003, 2001.

[25] H. Dutz *et al.*, "First measurement of the Gerasimov-Drell-Hearn sum rule for H-1 from 0.7-GeV to 1.8-GeV at ELSA", *Phys. Rev. Lett.*, vol. 91, p. 192001, 2003.

[26] M. Camen *et al.*, "Backward spin polarizability gamma(pi) of the proton", *Phys. Rev.*, vol. C65, p. 032202, 2002.

[27] D. Babusci, G. Giordano, A. I. L'vov, G. Matone, and A. M. Nathan, "Low-energy Compton scattering of polarized photons on polarized nucleons", *Phys. Rev.*, vol. C58, pp. 1013–1041, 1998.

[28] B. R. Holstein, D. Drechsel, B. Pasquini, and M. Vanderhaeghen, "Higher order polarizabilities of the proton", *Phys. Rev.*, vol. C61, p. 034316, 2000.

[29] V. A. Petrun'kin, "Scattering of low-energy photons on a system with spin 1/2", *Sov. Phys. JETP*, vol. 13, p. 808, 1961.

[30] V. A. Petrun'kin, "Scattering of low-energy photons on a system with spin 1/2", *Sov. J. Part. Nucl*, vol. 12, p. 278, 1981.

[31] F. Wissmann, *Compton Scattering from the Proton*. Berlin, Heidelberg: Springer Berlin Heidelberg, 2004, pp. 9–36.

[32] J. L. Powell, "Note on the Bremsstrahlung Produced by Protons", *Phys. Rev.*, vol. 75, no. 1, p. 32, 1949.

[33] O. Klein and T. Nishina, "Über die Streuung von Strahlung durch freie Elektronen nach der neuen relativistischen Quantendynamik von Dirac", *Zeitschrift fur Physik*, vol. 52, no. 11-12, pp. 853–868, 1929.

[34] I. Guiasu and E. E. Radescu, "Comment on Proton Electromagnetic Polarizabilities", *Phys. Rev.*, vol. D18, pp. 1728–1730, 1978.

[35] I. Guiasu, C. Pomponiu, and E. E. Radescu, "Elastic gamma Proton Scattering at Low-Energies and Intermediate-Energies", *Annals Phys.*, vol. 114, pp. 296–331, 1978.

[36] M. Schumacher, "Polarizability of the nucleon and Compton scattering", *Prog. Part. Nucl. Phys.*, vol. 55, pp. 567–646, 2005.

[37] S. Weinberg, "Phenomenological Lagrangians", *Physica A*, vol. 96, no. 1-2, pp. 327–340, 1979.

[38] A. I. L'vov, V. A. Petrun'kin, and M. Schumacher, "Dispersion theory of proton Compton scattering in the first and second resonance regions", *Phys. Rev.*, vol. C55, pp. 359–377, 1997.

[39] D. Drechsel, B. Pasquini, and M. Vanderhaeghen, "Dispersion relations in real and virtual Compton scattering", *Physics Reports*, vol. 378, no. 2, pp. 99–205, 2003.

[40] B. Pasquini, D. Drechsel, and M. Vanderhaeghen, "Proton spin polarizabilities from polarized Compton scattering", *Phys. Rev.*, vol. C76, p. 015203, 2007.

[41] D. Drechsel, M. Gorchtein, B. Pasquini, and M. Vanderhaeghen, "Fixed t subtracted dispersion relations for Compton Scattering off the nucleon", *Phys. Rev.*, vol. C61, p. 015204, 1999.

[42] R. A. Arndt, I. I. Strakovsky, and R. L. Workman, "Updated resonance photodecay amplitudes to 2-GeV", *Phys. Rev.*, vol. C53, pp. 430–440, 1996.

[43] R. Arndt, W. Briscoe, I. Strakovsky, and R. Workman, "Analysis of pion photoproduction data", *Phys. Rev. C*, vol. 66, p. 055213, 2002.

[44] D. Drechsel, S. Kamalov, and L. Tiator, "Unitary Isobar Model - MAID2007", *Eur. Phys. J. A*, vol. 34, pp. 69–97, 2007.

[45] H. W. Griesshammer, J. A. McGovern, D. R. Phillips, and G. Feldman, "Using effective field theory to analyse low-energy Compton scattering data from protons and light nuclei", *Prog. Part. Nucl. Phys.*, vol. 67, pp. 841–897, 2012.

[46] V. Lensky and V. Pascalutsa, "Manifestly-covariant chiral PT calculation of nucleon Compton scattering", *Pisma Zh. Eksp. Teor. Fiz.*, vol. 89, pp. 127–132, 2009, [JETP Lett.89,108(2009)].

[47] V. Lensky and V. Pascalutsa, "Predictive powers of chiral perturbation theory in Compton scattering off protons", *Eur. Phys. J.*, vol. C65, pp. 195–209, 2010.

[48] J. A. McGovern, "Compton scattering from the proton at fourth order in the chiral expansion", *Phys. Rev.*, vol. C63, p. 064608, 2001, [Erratum: Phys. Rev.C66,039902(2002)].

[49] S. R. Beane, M. Malheiro, J. A. McGovern, D. R. Phillips, and U. van Kolck, "Nucleon polarizabilities from low-energy Compton scattering", *Phys. Lett.*, vol. B567, pp. 200–206, 2003, [Erratum: Phys. Lett.B607,320(2005)].

[50] S. R. Beane, M. Malheiro, J. A. McGovern, D. R. Phillips, and U. van Kolck, "Compton scattering on the proton, neutron, and deuteron in chiral perturbation theory to O(Q**4)", *Nucl. Phys.*, vol. A747, pp. 311–361, 2005.

[51] V. Pascalutsa and D. R. Phillips, "Effective theory of the delta(1232) in Compton scattering off the nucleon", *Phys. Rev.*, vol. C67, p. 055202, 2003.

[52] J. A. McGovern, D. R. Phillips, and H. W. Griesshammer, "Compton scattering from the proton in an effective field theory with explicit Delta degrees of freedom", *Eur. Phys. J.*, vol. A49, p. 12, 2013.

[53] A. M. Baldin, "Polarizability of nucleons", *Nuclear Physics*, vol. 18, pp. 310 – 317, 1960.

[54] L. Lapidus, "Scattering of Gamma Quanta and Polarizability of Nuclei and Nucleons", *Sov. Phys. JETP*, vol. 16, p. 964, 1963.

[55] M. Tanabashi *et al.*, "Review of Particle Physics", *Phys. Rev.*, vol. D98, no. 3, p. 030001, 2018.

[56] J. Melendez, R. Furnstahl, H. Grießhammer, J. McGovern, D. Phillips, and M. Pratola, "Designing Optimal Experiments: An Application to Proton Compton Scattering", 4 2020.

[57] P. Pedroni and S. Sconfietti, "A new Monte Carlo-based fitting method", *Journal of Physics G: Nuclear and Particle Physics*, vol. 47, no. 5, p. 054001, mar 2020.

[58] G. E. Pugh, R. Gomez, D. H. Frisch, and G. S. Janes, "Nuclear Scattering of 50- to 130-Mev gamma Rays", *Phys. Rev.*, vol. 105, pp. 982–995, 1957.

[59] C. L. Oxley, "Scattering of 25-87 Mev Photons by Protons", *Phys. Rev.*, vol. 110, pp. 733–737, 1958.

[60] L. G. Hyman, R. Ely, D. H. Frisch, and M. A. Wahlig, "Scattering of 50- to 140-Mev Photons by Protons and Deuterons", *Phys. Rev. Lett.*, vol. 3, pp. 93–96, 1959.

[61] G. Bernardini, A. O. Hanson, A. C. Odian, T. Yamagata, L. B. Auerbach, and I. Filosofo, "Proton compton effect", *Nuovo cim.*, vol. 18, pp. 1203–1236, 1960.

[62] V. I. Goldansky, O. A. Karpukhin, A. V. Kutsenko, and V. V. Pavlovskaya, "Elastic γ-p scattering at 40 to 70 MeV and polarizability of the proton", *Nucl. Phys.*, vol. 18, pp. 473 – 491, 1960.

[63] F. J. Federspiel, R. A. Eisenstein, M. A. Lucas, B. E. MacGibbon, K. Mellendorf, A. M. Nathan, A. O'Neill, and D. P. Wells, "The Proton Compton effect: A Measurement of the electric and magnetic polarizabilities of the proton", *Phys. Rev. Lett.*, vol. 67, pp. 1511–1514, 1991.

[64] A. Zieger, R. Van de Vyver, D. Christmann, A. De Graeve, C. Van den Abeele, and B. Ziegler, "180-degrees Compton scattering by the proton below the pion threshold", *Phys. Lett.*, vol. B278, pp. 34–38, 1992.

[65] E. L. Hallin *et al.*, "Compton scattering from the proton", *Phys. Rev.*, vol. C48, pp. 1497–1507, 1993.

[66] B. E. MacGibbon, G. Garino, M. A. Lucas, A. M. Nathan, G. Feldman, and B. Dolbilkin, "Measurement of the electric and magnetic polarizabilities of the proton", *Phys. Rev.*, vol. C52, pp. 2097–2109, 1995.

[67] V. O. de León *et al.*, "Low-energy Compton scattering and the polarizabilities of the proton", *Eur. Phys. J.*, vol. A10, pp. 207–215, 2001.

[68] A. L'vov, "Compton Scattering on Proton at Energies Up to 400-{MeV} and Finite Energy Sum Rules", *Sov. J. Nucl. Phys.*, vol. 34, p. 597, 1981.

[69] P. S. Baranov, G. M. Buinov, V. G. Godin, V. A. Kuznetsova, V. A. Petrunkin, L. S. Tatarinskaya, V. S. Shirchenko, L. N. Shtarkov, V. V. Yurchenko, and Yu. P. Yanulis, "Elastic Scattering of Photon by Protons in the Low-Energy Region", *Yad. Fiz.*, vol. 21, pp. 689–698, 1975.

[70] M. MacCormick *et al.*, "Total photoabsorption cross-sections for H-1, H-2 and He-3 from 200-MeV to 800-MeV", *Phys. Rev.*, vol. C53, pp. 41–49, 1996.

[71] G. Audit *et al.*, "DAPHNE: A Large acceptance tracking detector for the study of photoreactions at intermediate-energies", *Nucl. Instrum. Meth. A*, vol. 301, pp. 473–481, 1991.

[72] T. A. Armstrong *et al.*, "Total hadronic cross-section of gamma rays in hydrogen in the energy range 0.265-GeV to 4.215-GeV", *Phys. Rev.*, vol. D5, pp. 1640–1652, 1972.

[73] D. Babusci, G. Giordano, and G. Matone, "A New evaluation of the Baldin sum rule", *Phys. Rev.*, vol. C57, pp. 291–294, 1998.

[74] V. Lensky and J. A. McGovern, "Proton polarizabilities from Compton data using covariant chiral effective field theory", *Phys. Rev.*, vol. C89, no. 3, p. 032202, 2014.

[75] A. C. Davison and D. V. Hinkley, *Bootstrap Methods and their Application*, ser. Cambridge Series in Statistical and Probabilistic Mathematics. Cambridge University Press, 1997.

[76] G. Blanpied *et al.*, "N —> delta transition and proton polarizabilities from measurements of p (gamma polarized, gamma), p (gamma polarized, pi0), and p (gamma polarized, pi+)", *Phys. Rev.*, vol. C64, p. 025203, 2001.

[77] J. Beringer *et al.*, "Review of Particle Physics", *Phys. Rev.*, vol. D86, p. 010001, 2012.

[78] H. Fiebig, W. Wilcox, and R. Woloshyn, "A Study of Hadron Electric Polarizability in Quenched Lattice QCD", *Nucl. Phys. B*, vol. 324, pp. 47–66, 1989.

[79] C. W. Bernard, T. Draper, K. Olynyk, and M. Rushton, "Lattice QCD Calculation of Some Baryon Magnetic Moments", *Phys. Rev. Lett.*, vol. 49, p. 1076, 1982.

[80] E. Chang, W. Detmold, K. Orginos, A. Parreno, M. J. Savage, B. C. Tiburzi, and S. R. Beane, "Magnetic structure of light nuclei from lattice QCD", *Phys. Rev. D*, vol. 92, no. 11, p. 114502, 2015.

[81] R. Bignell, W. Kamleh, and D. Leinweber, "Magnetic polarizability of the nucleon using a Laplacian mode projection", *Phys. Rev. D*, vol. 101, no. 9, p. 094502, 2020.

[82] T. R. Hemmert, B. R. Holstein, J. Kambor, and G. Knochlein, "Compton scattering and the spin structure of the nucleon at low-energies", *Phys. Rev.*, vol. D57, pp. 5746–5754, 1998.

[83] K. B. Vijaya Kumar, J. A. McGovern, and M. C. Birse, "Spin polarizabilities of the nucleon at NLO in the chiral expansion", *Phys. Lett.*, vol. B479, pp. 167–172, 2000.

[84] G. C. Gellas, T. R. Hemmert, and U.-G. Meissner, "Complete one loop analysis of the nucleon's spin polarizabilities", *Phys. Rev. Lett.*, vol. 85, pp. 14–17, 2000.

[85] S. Kondratyuk and O. Scholten, "Compton scattering on the nucleon at intermediate energies and polarizabilities in a microscopic model", *Phys. Rev.*, vol. C64, p. 024005, 2001.

[86] E. P. Wigner, "Resonance Reactions and Anomalous Scattering", *Phys. Rev.*, vol. 70, pp. 15–33, 1946.

[87] E. Wigner and L. Eisenbud, "Higher Angular Momenta and Long Range Interaction in Resonance Reactions", *Phys. Rev.*, vol. 72, pp. 29–41, 1947.

[88] A. Badalian, L. Kok, M. Polikarpov, and Y. Simonov, "Resonances in Coupled Channels in Nuclear and Particle Physics", *Phys. Rept.*, vol. 82, pp. 31–177, 1982.

[89] A2 Collaboration, Official website, accessed: 2020-04-03.

[90] MESA, Official website, accessed: 2020-04-03.

[91] Institut für Kernphysik, Official website, accessed: 2020-04-03.

[92] A. Jankowiak, "The Mainz Microtron MAMI: Past and future", *Eur. Phys. J. A*, vol. 28S1, pp. 149–160, 2006.

[93] M. Dehn, K. Aulenbacher, R. Heine, H. Kreidel, U. Ludwig-Mertin, and A. Jankowiak, "The MAMI C accelerator: The beauty of normal conducting multi-turn recirculators", *Eur. Phys. J. ST*, vol. 198, pp. 19–47, 2011.

[94] K. Kaiser *et al.*, "The 1.5-GeV harmonic double-sided microtron at Mainz University", *Nucl. Instrum. Meth. A*, vol. 593, pp. 159–170, 2008.

[95] W. Leo, *Techniques for Nuclear and Particle Physics Experiments: A How to Approach.* Springer Berlin Heidelberg, 1987.

[96] F. Rambo *et al.*, "Enhancement of the linear polarization of coherent bremsstrahlung by collimation of the photon beam", *Phys. Rev. C*, vol. 58, pp. 489–501, 1998.

[97] F. N. Afzal, "Measurement of the beam and helicity asymmetries in the reactions $\gamma p \to p\pi^0$ and $\gamma p \to p\eta$", Ph.D. dissertation, Rheinischen Friedrich-Wilhelms-Universität Bonn, 2019.

[98] A. Rigamonti and P. Carretta, *Structure of Matter: An Introductory Course with Problems and Solutions*, ser. UNITEXT, Collana di Fisica e Astronomia. Milan: Springer, 2009.

[99] F. Natter, P. Grabmayr, T. Hehl, R. Owens, and S. Wunderlich, "Monte Carlo simulation and analytical calculation of coherent bremsstrahlung and its polarisation", *Nuclear Instruments and Methods in Physics Research Section B: Beam Interactions with Materials and Atoms*, vol. 211, no. 4, pp. 465 – 486, 2003.

[100] D. Lohmann *et al.*, "Linearly polarized photons at MAMI (Mainz)", *Nucl. Instrum. Meth. A*, vol. 343, pp. 494–507, 1994.

[101] K. Livingston, "The Stonehenge Technique. A new method for aligning coherent bremsstrahlung radiators", *Nucl. Instrum. Meth. A*, vol. 603, p. 205, 2009.

[102] H. Bethe and W. Heitler, "On the Stopping of fast particles and on the creation of positive electrons", *Proc. Roy. Soc. Lond. A*, vol. A146, pp. 83–112, 1934.

[103] J. McGeorge *et al.*, "Upgrade of the Glasgow photon tagging spectrometer for Mainz MAMI-C", *Eur. Phys. J. A*, vol. 37, pp. 129–137, 2008.

[104] A2 Collaboration, Internal wiki, accessed: 2020-05-06.

[105] A. Thomas, "Crystal Ball Hydrogen (Deuterium) Target Manual", internal report, Johannes Gutenberg-Universität Mainz, 2013.

[106] A2 Collaboration, Official website, accessed: 2020-05-07.

[107] B. M. K. Nefkens, "The Crystal Ball Technical Report 1", report, UCLA, 1995.

[108] M. Oreglia, "A Study of the Reactions $\psi' \to \gamma\gamma\psi$", Other thesis, Stanford University, 12 1980.

[109] P. Pedroni, Pivate communication.

[110] R. Novotny, "Performance of the BaF-2 calorimeter TAPS", *Nucl. Phys. B Proc. Suppl.*, vol. 61B, pp. 137–142, 1998.

[111] A. Gabler *et al.*, "Response of TAPS to monochromatic photons with energies between 45-MeV and 790-MeV", *Nucl. Instrum. Meth. A*, vol. 346, pp. 168–176, 1994.

[112] A2 Collaboration, Internal wiki, accessed: 2020-05-11.

[113] A2 Collaboration, Internal wiki, accessed: 2020-05-12.

[114] F. Haas, "Testmessungen an einem Paarspektrometer zur Online-Überwachung eines Photonenstrahls", Master's thesis, Johannes Gutenberg-Universität Mainz, 2013.

[115] G. Braun, H. Fischer, J. Franz, A. Grunemaier, F. Heinsius, K. Konigsmann, M. Schierloh, T. Schmidt, H. Schmitt, and H. Urban, "TDC Chip and Readout Driver Developments for COMPASS and LHC-Experiments", no. hep-ex/9810048. EHEP-98-08, pp. 564–568. 5 p, Nov 1998.

[116] COMPASS Collaboration, Official website, accessed: 2020-05-13.

[117] LHCb Collaboration, Official website, accessed: 2020-05-13.

[118] R. Brun and F. Rademakers, "ROOT: An object oriented data analysis framework", *Nucl. Instrum. Meth. A*, vol. 389, pp. 81–86, 1997.

[119] ROOT, Official website, accessed: 2020-06-11.

[120] ROOT, Official website, accessed: 2020-06-11.

[121] ROOT, Official website, accessed: 2020-06-11.

[122] A2 Collaboration, Official GitHub repository, accessed: 2020-11-16.

[123] D. Werthemüller, "Experimental study of nucleon resonance contributions to η-photoproduction on the neutron", Ph.D. dissertation, Universität Basel, 2014.

[124] C. Collicott, "Probing proton structure through single polarization observables of Compton Scattering and π^0-photoproduction within the $\Delta(1232)$ region", Ph.D. dissertation, Dalhousie University, 2013.

[125] A2 Collaboration, Official GitHub repository, accessed: 2020-11-16.

[126] A2 Collaboration, Official GitHub repository, accessed: 2020-06-23.

[127] S. Agostinelli *et al.*, "GEANT4–a simulation toolkit", *Nucl. Instrum. Meth. A*, vol. 506, pp. 250–303, 2003.

[128] J. Allison *et al.*, "Geant4 developments and applications", *IEEE Trans. Nucl. Sci.*, vol. 53, p. 270, 2006.

[129] J. Allison *et al.*, "Recent developments in Geant4", *Nucl. Instrum. Meth. A*, vol. 835, pp. 186–225, 2016.

[130] Geant4, Official website, accessed: 2020-06-23.

[131] Geant4, Official website, accessed: 2020-06-23.

[132] D. Werthemüller, "Internal report: Calibration procedure of A2 data using the CaLib software." accessed: 2020-06-23.

[133] K. Livingston, "CLAS note 2011-020", accessed: 2020-10-12.

[134] K. Livingston, Private Comunication.

[135] B. Efron and R. Tibshirani, *An introduction to the bootstrap*. CRC press, 1994.

[136] J. McGovern, "Notes on angle-averaging." Internal note.

[137] Jan Hartmann, "Measurement of Double Polarization Observables in the Reactions p $\rightarrow$ p 0 and p $\rightarrow$ p with the Crystal Barrel/TAPS Experiment at ELSA", Ph.D. dissertation, Rheinische Friedrich-Wilhelms-Universität Bonn, 2017.

[138] G. D'Agostini, "On the use of the covariance matrix to fit correlated data", *Nucl. Instrum. Meth. A*, vol. 346, pp. 306–311, 1994.

[139] F. James and M. Roos, "Minuit: A System for Function Minimization and Analysis of the Parameter Errors and Correlations", *Comput. Phys. Commun.*, vol. 10, pp. 343–367, 1975.

[140] S. Wolf *et al.*, "Compton scattering by the proton using a large acceptance arrangement", *Eur. Phys. J. A*, vol. 12, pp. 231–252, 2001.

[141] G. Galler *et al.*, "Compton scattering by the proton", *Phys. Lett. B*, vol. 503, pp. 245–255, 2001.

[142] M. Biroth, P. Achenbach, E. Downie, and A. Thomas, "Design of the Mainz Active Polarized Target", *PoS*, vol. PSTP2015, p. 005, 2016.

[143] P. Martel, D. Hornidge, and E. Downie, "Neutron Polarizabilities: An A2 Collaboration proposal for an experiment at MAMI", Tech. Rep. MAMI-A2-02, 2020.